

Improving the Performance of Magnetic Steel Coatings

Matthew Gareth Thomas

Department of Chemistry

Cardiff University

2017



DECLARATION

This work has not been submitted in substance for any other degree or award at this or any other university or place of learning, nor is being submitted concurrently in candidature for any degree or other award.

Signed: (candidate) Date:

STATEMENT 1

This thesis is being submitted in partial fulfillment of the requirements for the degree of PhD

Signed: (candidate) Date:

STATEMENT 2

This thesis is the result of my own independent work/investigation, except where otherwise stated, and the thesis has not been edited by a third party beyond what is permitted by Cardiff University's Policy on the Use of Third Party Editors by Research Degree Students. Other sources are acknowledged by explicit references. The views expressed are my own.

Signed: (candidate) Date:

STATEMENT 3

I hereby give consent for my thesis, if accepted, to be available online in the University's Open Access repository and for inter-library loan, and for the title and summary to be made available to outside organisations.

Signed: (candidate) Date:

STATEMENT 4: PREVIOUSLY APPROVED BAR ON ACCESS

I hereby give consent for my thesis, if accepted, to be available online in the University's Open Access repository and for inter-library loans **after expiry of a bar on access previously approved by the Academic Standards & Quality Committee.**

Signed: (candidate) Date:

Acknowledgments

Over the course of this study, there are a number of people I would like to thank as without them, it would have been impossible to complete this achievement.

Firstly, I would like to thank my supervisors Professors Phil Davies and Mike Bowker who have given me the most excellent support and guidance of the course of my study.

I'd like to thank Cogent Power Ltd. for their funding of the project and especially the advice of Andrew Nolan, Keith Jenkins, and Fiona Robinson in the industrial aspects of the project.

Thank you, Dr David Morgan and Dr Colan Hughes for your help and advice in the implementation and analysis of the XPS and NMR experiments.

I would like to take the time to thank everyone in, and those who have left, the Surface Science Group: Vicky, Rob, Liza, Charlie, Ryan, Dan, Jonas, Cat, Ibrahim, and Hatem for your friendship over the past 4 years. Especially, I would like to thank Emir and Julia as our "outdoor discussion sessions" has helped maintain my sanity.

Bronwen, congratulations on your bachelor's degree; if the work and dedication that you presented during your dissertation are anything to go by you'll have a stellar career.

I'd also like to thank the Cogent group in the engineering department for helping understand the engineering side of things. I can only hope my chemistry advice was just as useful.

Finally, I would like to thank my parents, as without their love and support I would not be where I am today.

Abstract

Grain orientated magnetic steels have applications in the electrical industry as components of power transformers. Power losses are observed in these devices due to the magnetostrictive effect. Aluminium phosphate coatings are applied to the steel to impart a tensile strength to the steel inhibiting the effects of magnetostriction, reducing losses. This thesis examines the development and application of aluminium metaphosphate coatings with the aim of improving the currently used aluminium orthophosphate coatings.

The experiments described here show that aluminium metaphosphate can be formed using a variety of readily available aluminium precursors and that the products are stable to the effects of thermal hydration. A combination of bulk and surface analysis techniques suggest that there is need to re-examine the accepted assignments of the O(1s) region of the XPS for aluminium metaphosphates.

The testing of the applications of the metaphosphates as stress coatings has yielded results indicating improved performances over the orthophosphate coatings. SEM analysis has shown that this is due to the formation of a phosphate film across the surface of the substrate imparting a greater degree of tension than orthophosphate coatings.

Investigations examined the proposal that the low temperature synthesis of mullite ($\text{Al}_6\text{Si}_2\text{O}_{13}$) is facilitated through the addition of Jahn-Teller active complexes. The findings showed that the addition of stable low-spin complexes resulted in the formation of mullite by 800 °C. Also, tested was the hypothesis that this synthesis route resulted in the formation of nano-scale mullite, but SEM image data has discounted this.

Table of Contents

Chapter 1: Introduction.....	1
Chapter 2: Experimental.....	19
Chapter 3: The Formation of Aluminium Metaphosphate.....	47
Chapter 4: The Analysis and Performance of Tensile Stress Coatings.....	90
Chapter 5: Mullite Powders as Tensile Stress Coatings.....	137
Chapter 6: Conclusions and Future Work.....	185

Detailed sub-headings and page numbers can be found in the contents sections of each chapter

Chapter 1: Introduction

Contents

1.1: Introduction	2
1.2: Electrical Steel.....	2
1.2.1: The Processing of Electrical Steels	3
1.2.2: The Magnetic Properties of Electrical Steel.....	5
1.2.3: Magnetostriction	7
1.3: Stress Coatings for Electrical Steels	9
1.4: Contemporary Research	11
1.5: Thesis Aims.....	14
1.6: References	15

1.1: Introduction

This Chapter aims to provide a background on the concepts of electrical steels and the power loss issues that arise from the magnetostriction effect. An historical evaluation will be provided on the industrial production of electrical steels and their coatings. This is followed with an introduction to the magnetostrictive effect and the use of tensile strength coatings towards inhibiting it. An overview of contemporary research will also be given to allow this study to be placed in a modern context. Later chapters in this study examine the use of various tensile strength coatings (including aluminium orthophosphate: AlPO_4 , aluminium metaphosphate: $\text{Al}(\text{PO}_3)_3$ and mullite: $\text{Al}_6\text{Si}_2\text{O}_{13}$) as a method of inhibiting the effects of magnetostriction.

1.2: Electrical Steel

The advent of electrical steels began with the work of Hadfield, who found that a reduction of power losses of up to four times could be achieved through the incorporation of aluminium or silicon in the steel¹. These processes led to the development of grain orientated steel (GOS) in 1934 by Goss² and its commercialisation by ARMCO in 1939¹.

The Goss process involves a series of hot and cold rollings, which result in the formation of crystal grains orientated to the [001] direction and aligned to the rolling direction. During this process, the steel is heated to a temperature of 1200 °C, resulting in the stimulation of secondary crystallisation of these grains whilst the addition of manganese sulphide prevents the formation and growth of other grains in what is known as a cube on edge process³. The regular orientation of the [001] grains greatly enhances the magnetic properties of the steel reducing energy losses. Steels produced via this method are generally referred to as conventional grain orientated (CGO) steel.

Through the refinement of the Goss production process, the magnetic properties of CGO steels were further enhanced by improvements in the purity of the resulting steel product. High permeability (HiB) steels were introduced by Nippon steel in 1965¹. This method improves on Goss' method by the removal of one of the cold rolling phases and the introduction of aluminium nitride (AlN). This results in an improvement in the alignment of the grains to the rolling direction and in the formation of much larger grains compared to CGO steel^{1,4}.

1.2.1: The Processing of Electrical Steels

After production of the CGO or HiB steel, the steel must undergo further processing steps to ensure its suitability for use as electrical steel; the full schematic for the processing steps are shown in figure 1.1.

In the first stage of the process, the steel is trimmed to size, followed by an annealing at temperatures between 950 and 1100 °C. The steel then undergoes de-scaling involving an acid wash and shot-bombardment (in which iron is fired at the surface) which results in the removal of dirt and iron oxide from the steel. The next stage of processing involves a series of cold rollings in order to reduce the thickness of the steel to the desired size which, depending on requirements, ranges from 0.23 to 0.35 mm. Following this, the steel is furnace annealed to remove any residual oil present from the cold rolling phases followed by heating under an atmosphere of hydrogen and nitrogen (with a composition ratio of 3:1) at 850 °C. This heating is designed to remove the relatively high levels of carbon in the steel which negatively affects the magnetic properties of the steel; carbon levels are reduced to less than 0.003%. Additional contaminants present in the steel (e.g. sulfur) are removed which results in a decrease in the brittleness of the resulting product. At the final part of this line the steel is coated with a slurry of magnesium oxide (MgO) and cured at 850 °C. In the following stage, the steel furnace annealed under a dry hydrogen atmosphere for a

period of five days at 1200 °C. This curing process promotes the growth of the grains responsible for the magnetic properties of electrical steels. Also during this process, there is a reaction between the applied MgO coating and fayalite (Fe_2SiO_4) present on the steel surface producing a glass film consisting of forsterite (Mg_2SiO_4). The forsterite film acts as a protective coating for the steel and provides a layer of electrical insulation for the steel sheets.

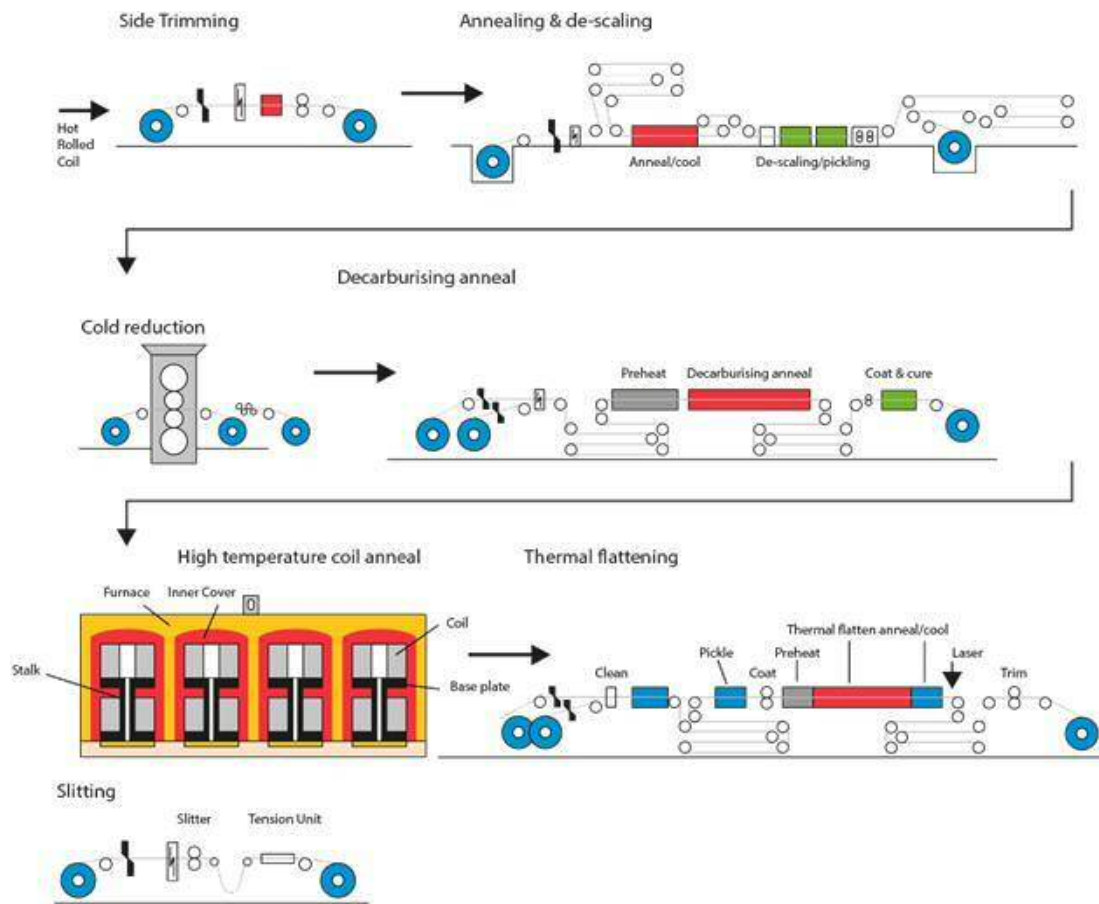


Figure 1.1: Schematic Diagram illustrating the production process for electrical steels at Cogent Power Ltd⁵.

The final stage of the process is the application of a phosphate coating. The coating is applied as the steel passes through a thermal flattening line at a temperature of 850 °C. As well as flattening the steel, this coating process provides a tensile stress to the steel which leads to an improvement in its magnetic properties; a schematic for the final coating process is shown in figure 1.2. With the processing now complete, the coated steel undergoes a final trim and if needed a laser scribing treatment which is used to reduce the size of the magnetic domains in the product.

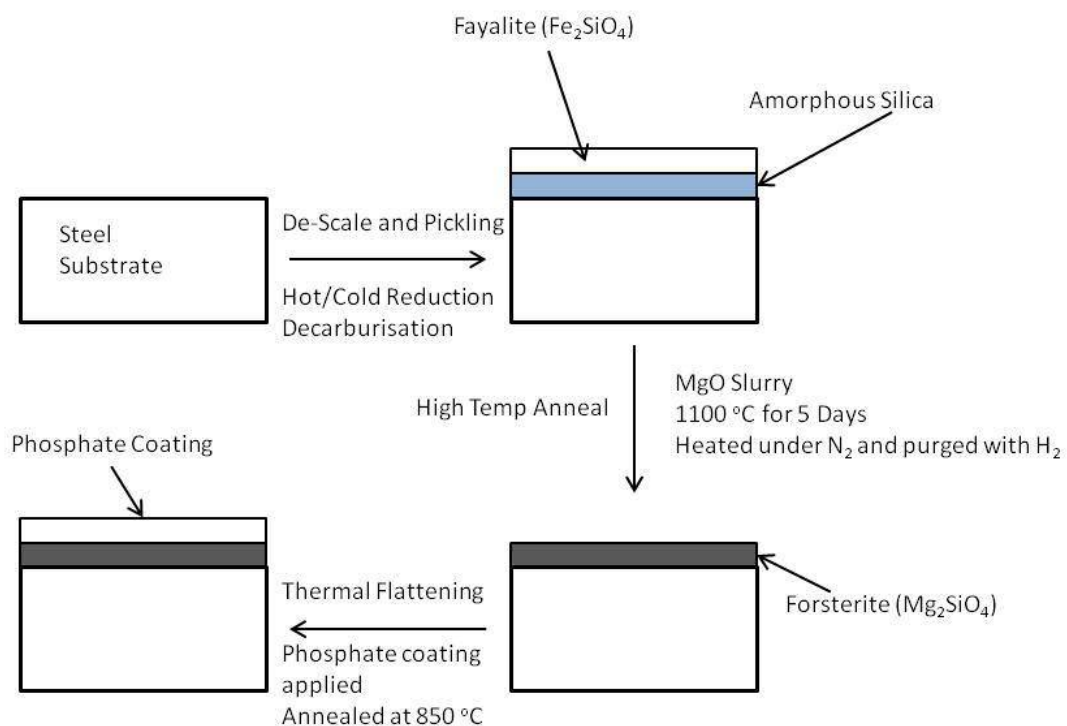


Figure 1.2: Diagram showing the coating application process for electrical steels.

1.2.2: The Magnetic Properties of Electrical Steel

Electrical steels are an example of a ferromagnetic material; ferromagnetic materials exhibit a spontaneous net magnetisation without the input of an external magnetic field. This property evolves from the parallel alignment of the magnetic dipoles of the electrons in the material, which arises due to the minimisation of energy interactions between neighbouring atoms.

Figure 1.3 shows an example of a hysteresis curve, which is a measure of the reliance of a magnetic system on its past and present environments and is given as the magnetic flux (B) against applied field strength (H). At the points of the intercepts with the B axis, the field strength is 0 and the magnetic flux is termed remanence (B_r)⁶. Soft magnetic materials (such as electrical steels) have a low remanence meaning the material is magnetised and demagnetised easily. Hard materials have a large remanence and so will remain magnetised for longer periods of time. With a large enough remanence, it is possible of a material to become permanently magnetised.

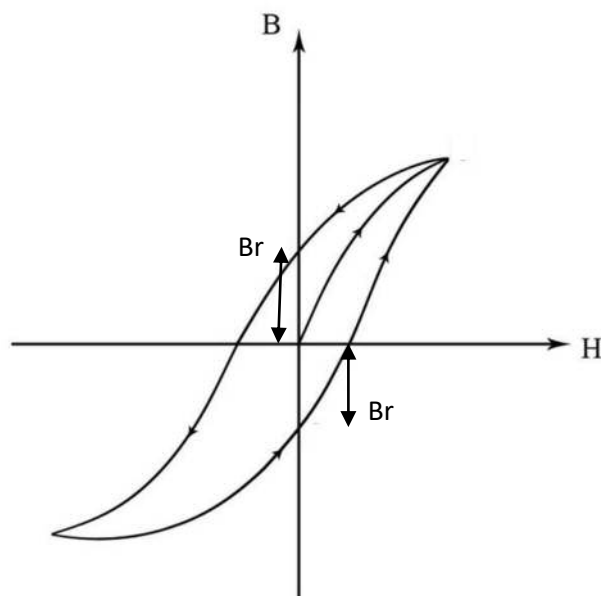


Figure 1.3: Example of a hysteresis curve showing the change in magnetic flux (B) against changes in field strength (H).

The increase of flux with respect to increasing field strength is due to the alignment of magnetic domains within the material; these domains are areas of uniform direction of the materials magnetic dipoles. At the extremes of the curve, plateauing is observed as a result of complete alignment of the magnetic domains in the material denoting magnetic saturation. The domain feature of magnetic materials arises from the attempts of the material to reduce its internal energy⁶. A ferromagnetic material with a single domain

would act as though it were a permanent magnet with the ends of domain being the magnetic poles⁷. This would result in the formation of a large magnetic field extending far out from the sample with a large amount of energy stored within the field. This amount of energy can be reduced if the sample forms two domains with oppositely aligned poles as this reduces the size of the external magnetic field. As more domains form, this energy is reduced further; however the walls between domains also store energy. The domain wall energy increases with magnetic anisotropy, which relates to the degree of alignment of the poles between neighbouring domains meaning the highest amount of domain wall energy occurs between domains with anti-parallel pole alignments⁸. The formation of domains continues until the energy reduced from the formation of domains is equal to that of the energy between the walls of the domains (Figure 1.4).

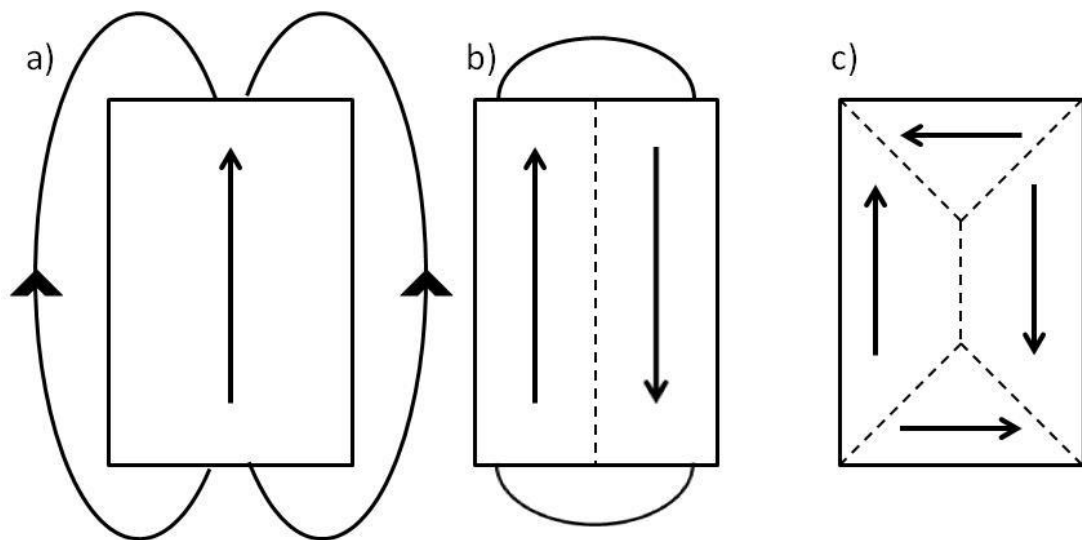


Figure 1.4: *The alignment of magnetic dipoles and external magnetic field in a ferromagnetic material for a) a single domain, b) a double domain and, c) a multi domain system.*

1.2.3: Magnetostriction

The magnetostrictive effect occurs in ferromagnetic systems when an applied magnetic field causes a saturation of magnetic alignments across all domains in the material. As

discussed in section 1.2.2, the magnetic dipoles in each domain are aligned but are offset between domains in order to reduce internal energy. On application of a magnetic field of sufficient strength, the material becomes magnetically saturated with the dipoles being aligned. This results in the multi-domain system converting to a single domain system; causing the formation of the hysteresis loop shown previously in Figure 1.4.

The reorganisation of the domain structure causes a strain to be placed on the material and leads to deformation of the material's dimension along the direction of the applied field (Figure 1.5); this is the magnetostrictive effect. This effect causes energy losses through the material via frictional heat and because A/C current causes a 180° change in field direction every $1/50^{\text{th}}$ of a second is responsible for the distinctive humming sound produced by electrical transformers.

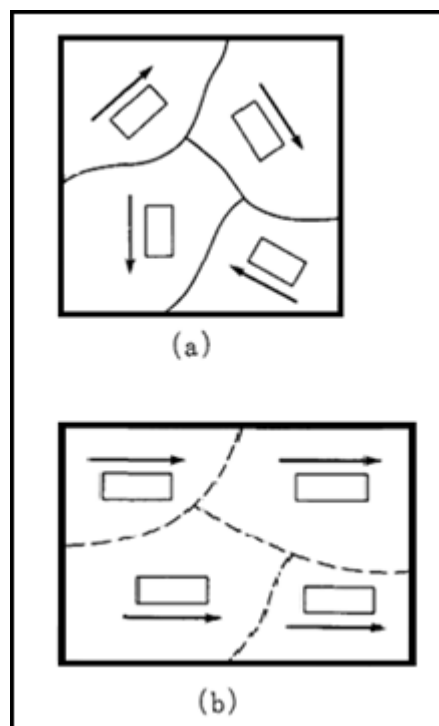


Figure 1.5: *The effect of magnetostriction on electrical steel; with a) no applied field and b) with an applied field⁹.*

Since this effect causes power losses efforts have been made to reduce the effects of magnetostriction on electrical steels. The industry standard for the reduction of magnetostriction is the application of a stress coating to the steel which provides a tensile hold to the substrate with the aim of physically preventing the change in dimensions of the material. These coatings (historically phosphate based) are discussed subsequently with the chemistry and performance evaluated in chapters 3 and 4 respectively.

1.3: Stress Coatings for Electrical Steels

To reduce the effects of magnetostriction, electrical steels are coated with a film designed to provide a tensile stress to the sample aimed at preventing the oscillation of domain sizes when subject to the changing magnetic field; historically these films have been phosphate based coatings. The first studies of these coatings date back to the 1970's¹ and initial analysis of the coatings showed that tension was being applied to the sample, with the applied stress measuring at 1.2 MPa^{10, 11}. It was also found that these coatings were much more effective when applied to samples with better degrees of grain orientation^{1, 12}.

Development of phosphate based coatings began by ARMCO in the late 1940's/ early 1950's^{13, 14} with development of coatings consisting of phosphoric acid and magnesia¹⁴ and later the introduction of the phyllosilicate muscovite $((\text{KF})_2(\text{Al}_2\text{O}_3)_2(\text{SiO}_2)_6)^{13}$. The addition of muscovite was aimed at reducing the issue of stopping the steel sheet laminations from sticking to one another; a problem that arose from coatings fusing to the steel whilst heating when the steel while it was rolled into a coil. The crystal structure of muscovite being plate-like allowed for the sheets to slide over each other alleviating this problem; the coating could be applied to the steel using rollers (with an annealing temperature of 760 °C). This method inhibited the sticking of laminations, but resulted in the formation of very hard sheets which greatly reduced the life span of cut laminations. The addition of

aluminium hydrate to phosphate based coatings by Steinhertz led to a less damaging coating with a reduction of burring on the steel sheets edges¹³.

Later developments led to the development of coatings based on magnesium oxide, aluminium oxide and phosphoric acid in various ratios throughout the 1970s^{3, 15, 16}. This coating mixture results in the formation of magnesium and aluminium phosphates through the reaction of the oxides with phosphoric acid. These coatings also saw the introduction of colloidal silica to the coating solution. The added silica was kept at less than 40% total volume to ensure the formation of a good glass film³. The introduction of silica to the coating was found to have a beneficial effect on the overall power loss of the steel samples. Studying the effects of the silica to phosphate ratio, loss reduction was found to increase with silica addition to the optimal value of 0.7 with performance dropping with continued silica addition; this is shown in figure 1.6^{17, 18}.

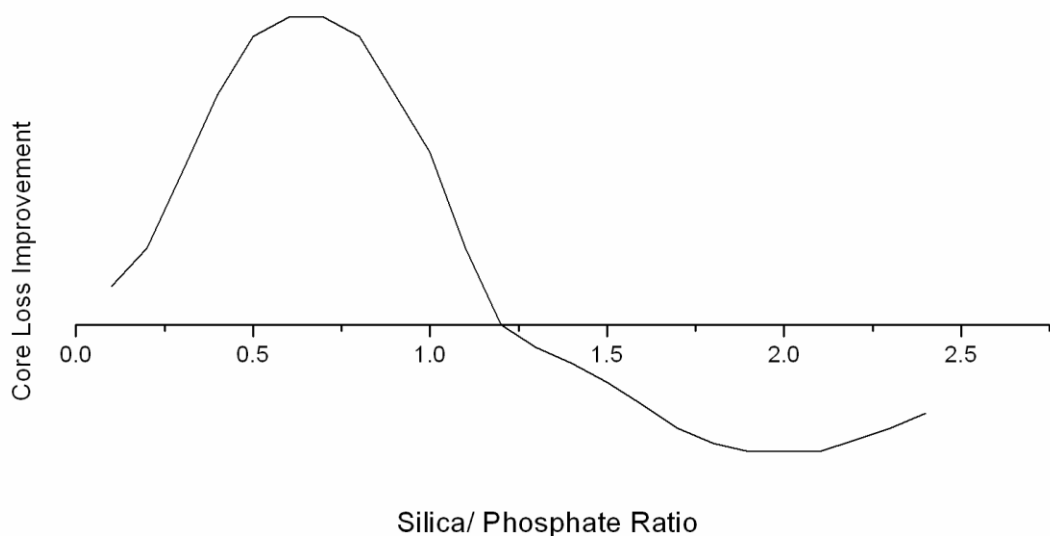


Figure 1.6: *The effects of Si:P ratio in the composition of stress coatings on improving power losses in electrical steels^{17, 18}.*

1.4: Contemporary Research

A great proportion of modern investigations into the field of magnetostriction focuses on the causes and reduction of the magnetostrictive effect through the study of the steel substrate¹⁹⁻⁴⁶. An example is a study by Niwa et al., of the magnetic properties of electrical steel sheets as a function of temperature³⁴. The investigation found that magnetostrictive effect exhibit by the samples increased with a non-uniform temperature distribution across the sample. It was found that with a temperature difference of 10 °C across the sample the magnetostriction increased by three times compared to uniform temperatures which was attributed to a large localised compressive stress in the centre of the sample when non-uniformly heated. In another study by Phway and Moses, the magnetostrictive trends of electrical steels under varying frequencies of magnetisation was investigated³⁷. For non-grain orientated 6.5% Si steels, measured magnetostriction was close to zero with peaks evolving at certain magnetic frequencies (figure 1.7). The frequencies at which magnetostriction was observed, was found to correspond to the harmonic resonance points of the steel samples. The study showed that even if a material is designed with no magnetostrictive properties, the effect can still potentially be observed if certain magnetic frequencies are present.

A 2012 study by Klimczyk et al. examined the effects of various sample cutting techniques on measured values of magnetostriction³¹. A variety of cutting techniques were employed across the work; guillotine, electrical discharge machining, and laser cutting. The magnetostriction measurements of the samples show a large variance depending on cutting technique. The increases in magnetostriction have been attributed to the additional compressive stresses applied to the samples during the cutting process.

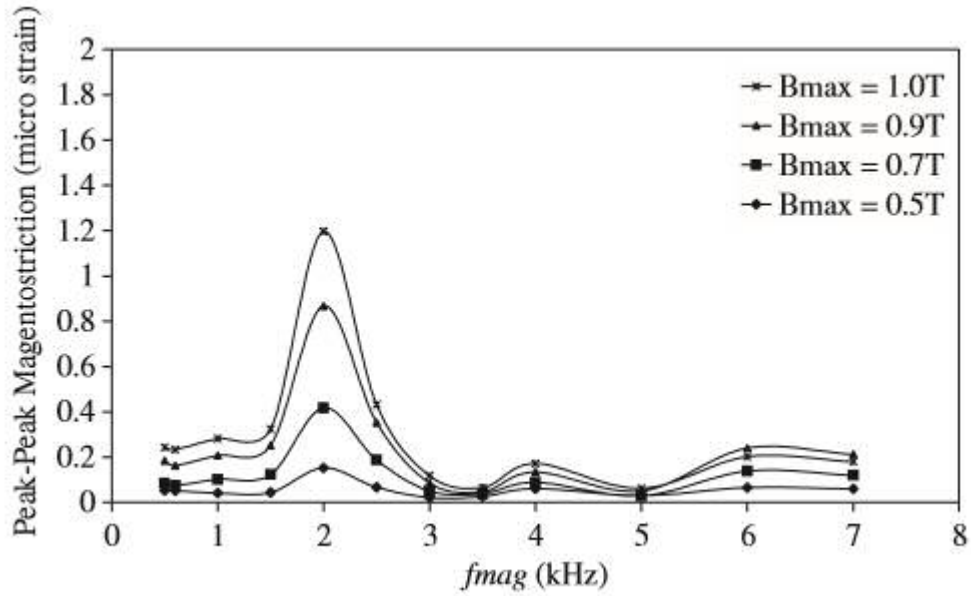


Figure 1.7: Chart illustrating the exhibited magnetostriction with respect to the resonance frequency of an applied magnetic field. Copied from reference³⁷

As well as the examination of the magnetic properties of electrical steels, a great deal of modern research has been conducted into the magnetostrictive effect of many other materials⁴⁷⁻⁶⁰. The various researches revolve around the use of rare earth metal and iron crystals. R-Fe (R = rare earth metal) compounds have been previously established as having large magnetostrictive properties⁶⁰. The rare earth metal sub-lattice provides a high magnetic anisotropy whilst spontaneous magnetisation occurs through the iron (or other transition metal) sub-lattice^{48, 51}. Whilst the work into magnetostriction of electrical steel revolves around the reduction of the power losses caused by the effect, the applications of rare earth metal compounds make use of the large magnetostrictions to produce products such as magnetically controlled cantilevers, memory and data storage devices, and analytical equipment of magnetic fields^{58, 59}.

With regards to contemporary research into aluminium phosphate based tensile stress coatings; comparatively little research has been conducted over the last 15 years, though with some work existing on phosphate coatings for other applications⁶¹⁻⁶³. A 2005 study by

Formanek et al. examined the evolution of aluminium phosphate coatings with the addition of ceramic (alumina and ceria) binders⁶⁴. The investigation tracked the evolution of phosphate species with respect to annealing temperature. Whilst the study provided data on the composition of the coatings, showing the transition of aluminium orthophosphate to metaphosphate, the coatings were designed and tested for their ability inhibit corrosive and oxidative effects on the substrate rather than an examination of its tensile stress properties. Though the research into aluminium phosphate based tensile stress coatings has been limited in recent years, there have been investigations into the development of stress coatings formulated with other materials. A series of studies by Goel et al, examined the use of industrially atypical coating techniques and formulations, including Cr-Al-N, Co-Ni-P, and Co-P-Carbon nanotubes⁶⁵⁻⁶⁷. The novel coatings were found to improve the performance of the electrical steel substrates by imparting a tensile strength reducing the magnetostrictive effect; this led to reductions in power loss by up to 15% in the case of the Co-P-CNT based coatings.

With the focus of this work being the analysis and modification of aluminium phosphate based coatings, this study should have value from an industrial viewpoint as any improvements found through this investigation would require minimal deviations from any industrial standards. This study will also provide an analysis of the reaction pathways in the formation of aluminium metaphosphate from both bulk and surface analysis techniques. Previous studies into aluminium metaphosphate have focused on either one aspect or the other, so an analysis of data through a combination of techniques may yield results of academic interest.

1.5: Thesis Aims

The overall aim of the research described in this thesis is to improve the performance of tensile stress coatings for reducing the effects of magnetostriction. The study will involve the analysis on the formation of the coatings, using a range of both bulk and surface analysis techniques. The performance of these coatings at reducing the effects of magnetostriction on steel substrates will be compared against the current on-line standard. The experimental procedures used throughout the study and the details of the analysis techniques used can be found in chapter 2.

The experiments performed over the course of this study can be split into three sections. Chapter 3 examines attempts at the formation of aluminium metaphosphate from the reaction of readily available precursors with phosphoric acid. The chapter will examine the formation of these phosphates with respect to annealing temperature, using both bulk and surface methods to catalogue their chemistry. Chapter 4 will look at the implementation of these phosphates as tensile coatings. Along with chemical analysis, the performance of the coatings will be tested against the current on-line standard coatings (aluminium orthophosphate based) at reducing the effects of magnetostriction. In chapter 5 an alternative to phosphate based coatings will be examined. The use of the aluminosilicate mullite ($\text{Al}_6\text{Si}_2\text{O}_{13}$) will be examined for its ability to reduce the magnetostrictive effect. The study will also examine the attempts at a low temperature and small particle size synthesis of mullite.

A summary of the findings given throughout this study can be found in Chapter 6. It will provide the conclusions of the work and a discussion of potential follow-up work that could further the understanding and performance of tensile coatings.

1.6: References

1. A. J. Moses, *IEE Proceedings A - Physical Science, Measurement and Instrumentation, Management and Education*, 1990, **137**, 233-245.
2. N. P. Goss, US Pat 1965559, 1934.
3. M. H. Haselkorn and D. S. Loudermilk, Google Patents, 1982.
4. B. Fukuda, K. Sato, T. Sugiyama, A. Honda and Y. Ito, in *ASM Conf. Hard and soft magnetic materials symp 8710-008*, Cincinnati, 1987.
5. C. Power, GOS Processing Diagram, <http://cogent-power.com/products/grain-oriented-electrical-steel/process-diagram>.
6. W. J. Duffin, *Electricity & Magnetism* McGraw-Hill Education, London, 1997.
7. J. W. Shilling and G. L. Houze, *IEEE Transactions on Magnetism*, 1974, **MA10**, 195-223.
8. S. Chikazumi, *Physics of Magnetism*, Robert E. Kriger Publishing Company, Malabar, 1978.
9. P. Klimczyk, PhD Thesis in *Novel Techniques for Characterisation and Control of Magnetostriction in G.O.S.S.*, Cardiff University, 2012.
10. A. J. Moses, S. M. Pegler and J. E. Thompson, *Electrical Engineers, Proceedings of the Institution of*, 1972, **119**, 1222-1228.
11. S. Szymura and B. Wyslocki, *Acta Physica Polonica A*, 1976, **49**, 627-631.
12. S. D. Washko and E. G. Choby, *IEEE Transactions on Magnetism*, 1979, **15**, 1586-1591.
13. H. A. Steinherz, US2743203, 1956.
14. C. E. Gifford, US Pat US2501846, 1950.
15. J. D. Evans, US Pat US3996073, 1976.
16. J. Evans, US Pat US3996073, 1976.
17. O. Tanaka, H. Kobayashi and E. Minematsu, *Journal of Materials Engineering*, 1991, **13**, 161-168.
18. D. Poultney and D. Snell, *Journal of Magnetism and Magnetic Materials*, 2008, **320**, e649-e652.
19. G. Ban, *Journal of Magnetism and Magnetic Materials*, 2003, **254**, 324-327.
20. G. Ban and P. E. Di Nunzio, *Journal of Magnetism and Magnetic Materials*, 2003, **254**, 265-268.

21. A. Belahcen, D. Singh, P. Rasilo, F. Martin, S. Gorji Ghalamestani and L. Vandeveld, *Ieee Transactions on Magnetics*, 2015, **51**.
22. F. Bohn, A. Gundel, F. J. G. Landgraf, A. M. Severino and R. L. Sommer, *Physica B-Condensed Matter*, 2006, **384**, 294-296.
23. C. Burgy, M. Wun-fogle, J. B. Restorff, E. Della Torre and H. ElBidweihi, *Physica B-Condensed Matter*, 2014, **435**, 129-133.
24. G. J. Cai, C. S. Li, B. Cai and Q. W. Wang, *Journal of Magnetism and Magnetic Materials*, 2017, **430**, 70-77.
25. S. Y. Cha, C. G. Kim and S. K. Chang, *Journal of Magnetism and Magnetic Materials*, 2002, **242**, 205-207.
26. D. Z. Chen, W. Zhao, B. D. Bai and B. I. Kwon, *International Journal of Applied Electromagnetics and Mechanics*, 2016, **52**, 1477-1484.
27. W. J. Gong, Z. G. Zhang, R. F. Hou, H. Wang, Z. Y. Xu, A. L. Lin, J. He, W. Fan and J. P. Wang, *Ieee Transactions on Magnetics*, 2015, **51**.
28. M. Hirano, Y. Ishihara, K. Harada and T. Todaka, *Journal of Magnetism and Magnetic Materials*, 2003, **254**, 43-46.
29. O. Hubert, L. Daniel and R. Billardon, *Journal of Magnetism and Magnetic Materials*, 2003, **254**, 352-354.
30. E. Hug, O. Hubert and J. J. Van Houtte, *Materials Science and Engineering a-Structural Materials Properties Microstructure and Processing*, 2002, **332**, 193-202.
31. P. K. Klimczyk, P. Anderson, A. Moses and M. Davies, *Ieee Transactions on Magnetics*, 2012, **48**, 1417-1420.
32. G. Loisos, A. J. Moses and P. Beckley, *Journal of Magnetism and Magnetic Materials*, 2003, **254**, 340-342.
33. S. S. Mbengue, N. Buiron and V. Lanfranchi, *Journal of Magnetism and Magnetic Materials*, 2016, **404**, 74-78.
34. H. Niwa, S. Yanase, S. Hashi and Y. Okazaki, *Journal of Magnetism and Magnetic Materials*, 2003, **254**, 376-378.
35. Y. Oda, H. Toda, N. Shiga, S. Kasai and T. Hiratani, *Ieee Transactions on Magnetics*, 2014, **50**.
36. Y. Okazaki, S. Yanase, H. Niwa and Y. Tani, *Electrical Engineering in Japan*, 2004, **149**, 8-14.
37. T. P. P. Phway and A. J. Moses, *Journal of Magnetism and Magnetic Materials*, 2008, **320**, E611-E613.
38. J. Polak, M. Petrenec and S. Degallaix, *Scripta Materialia*, 2002, **47**, 731-736.
39. P. Rasilo, D. Singh, A. Belahcen and A. Arkkio, *Ieee Transactions on Magnetics*, 2013, **49**, 2041-2044.

40. D. Singh, F. Martin, P. Rasilo and A. Belachen, *Ieee Transactions on Magnetism*, 2016, **52**.
41. S. Somkun, A. J. Moses and P. I. Anderson, *Iet Electric Power Applications*, 2016, **10**, 932-938.
42. S. Somkun, A. J. Moses, P. I. Anderson and P. Klimczyk, *Ieee Transactions on Magnetism*, 2010, **46**, 302-305.
43. T. Tomida, *Ieee Transactions on Magnetism*, 2002, **38**, 3186-3188.
44. Y. Ushigami, M. Mizokami, M. Fujikura, T. Kubota, H. Fujii and K. Murakami, *Journal of Magnetism and Magnetic Materials*, 2003, **254**, 307-314.
45. D. Vanoost, S. Steentjes, J. Peuteman, G. Gielen, H. De Gersem, D. Pissoort and K. Hameyer, *Journal of Magnetism and Magnetic Materials*, 2016, **414**, 168-179.
46. M. Wun-Fogle, J. B. Restorff, J. M. Cuseo, I. J. Garshelis and S. Bitar, *Ieee Transactions on Magnetism*, 2009, **45**, 4112-4115.
47. A. V. Andreev and S. Danis, *Journal of Alloys and Compounds*, 2009, **470**, 24-26.
48. D. S. Khoshnoud, L. Motevalizadeh and N. Tajabor, *Physica B-Condensed Matter*, 2013, **426**, 90-93.
49. M. Kuhnt, M. Marsilius, T. Strache, C. Polak and G. Herzer, *Scripta Materialia*, 2017, **130**, 46-48.
50. J. J. Liu, X. C. Liu, W. S. Zhang and P. Z. Si, *Journal of Magnetism and Magnetic Materials*, 2009, **321**, 4052-4056.
51. X. Y. Liu, J. J. Liu, Z. B. Pan, X. H. Song, Z. R. Zhang, J. Du and W. J. Ren, *Journal of Magnetism and Magnetic Materials*, 2015, **391**, 60-64.
52. T. Y. Ma, C. B. Jiang, X. Xu and H. B. Xu, *Journal of Alloys and Compounds*, 2005, **388**, 34-40.
53. N. V. Mushnikov and E. G. Gerasimov, *Journal of Alloys and Compounds*, 2016, **676**, 74-79.
54. Z. W. Ouyang, G. H. Rao, H. F. Yang, W. F. Liu, G. Y. Liu, X. M. Feng and J. K. Liang, *Journal of Physics-Condensed Matter*, 2003, **15**, 2213-2220.
55. W. J. Ren, S. W. Or, H. L. W. Chan, W. F. Li, X. G. Zhao, X. P. Song and Z. D. Zhang, *Ieee Transactions on Magnetism*, 2004, **40**, 2766-2768.
56. A. P. Ring, H. L. Ziegler, T. Lograsso, D. Schlager, J. E. Snyder and D. C. Jiles, *Journal of Applied Physics*, 2006, **99**.
57. S. K. Saha, M. D. Rahaman, M. A. Zubair and A. Hossain, *Journal of Alloys and Compounds*, 2017, **698**, 341-356.

58. M. M. Selvi, P. Manimuthu, K. S. Kumar and C. Venkateswaran, *Journal of Magnetism and Magnetic Materials*, 2014, **369**, 155-161.
59. Y. J. Seo, K. Harii, R. Takahashi, H. Chudo, K. Oyanagi, Z. Y. Qiu, T. Ono, Y. Shiomi and E. Saitoh, *Applied Physics Letters*, 2017, **110**.
60. L. Zhai, Y. G. Shi, S. L. Tang, Y. Wang, L. Y. Lv and Y. W. Du, *Journal of Alloys and Compounds*, 2009, **487**, 34-37.
61. L. F. Kravchenko, V. D. Kurochkin, M. V. Kolomytsev, O. M. Romanenko and N. A. Derenovskaya, *Powder Metallurgy and Metal Ceramics*, 2007, **46**, 398-403.
62. S. Stoeckel, S. Ebert, M. Boettcher, A. Seifert, T. Wamser, W. Krenkel, S. Schulze, M. Hietschold, H. Gnaegi and W. A. Goedel, *Chemical Vapor Deposition*, 2014, **20**, 388-398.
63. M. Vippola, J. Vuorinen, P. Vuoristo, T. Lepisto and T. Mantyla, *Journal of the European Ceramic Society*, 2002, **22**, 1937-1946.
64. B. Formanek, K. Szymanski, B. Szczucka-Lasota and A. Wlodarczyk, *Journal of Materials Processing Technology*, 2005, **164**, 850-855.
65. V. Goel, P. Anderson, J. Hall, F. Robinson and S. Bohm, *Ieee Transactions on Magnetism*, 2016, **52**.
66. V. Goel, P. Anderson, J. Hall, F. Robinson and S. Bohm, *Journal of Magnetism and Magnetic Materials*, 2016, **407**, 42-45.
67. V. Goel, P. Anderson, J. Hall, F. Robinson and S. Bohm, *Aip Advances*, 2016, **6**.

Chapter 2: Experimental

Contents

2.1 Introduction	20
2.2 Sample Preparations	20
2.2.1: Preparation of Powdered Aluminium Metaphosphate	20
2.2.2: Thermal Hydration of Phosphate Samples	20
2.2.3: Preparation of Mullite Samples	21
2.2.4: Supporting Aluminium Phosphate on Mullite	21
2.2.5: Preparation of Steel Samples.....	21
2.2.6: Coating Steel Samples.....	21
2.3 ATR-FTIR Spectroscopy	22
2.4 Raman Spectroscopy.....	25
2.5 NMR Spectroscopy.....	26
2.6 X-Ray Diffraction	30
2.7 X-Ray Photoelectron Spectroscopy.....	32
2.8 Scanning Electron Microscopy	38
2.9 Coating Effectiveness Testing Procedures	40
2.10 Experimental Strategy.....	44
2.11 References	46

2.1 Introduction

In this chapter, details on the preparation of samples and the techniques used in analysing them are presented. The experimental details for the preparation of both powder samples and coated films are provided. Following, is the basic background theory of the analytical techniques used throughout this study.

2.2 Sample Preparations

2.2.1: Preparation of Powdered Aluminium Metaphosphate

The preparation of aluminium metaphosphate was attempted using various precursors: aluminium hydroxide ($\text{Al}(\text{OH})_3$), aluminium nitrate nonahydrate ($\text{Al}(\text{NO}_3)_3 \cdot 9\text{H}_2\text{O}$), and aluminium chloride hydrate (AlCl_3).

AlX_3 ($\text{X} = \text{OH}$ (Sigma-Aldrich, Reagent Grade), NO_3 (Sigma-Aldrich, ACS Reagent, >98%) or Cl (Sigma-Aldrich, 99.99%)) was added to water (50 ml at 298K) and mixed until dissolved. H_3PO_4 (8.75 ml, Sigma-Aldrich, 85 %wt, 99.99% purity) was added and the solution was allowed to mix for 30 minutes. The reaction mixture was then heated on a hotplate to evaporate the water resulting in the formation of a viscous gel. The gel was then heated in air in a furnace to 800 °C forming a white powder; samples were taken at 300, 500 and 800 °C for analysis. The amount of AlX_3 added was to give a desired P/Al ratio; in this study, the ratios examined were 3:1 and 4:1.

2.2.2: Thermal Hydration of Phosphate Samples

Samples were tested for susceptibility to thermal hydration by placing them in a heated humidity chamber. Samples were heated to 65 °C in a humid atmosphere and periodically analysed to test for thermal hydration.

2.2.3: Preparation of Mullite Samples

Mullite was synthesised via the route proposed by Bagchi et al¹. A 0.5 M solution of $\text{Al}(\text{NO}_3)_3 \cdot 9\text{H}_2\text{O}$ was prepared to which $\text{Al}(\text{iOPr})_3$ and $\text{Si}(\text{OC}_2\text{H}_5)_4$ were added so that the ratio of $\text{Al}(\text{iOPr})_3$: $\text{Al}(\text{NO}_3)_3 \cdot 9\text{H}_2\text{O}$ was 3.5:1 and the ratio of Al:Si was 3:1 and 0.002 M CuSO_4 was added. The solution was stirred for 3 hours then heated to form a gel. The gel was dried at 105 °C and ground into a powder before being heated to 800 °C for 2 hours.

Modifications to the synthesis of the mullite, to examine the low temperature synthesis, were also made by substituting CuSO_4 with $\text{Fe}(\text{NO}_3)_3 \cdot 9\text{H}_2\text{O}$, $[\text{Fe}(\text{CN})_6]\text{K}_3$, CrCl_3 , $\text{Mn}(\text{OAc})_3$ were added using the same molar ratios. Additionally, changes to curing temperatures and times were made for all reactions; samples were cured at 300, 500 and 800 °C for two hours and at 800 °C for 1 and 1.5 hours.

2.2.4: Supporting Aluminium Phosphate on Mullite

The aluminium phosphate preparation method detailed in section 2.2.1 was followed. After the addition and mixing of phosphoric acid, mullite powder was added to the solution after which the procedure was resumed. Samples were taken at 300, 500 and 800 °C

2.2.5: Preparation of Steel Samples

Steel samples were prepared from Cogent Power coated magnetic steel strip by pickling in 20 %wt NaOH solution for 10 minutes, removing the pre-existing phosphate layer leaving the underlying forsterite layer. Steel samples (unless stated otherwise) used are rectangular strips with the dimensions 305 mm by 30 mm known as Epstein strips and are an industry standard used for such studies.

2.2.6: Coating Steel Samples

Coating mixtures were prepared from the various methods listed above; solutions were taken prior to the formation of gels. To the solutions, colloidal silica (SiO_2 , Ludox SM-40,

Sigma Aldrich) was added so that the Si:Al ratio was 2:1 and allowed to mix for a minimum of 30 minutes (test dependant).

Solutions were coated onto the steel substrates using either a spiral bar coater (Elcometer) with a coating depth of 12 μm for single sided coatings or using a bench-top electronic roller for double sided coatings. The coated substrates were cured at 850 $^{\circ}\text{C}$ for various times ranging from 30 seconds to 60 minutes.

Detailed information on the reaction conditions are listed in the respective discussions found later in this study.

2.3 ATR-FTIR Spectroscopy

Infrared (IR) spectroscopy is a widely used experimental technique for probing molecular bonds. A vibrational adsorption technique, a molecule will absorb radiation of the frequency of the vibrations of the molecular bonds present. The common wavelength range used in IR spectroscopy is 400-4000 cm^{-1} ; the mid-infrared region. Banwell and McCash² provide a detailed explanation of the theory of IR spectroscopy and the interaction between molecular bonds and infrared radiation, the section details the specific experimental setup used throughout this study.

The absorbed radiation causes the molecular excitation from one vibrational energy level to higher level. When the frequency of the incident radiation matches the energy gap between the vibrational energy levels of the sample molecule, the transition will occur. Since the adsorbed frequencies of radiation are not detected by spectrometer instrumentation, a spectrum is created by the drop off in signal intensity as shown in figure 2.1. The vibrational excitations result in stretching and bending modes in the atomic bonds between atoms in the sample. These vibrations are governed by Hooke's Law (Eq. 2.1) which shows that the lighter the atoms, the more energy is required to excite the

vibrations. This effect leads to the formation of regions in the spectra based on atomic mass and bond type³.

$$\nu = (1/(2\pi c))(k/\mu)^{1/2}$$

Equation 2.1: Equation defining the excitation frequency of vibrations during IR spectroscopy, where:

ν = energy wavenumber, c = speed of light, k = force constant, μ = reduced mass.

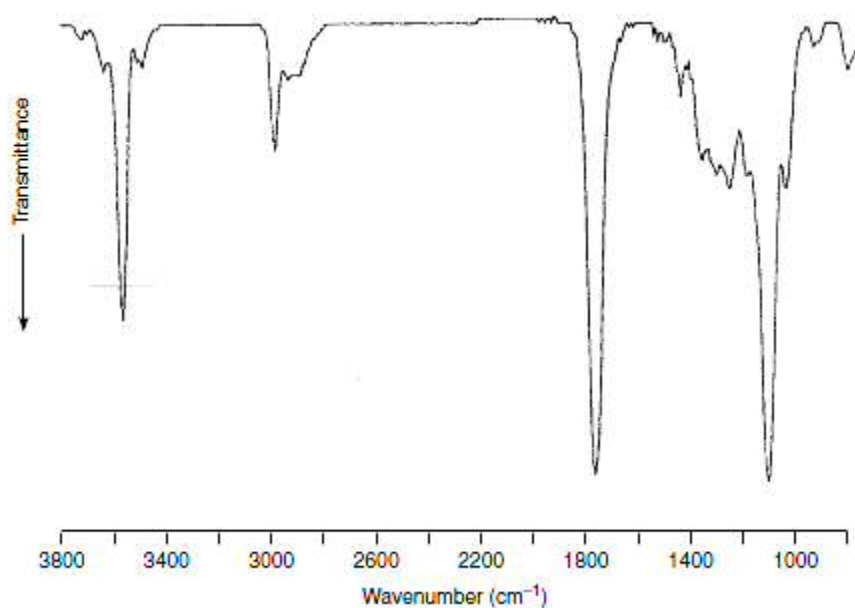


Figure 2.1: Example of an infra-red spectrum. The peaks at which transmission drops relate to the adsorption of IR radiation by molecular bonds.

The spectrometer used throughout the study is a Varian 600 UMA FT-IR Microscope with an attenuated total reflectance (ATR) germanium attachment. An FTIR (Fourier Transform Infrared) spectrometer employs a mirrored interferometer which the transmitted radiation passes through before the sample. This results in the production of an interferogram which can be mathematically processed via a Fourier transform to produce a spectrum. The benefits of using a Fourier transform are increased speed in the collection of spectra and an improvement in the signal-to-noise ratio due to all frequencies being collected simultaneously.

The use of an ATR attachment provides additional improvements over traditional IR spectroscopy; improved signal intensity, improved surface sensitivity and reduced sample preparation time. In ATR-IR spectroscopy, a high refractive index crystal is brought into contact with the sample. The incident radiation is internally refracted through the crystal causing the formation of an evanescent wave, when it hits the surface of the crystal, which partially extends into the sample (figure 2.2). Any adsorption of the evanescent wave by the sample is detected and used to produce the spectrum with a surface sensitivity of approx 1 micron. However, the disadvantages of this technique are that it requires a good contact between the sample and the crystal and that the refractive index of the crystal must be higher than that of the sample.

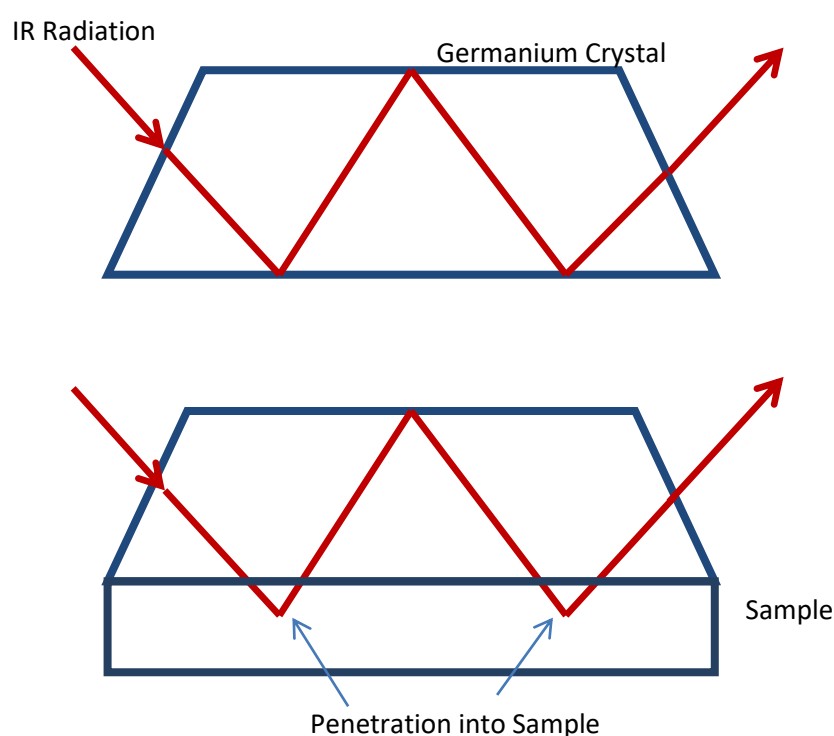


Figure 2.2: Schematic of IR radiation resonance through germanium ATR crystal and evanescent penetration into sample.

2.4 Raman Spectroscopy

Akin to IR spectroscopy, Raman spectroscopy is a vibrational technique which probes molecular bonds. Whilst the selection rules for IR spectroscopy require a permanent electric dipole to be active, in Raman spectroscopy a change in polarisability is required and as such these are complimentary techniques. As in the case of IR spectroscopy, Banwell and McCash² provide detailed explanations of the background theory, here a summary of the Raman technique is provided.

In Raman spectroscopy, the sample is irradiated with monochromatic light during which the photons can interact in numerous ways with the sample. The majority of the photons exhibit Rayleigh or elastic scattering in which there is no change in the incident and emitted photons. The remaining small percentage of photons exhibit Raman or inelastic scattering, when there is a change in energy between the incident and scattered radiation. An energy gain in the photon is known as Stokes scattering and an energy loss is known as Anti-Stokes scattering (figure 2.3).

The Raman Effect occurs due to the interaction of the incident photon with an oscillating electric field. This causes an electric dipole moment in the sample which emits radiation with a larger or smaller energy than the incident photon. Due to the quantisation of energy, the scattered light will only be altered by discrete amounts and as such, the Raman shifts away from the frequency of the incident radiation can be measured to provide a spectrum.

The experimental setup used in this study, is a Renishaw microscope with an argon (Ar^+) laser giving a monochromatic wavelength of 514 nm.

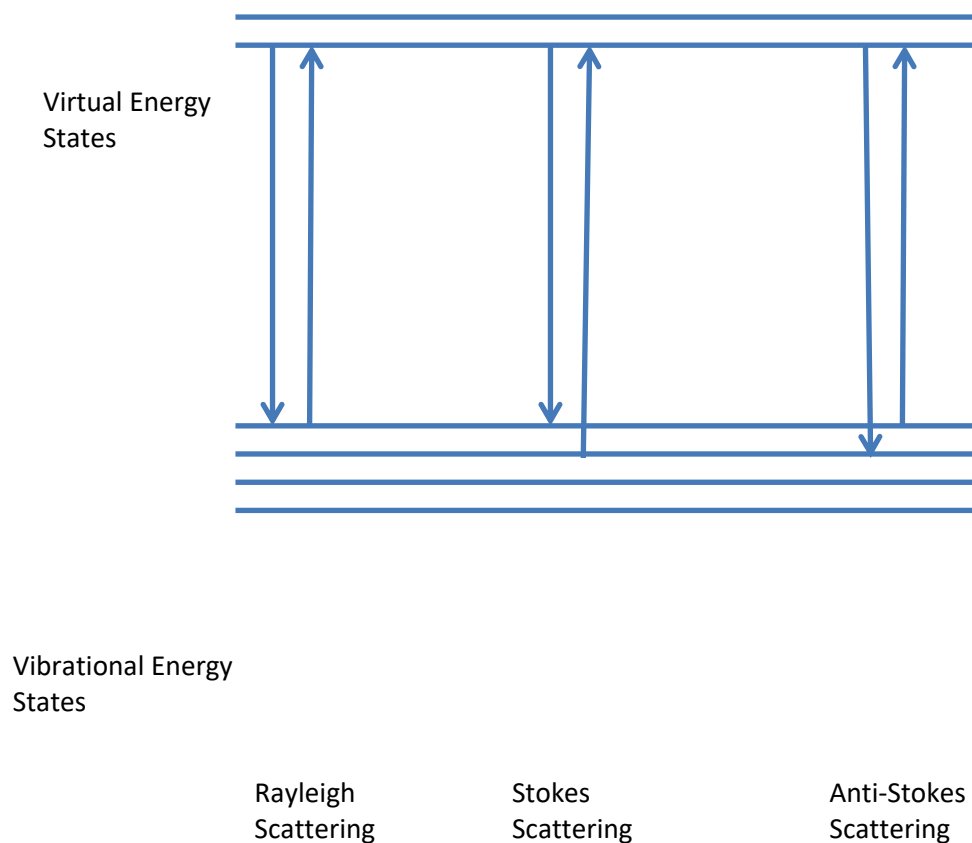


Figure 2.3: Energy Diagram illustrating elastic and inelastic scattering processes in vibrational spectroscopy.

2.5 NMR Spectroscopy

Nuclear magnetic resonance (NMR) spectroscopy is a widely used technique which probes the chemical environments of atomic nuclei. NMR spectroscopy is based on the magnetic properties of nuclei (such as angular momentum or magnetic moments). These give nuclei the property of spin, which relate to the spin quantum number (I) and magnetic quantum number (m_I). The spin states of a nucleus are normally energetically degenerate; however within the effect of magnetic field, an energy gap becomes present between the spin states which is related to the effect of strength of the field (known as the Zeeman effect)(figure 2.4). The energy gap between the now non-degenerate spin states is in the region of the

ultrahigh frequency end of the radio wave region of the EM spectrum meaning that this frequency of radiation is able to excite a nucleus from the lower to higher spin state⁴.

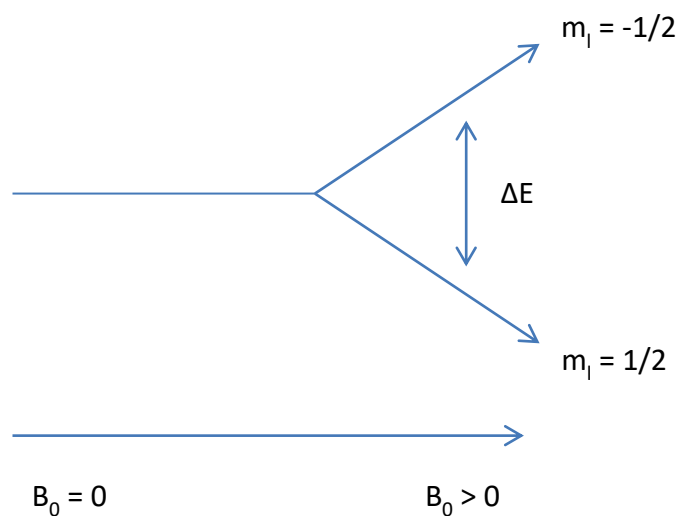


Figure 2.4: Diagram of the Zeeman Effect, the loss of degeneracy in nuclear spin states upon application of a magnetic field.

The surrounding electrons of the atom cause the local magnetic field of the nucleus to differ in magnitude from the applied field. These changes in the field alter the energy gap between the two spin states and so nuclei in differing chemical environments excite at different frequencies; and effect known as “chemical shift”. The frequencies at which the nuclear spin states of the probed nuclei resonate differ depending on the chemical environment it exists in. The presence of the applied magnetic field causes the electrons in the sample to generate a counteractive field. The presence of this field results in an electronic shielding effect on the nucleus against the effects of the applied field. If probed nuclei are bonded to atoms with differing electronegativity, the resonance frequencies will also differ giving rise to the chemical shift; e.g. the presence of an electron withdrawing group will reduce the shielding of the probed nucleus. The measured shifts in NMR spectroscopy are given against a reference molecule as described in equation 2.2; given that the resonance frequency of the sample and reference are given in Hz and the

spectrometer frequency is given in MHz the units for chemical shift are quoted in ppm (10^{-6}).

$$\delta = (v_{\text{sample}} - v_{\text{ref}}) / v_{\text{spec}}$$

Equation 2.2: Equation defining the chemical shift of NMR in ppm, where: v_{sample} = resonant freq of sample (Hz), v_{ref} = resonant freq of reference (Hz), v_{spec} = spectrometer frequency (MHz)

As well as the interactions with the electronic shielding effects described above, the probed nuclei can interact with other nearby nuclei through a coupling of spin states, known as J-coupling, and leads to signal multiplicity in the resulting spectrum. The multiplicity of the peaks (for spin $\frac{1}{2}$ nuclei) is $n + 1$, where n is the number of J-coupled spins (that are chemically inequivalent) to the probed nuclei. The multiplet peaks have an intensity that follows the coefficients of Pascal's triangle.

The combination of the effects of chemical shift and J-coupling allows NMR to differentiate between nuclei in different chemical environments and why it is such a powerful analytical tool⁵; an example NMR spectrum is given in Figure 2.5.

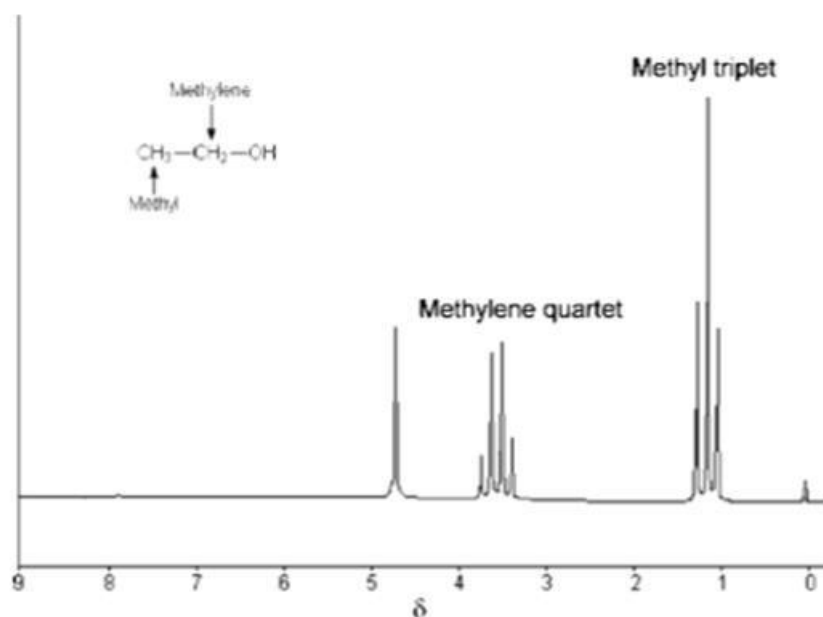


Figure 2.5: Example ^1H NMR spectrum for an ethanol molecule. Taken from reference⁶

In the figure the ^1H NMR spectrum for ethanol is shown. The signal assigned to the methyl group shows a triplet multiplet, arising from the coupling of the methyl protons to the two protons of the methylene group. In turn, the methylene signal shows a quartet splitting as those protons are coupled to the 3 of the methyl group. The third signal corresponds to the hydroxyl group and is furthest downshifted from as its proton has the greatest degree of deshielding from the electronegative oxygen⁶.

All the samples studied in later chapters, are solids and additional experimental considerations are required to account for this. The rigid alignment of solids against the magnetic field causes severe line broadening in spectra due to a variance in the local magnetic field of the nucleus that liquids and solutions avoid due to translational and rotational motions. This makes NMR spectra of solids difficult to analyse compared to liquids and solutions due to dipolar coupling of nuclei. To compensate for this, solid NMR samples are rotated at 54.7° to the field which negates the effect of the dipole coupling in solids (d) which is proportional to $3\cos^2\theta - 1$. This is known as the magic angle and allows for the formation of high resolution solid state NMR spectra⁴.

Figure 2.6 shows a basic schematic of an NMR spectrometer. The analysed sample is placed into the holder and inserted in the analysis chamber where it is surrounded by the superconducting magnet. Due to the heat generated by the magnet, it is required to be continuously cooled whilst in operation. With the magnetic field activated, the sample can be probed through radiowave irradiation which is subsequently analysed by the systems electronics to produce the resulting spectrum.

Spectra were acquired using Chemagnetics Infinity Plus spectrometer. High resolution solid state ^{31}P NMR spectra were acquired at room temperature at a Larmor frequency of 121.50 MHz. Samples were contained in a 4 mm rotor with MAS at 12 kHz using Methyl-diphenylphosphine oxide as a reference.

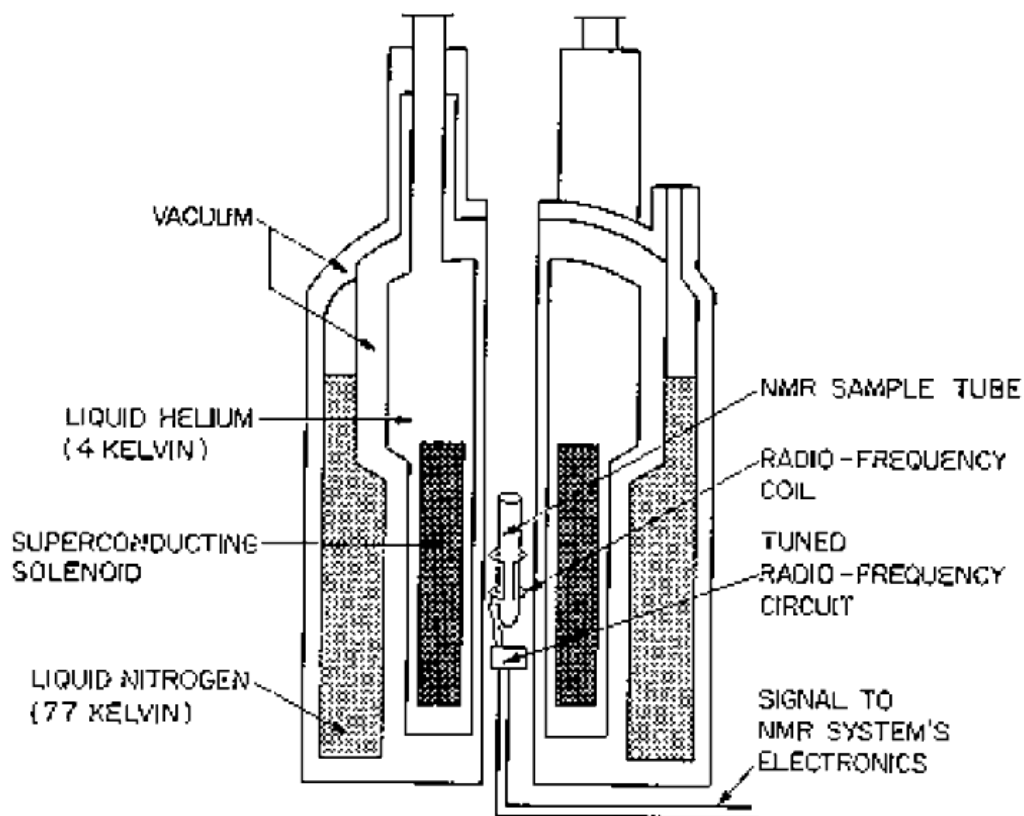


Figure 2.6: Schematic diagram of an NMR spectrometer. Taken from reference⁶

2.6 X-Ray Diffraction

X-ray diffraction (XRD) is a technique capable of probing both particle size and phase identification. Due to the comparable size between the wavelength of an x-ray and the atomic spacing in solids, the x-ray can be diffracted by a well ordered solid. The angle of diffraction can be calculated using the Bragg equation⁷ (equation 2.3):

$$n\lambda = 2d\sin(\theta)$$

Equation 2.3: The Bragg Equation showing the diffraction of X-rays from a crystalline solid where: n = an integer, λ = wavelength of x-rays, d = lattice spacing and, θ = diffraction angle

For the diffracted waves shown in figure 2.7, the path difference of the two waves is given as $AB + BC$ which is equal to $2d\sin(\theta)$. For situations where this path length is equal to $n\lambda$

where n is an integer, constructive interference occurs resulting in a detectable signal, otherwise, the waves will be out of phase causing destructive interference⁷.

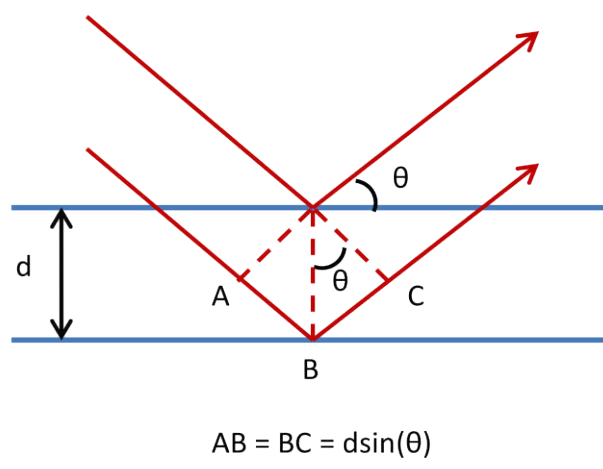


Figure 2.7: X-ray diffraction in a solid.

The technique uses monochromatic x-ray radiation source which when constructively diffracted (as described above in Eq. 2.3 and Fig. 2.7) can be used in the identification and analysis of crystalline samples. For the interference of the diffracted x-ray to be constructive, the analysed sample must have a consistent d-spacing and thus must have a long range ordering (i.e. a crystalline material). A diffraction profile is constructed by irradiating the sample and measuring the angles of the constructively diffracted x-rays. The angles of diffraction are related to the orientation of the lattice atomic planes, so the resulting diffractogram can be used to identify the crystal phases present in the sample. Analysis of the diffractogram usually requires access to a library or database of reference compounds which can complicate the analysis of unknown samples which consist of multiple or mixed phases⁸.

Figure 2.8 show a schematic diagram of an x-ray diffractometer setup. The incident beam is diffracted from the sample and the angle to be analysed can be set by the movement of the detector (and the x-ray tube) across the goniometer. A series of slits are also put in place at

the ends of the incident and diffracted arms. These slits act to alter the beam width and can be used to give a more accurate scan of a given diffraction angle.

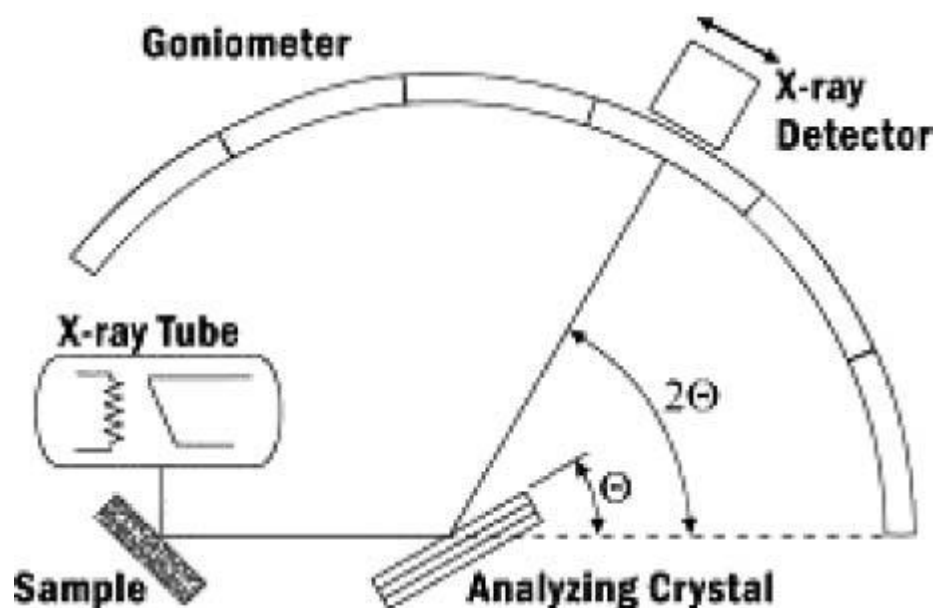


Figure 2.8: Example schematic of an x-ray diffractometer, showing the analysis of the diffraction of radiation at a given angle of 2θ . Taken from reference⁸

The x-ray diffractometer used throughout this investigation is a Panalytical X-pert pro with copper $K\alpha$ radiation at a current of 40 mA and a voltage 40 kV. Signals were analysed using the High Score Plus database.

2.7 X-Ray Photoelectron Spectroscopy

X-ray photoelectron spectroscopy (XPS) is a widely used analytical technique sensitive to the chemical state of elements at the surface of a sample. XPS can be used both as a method for the identification of species present on the surface and as a tool for providing chemical information of the surface and adsorbents.

The XPS technique relies upon the photoelectric effect in which an electron is ejected from an atom by an absorbed photon ($h\nu$) whose energy exceeds the binding energy of the electron in the atom and the work function (ϕ), Figure 2.9.

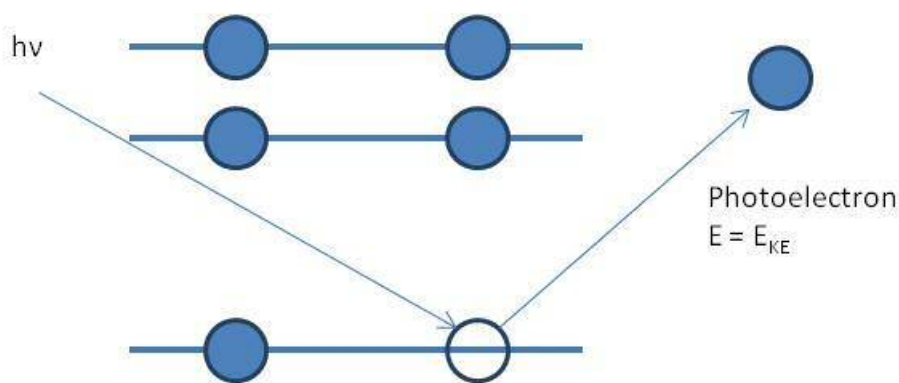


Figure 2.9: The emission of a photoelectron by an x-ray during XPS

Equation 2.4 shows that through analysis of the kinetic energy of the emitted electron and by using a monochromatic light source, the binding energy of the electron can be calculated. The process for core shell electron ejection is shown in figure 2.5, which is vital to chemical identification as core shell electrons are not involved in chemical bonding so binding energies are identifiable to specific elements. As well as corresponding to the specific element, the binding energy of the electron is also dependent on the oxidation state of the element which can provide further information of the surface species.

$$E_{KE} = h\nu - E_B + \phi$$

Equation 2.4: Equation showing the relationship between the kinetic and binding energies of photoelectrons and the incident photon, where: E_{KE} = kinetic energy, h = Planks constant, ν = photon frequency, E_B = binding energy and, ϕ = work function

The binding energy of the electron in the core shell is defined by the electrostatic interactions between it and the atomic nucleus and is altered by the shielding effects of all other electrons present in the atom; including valence electrons. From this, any change in the bonding environment of the atom will affect the electronic shielding resulting in an alteration of the binding energy of the photoelectron. This creates a chemical shift effect allowing for an analysis of atoms in differing bonding environments within a sample. For photo electrons ejected from an S orbital, a single peak is observed on the resulting XP

spectra; however in p orbitals and above 2 signals are seen. This effect is known as spin orbit splitting and arises from the total angular momentum of the orbitals (J) shown in equation 2.5. The spin angular momentum number (s) has a value of 1/2, with the variance coming from the angular momentum quantum number (l) of the orbitals. For the s orbital, l = 0 resulting in a single peak; however for the other orbitals where l > 0 two values of J are obtained showing the formation of two peaks in the XP spectra. In the example of the p orbital (l = 1), j is valued at 1/2 and 3/2 with an area ration of 1:2; the values for J and the peak ratios for the other orbitals are given in table 2.1.

$$J = l \pm s \quad l = 0(s), 1(p), 2(d)...$$

Equation 2.5: Equation for the total angular momentum (J) of an atomic orbital, where l = angular momentum quantum number and s = spin angular momentum number

Orbital	Angular Momentum Quantum Number (l)	Angular Momentum (J)		Peak Ratio
s	0	1/2		N/A
p	1	1/2	3/2	1:2
d	2	3/2	5/2	2:3
f	3	5/2	7/2	3:4

Table 2.1: Table showing the effects of spin orbit splitting in various orbitals during XP spectroscopy

After the ejection of the photoelectron, there are the two possible relaxation processes for the newly generated ion. Firstly, the transition of an electron from a higher orbital onto the empty core hole causes the emission of an x-ray in a process known as x-ray fluorescence. In the second process, the relaxation of the electron into the core hole causes the ejection of a second electron in what is known as the Auger process; these two processes are shown in figure 2.10. The presence of Auger electrons can be used for elemental analysis and peak

positions are susceptible to chemical shift effects; however the energy of Auger electrons is independent of the energy of the incident radiation.

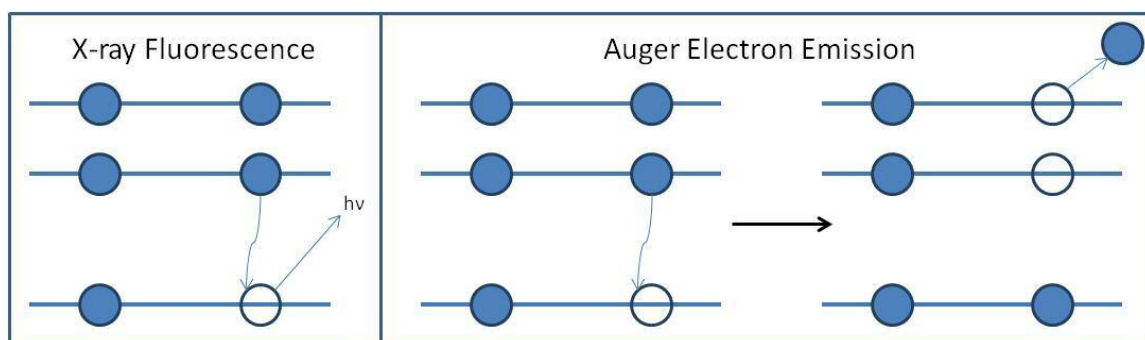


Figure 2.10: The relaxation processes after photoemission: X-ray fluorescence and Auger emission.

The inelastic mean free path (λ) defines the average distance an electron can travel before being inelastically scattered through a collision with a constituent atom in the sample. XPS is a surface sensitive technique due to the relatively short inelastic mean free path (λ) of the photoelectron in solids. The photoelectrons created in XP spectroscopy have energies from approximately 30 – 2500 eV and have a λ value of around 0.5 – 3 nm meaning that only a small number of electrons beneath this depth will have the same energy from the time they were expelled from the sample⁹; an example of a plot of the mean free path versus the kinetic energy of the electron are given in figure 2.11.

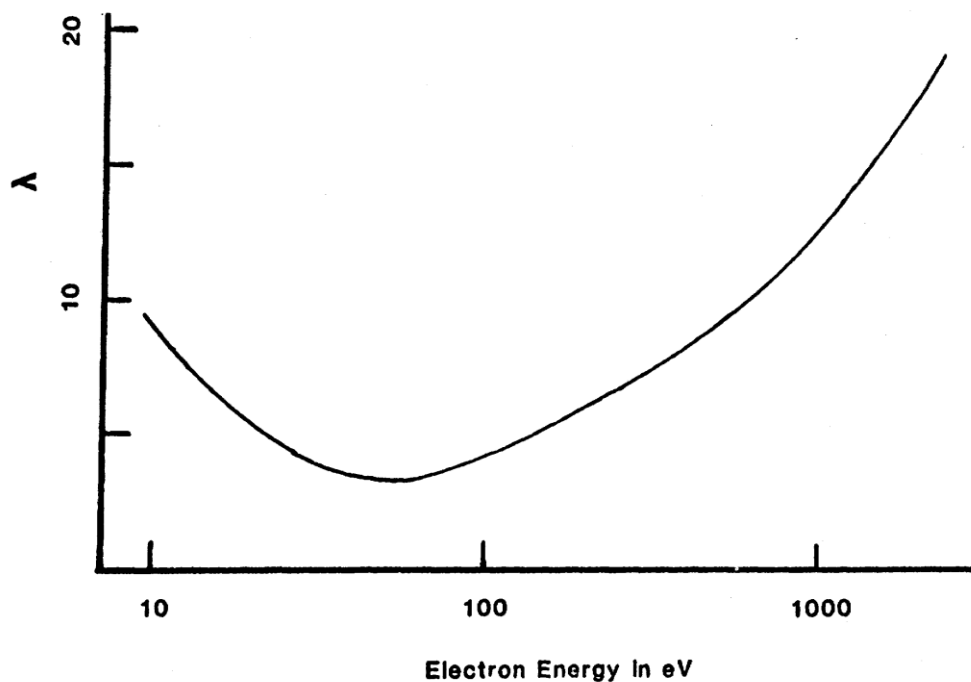


Figure 2.11: Graph showing the relationship of the mean free path of photoelectrons in a solid (λ) against electron energy (eV). Taken from reference⁹.

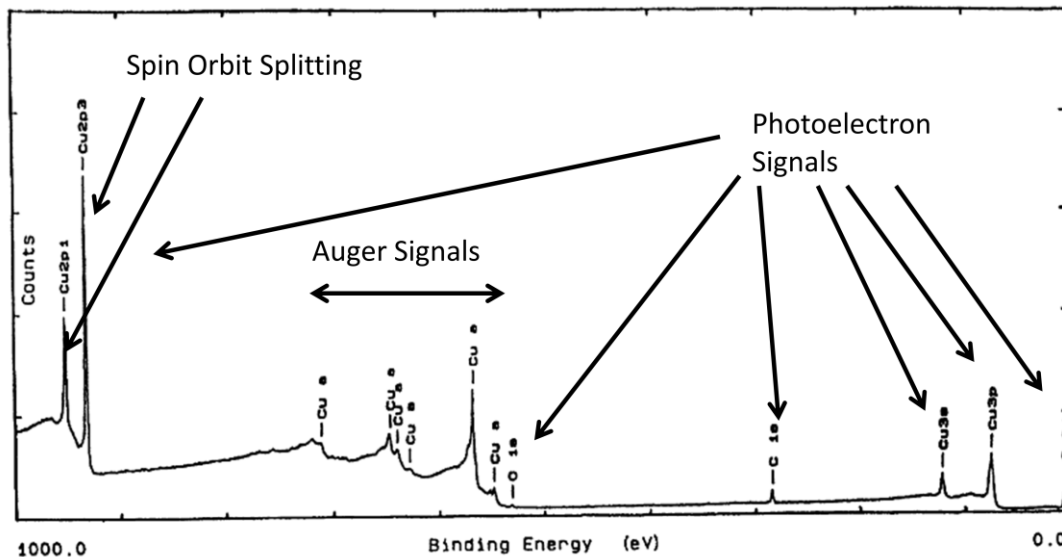


Figure 2.12: XP spectrum of a copper sample with notated peaks for photoelectrons, auger electrons and an example of spin orbit splitting. Taken from reference⁹.

An example XP spectrum of a copper sample is shown in figure 2.12 and highlights the spectral features described above. Signals for photoelectrons are present across the range of the spectrum for electrons emitted from the core shells of the sample. The photoelectron signals at ~950 eV show an example of spin orbit splitting of the Cu(2p) into the 1/2 and 3/2 peaks with an area ratio of 1:2. Also detected are the Auger signals from electrons ejected through relaxation.

A primary requirement for the acquisition of XP spectra is the presence of a vacuum. Under an atmosphere, ejected photoelectrons could undergo collisions with the gaseous molecules present, reducing detection quality of the sample. Operating under a vacuum also gives the advantage of the absence of any contaminants adsorbing onto the surface. For these reasons, modern XP spectra are acquired under ultra-high vacuum with a chamber pressure between 10^{-8} and 10^{-9} Pa.

The most common laboratory source of X-rays are from $K\alpha$ lines of Mg (1253.6 eV) or Al (1486.6 eV) anodes consisting of a thin coating of the metal on a Cu substrate. The production of the x-rays occurs when the anode is bombarded with electrons with a potential of 10-15 kV and a filament current of 10 – 100 mA.

Detection of the photoelectrons is achieved through the use of a hemispherical analyser that focuses electrons of a specific energy onto the electron counter; a schematic diagram is given in figure 2.13. A potential is applied to both the inner and outer edges of the hemisphere; this results in the filtering the emitted photoelectrons by their energy only allowing a select kinetic energy through⁹.

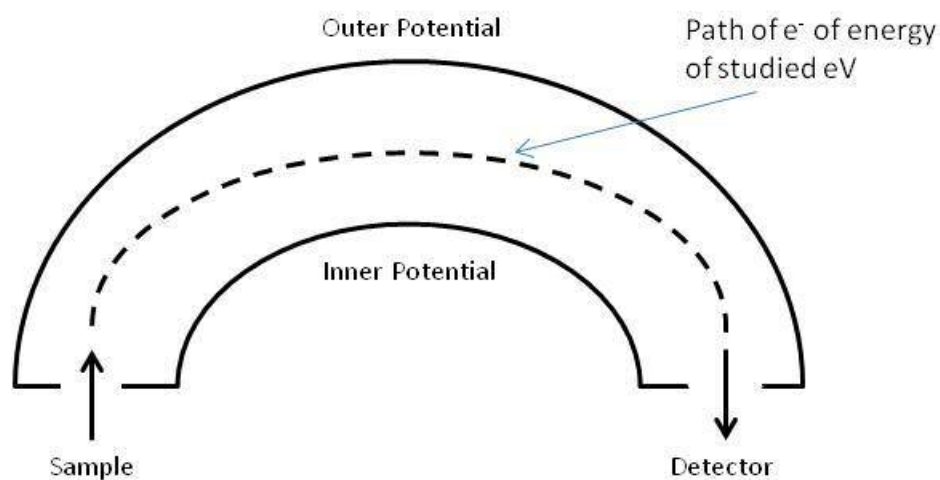


Figure 2.13: Basic schematic of a hemispherical analyser used in XPS. The dotted line shows the escape path of travelling electrons which can be tailored to a specific eV via changing the potentials at the perimeters.

The XP spectra for all samples were recorded using a Kratos Axis Ultra-DLD photoelectron spectrometer using a monochromatic Al K α x-ray source. The XPS data was analysed using CasaXPS¹⁰ with all binding energies referenced to the C(1s) peak at 284.7 eV with an uncertainty of ~ 0.2 eV. Curve fits were made using Gaussian-Lorentzian (GL(30)) lineshapes.

2.8 Scanning Electron Microscopy

Scanning electron microscopy (SEM) is an imaging technique, which uses a focused beam of electrons to create an image with nano-scale resolution. An electron gun with a tungsten filament is used to create a beam of electrons, through the passing of a current to temperatures of around 2500 °C, accelerated to a voltage between 1 kV and 60 kV. The beam is focused through a series of electromagnetic condenser lenses to give a beam diameter of around 2-10 nm and finally through a lens which allows the beam to raster across the sample surface¹¹.

Figure 2.14 shows the two types of electron based interactions that occur when the incident beam is scanned across the surface. Secondary electrons are low energy (<50 eV)

electrons which are ejected from the core shell of atoms within the sample. The low energy of these electrons means that only those excited from the top surface layers ($< 10\text{ nm}$) are detected. The shape of the sample being analysed affects the number of secondary electrons emitted, edges emit more secondary electrons than flat surfaces; this results in the formation of a well defined three dimensional image.

The second type of electron interaction is the backscattered electron. These are high energy electrons that have been elastically scattered from the incident electron beam. The electrons are backscattered more strongly from heavier elements than lighter ones and so these are able to provide excellent contrast images for there is a large disparity in the masses of the samples being analysed.

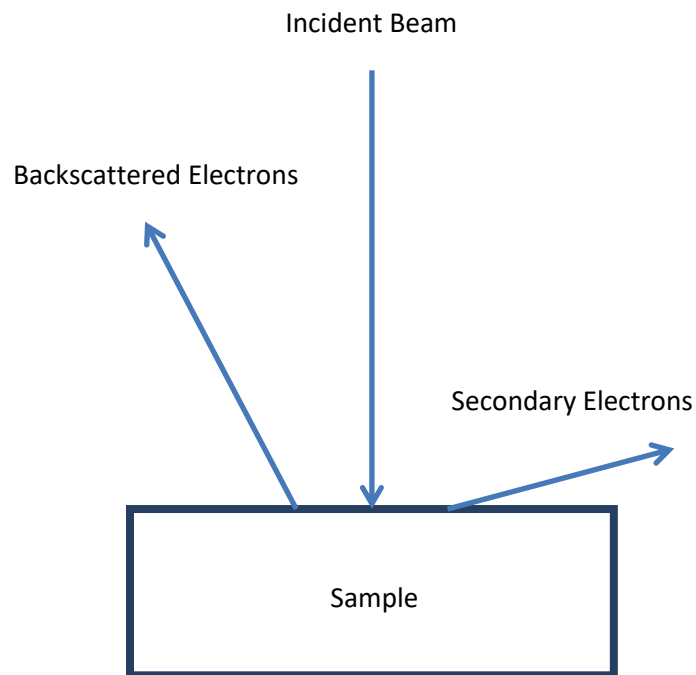


Figure 2.14: Diagram illustrating electron based interactions in SEM

2.9 Coating Effectiveness Testing Procedures

A magnetostriction-stress device has been employed throughout this study to test the effectiveness of coatings on magnetic steel; figure 2.15 shows an image of the magnetostriction-stress device used in this study. An in depth review of the engineering features and design philosophy can be found in the works by Kilmczyk¹² and Goel¹³, this section will briefly outline the operation of the technique and data analysis required for an understanding of this study.

The device mimics the magnetic effects that electrical steels would be subject to when part of an electrical circuit by applying a magnetic field over the sample. To test the effectiveness of the coatings, this is done while under a cycle of tensile and compressive stress. Since the coatings are designed for their tensile properties, beginning the test at a high tensile stress and lowering into compressive stress allows for a comparative gauge of the effectiveness of samples.



Figure 2.15: Photograph of the Magnetostriction-Stress Device

Figure 2.16 shows an example graph of magnetostrictive-stress tests. In this example, the line to the left is performing as a better coating than that on the right. As the tensile stress is lowered, the sample coating contributes a greater and greater share of tensile resistance

to the magnetostrictive effect. Measurements for the effectiveness of a coating are taken by reading the value of the applied stress at the point where the line begins to take off; i.e. the stress value at the point where the effects of magnetostriction are first exhibited. In figure 2.16 the blue line has a stress value of -3 MPa and the red line has a stress of -1 MPa. A comparison between the relative effectiveness of coatings can then be made by calculating the stress shift of samples. In the above example, magnetostriction is observed on the red sample first showing that the coating provides less tensile holding than the blue sample as the effects of magnetostriction are observed earlier with an improvement in applied stress of 2 MPa.

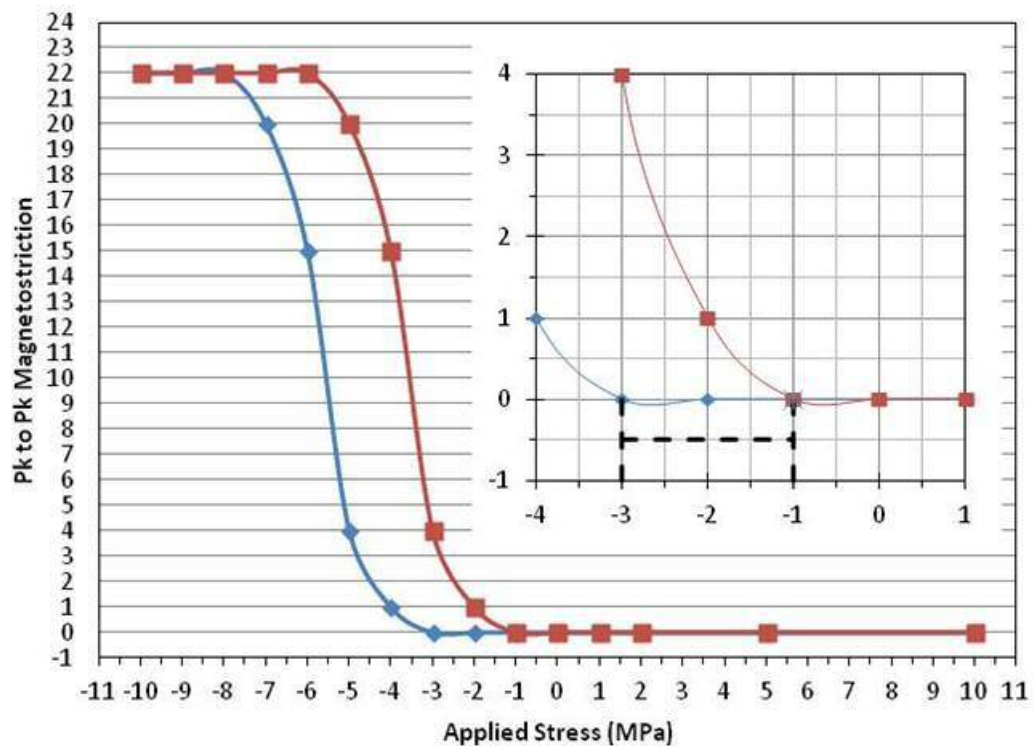


Figure 2.16: Example magnetostriction-stress curves

This testing method has the benefits of being quick to run and easy to change samples and showing good repeatability (figure 2.17). However, its major disadvantages are that for accurate data the samples must be of the required length and width, there is a maximum

thickness for coatings as the sample “slots” into the testing device and no bending or deformities to the sample can be accommodated. If any of the previous issues are present in the sample then the accuracy of the data can be affected¹². This is demonstrated in figure 2.18 which shows the effects of varying pressure applied on the sample by the clamping frame of the apparatus; the figure shows that the application of pressure drastically alters the measured magnetostriction values at lower applied stress. Since this clamping is required in the set-up process and is done manually, taking absolute measurements of magnetostriction at the lowest stress can be inaccurate and so a comparison of the stress shifts at the take off point is the preferred method for analysing the magnetostrictive effect.

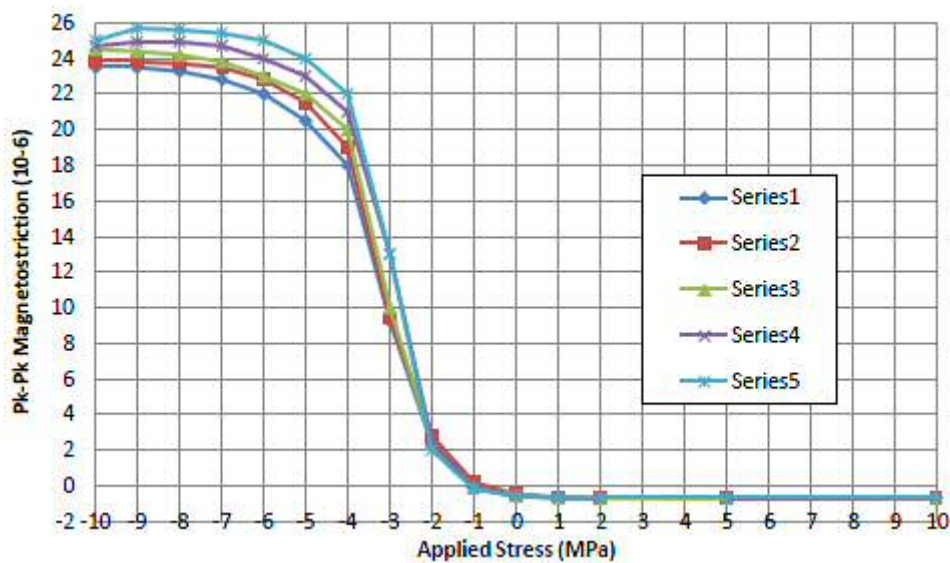


Figure 2.17: Repeated magnetostriction-stress curves for a sample of coated electrical steel. Taken from reference¹²

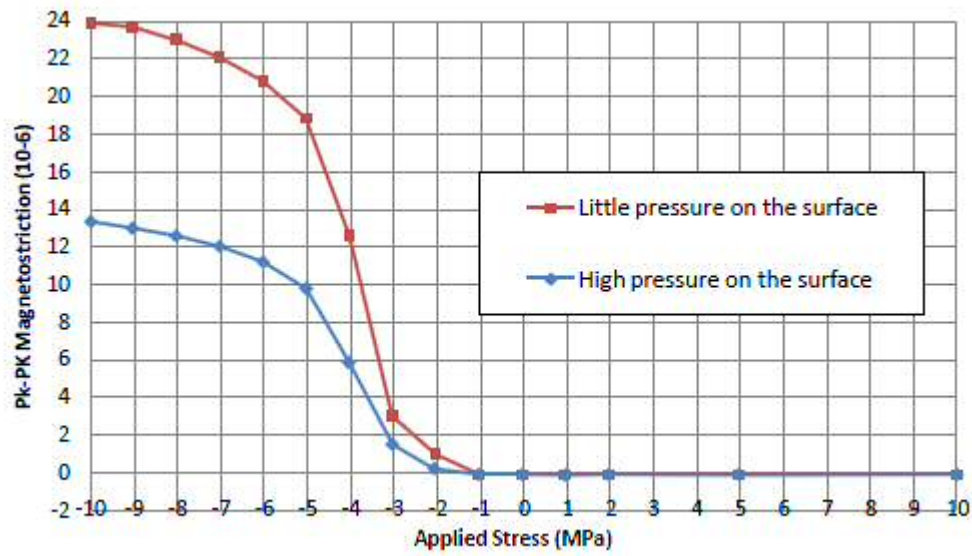


Figure 2.18: Magnetostriction-stress curves for a sample with varying degrees of pressure applied to the surface. Taken from reference¹²

The uncertainty and error of the magnetostriction testing device have been calculated and evaluated in multiple sources^{12, 13}; the error values for the measurements in magnetostriction are shown in figure 2.19. The figure shows three regions of uncertainty in the y-axis with high tensile stress region having the lowest error of $\pm 0.5\%$ increasing as tensile stress lowers in the next two regions to $\pm 5.5\%$ and $\pm 4.3\%$ respectively.

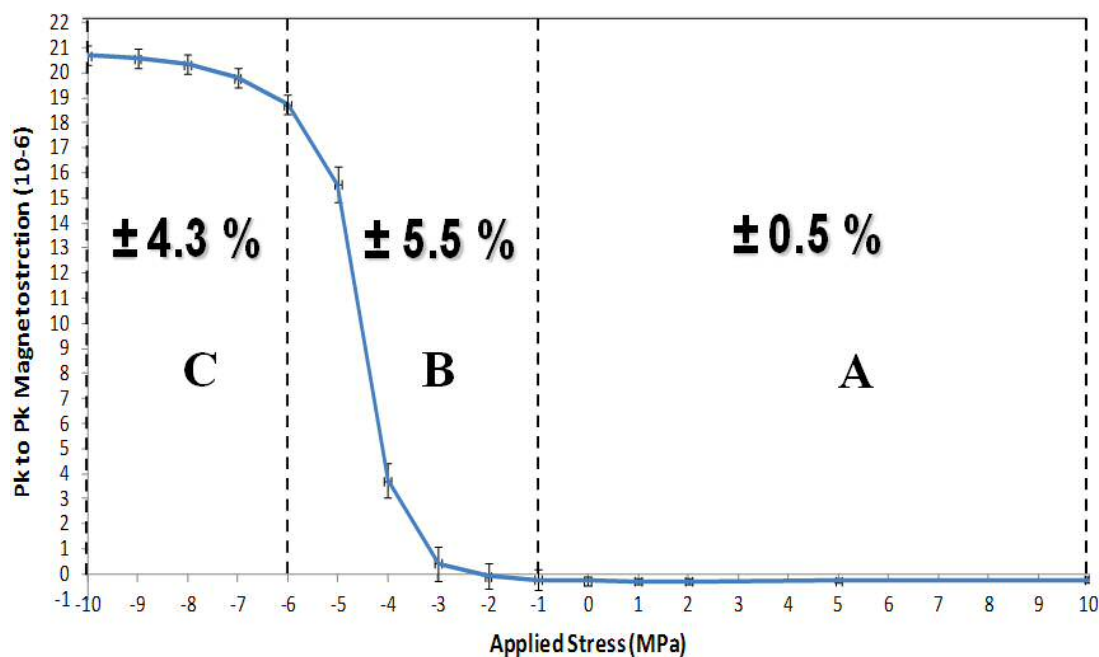


Figure 2.19: Regions of error in the y-axis of data collected from the magnetostriction-stress device; three distinct areas of differing error are seen. Taken from reference¹².

2.10 Experimental Strategy

The above experimental procedures and analysis techniques can be combined to allow for a proper investigation into the formation and application of tensile strength coatings.

The use of the vibrational spectroscopy (ATR-FTIR & Raman) techniques allows for an extremely rapid (< 1 min) identification of functional groups of a sample. These techniques will allow for the determination of the phosphate products formed from the various reactions listed above and coupled with the rapid time for data collection will allow for a quick identification of experimental outcomes. The techniques can be used to examine formation temperatures of products in the examination of thermal evolution and will be applied when examining the stability of the reaction products by tracking the formation/degradation of peaks.

A more detailed study on the bulk features of the reaction products will come through the use of XRD and ^{31}P NMR. XRD allows for the identification and analysis of various crystalline phases present in the samples, whilst NMR probes the various chemical environments of ^{31}P nuclei within the sample. These analysis techniques will allow for an analysis of both final products and species present at intermediate reaction temperatures. Combining these techniques allows for the gathering of a complementary set of data; XRD examines the phases of crystalline species gathering data on the long range order of samples and with NMR probing nuclear environments it presents information on short range order of species present within the sample.

As well as chemical analysis techniques which examine the bulk properties of samples, surface analysis techniques are also being employed in this study. XPS gives information of the surface characteristics of samples. XPS will be employed on the powdered samples to allow for the surface profile of the aluminium phosphate species synthesised to be fully characterised; in combination with the bulk analysis. With the surface properties of the samples analysed, it should be easier to assign XP signals when the phosphate species are formulated as film coatings where the use of surface techniques have increased value by focusing on the coating and not collecting data on the substrate. With XPS gathering information on the chemical features of the coatings, SEM can be used to gain information on the physical nature of the coatings. SEM can be utilised to examine the nature of the coatings both comparatively between various coating formulations and against annealing time tracking the evolution of phosphates within the coatings.

Magnetostriction-stress testing data will provide information on the performance of the coatings, evaluating their ability inhibit the magnetostrictive effect on the substrate. This data and any observed trends can be subsequently explained by the information gathered by previous analysis techniques.

2.11 References

1. B. Bagchi, S. Das, A. Bhattacharya, R. Basu and P. Nandy, *Journal of the American Ceramic Society*, 2009, **92**, 748-751.
2. C. N. Banwell and E. M. McCash, *Fundamentals of Molecular Spectroscopy*, 1994.
3. B. Stuart, *Infrared Spectroscopy: Fundamentals and Applications*, 2004.
4. H. Gunther, *NMR Spectroscopy*, 2013.
5. T. Muehl and S. Myhra, *Proceedings of the International Conference on Nanoscience and Technology*, 2007, **61**, 847-851.
6. R. W. Darbeau, *Applied Spectroscopy Reviews*, 2006, **41**, 401-425.
7. C. Hammond, *The Basics of Crystallography and Diffraction*, 2001.
8. A. A. Bunaciu, E. G. Udristioiu and H. Y. Aboul-Enein, *Critical Reviews in Analytical Chemistry*, 2015, **45**, 289-299.
9. N. H. Turner and J. A. Schreifels, *Analytical Chemistry*, 1998, **70**, 229R-250R.
10. CasaXPS, www.casaxps.com.
11. K. D. Vernon-Parry, *III-Vs Review*, 2000, **13**, 40-44.
12. P. Klimczyk, PhD Thesis in *Novel Techniques for Characterisation and Control of Magnetostriction in G.O.S.S.*, Cardiff University, 2012.
13. V. Goel, PhD Thesis in *Novel Coating Technologies for Electrical Steels*, Cardiff University, 2016.

Chapter 3: The Formation of Aluminium

Metaphosphate

Contents

3.1: Introduction	48
3.2: The Thermal Transition of Orthophosphate to Metaphosphate	50
3.3: Chapter Aims.....	53
3.4: The Synthesis of Aluminium Metaphosphate from Various Precursors.....	53
3.4.1: Vibrational Spectroscopy of Aluminium Phosphates	54
3.4.1.1: ATR-FTIR Spectroscopy	54
3.4.1.2: Raman Spectroscopy.....	57
3.4.2: X-Ray Diffraction	57
3.4.3: Nuclear Magnetic Resonance Spectroscopy.....	61
3.4.4: X-Ray Photoelectron Spectroscopy.....	63
3.4.5: Stability towards Thermal Hydration	72
3.5: Effects of the Phosphorus:Aluminium Ratio.....	74
3.5.1: Vibrational spectroscopy	75
3.5.2: ³¹ P Nuclear Magnetic Resonance Spectroscopy	78
3.5.3: X-ray Photoelectron Spectroscopy	81
3.6: Summary	87
3.7: References	88

3.1: Introduction

This chapter examines the formation, structure, and stability of the aluminium phosphate powders which are used in the synthesis of tensile stress coatings. Phosphates are the primary constituent in stress coatings which are used to reduce energy losses due to magnetostriction on magnetic steels. Tensile stress coatings have been in use since 1965 and phosphates have been studied extensively since that date¹ because phosphate based coatings have been shown to reduce energy losses by up to 15%².

Figure 3.1 shows the various structural forms of phosphates: orthophosphate (PO_4^{3-}), pyrophosphate ($\text{P}_2\text{O}_7^{4-}$), and metaphosphate (PO_3^-). This study focuses on aluminium metaphosphate ($\text{Al}(\text{PO}_3)_3$), primarily on the conversion of orthophosphate (AlPO_4) to metaphosphate and the direct synthesis of aluminium metaphosphate from precursor compounds.

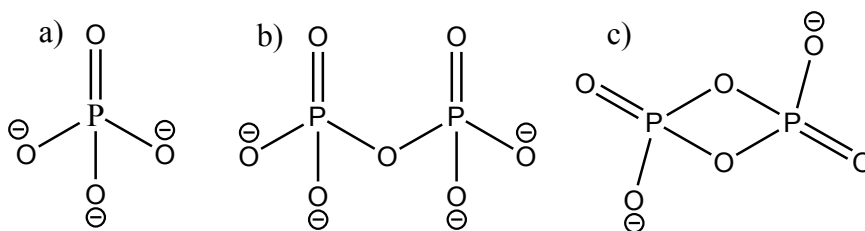


Figure 3.1: The various structural forms of phosphates: a) orthophosphate, b) pyrophosphate, c) metaphosphate

As well as its uses in tensile coatings for magnetic steels, there is a great amount of literature investigating the role of aluminium phosphate as ceramic binders³⁻⁹ and in corrosion resistive materials¹⁰⁻¹⁴. Aluminium phosphate used for ceramic binders, are formed from the reaction of aluminium hydroxide and phosphoric acid and curing in air. This process causes hydrated orthophosphate units to polymerise together to form poly and metaphosphates, defined using Q notation to differentiate between the amount bridging oxygen functionality summarised in figure 3.2

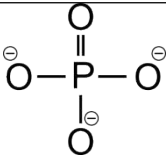
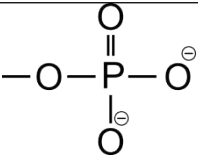
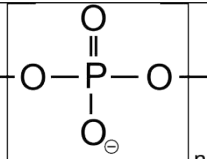
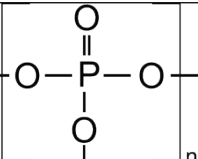
				
Name & formula	Orthophosphate PO_4^{3-}	Pyrophosphate $\text{P}_2\text{O}_7^{2-}$	Polyphosphates $[\text{PO}_3^-]_n$	Metaphosphate $[\text{P}_n\text{O}_{2n+1}]$
Label	Q_0	Q_1	Q_2	Q_3
BO/NBO ratio	0	0.33	1	3
O/P ratio	4	3.5	3	2.5

Figure 3.2: Schematic showing the Q notation of phosphate units as polymerisation increase and the ratios of bridging to non-bridging oxygen species.

Tricot⁴ found that on curing, various aluminium phosphate binders, prepared from the reaction of aluminium hydroxide and phosphoric acid resulted in the formation of aluminium metaphosphate. On examination of the phosphorous aluminium ratios, they found an increase in the ratio resulted in the formation of aluminium metaphosphate at lower annealing temperatures. Studies have also shown that phosphate binders with P/Al ratios of 3 or higher were significantly more chemically stable than those with a ratio of less than 3. Vippola⁶ et al were able to identify that the aluminium metaphosphate species present in binder with the P/Al ratio of 1:4.2 was the cyclic metaphosphate $\text{Al}_2\text{P}_6\text{O}_{18}$. The stability of the phosphate glasses was examined in a study by Kobayashi¹⁵ and found that the glasses were prone to hydration through the P=O bonds present arguing the relative weakness of the π -bond against the P-O σ -bonds present in the system. The stability of phosphate systems towards hydration is an important consideration in their design and so is an aim of this work discussed in section 3.3.

3.2: The Thermal Transition of Orthophosphate to Metaphosphate

The current standard stress coatings used by Cogent Power are based upon aluminium orthophosphate (AlPO_4), colloidal silica (SiO_2) and water; the phosphate is believed to be responsible for the stress properties of the coating.

Previous studies in the field have been undertaken on the effects of thermal annealing of aluminium orthophosphate by Bemmer¹⁶. Figures 3.3 and 3.4 show the IR and Raman spectra for aluminium orthophosphate (AlPO_4) as received and upon annealing to 850 °C. No change was observed in the spectra after annealing. If there were polymerisation of the orthophosphate units into pyro- and metaphosphate noticeable changes in the spectra would be expected. If the condensation of the orthophosphate were to occur, then bands corresponding to the formation of P-O-P bonds would emerge at approximately 800 – 1050 cm^{-1} or 950 – 1000 cm^{-1} depending on the formation of cyclic or linear aluminium metaphosphate respectively⁹.

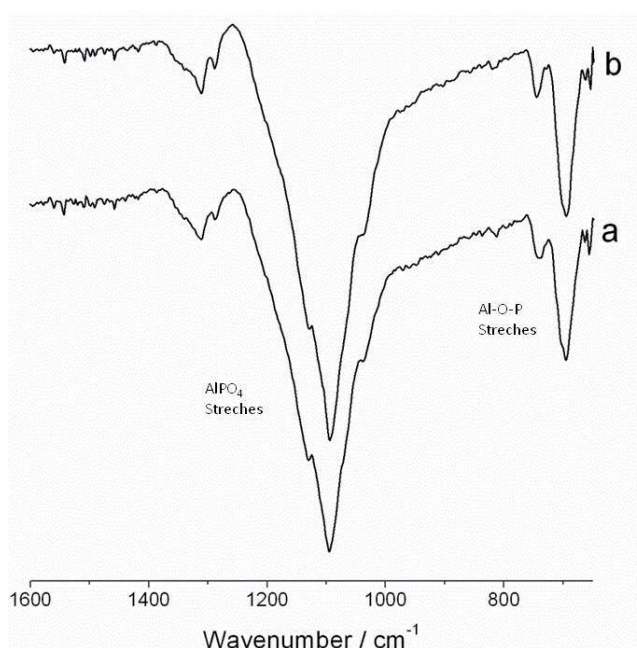


Figure 3.3: ATR-FTIR spectra for AlPO_4 a) as received and b) after annealing to 800 °C¹⁶

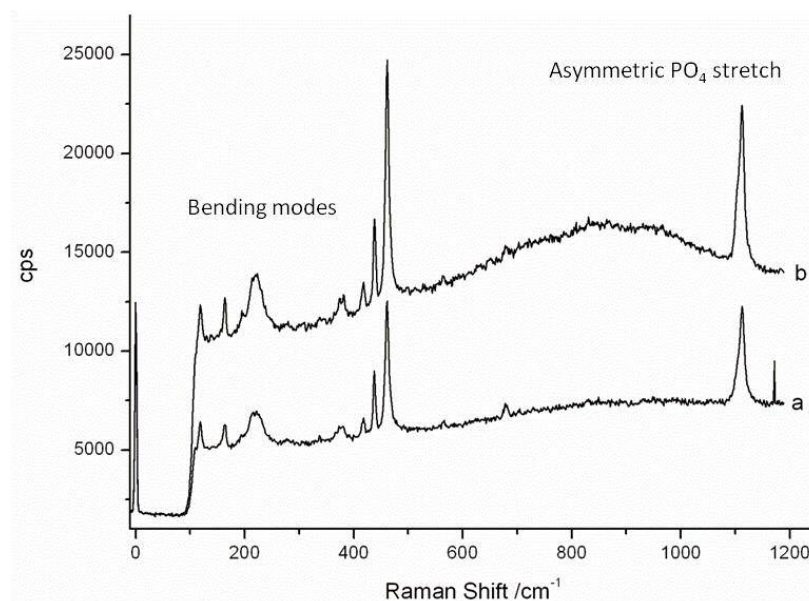


Figure 3.4: Raman spectra for AlPO_4 a) as received and b) after annealing to 800°C ¹⁶

Bemmer also studied the formation of magnesium phosphates which also have applications as stress coatings. The coatings consist of aluminium phosphate, magnesium oxide, phosphoric acid, colloidal silica and water; effectively a modification of the standard on line coating with the addition of MgO and H_3PO_4 . The reaction between MgO and H_3PO_4 has been previously studied by Finch et al¹⁷. The IR and Raman spectra show an evolution of peaks as the annealing temperature is increased. These peaks, in both spectra, were attributed to P-O-P bonds indicating the formation of some kind of polyphosphate. In the spectra the evolution of peaks is seen after annealing to 500°C , the IR spectra sees peaks at 1294.23 and 1317.38 cm^{-1} and the Raman 1168.03 cm^{-1} . XRD analysis of the samples of the sample show that the evolved species by 800°C can be attributed to the magnesium metaphosphate, magnesium cyclotetraphosphate ($\text{Mg}_2(\text{PO}_3)_4$).

This data shows that polymerisation of the orthophosphate units occurs when using magnesium phosphate but not aluminium phosphate. Industrial testing data has also shown that coatings containing the addition of MgO and H_3PO_4 perform better in imparting greater tension on the steel substrates than the purely aluminium phosphate coatings. This

can be attributed the formation of a metaphosphate network adsorbed onto the substrate giving a better tensile holding than the monomer orthophosphate units. However, these coating were found to be prone to thermal hydration, resulting in degradation of the coatings thermal properties. Bemmer again investigated this, finding that there is a breakdown of the metaphosphate networks after exposure to warm, humid atmospheres¹⁶.

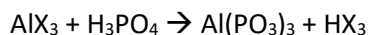
Chromium oxide (CrO_3) has also been studied as an additive to aluminium phosphate mixtures. Work conducted found that the small cation size of the chromium ion increased disorder in phosphate chains resulting in the formation of amorphous chains at lower curing temperatures and promoting the condensation reaction of the hydrated phosphates⁹. It has also been found that the addition of chromium has a positive effect on the stability of phosphate binders. Cured binders have been found to be more unstable towards hydration than those without the addition of chromium⁵. Bemmer¹⁶ found that the addition of CrO_3 to aluminium orthophosphate does facilitate the conversion of aluminium orthophosphate to aluminium metaphosphate after annealing to 800 °C. The use of chromium oxide in the coating mixture also gave rise to an improvement in the performance of the coating versus the coating mixture without the added chromium giving further evidence that metaphosphate is preferred to orthophosphate in designing tensile coatings. However, the toxicity of chromium VI means that it cannot be employed on an industrial scale.

3.3: Chapter Aims

The aim of this work is to extend the previous studies described above by examining the possible formation of aluminium metaphosphate with the aim of formulating a tensile coating with the performance of the magnesium metaphosphate coatings but more stable to the effects of thermal hydration. The structure of the compounds have been analysed by diffractive (XRD) and spectroscopic (ATR-FTIR, Raman, XPS, ^{31}P NMR) techniques and the stability towards thermal hydration have been tested.

3.4: The Synthesis of Aluminium Metaphosphate from Various Precursors

Since the formation of aluminium metaphosphate from orthophosphate is not possible under the required reaction temperatures, the synthesis of aluminium metaphosphate was attempted through the reaction of phosphoric acid and various aluminium precursors (Equation 3.1):



Eq 3.1: Equation for the formation of $\text{Al}(\text{PO}_3)_3$ from the reaction of an aluminium precursor and phosphoric acid

The details of the synthesis methods are discussed in section 2.2.1. Briefly, solutions of aluminium precursor are reacted with phosphoric acid and the resulting mixture is heated into a gel and furnace cured in air. Samples were taken at 300, 500, and 800 °C in order to track the thermal formation of aluminium metaphosphate. The precursors used in this study are aluminium hydroxide ($\text{Al}(\text{OH})_3$), aluminium nitrate ($\text{Al}(\text{NO}_3)_3$), and aluminium chloride (AlCl_3). Powders of precursors were synthesised with a P/Al ratio of 3/1 and analysed using a variety of spectroscopic and diffraction techniques.

3.4.1: Vibrational Spectroscopy of Aluminium Phosphates

3.4.1.1: ATR-FTIR Spectroscopy

Figure 3.5 shows the ATR-FTIR spectra for the samples prepared from aluminium hydroxide. As curing temperature increases from 300 to 500 and 800 °C an evolution of sharp peaks are observed. Peaks at 1305 and 1282 cm^{-1} are attributed to P=O π bands and the peaks at 1186 and 1142 cm^{-1} to P-O σ bands. The peaks at 738 and 730 cm^{-1} correspond to Al-O-P bands; these peaks show that aluminium phosphate is being formed at 500 °C and above. The bands at 1070, 1060, 1025 and 811 cm^{-1} are attributed to P-O-P vibrations, these bands are indicative of the formation of metaphosphate. Figures 3.7 and 3.8 show the IR spectra for samples synthesised from aluminium nitrate and chloride respectively. The evolution of nitrate spectra show good correlation to the hydroxide spectra, showing the evolution of peaks at 1080, 1056, 1026, and 810 cm^{-1} indicating metaphosphate formation^{18, 19}.

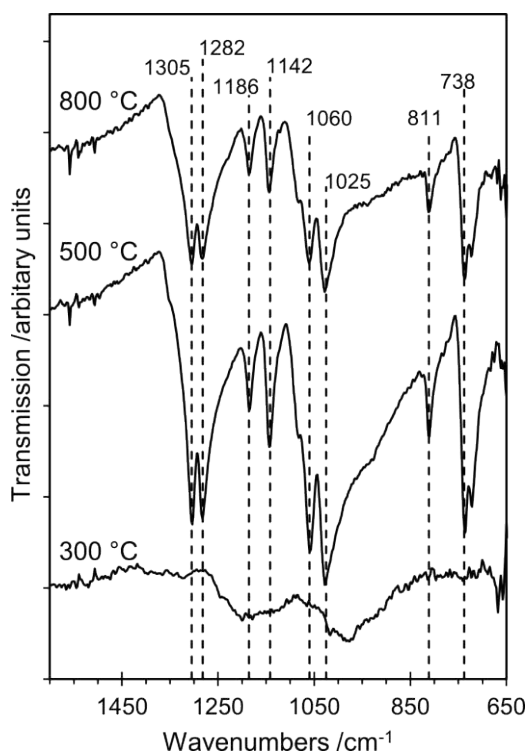


Figure 3.5: ATR-FTIR spectra for samples prepared from $\text{Al}(\text{OH})_3$ annealed to 300, 500 and 800 °C

Wavenumber /cm ⁻¹	Peak Assignment
1305	P=O
1282	P=O
1186	P-O
1142	P-O
1070	P-O-P
1060	P-O-P
1025	P-O-P
811	P-O-P
738	Al-O-P
730	Al-O-P

Figure 3.6: Tabulation of the peaks for the ATR-FTIR spectra for AlOH_3 samples

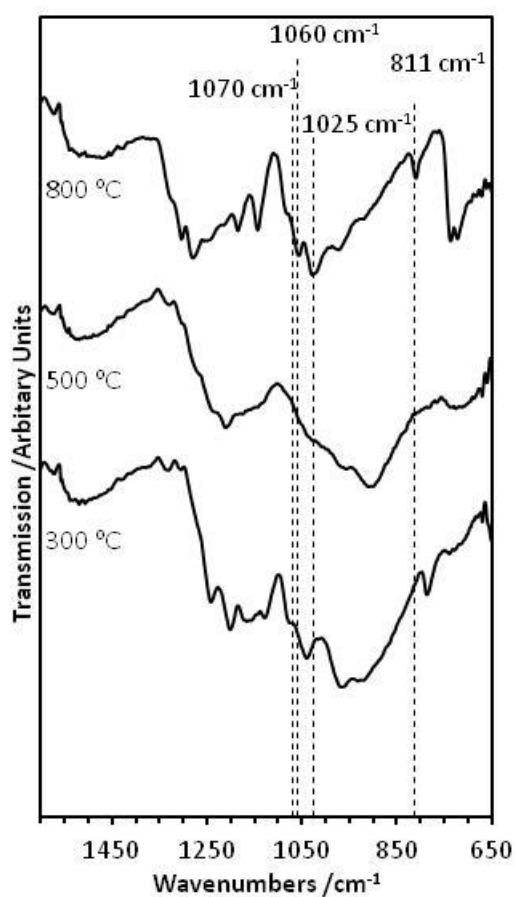


Figure 3.7: ATR-FTIR spectra for samples prepared from $\text{Al}(\text{NO}_3)_3$ annealed to 300, 500 and 800 °C

For the hydroxide and nitrate samples, samples were taken at 300, 500 and 800 °C. However, for the chloride based samples, the reaction mixture was still a gel at this temperature so the first sample was taken at 400 °C. The samples taken at 400 and 500 °C were still very wet and did not become a “dry” powder until 800 °C. To prevent any potential damage to ATR crystal, the samples annealed to 400 and 500 °C were not analysed. The IR spectra at 800 °C does again give good correlation to the previous samples, strong sharp peaks at 1060, 1028, and 812 cm^{-1} and a shoulder at 1083 cm^{-1} agree, with the previous peak assignments, showing the formation of aluminium metaphosphate.

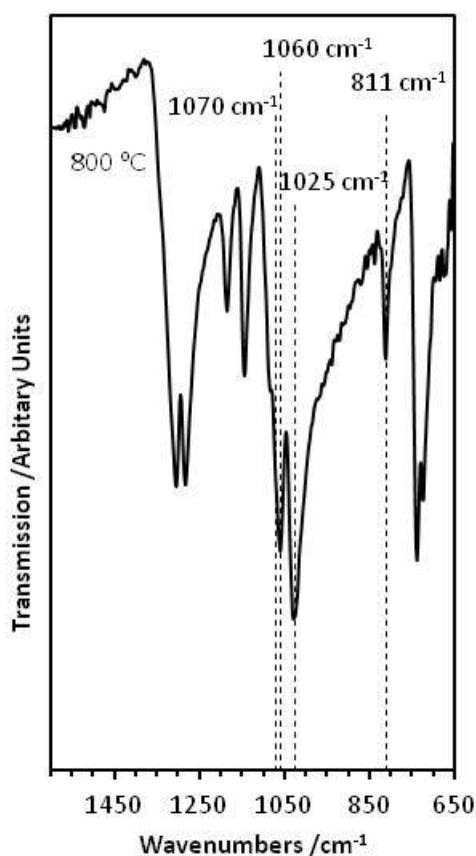


Figure 3.8: ATR-FTIR spectra for samples prepared from AlCl_3 annealed to 800 °C

3.4.1.2: Raman Spectroscopy

Figure 3.9 shows a comparison of the Raman spectra taken for the samples at 800 °C. The peaks assigned in the region of 100-600 cm^{-1} are assigned to lattice vibrations. The peaks at 760, 795, 830, 920, 950, 1020, 1095, and 1145 cm^{-1} are attributed to PO_x stretches, indicating the formation of phosphates at this temperature. The peaks at Raman shifts of 610, 640, and 690 cm^{-1} correspond to P-O-P symmetric stretches showing the formation of aluminium metaphosphate^{18, 19}.

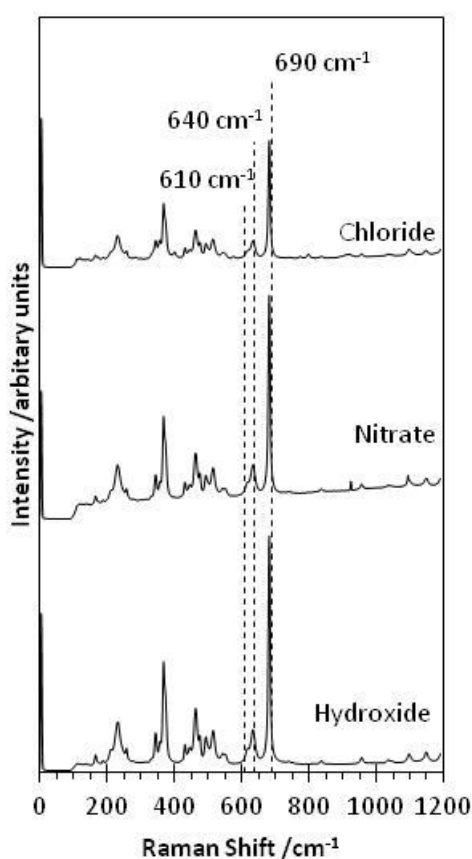


Figure 3.9: Raman spectra for samples prepared with a P/Al ratio of 3/1 annealed to 800 °C

The Raman spectra shown above and the infrared data correlate well with the formation of aluminium phosphate. Both data sets show the formation of bonds indicative of not just aluminium phosphates but aluminium metaphosphate. However, the vibrational spectroscopy data does not give full data on the mechanisms of formation or the

intermediates involved in the formation of aluminium metaphosphate and so additional analysis techniques are required.

3.4.2: X-Ray Diffraction

X-ray diffraction has been employed to identify the crystalline phases present in the samples over the course of heating. Figure 3.10 shows the XRD spectra for annealed samples synthesised from $\text{Al}(\text{OH})_3$. There are a series of weak crystalline signals observed in the sample at 300 °C, these signals have been attributed to the presence of the precursor H_3PO_4 , and the intermediary species of $\text{AlH}_3(\text{PO}_4)_2 \cdot 3\text{H}_2\text{O}$ and alumina (Al_2O_3)^{3, 9, 20, 21}. However, there are still a number of peaks which have not yet been assigned to a crystalline phase, showing that there are still unknown intermediaries present in the reaction mechanism at this temperature. At 500 °C a strong diffraction pattern emerges which can be attributed to the cubic and monoclinic phases of aluminium metaphosphate. On heating to 800 °C, the crystal phase observed is cubic metaphosphate. This data corroborates what is observed in the vibrational spectra that from 500 °C aluminium metaphosphate is being formed. The diffraction data shows the formation of two crystal phases at 500 °C which converts into one phase by 800 °C; information which is not observed from the vibrational spectra of the samples^{9, 22}.

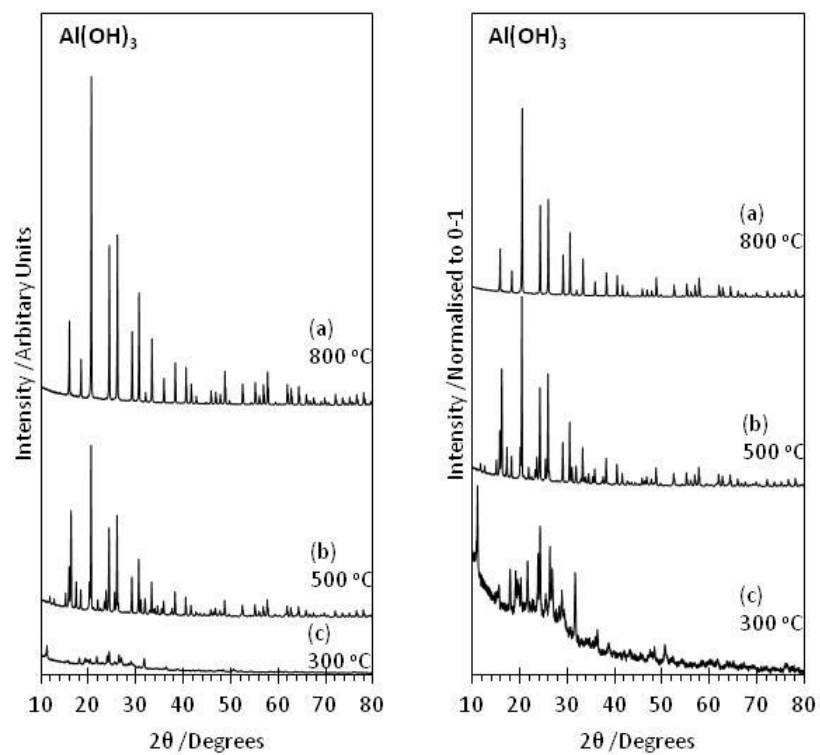


Figure 3.10: XRD for samples prepared from Al(OH)_3 annealed to 300, 500 and 800 °C

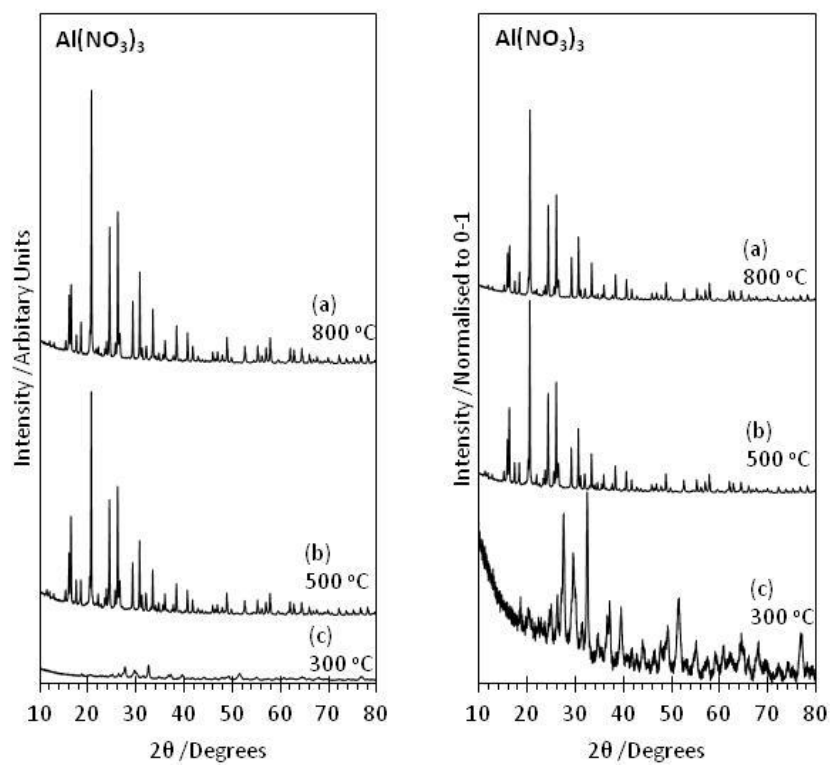


Figure 3.11: XRD for samples prepared from $\text{Al(NO}_3)_3$ annealed to 300, 500 and 800 °C

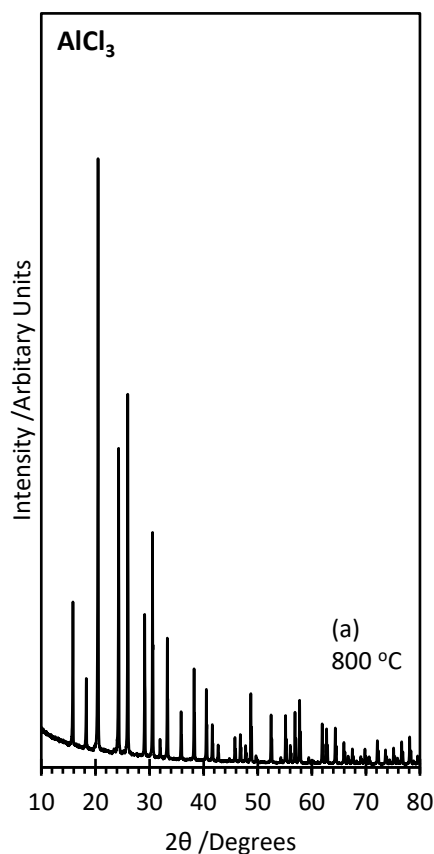


Figure 3.12: XRD for samples prepared from AlCl_3 annealed to 300, 500 and 800 °C

In the nitrate based samples (figure 3.11), there are similarities to the hydroxide based samples. Low intensity peaks at 300 °C attributed to H_3PO_4 , $\text{AlH}_3(\text{PO}_4)_2 \cdot 3\text{H}_2\text{O}$, and Al_2O_3 which evolve into cubic and monoclinic $\text{Al}(\text{PO}_3)_3$ at 500 °C. After heating to 800 °C only the cubic phase was present in the hydroxide based sample, however in the nitrate based sample the monoclinic aluminium metaphosphate phase is still present. This gives evidence that changing the nature of the aluminium precursor used does alter the mechanism for the formation of aluminium phosphates or that further annealing is required for the monoclinic phase to convert to the cubic phase using $\text{Al}(\text{NO}_3)_3$ as the precursor. For the same reasons given above, the wet nature of the chloride based samples prevented diffraction data being obtained for the samples heated to 400 and 500 °C (figure 3.12). The diffraction pattern here shows only the presence of the cubic phase of $\text{Al}(\text{PO}_3)_3$, however

more data is required to determine intermediate pathways of metaphosphate formation when using aluminium chloride as the reaction precursor.

3.4.3: Nuclear Magnetic Resonance Spectroscopy

NMR spectroscopy has been widely used to examine the formation of a variety of phosphates^{4, 23-29}. ³¹P NMR probes the phosphorus environments in the sample and allows for complementary analysis with XRD as NMR can probe non-crystalline environments allowing for greater insight into the formation of aluminium metaphosphate from the various precursors.

Figure (3.13) shows the ³¹P NMR spectra for the phosphate samples annealed to 800 °C. In the three spectra an observed trend is the shifting of peaks towards more negative chemical shifts as the annealing temperature increases. This trend is attributed to the increased polymerisation of the phosphates and a resulting increased shielding of ³¹P nuclei which causes peaks to resolve at lower chemical shifts.

At 800 °C the observed peaks are in agreement with the x-ray diffraction data presented in Figures 3.10-12; in the hydroxide and chloride samples a single peak assigned to cubic metaphosphate is observed at -50.5 ppm and in the nitrate sample an additional two peaks at -36.5 and -43.0 ppm assigned to monoclinic Al(PO₃)₃. The presence of only these peaks in the samples shows that by 800 °C, only crystalline aluminium metaphosphate is present in the samples.

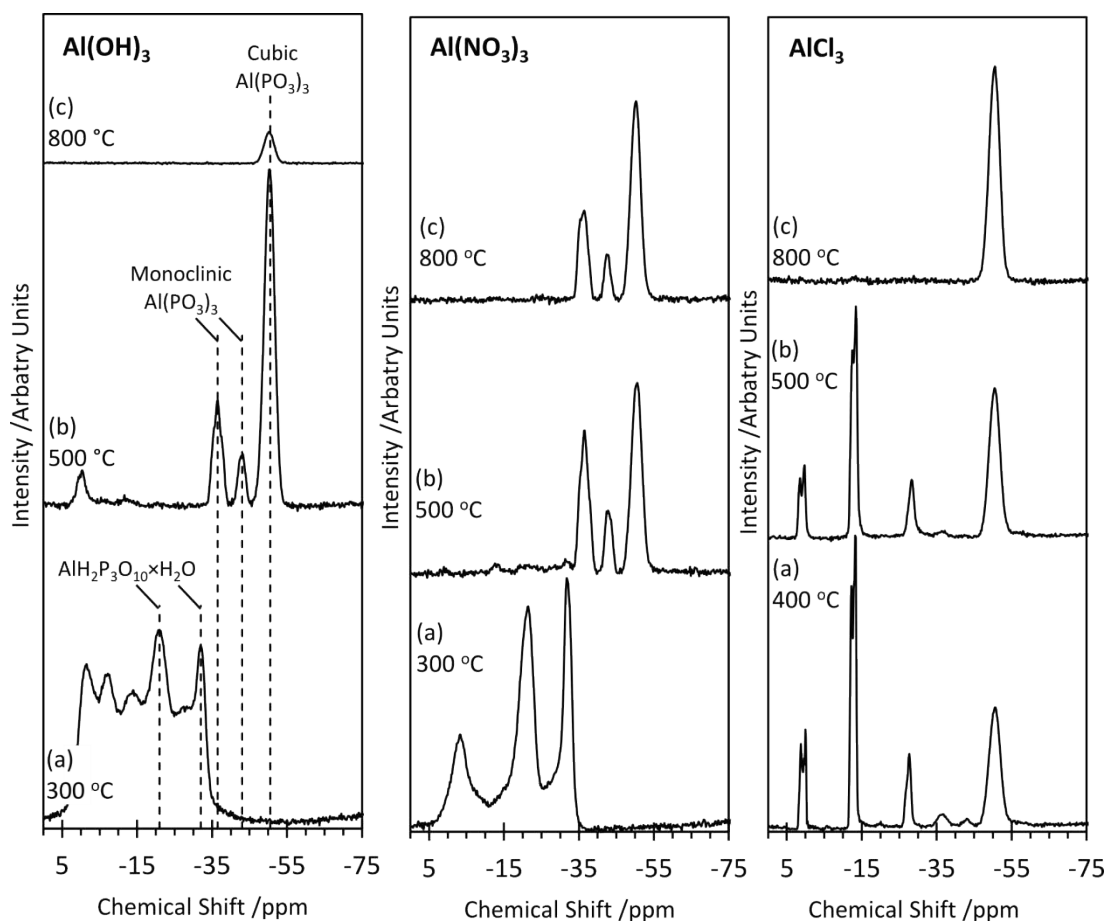


Figure 3.13: ^{31}P spectra for the samples prepared from the three precursors annealed to 300, 500 and 800 °C

In the spectra for the hydroxide based samples, a broad peak overlapping peak structure is observed between 5.0 and -40.0 ppm. This structure indicates the presence of an amorphous phosphorous environment including the presence of hydrated phosphate groups such as phosphoric acid in the peaks at -1.0, -7.0, and -14.0 ppm. The peaks at -21.0 and -32 ppm have been previously assigned by Tricot et al⁴ as aluminium tripolyphosphate ($\text{AlH}_2\text{P}_3\text{O}_{10}\text{xH}_2\text{O}$). Annealing to 500 °C, the appearance of the peaks attributed to monoclinic and cubic $\text{Al}(\text{PO}_3)_3$ are observed which at 800 °C become pure cubic metaphosphate.

In the case of the nitrate based samples, at 300 °C the broad amorphous peak observed in the hydroxide spectra is absent, but $\text{AlH}_2\text{PO}_3\text{O}_{10}\text{H}_2\text{O}$ is still present at this temperature. At 500 °C, both monoclinic and cubic $\text{Al}(\text{PO}_3)_3$ are observed and are still present at 800 °C which is in agreement with the diffraction data.

More substantial differences are observed in the spectra for the AlCl_3 samples. At 400 °C, a minimal amount of monoclinic $\text{Al}(\text{PO}_3)_3$ is observed with a comparatively much stronger cubic $\text{Al}(\text{PO}_3)_3$ peak; on annealing to higher temperatures, only cubic metaphosphate is present. Additional differences in the chloride samples from the hydroxide and nitrate samples are the presence of peaks at 1.0, 0.0, -12.0, -13.5 and -28.0 ppm, which are yet to be assigned and have been identified using other analytical methods; the chemical shift of the peaks would suggest though that corresponding species are at most low order polyphosphates or pyrophosphates. These drastic differences in the spectra add further weight to the suggestion that the choice of precursor does alter the mechanism of formation of aluminium metaphosphate; including the temperature of $\text{Al}(\text{PO}_3)_3$ evolution and the crystalline phases evolved.

3.4.4: X-Ray Photoelectron Spectroscopy

The analytical data shown above has concentrated on bulk analysis of the samples (ATR-IR has some degree of surface sensitivity with sampling depth of ~ 1 micrometer). X-ray photoelectron spectroscopy (XPS) has been employed to probe the surface behaviour of the samples as annealing temperature increases.

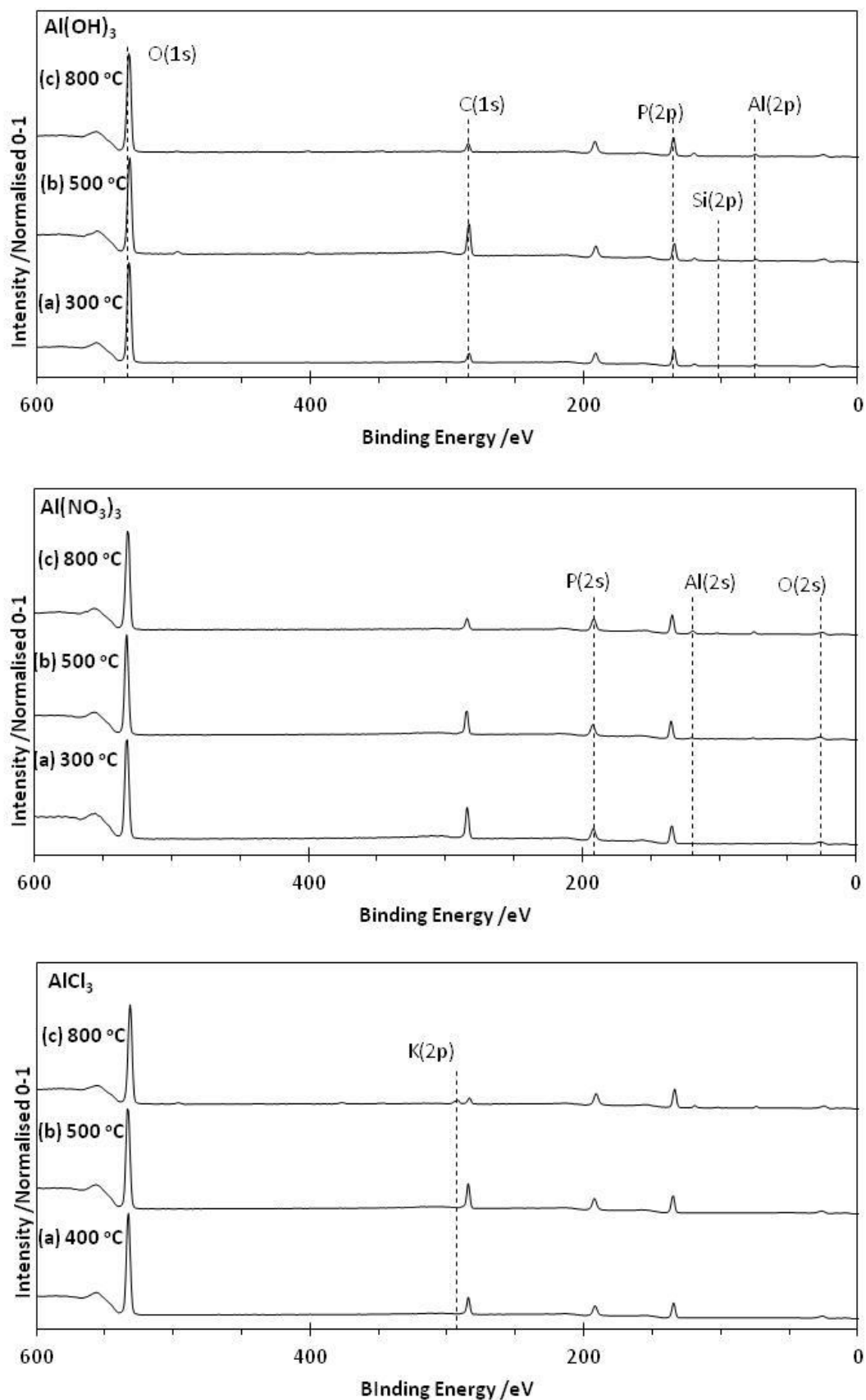


Figure 3.14: Wide-Scan XPS spectra for the samples prepared from the three precursors annealed to 300, 500 and 800 °C

The wide scan XP spectra (from 0 – 600 eV) for all of the samples annealed from 300 – 800 °C are shown in figure 3.14; the peaks at approximately 75, 135, and 533 eV correspond to Al(2p), P(2p), and O(1s) signals respectively and are discussed in their relative sections below with the aid of narrow scans. Additional features of the spectra are the peaks at 284.7 eV, which is assigned to C(1s) from the presence of adventitious carbon. Adventitious carbon is a layer, around 1 – 2 nm thick, of carbon (C-C) which is present on the surface after even brief exposure of a sample to atmosphere. Whilst the carbon species are contaminants, their presence is useful as the C(1s) peak can be used as the reference peak when calibrating spectra. The peaks at 191.8 eV are from P(2s) photoelectrons, expected from the presence of P(2p) signals; this is also the case for the Al(2s) and O(2s) signals detected at 119.8 and 25.5 eV respectively.

Also to be noted is the presence of surface contaminants on three of the samples: the AlCl₃ at 800 °C, the Al(NO₃)₃ at 800 °C and Al(OH)₃ at 500 °C. Potassium contamination is observed in the AlCl₃ with a K(2p) signal observed at 293 eV. With the Al(OH)₃ and Al(NO₃)₃ samples silicon is the contaminant with a Si(2p) signal at an energy of 101.9 eV.

Figure (3.15) shows the Al(2p) spectra for the samples across the annealed temperatures. For the hydroxide samples, a signal is seen across the temperature range with the peak at 75.3 eV at 300 °C, shifting to 75.1 eV at 800 °C; the peak positions show that the aluminium present is Al³⁺ which is expected for aluminium phosphate species. Metallic aluminium species would be observed at a peak position of (approx.) 72.6 eV, with a more asymmetric peak due to greater spin-orbit splitting³⁰. In the nitrate and chloride samples however, peak signals are not observed at lower temperatures. In the nitrate sample, there is an absence of a peak at 300 °C and in the chloride samples no signal is seen until the sample is annealed to 800 °C. The absence of these peaks corresponds to the physical appearance of the samples. The samples with no Al(2p) peak were visibly wet and tacky, this observation

together with the XP spectra can be attributed the aggregation of hydrated phosphate species (such as phosphoric acid) on the surface of the samples at lower temperatures. NMR spectra also show the presence of hydrated phosphate species corroborating this theory. As the annealing temperature increases, water in the surface species is driven off resulting in either the desorption or reaction with bulk phosphate and aluminium substrates to form aluminium metaphosphate at higher temperatures.

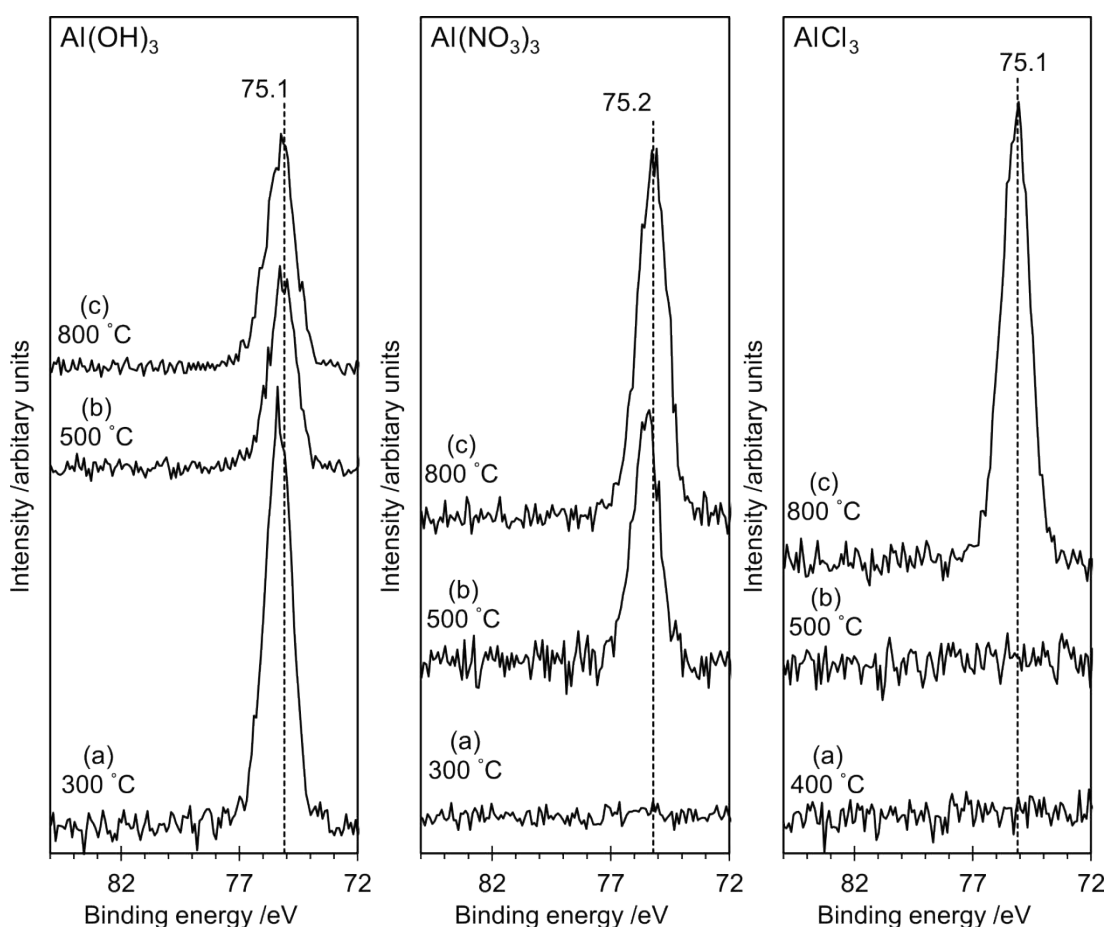


Figure 3.15: Al(2p) XP spectra for the samples prepared from the three precursors annealed to 300, 500 and 800 °C

The P(2p) spectra (figure 3.16), show a single peak across all of the samples at 135 eV shifting to lower binding energies as the annealing temperature increases. These signals are consistent with literature data^{31, 32} and the NIST database average of 134.8 eV for aluminium phosphates³³. Compared to XPS spectra of the sodium phosphates however,

there is a much larger and differing shifts of binding energy of 2 eV from 132.5 eV for sodium orthophosphate to 134.5 eV for sodium metaphosphates.

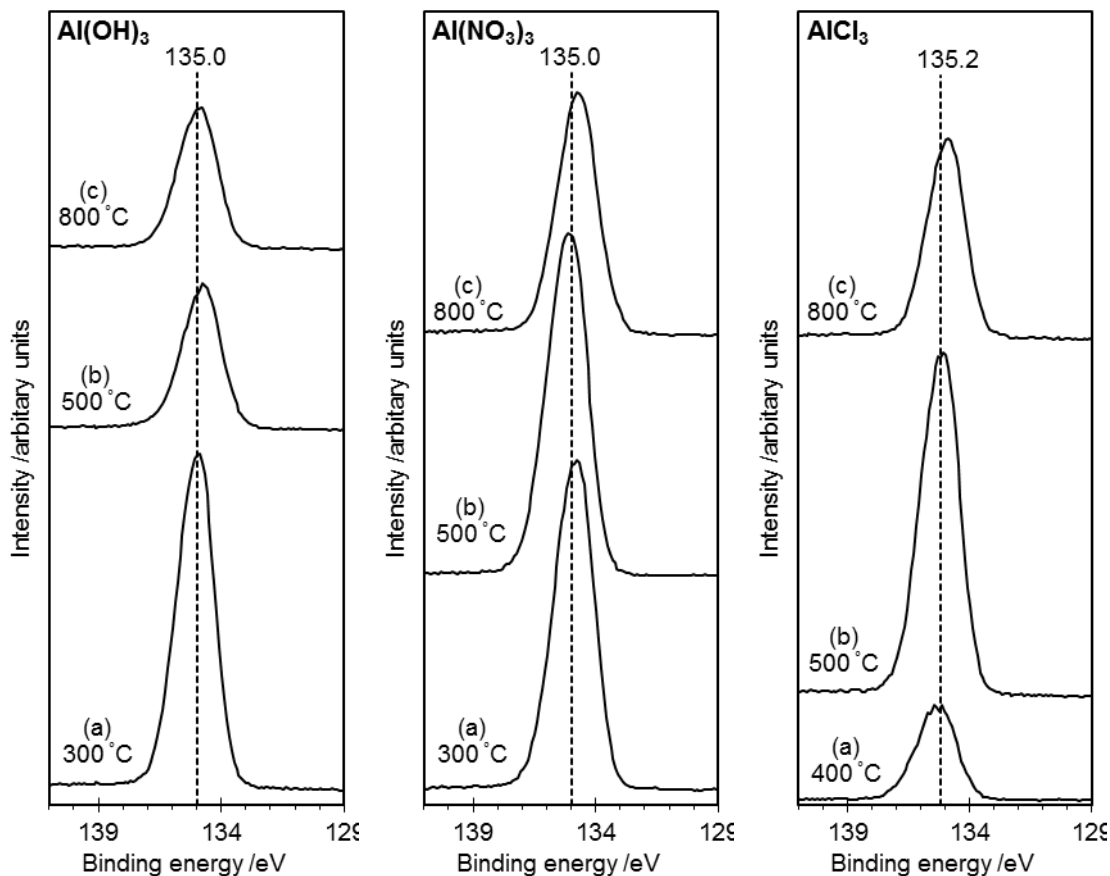


Figure 3.16: P(2p) XP spectra for the samples prepared from the three precursors annealed to 300, 500 and 800 °C

Figure 3.17 shows the O(1s) region for the annealed samples. Curve fitting shows two distinguishable peaks at binding energies of 533.7 and 533.2 eV. As annealing temperature increases, there is a shift in the relative peak intensity towards lower binding energy, which is summarised in Table 3.17. Since the ^{31}P NMR and XRD data have shown that the only species present at 800 °C is aluminium metaphosphate, then the peaks observed in the O(1s) signal cannot be attributable to other compounds. The assignments of these peaks have been made using the arguments put forth by Gresh et al³⁴, that two features of the peaks are attributed to the two types of oxygen species present in aluminium

metaphosphate the bridging oxygen (BO) and non-bridging oxygen (NBO), which is also present in the orthophosphate unit.

As the bulk characterisation shows the progressive polymerisation of orthophosphate into metaphosphate as annealing temperature increases, the O(1s) peak at lower binding energy (532.1 – 532.5 eV) can be assigned as the bridging oxygen and the peak at higher binding energy (533.6 – 534.0 eV) to the non-bridging oxygen. With these assignments, the surface ratio of BO/NBO can be calculated from the relative areas of the peaks and are shown in Table 3.18; the changes in the ratio as annealing temperature support the conversion of orthophosphate to metaphosphate.

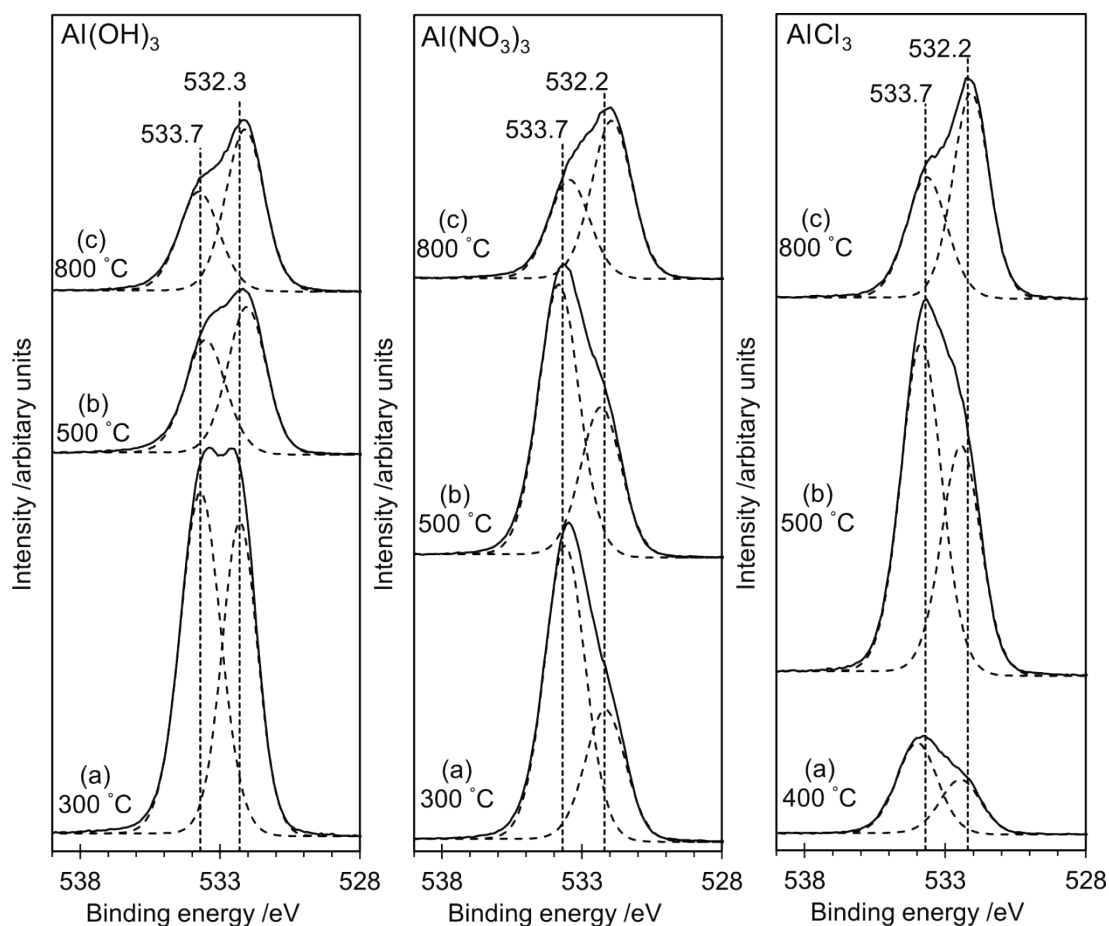


Figure 3.17: O(1s) XP spectra for the samples prepared from the three precursors annealed to 300, 500 and 800 °C

Reactant		Annealing temperature /°C					
		300/400		500		800	
Al(OH) ₃	Binding energy	533.7	532.3	533.5	532.0	533.8	532.1
	% of peak area	55.5	44.5	44.6	55.4	39.0	61.0
	Peak area ratio	0.8		1.2		1.6	
Al(NO ₃) ₃	Binding energy	533.6	532.2	533.8	532.3	533.7	532.1
	% of peak area	69.1	30.9	64.4	35.6	38.5	61.5
	Peak area ratio	0.5		0.6		1.6	
AlCl ₃	Binding energy	534.0	532.5	533.9	532.4	533.7	532.1
	% of peak area	62.4	37.6	59.8	40.2	39.6	60.4
	Peak area ratio	0.6		0.7		1.5	

Figure 3.18: Tabulation of the peak areas for the O(1s) XP spectra for the samples prepared from the three precursors annealed to 300, 500 and 800 °C

In the cases of the samples in which no Al(2p) signal is observed an issue may arise in the O(1s) peak assignments due to no aluminium phosphate species being present on the surface of the samples. However, as previously stated, the physical appearance of the samples and previous data suggest that they are still strongly hydrated and the surface of the samples consists of hydrated phosphoric acid species. As the annealing temperature increases and water is driven off the surface the hydrated phosphates may begin to polymerise into hydrated poly-phosphates, such as the case H_3PO_4 into $\text{H}_4\text{P}_2\text{O}_7$. This explains the observed trend in the O(1s) spectra of the chloride based samples in which no aluminium signal is observed at 400 and 500 °C.

Whilst the assignments, of the O(1s) region of the XP spectra are in conclusive agreement with the bulk and surface data shown earlier in our discussion, there is some disagreement with previous assignments in the literature. In the study by Gresch et al³⁴ on a series of model sodium phosphates, concluded that the peak at lower binding energy is attributed to the non-bridging oxygen. In their spectra of P_4O_{10} , the O(1s) signal is dominated by the peak at higher binding energy with a BO/NBO ratio that is expected for the molecule. From this, their conclusions were that the bridging oxygen appears at higher binding energies than non-bridging oxygen.

The assignments used by Gresch³⁴ have also been used by others in studies on various other phosphates, such as Rotole and Sherwood's analysis of model aluminium phosphates^{32, 35}, Crobu et al. in their work on zinc phosphates³⁶ and Karabulut et al on iron phosphate glasses³⁷. In these studies, the shape of the O(1s) spectra for metaphosphate samples are all very similar; the peak intensity is distributed towards the lower binding energy component. If the BO/NBO assignments given by Gresch are correct, then the majority of the surface oxygen species of the samples are non-bridging despite the bulk analysis showing that the materials are aluminium metaphosphate by 800 °C.

The assignments made by Gresch are based upon on the electronegativity of bridging and non-bridging oxygen species and thus are sensible on the basis of chemical shift in XPS. This does explain the universal acceptance on the bridging/non-bridging oxygen peak assignments across numerous literature sources in work on phosphate species³⁸⁻⁴³. Across this study, the bulk and surface properties of the aluminium phosphate species which can assist in proposing a reassignment of the O(1s) peaks for aluminium metaphosphate. The bulk data for the samples showed the trend that with increasing annealing time, there is a polymerisation of phosphate units that, as shown by XRD and ³¹P NMR, by 800 °C have fully converted into Al(PO₃)₃ (i.e. there is an increasing number of P-O-P bonds within the sample). If this trend is tied to the O(1s) XPS data again showing the increase of the peak ration towards the signal at lower binding energy, then it can be argued that as the number of bridging oxygen increases the peak corresponding to those oxygen should also increase.

The arguments put forward by Gresch are logical and do fit the work on sodium phosphates; shown by their adoption by the wider academic community as the accepted peak assignments. However, the combination of the bulk and surface data presented for aluminium phosphates suggests that more care should be used when using Gresch's work for non-sodium phosphates. Given that the assignments are based on electronegativity, a

change in the counterion may potentially have an effect on the relative peak positions; in this case from sodium (0.93 on the Pauling scale) to aluminium (1.61 Pauling).

A single XP spectrum taken alone, without the bulk and additional surface XPS data tracking the evolution of species with relation to temperature could use the Gresch assignments to argue the low binding energy peak of a metaphosphate sample were the non-binding oxygen by arguing that the peak relates to terminal units. However, when the bulk and surface data is taken together as a whole, in the context of the thermal evolution of aluminium metaphosphate then these assignments should be revisited. Indeed, there is a trend in Gresch's work which shows the increasing intensity of the peak he assigned to the BO (the higher binding energy peak) when the P/Na molar ratio was increased in the reaction mixture. In that case, additional phosphates were added resulting in the formation of increased bridging oxygen which lead to the case of the corresponding XPS peak increasing in intensity. From this it can be concluded that Gresch's XPS assignments for the O(1s) region are valid for the case of sodium phosphates; but the work presented here shows that greater care should be used in applying these assignments to aluminium phosphates. As stated above, there is the possibility the choice in counter-ion is the cause for the switching of the BO/NBO signals and so further research should be conducted before using either the assignments given in this study or the assignments given by Gresch for studies into other metal phosphates.

Another correlation between the bulk and surface data is the intermediate polyphosphates observed in the bulk, and their effects on the Al(2p)/P(2p) XP spectra. ^{31}P NMR data shows the presence of partially polymerised hydrated phosphate species. These species were shown to aggregate on the surface of the samples shown by the absence of any Al(2p) signal at the lower temperatures of the $\text{Al}(\text{NO}_3)_3$ and AlCl_3 samples, but whilst observing P(2p) signals. A number of these were also described as being visibly wet. This can be

attributed to the fact that the phosphates are insoluble in water, but are partially soluble in acidic nitrate and chloride solutions. Hence, this shows why the $\text{Al}(\text{NO}_3)_3$ and AlCl_3 samples took longer to dry and may potentially elude to the mechanistic differences observed depending on the choice of aluminium precursor.

3.4.5: Stability towards Thermal Hydration

Magnesium phosphate based coatings have shown to outperform aluminium orthophosphate in imparting tensile properties to steel substrates. However the magnesium metaphosphate samples were prone to thermal hydration leading to degradation. It has been shown that aluminium metaphosphate has been formed from the three various precursors, and now the stability of the samples towards thermal hydration can be tested by the method detailed in section 2.2.2.

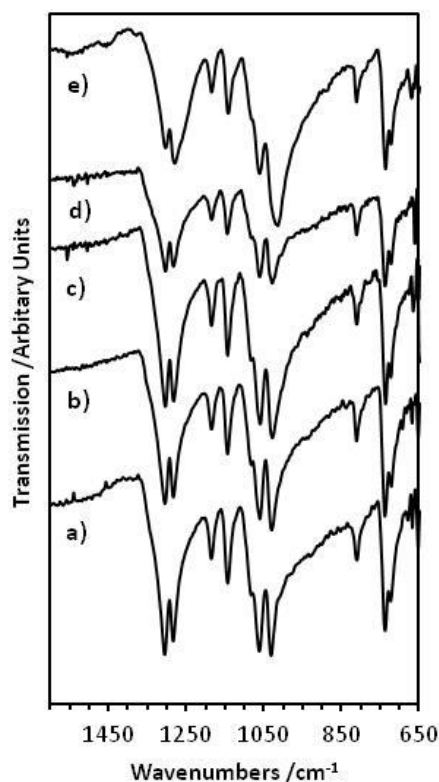


Figure 3.19: ATR-FTIR spectra for samples prepared from $\text{Al}(\text{OH})_3$ annealed to 800°C and left in the humidity chamber for a) 2, b) 3, c) 4, d) 6 and e) 9 weeks

Figures 3.19, 3.20 and 3.21 show the ATR-IR spectra for the samples annealed to 800 °C from $\text{Al}(\text{OH})_3$, $\text{Al}(\text{NO}_3)_3$ and AlCl_3 respectively. The samples were left in the humidity chamber for 9 weeks, and tested at periods of 2, 3, 4, 6, and 9 weeks. Degradation of the magnesium metaphosphate was observed from the loss of intensity of the bands assigned to P-O-P bonds and a shift of the P=O assigned bands to higher wavenumbers as the metaphosphate network breaks down over a period of 3 weeks¹⁶. As seen across all of the samples, there is no observed change in the bands assigned to aluminium metaphosphate in the spectra over the 9 week period. From this it can be concluded that aluminium metaphosphate synthesised from various precursors is significantly more stable towards the effects of thermal hydration than its magnesium analogues.

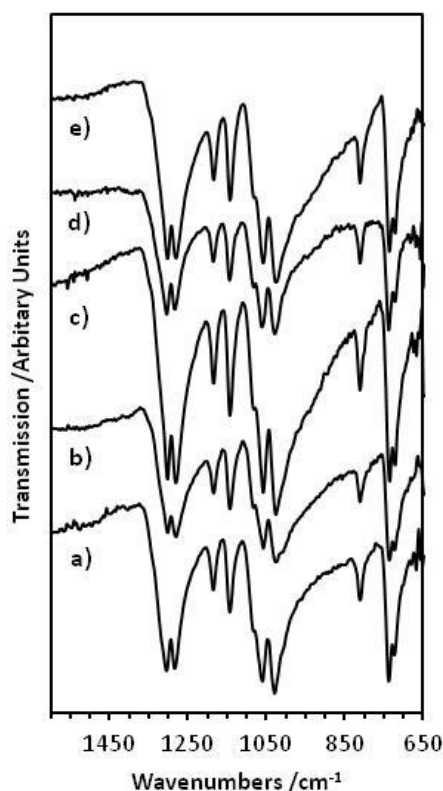


Figure 3.20: ATR-FTIR spectra for samples prepared from $\text{Al}(\text{NO}_3)_3$ annealed to 800 °C and left in the humidity chamber for a) 2, b) 3, c) 4, d) 6 and e) 9 weeks

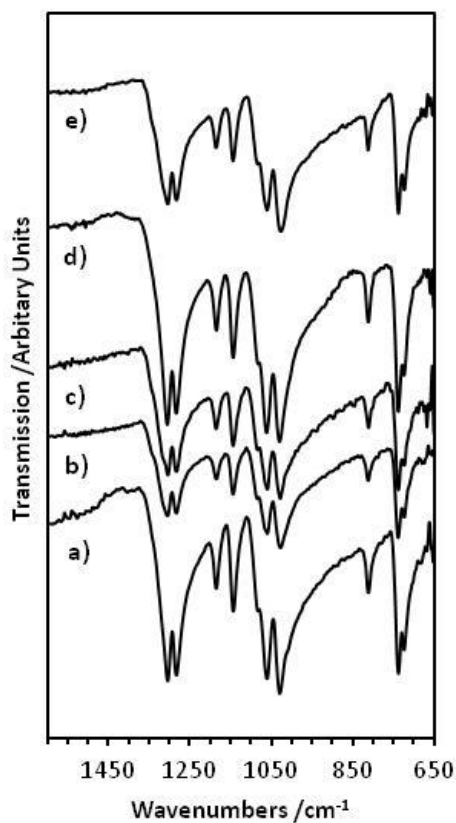


Figure 3.21: ATR-FTIR spectra for samples prepared from AlCl_3 annealed to $800\text{ }^\circ\text{C}$ and left in the humidity chamber for a) 2, b) 3, c) 4, d) 6 and e) 9 weeks

3.5: Effects of the Phosphorus:Aluminium Ratio

To examine the effects of reagent ratio on the formation of aluminium metaphosphate, the P/Al ratio was adjusted from 3/1 to 4/1. The analytical techniques shown above were used again on the following samples, allowing a direct comparison between of the bulk and surface character of the samples and to determine any mechanistic differences between the different samples.

3.5.1: Vibrational spectroscopy

ATR-FTIR spectra were obtained from the hydroxide and nitrate samples annealed to 300, 500, and 800 °C. Again, due to the wet nature of the chloride based samples, only the spectrum for the sample annealed to 800 °C was taken.

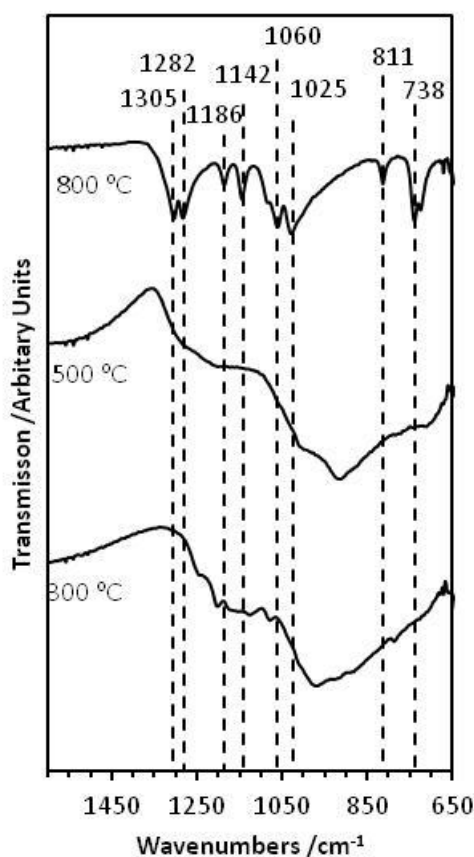


Figure 3.22: ATR-FTIR spectra for samples prepared from Al(OH)_3 with a P/Al ratio of 4/1 annealed to 300, 500 and 800 °C

In Figure 3.22, the IR spectra for the hydroxide based samples are shown. The spectrum at 800 °C shows an evolution of peaks corresponding to the formation of aluminium metaphosphate, as with the 3/1 hydroxide species. The peaks at 811, 1025, 1060, and 1070 cm^{-1} show the formation bridging oxygen (P-O-P), the main indication of the formation of metaphosphate^{18, 19}. In the samples annealed at lower temperatures however there are only large broad peaks across the regions where peaks would be observed in the formation

of aluminium metaphosphate ($1070 - 810 \text{ cm}^{-1}$) and aluminium phosphate in general ($1350 - 1100 \text{ cm}^{-1}$ for P-O stretches and $650 - 750 \text{ cm}^{-1}$ for Al-P stretches), the 3/1 samples showed the evolution of strong sharp peaks across these regions showing the formation of aluminium metaphosphate at this temperature. The data shows that the required temperature for the formation of $\text{Al}(\text{PO}_3)_3$ increases as the ratio of P/Al increases when using $\text{Al}(\text{OH})_3$ as a precursor.

In the spectra of the nitrate based samples (figure 3.23), we again observe the formation aluminium metaphosphate by 800°C from the presence of the relevant peaks at 800 , 1025 , 1050 , and 1070 cm^{-1} . In this instance, unlike the hydroxide samples, the peaks at 500°C are fully resolved into aluminium metaphosphate and beginning to evolve at 300°C . Again, to compare to the 3/1 samples there are clear differences in the spectra when prepared using different P/Al ratios. The peaks appear to be more resolved than their 3/1 counterparts, possibly suggesting less of a presence of the amorphous and wet intermediates. The chloride based samples shown in figure 3.24 were again only run on the 800°C sample due to possible damage to the ATR crystal from the wet samples taken at $400/500^\circ\text{C}$. This spectrum again shows the formation of aluminium metaphosphate from the peaks at 800 , 1010 , and 1070 cm^{-1} giving a good comparison to the 3/1 samples.

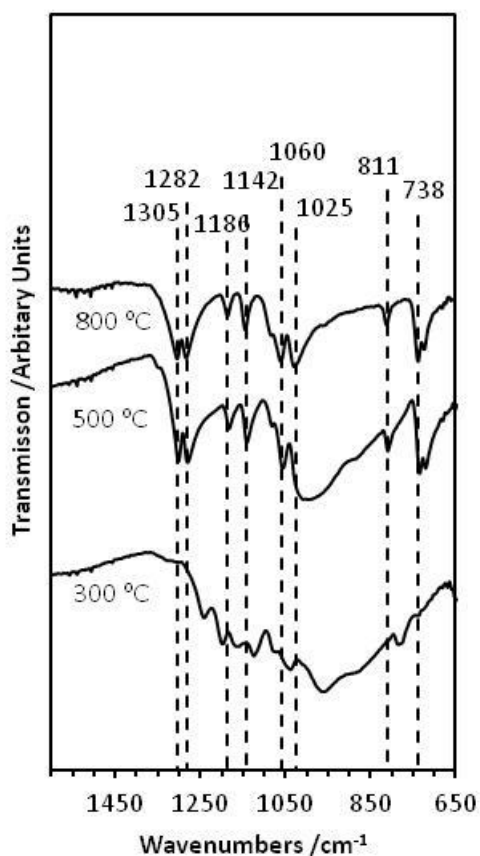


Figure 3.23: ATR-FTIR spectra for samples prepared from $\text{Al}(\text{NO}_3)_3$ with a P/Al ratio of 4/1 annealed to 300, 500 and 800 °C

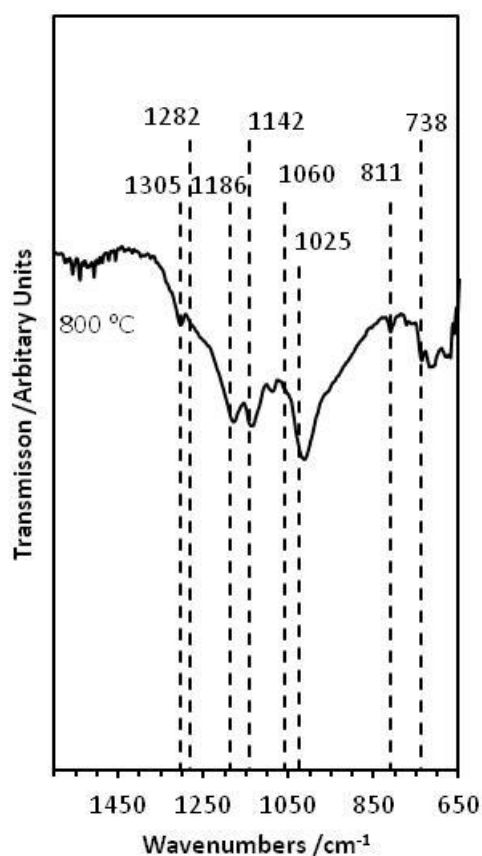


Figure 3.24: ATR-FTIR spectrum for samples prepared from AlCl_3 with a P/Al ratio of 4/1 annealed to 800 °C

The Raman spectra of the samples annealed to 800 °C (figure 3.25), once again give a good comparison to the 3/1 samples and corroboration of the IR data, showing the polymerisation of phosphate units in all three samples at 800 °C. The peaks at 610, 640 and 690 cm^{-1} are assigned to the symmetric stretches of the P-O-P bonds showing the polymerisation of the phosphate.

As in the case of the samples formulated with a 3/1 acid/oxide ratio, the vibrational spectroscopy shown is a useful snapshot of the formation of aluminium metaphosphate, but for more in-depth information on the bulk mechanisms and surface behaviour, more analysis is required and the samples have been studied by NMR, XRD and XPS.

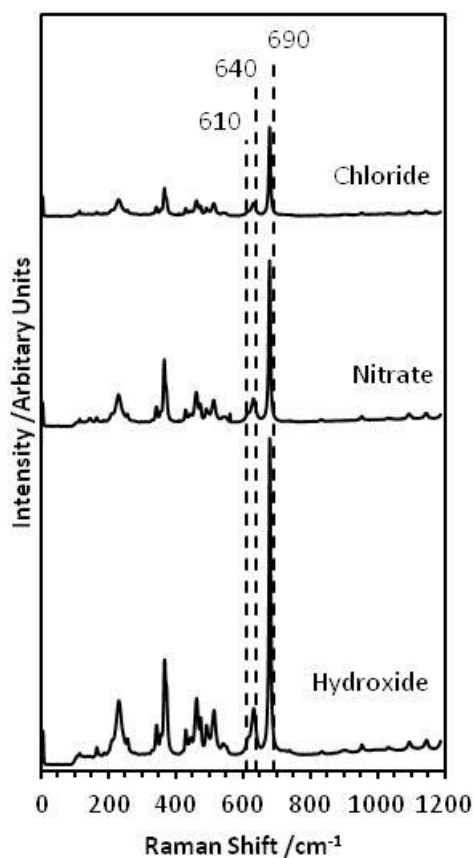


Figure 3.25: Raman spectra for samples prepared with a P/Al ratio of 4/1 annealed to 800 °C

3.5.2: ³¹P Nuclear Magnetic Resonance Spectroscopy

³¹P NMR has shown itself to be a powerful analytical tool in the analysis of phosphate evolution in the 3/1 samples. The spectra were able to highlight key differences in the formation of metaphosphate using different precursors and highlight the different non-crystalline intermediates present in the samples. Using NMR on these samples should allow for an excellent comparison between the samples and the effect of changing the P/Al ratio.

As in the case of the 3/1 samples, the ³¹P NMR spectra (figure 3.26) show an overall trend of peaks shifting towards lower chemical shifts; a sign of increasing phosphate polymerisation due to the increased shielding of the ³¹P nuclei.

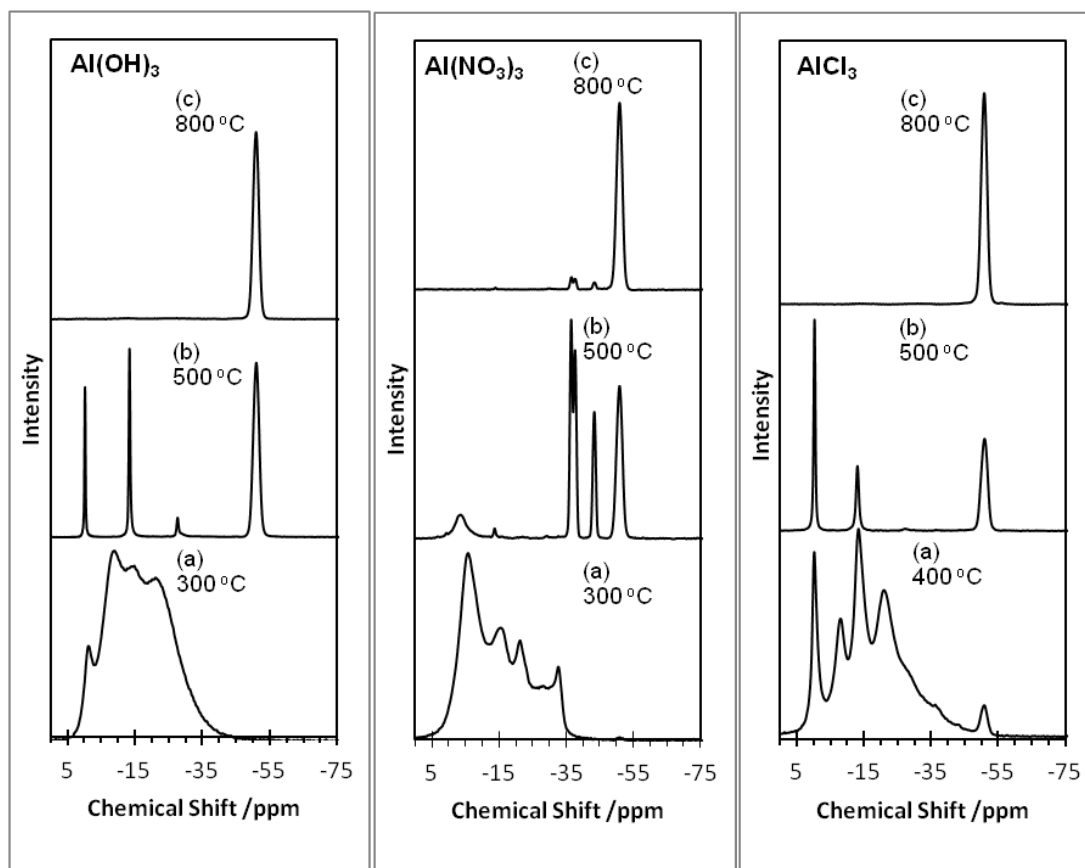


Figure 3.26: ^{31}P spectra for the samples prepared from the three precursors with a P/Al ratio of 4/1 annealed to 300, 500 and 800 °C

There are clear similarities but also differences in the spectra for the hydroxide based samples as the P/Al ratio increases from 3/1 to 4/1. In both samples, there are broad sets of overlapping peaks at 300 °C. They share observable peaks seen at -1, -7, and -14 ppm which are attributed to hydrated phosphate species such as phosphoric acid. However, the spectrum also shows an absence of the peaks at -36.5 and -43.0 ppm present in the 3/1 which was assigned to aluminium tripolyphosphate. This difference gives an initial indication that there are mechanistic differences in the formation of aluminium phosphate when adjusting the P/Al ratio. On heating to 500 °C, the evolution of cubic aluminium metaphosphate is observed as with the 3/1 samples however there is no evolution of monoclinic aluminium metaphosphate at these temperatures again showing differences in

the two preparation methods, by 800 °C there is full conversion to aluminium metaphosphate.

In the nitrate samples, at 500 °C peaks at -36.5, -43.0, and -50.5 ppm show evolution of monoclinic metaphosphate as well as cubic metaphosphate. After annealing to 800 °C, there is a strong cubic aluminium metaphosphate signal present, with a great reduction in the intensity of the signals corresponding to monoclinic metaphosphate. This is markedly different from the analogous 3/1 samples where there is little change in the relative intensities in the cubic and monoclinic signals on annealing from 500 to 800 °C. The ³¹P NMR shows, when combined with the hydroxide data, compelling evidence that there is a substantial impact on the formation of aluminium metaphosphate.

In the AlCl₃ based samples, the formation of both cubic and monoclinic metaphosphate is observed at 400 °C converting fully to cubic aluminium metaphosphate on annealing to 500 and 800 °C. This follows the same trend observed in the 3/1 sample in which minimal monoclinic metaphosphate is formed.

As shown, increasing the ratio of P/Al appears to reduce the amount of monoclinic metaphosphate formed in the intermediate temperature ranges. Tricot et al.⁴, in a study of phosphate formation from aluminium hydroxide, showed that using an excess of phosphoric acid resulted in the direct formation of cubic metaphosphate from the hydrated phosphate species, bypassing the monoclinic phosphate species. This argument holds true for the Al(OH)₃ based samples, but the effects of excess phosphate in the reaction mixtures for the Al(NO₃)₃ and AlCl₃ samples still require explanation.

3.5.3: X-ray Photoelectron Spectroscopy

The wide scan spectra for the samples are presented in figure 3.27, as with the previous 3/1 samples the peaks for Al(2p), P(2p), and O(1s) at 75.1, 532, and 134.5 eV respectively will be discussed in their relevant sections. Again, with the previous samples, the peaks corresponding to adventitious carbon (284.7 eV), Al(2s) (119.2 eV), P(2s) (191.1 eV), and O(1s) (25.1 eV) are present. Additionally to note, like the 3/1 samples there are signals showing silicon contamination at 101.9 eV relating to Si(2p) across numerous samples and the Si(2s) signal observed at 152.6 eV.

On examination of the Al(2p) signals (figure 3.28) for the samples, both similarities and differences are observed when compared to the 3/1 samples. The hydroxide samples are very comparable to their counterparts, with signals detected at 75.1 eV at 300 °C shifting slightly to 75.3 eV at 500 °C before shifting back 75.1 eV on heating to 800 °C. The chloride based samples also show a very similar situation to the 3/1 samples. No aluminium signals are observed at 400 and 500 °C with a peak evolving at 75.1 eV upon annealing to 800 °C. As before, combined with the physical observations of the sample, the lack of an aluminium signal at the lower temperatures is attributable to the aggregation of hydrated phosphate species on the surface of the samples at 400 and 500 °C. As the annealing temperature increases to 800 °C, the water is driven off forming aluminium metaphosphate resulting in the emergence of an Al signal.

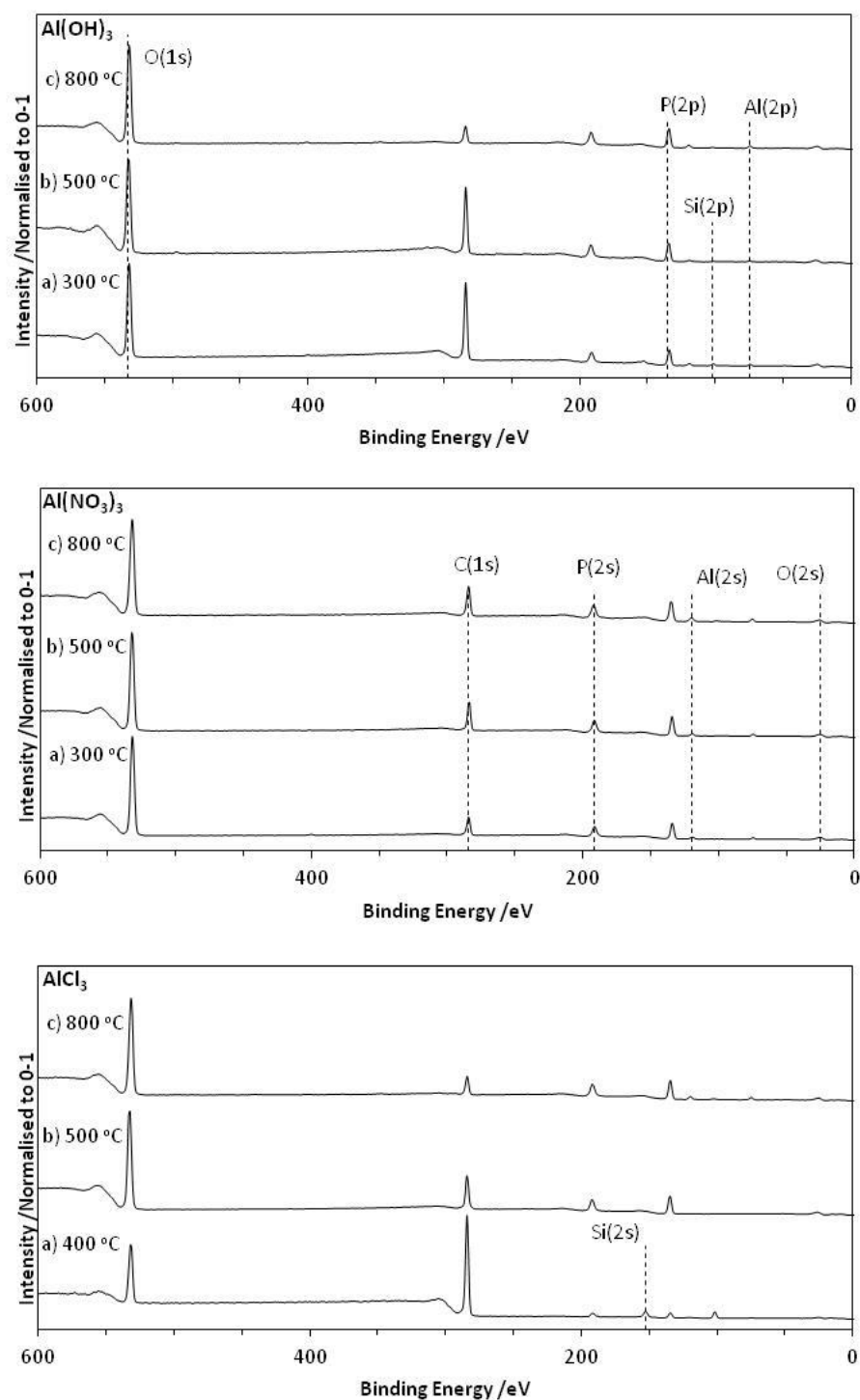


Figure 3.27: Wide-Scan XPS spectra for the samples prepared from the three precursors with a P/Al ratio of 4/1 annealed to 300, 500 and 800 °C

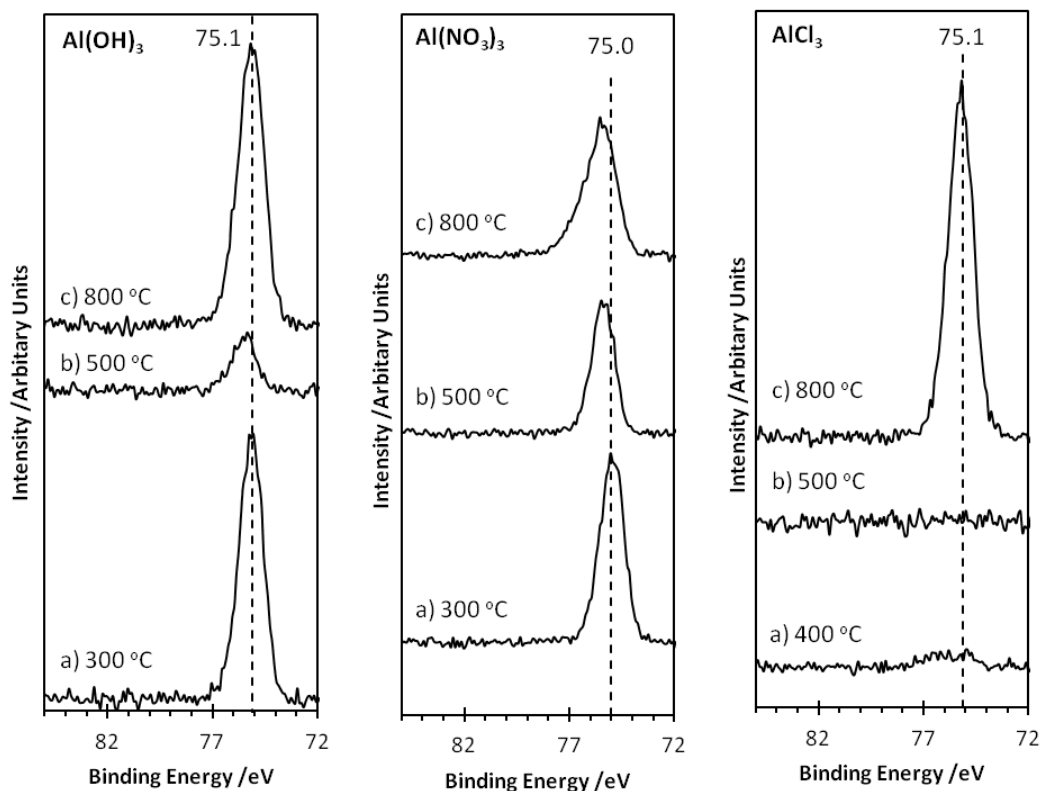


Figure 3.28: *Al(2p) XPS spectra for the samples prepared from the three precursors with a P/Al ratio of 4/1 annealed to 300, 500 and 800 °C*

The nitrate based samples, show an Al(2p) peak across all three temperature at 75.0 eV at 300 °C shifting to ~75.4 eV at 500 and 800 °C. Here, the first differences from the 3/1 samples in the XP spectra are observed. In the 3/1 samples, at 300 °C no Al(2p) signal is detected, but a strong peak is present in the 4/1 samples. It is possible from this data to hypothesise that when using aluminium nitrate as a precursor with an excess of phosphoric acid the condensation of orthophosphate units occurs more readily resulting in water being driven out of the system at lower temperatures. This is corroborated by the NMR data which showed that cubic aluminium metaphosphate is formed more readily and directly, without the formation of monoclinic metaphosphate.

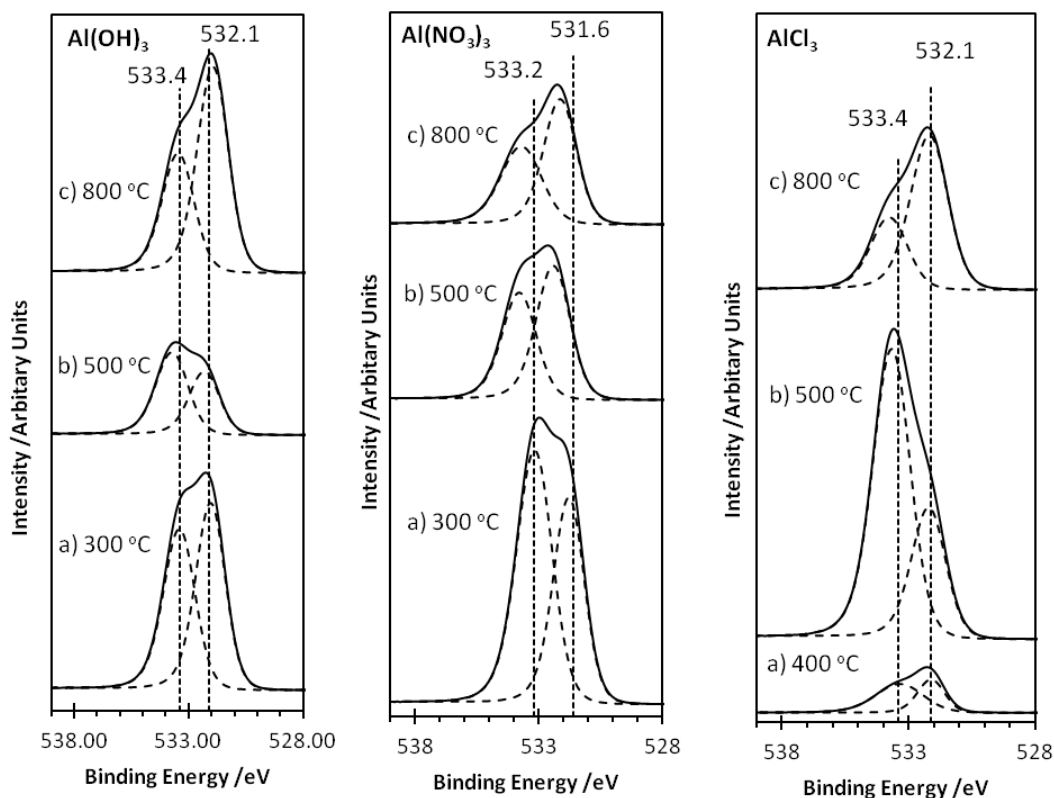


Figure 3.29: O(1s) XPS spectra for the samples prepared from the three precursors with a P/Al ratio of 4/1 annealed to 300, 500 and 800 °C

The O(1s) region (figure 3.29) has been shown to be able to differentiate between the two oxygen species present in the polymerised phosphates; the bridging oxygen (BO) and the non-bridging oxygen (NBO) which we have assigned to 532.1 eV and 533.4 eV respectively. The assignments given in the 3/1 samples were the BO to the lower binding energy peak and the NBO to the higher binding energy peak. The 3/1 samples showed a shifting of peak intensity towards increasing the BO/NBO ratio as annealing temperature increases. This general trend is also observed in the 4/1 samples but there are differences between the spectra that require mentioning. In the hydroxide and chloride samples, the BO/NBO ratio decreases on heating to 500 °C before rising upon heating to 800 °C; this is not observed in the nitrate samples, which follow the trend observed in the 3/1 samples where the BO/NBO ratio steadily increases with annealing temperature. At 800 °C, there are clear

differences in the BO/NBO ratio both between the precursors and the P/Al ratio. The hydroxide sample shows a good comparison between the P/Al of 3/1 and 4/1 samples with BO/NBO ratios of 1.6 and 1.7 respectively at 800 °C. The nitrate sample shows a slightly lower BO/NBO ratio as the P/Al ratio increases, 1.6 to 1.3 and the chloride sample shows a comparatively large increase from 1.5 to 2.2.

Reactant		Annealing temperature /°C					
		300/400		500		800	
Al(OH) ₃	Binding energy	533.4	532.1	533.7	532.3	533.4	531.9
	% of peak area	47.7	52.3	57.4	42.6	36.9	63.1
	Peak area ratio	1.1		0.7		1.7	
Al(NO ₃) ₃	Binding energy	533.2	531.6	533.7	532.4	533.6	532.1
	% of peak area	58.4	41.6	44.5	55.5	43.4	55.6
	Peak area ratio	0.7		1.2		1.3	
AlCl ₃	Binding energy	533.4	532.1	533.6	532.2	533.7	532.1
	% of peak area	60.4	39.6	70.5	29.5	31.3	68.7
	Peak area ratio	0.7		0.4		2.2	

Figure 3.30: Tabulation of the peak areas for the O(1s) XP spectra for the samples prepared from the three precursors annealed to 300, 500 and 800 °C

The effect of altering the ratio of P to Al does appear to have a notable effect on the aluminium metaphosphate formed as the annealing temperature increases to 800 °C. In the hydroxide samples, the NMR data shows no formation of monoclinic metaphosphate formation at 500 °C in the samples with excess phosphoric acid added. This is a possible explanation for the decrease of the BO/NBO ratio when heating from 300 to 500 °C. The surface at this temperature may have less metaphosphate and more lower order polyphosphates or orthophosphates than the 3/1 sample; upon heating to 800 °C, the sample fully converts to cubic metaphosphate and the chemistry 3/1 and 4/1 samples become comparable and so have a similar BO/NBO ratio.

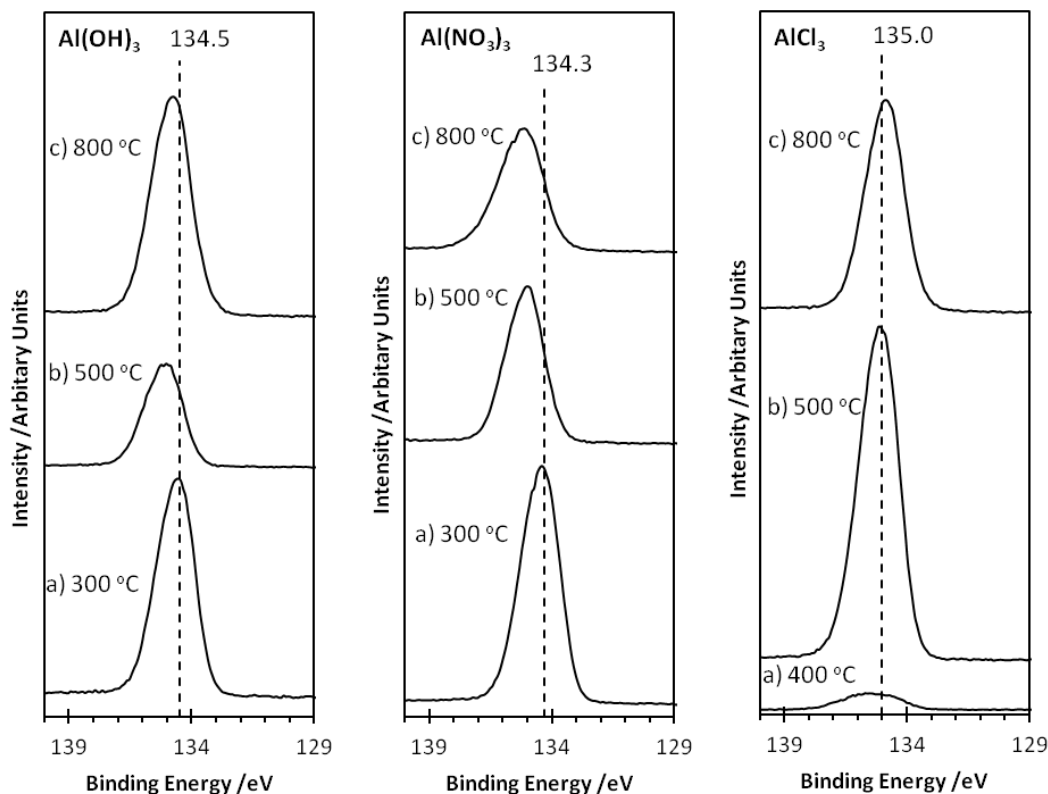


Figure 3.31: *P(2p)* XPS spectra for the samples prepared from the three precursors with a P/Al ratio of 4/1 annealed to 300, 500 and 800 °C

Whilst this argument fits the data for the hydroxide based samples, there is more ambiguity for the nitrate and chloride based samples. At 500 °C the BO/NBO for the nitrate samples is 1.2 for the P/Al of 4/1 samples (double the value for the 3/1 samples), despite the bulk characterisation being very similar; in both samples the formation of cubic and monoclinic metaphosphate is observed. In the chloride samples, the BO/NBO is drastically higher for the 4/1 sample than 3/1 sample (2.2 and 1.5 respectively) at 800 °C in which only minimal monoclinic metaphosphate is formed in entire reaction at all.

3.6: Summary

In this chapter the formation of aluminium metaphosphate has been studied in relation to its potential use as a tensile coating for use on magnetic steel substrates. Whilst all of the samples were successful in forming aluminium metaphosphate fully by 800 °C, there were noticeable differences between the samples.

Depending on the precursor used, there is a difference in both the formation mechanism and structure of metaphosphate formed throughout the reaction and after fully annealing to 800 °C. The samples were also found to be stable to the effects of thermal hydration unlike their magnesium analogues which gives a good indication that they may perform well as tensile stress coatings for magnetic steel.

Analysis of the combination of surface and bulk data of the samples appears to give information somewhat contradictory to the currently accepted analysis of the surface properties of aluminium metaphosphate. The data here suggests that the assignments for the bridging and non-bridging oxygen species in O(1s) spectra should be reversed and so at least care should be taken in analysing the surfaces of phosphate species in the future.

Gresch's results on sodium phosphates showed an opposite pattern for the results presented for aluminium phosphates in this study. Their O(1s) XPS signal is dominated by the high binding energy peak for metaphosphate and by the low binding energy peak for the orthophosphate. This is consistent for the respective assignments of the peaks to bridging and non-bridging oxygens respectively. From this the concluding suggestion is that whilst there is a similarity in the polymerisation behaviour between metal phosphate species, sodium phosphates produce varied XP spectra compared to metals of higher valency. Therefore, Gresch's peak assignments should be limited in use outside of the analysis of sodium phosphates.

Using the knowledge and information gain from this chapter, coatings of the phosphates can now be created and tested for both their chemical properties and their performance as tensile coatings for magnetic steel substrates; this topic is discussed in chapter 4.

3.7: References

1. A. J. Moses, *IEEE Proceedings-a-Science Measurement and Technology*, 1990, **137**, 233-245.
2. S.-S. Cho, S.-B. Kim, J.-Y. Soh and S.-O. Han, *IEEE Transactions on Magnetics*, 2009, **45**, 4165-4168.
3. L.-Y. Hong, H.-J. Han, H. Ha, J.-Y. Lee and D.-P. Kim, *Composites Science and Technology*, 2007, **67**, 1195-1201.
4. G. Tricot, D. Coillot, E. Creton and L. Montagne, *Journal of the European Ceramic Society*, 2008, **28**, 1135-1141.
5. D.-P. Kim, H.-G. Woo, H. Ha, F. Cao, H.-S. Myung, J.-S. Rho and K.-S. Han, *Composites Science and Technology*, 2003, **63**, 493-499.
6. M. Vippola, J. Keranen, X. D. Zou, S. Hovmoller, T. Lepisto and T. Mantyla, *Journal of the American Ceramic Society*, 2000, **83**, 1834-1836.
7. J. H. Morris, P. G. Perkins, A. E. A. Rose and W. E. Smith, *Chemical Society Reviews*, 1977, **6**, 173-194.
8. M. N. Singh, I. Singh and J. L. Pandey, *Anti-Corrosion Methods and Materials*, 1997, **44**, 90-98.
9. H. J. Han and D. P. Kim, *Journal of Sol-Gel Science and Technology*, 2003, **26**, 223-228.
10. S. Ahmaniemi, M. Vippola, P. Vuoristo, T. Mantyla, M. Buchmann and R. Gadow, *Wear*, 2002, **252**, 614-623.
11. E. Cuynen, G. Goeminne, P. Van Espen and H. Terryn, *Surface and Interface Analysis*, 2000, **30**, 589-591.
12. S. Feliu and V. Barranco, *Electrochimica Acta*, 2004, **49**, 951-964.
13. B. Formanek, K. Szymanski, B. Szczucka-Lasota and A. Wlodarczyk, *Journal of Materials Processing Technology*, 2005, **164**, 850-855.
14. A. Kalendova, *Anti-Corrosion Methods and Materials*, 2003, **50**, 82-90.
15. K. Kobayashi, *Journal of Materials Science Letters*, 2001, **20**, 1121-1123.
16. V. L. Bemmer, PhD Thesis in The Properties of Electrical Steels and Their Coatings, Cardiff University, 2013.
17. T. Finch and J. H. Sharp, *Journal of Materials Science*, 1989, **24**, 4379-4386.
18. R. L. Frost, *Spectrochimica Acta Part a-Molecular and Biomolecular Spectroscopy*, 2004, **60**, 1439-1445.
19. A. John, D. Philip, K. R. Morgan and S. Devanarayanan, *Spectrochimica Acta Part a-Molecular and Biomolecular Spectroscopy*, 2000, **56**, 2715-2723.
20. D. C. Chen, L. P. He and S. P. Shang, *Materials Science and Engineering a-Structural Materials Properties Microstructure and Processing*, 2003, **348**, 29-35.
21. M. Vippola, J. Vuorinen, P. Vuoristo, T. Lepisto and T. Mantyla, *Journal of the European Ceramic Society*, 2002, **22**, 1937-1946.
22. J. M. Chiou and D. D. L. Chung, *Journal of Materials Science*, 1993, **28**, 1447-1470.

23. R. K. Brow, R. J. Kirkpatrick and G. L. Turner, *Journal of the American Ceramic Society*, 1990, **73**, 2293-2300.
24. L. Griffiths, A. Root, R. K. Harris, K. J. Packer, A. M. Chippendale and F. R. Tromans, *Journal of the Chemical Society-Dalton Transactions*, 1986, 2247-2251.
25. R. J. Kirkpatrick and R. K. Brow, *Solid State Nuclear Magnetic Resonance*, 1995, **5**, 9-21.
26. R. K. Brow, *Journal of the American Ceramic Society*, 1993, **76**, 913-918.
27. D. Laurencin, C. Gervais, H. Stork, S. Kraemer, D. Massiot and F. Fayon, *Journal of Physical Chemistry C*, 2012, **116**, 19984-19995.
28. M. A. Aramendia, V. Borau, C. Jimenez, J. M. Marinas, F. J. Romero and J. R. Ruiz, *Journal of Solid State Chemistry*, 1998, **135**, 96-102.
29. J. Zhu and Y. Huang, *Canadian Journal of Chemistry-Revue Canadienne De Chimie*, 2011, **89**, 803-813.
30. N. X. Database, srdata.nist.gov/xps, Accessed Apr 2017.
31. J. A. Rotole and P. M. A. Sherwood, *Surface Science Spectra*, 1998, **5**, 4-10.
32. J. A. Rotole and P. M. A. Sherwood, *Surf. Sci. Spectra*, 1998, **5**, 67-74.
33. N. X.-R. P. S. Database, srdata.nist.gov/xps, Accessed Aug 13 2015.
34. R. Gresch, W. Mullerwarmuth and H. Dutz, *Journal of Non-Crystalline Solids*, 1979, **34**, 127-136.
35. J. A. Rotole and P. M. A. Sherwood, *Surf. Sci. Spectra*, 1998, **5**, 60-66.
36. M. Crobu, A. Rossi, F. Mangolini and N. D. Spencer, *Analytical and Bioanalytical Chemistry*, 2012, **403**, 1415-1432.
37. M. Karabulut, G. K. Warasinghe, C. S. Ray, D. E. Day, O. Ozturk and G. D. Waddill, *Journal of Non-Crystalline Solids*, 1999, **249**, 106-116.
38. R. K. Brow, *Journal of Non-Crystalline Solids*, 1996, **194**, 267-273.
39. R. K. Brow and Z. A. Osborne, *Surface and Interface Analysis*, 1996, **24**, 91-94.
40. M. Eglin, A. Rossi and N. D. Spencer, *Tribology Letters*, 2003, **15**, 199-209.
41. P. Massiot, M. A. Centeno, M. Gouriou, M. I. Dominguez and J. A. Odriozola, *Journal of Materials Chemistry*, 2003, **13**, 67-74.
42. A. Speghini, E. Sourial, T. Peres, G. Pinna, M. Bettinelli and J. A. Capobianco, *Physical Chemistry Chemical Physics*, 1999, **1**, 173-177.
43. M. Zeyer, L. Montagne, V. Kostoj, G. Palavit, D. Prochnow and C. Jaeger, *Journal of Non-Crystalline Solids*, 2002, **311**, 223-232.

Chapter 4: The Analysis and Performance of Tensile Stress Coatings

Contents

4.1 Introduction	91
4.2: Tensile Stress Coatings.....	91
4.3: Analysis of the Performance of $\text{Al}(\text{PO}_3)_3$ Based Stress Coatings.....	95
4.3.1: Coatings with a Phosphorous/Aluminium Ratio of 3/1	95
4.3.2: Coatings with a Phosphorous/Aluminium Ratio of 4/1	99
4.3.2.1: ATR-FTIR Spectroscopy	106
4.3.2.2: Scanning Electron Microscopy	109
4.3.2.3: X-Ray Photoelectron Spectroscopy.....	112
4.4: Stress Relief Annealing Treatment.....	119
4.5: Ensuring Substrate Uniformity.....	127
4.6: Summary	134
4.7: References	136

4.1 Introduction

In this Chapter the formulation of tensile stress coatings, based on aluminium metaphosphate ($\text{Al}(\text{PO}_3)_3$), for use on magnetic steel substrates and their effectiveness at reducing the magnetostrictive effect are discussed. In Chapter 3, the relatively low temperature formation and chemical analysis of $\text{Al}(\text{PO}_3)_3$ from readily available precursors was examined. It was found that from the reaction of these AlX_3 ($\text{X} = \text{OH}, \text{NO}_3, \text{or Cl}$) precursors with phosphoric acid (H_3PO_4) resulted in the formation of powder $\text{Al}(\text{PO}_3)_3$ by 800 °C, making this reaction viable for use in the production of magnetic steel coatings by Cogent Power Ltd, which uses a current online furnace temperature of 850 °C.

These formulated coatings will be compared against the current online standard coatings prepared from aluminium orthophosphate (AlPO_4) and under the current hypothesis are expected to outperform it. The coatings are designed to provide a tensile holding to the substrate which reduces power loss through inhibiting the magnetostrictive effect. The use of metaphosphate based coatings is expected to form a network across the surface, imparting a greater degree of tensile strength to the substrate compared to orthophosphate coatings. This based on industrial testing on magnesium phosphate coatings which form metaphosphate upon annealing and provide improvements on inhibiting the magnetostrictive effect compared to aluminium orthophosphate coatings.

4.2: Tensile Stress Coatings

The designed purpose of the applied coatings is to inhibit the effects of the magnetostrictive effect through providing a tensile hold to the substrate, physically stopping the magnetostrictive expansion. The magnetostrictive effect arises through the inversion of magnetic domains in the substrate when exposed to a magnetic field¹. This inversion causes an expansion and contraction of the substrate and is responsible for the

distinctive humming noise produced by electrical transformers. When the steel substrate is employed in transformers, a portion of the electrical energy being passed through the steel is transferred to this process resulting in a loss of power. By using a tensile stress coating, the expansion/contraction of the substrate can be stopped, reducing the losses of power being transferred through the system.

The coating is applied to the substrate, and heated to 850 °C; this causes thermal expansion of the steel substrate and the coating is cured. After the coating is cured, the sample is cooled and tension from the coating is applied during the thermal contraction. Due to the nature and production process of the steel (which is reviewed in more detail in chapter 1), the contraction is not uniform relative to the expansion which can be seen in figure 4.1.

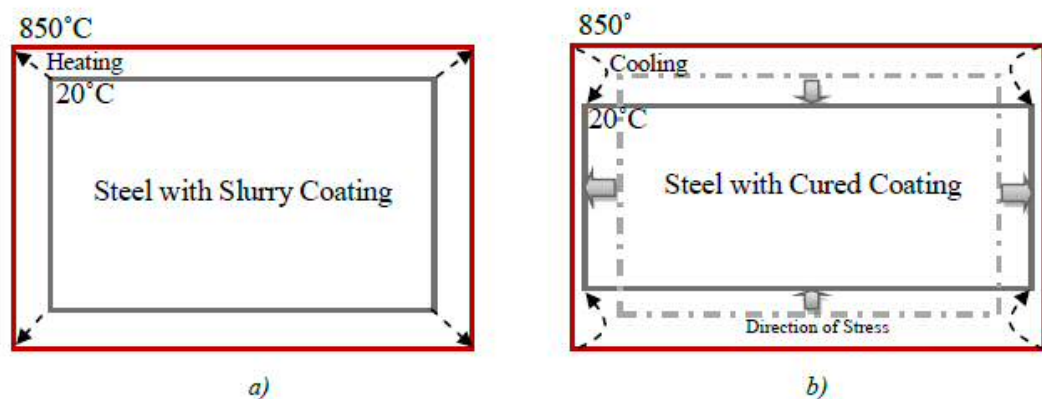


Figure 4.1: Schematic of the thermal expansion and contraction of grain orientated steel with tensile stress coating on a) heating and b) cooling. Dashed arrows show thermal expansion and contraction and solid arrows denote the net dimension change of the substrate. Figure taken from reference².

The tension coating now applied to the steel imparts a physical stress to the substrate which can limit the effects of the magnetostrictive effect through stopping the physical expansion/contraction caused through the inversion of the magnetic domains after exposure to a magnetic field. The effectiveness of the coatings can be tested by exposing

the samples to a magnetic field whilst under varying degrees of mechanical stress. The technique is discussed in more detail in section 2.9; by applying a relatively large tensile stress to the sample and lowering the stress whilst measuring the extent of the magnetostrictive effect on the sample the effectiveness of the coating can be determined. At high stresses, magnetostrictive effect is inhibited by the applied mechanical clamping. As the applied stress is lowered the coating becomes more responsible for inhibiting the magnetostrictive effect; resulting in formation of a magnetostriction-stress curve. The relative effectiveness of coatings can be determined through examining the stress shift of curves at the point that the curves take-off; the stress when the magnetostrictive effect is first observed in the sample (a generic example is shown in figure 4.2). At high applied tensile stress, no magnetostrictive stress is observed due to the mechanical clamping of the samples. As the stress is incrementally reduced, the coatings are more and more responsible for inhibiting the magnetostrictive effect. A more effective coating will exhibit the magnetostrictive effect at lower stresses than a less effective one; this allows for a comparison of the effectiveness of the coatings by measuring the stress shifts of the curves. In figure 4.2, the left curve begins to exhibit the magnetostrictive effect at an applied stress of -3 MPa whereas the right curve shows the effect at -1MPa. With the left most curve exhibiting magnetostriction at lower stresses, the performance of the sample is superior to the right curve by a stress shift of 2 MPa $(-3 \text{ MPa}) - (-1 \text{ MPa}) = 2 \text{ MPa}$).

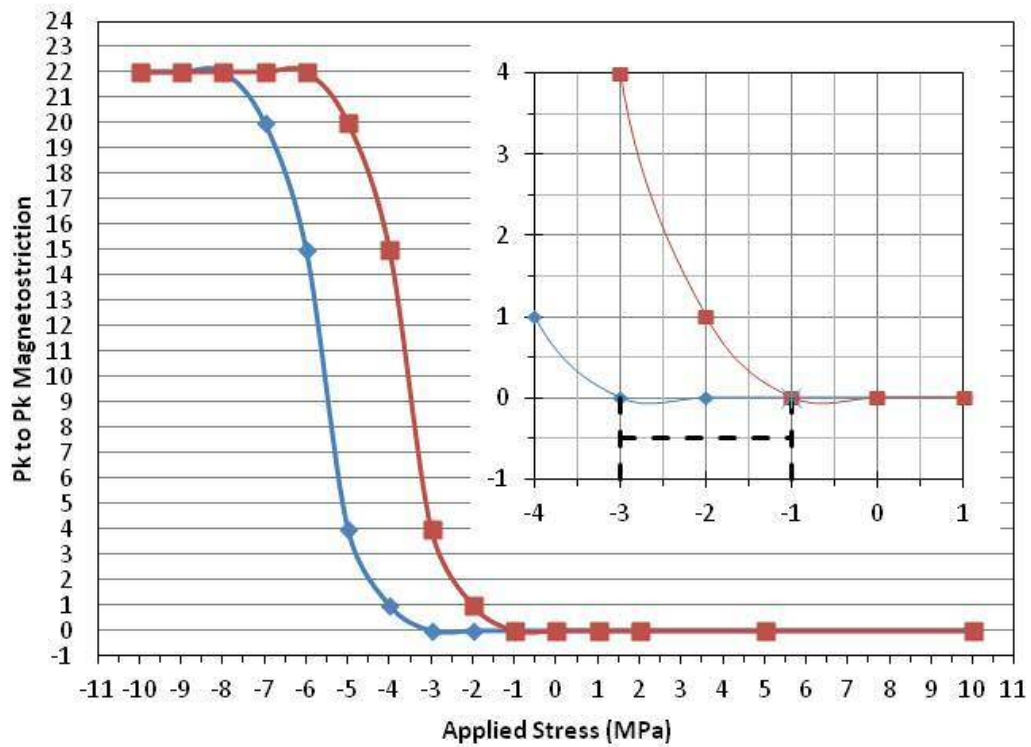


Figure 4.2: Generic example of two magnetostriction-stress curves. An improvement in the stress shift of 2 MPa from the red (square) to the blue (diamond) curve is highlighted.

This chapter examines the use of $\text{Al}(\text{PO}_3)_3$ based coatings and their relative effectiveness against the current standard on-line coating formulated from AlPO_4 . The aluminium metaphosphate coatings are expected to outperform the orthophosphate coatings due the formation of a metaphosphate network across the surface of the substrate. This hypothesis has arisen from the comparison of the performance of AlPO_4 against their magnesium analogues in industrial trials. The magnesium orthophosphate coatings were found to outperform the aluminium phosphate coatings which was attributed to the formation of magnesium metaphosphate during the annealing process which did not occur in the aluminium based coatings. However, the magnesium phosphate coatings were found to be prone to degradation via hydration, limiting their use as coatings. $\text{Al}(\text{PO}_3)_3$ coatings are being examined in this study to assess whether the formation of aluminium metaphosphate networks will outperform the orthophosphate coatings and will be more

stable than the magnesium analogues. Chapter 3 gives a review of work conducted on the comparisons of aluminium and magnesium phosphate powders and shows a study on the formation of aluminium metaphosphate by the 850 °C the temperature used in the industrial coating process from readily available precursors and the stability of the resulting powders against hydration.

4.3: Analysis of the Performance of $\text{Al}(\text{PO}_3)_3$ Based Stress Coatings

4.3.1: Coatings with a Phosphorous/Aluminium Ratio of 3/1

The preparation of the coatings is detailed fully in section 2.2.6. Briefly, the coatings were prepared through the reaction mixture of the aluminium precursor and phosphoric acid. Colloidal silica was then added to the reaction mixture and the coating mixture applied onto the steel substrate and annealed at 850 °C for varying time periods. The addition of silica has been shown to have a beneficial effect on loss reduction^{3,4}.

The first samples tested for analysis were the hydroxide and nitrate based aluminium phosphate coatings with a phosphorous-aluminium ratio of 3/1. Analysis of the powders showed that the samples formed aluminium metaphosphate after heating to 800 °C. Using these mixtures as coatings could now allow for a comparison of the performance of aluminium orthophosphate and metaphosphate coatings.

The magnetostriction-stress curves for the hydroxide based samples annealed at 850 °C for 5, 10, 15, 20, 25, and 30 seconds are shown in figure 4.3. The relative effectiveness of the coatings are assessed by the stress at which the samples begin to exhibit the magnetostrictive effects.

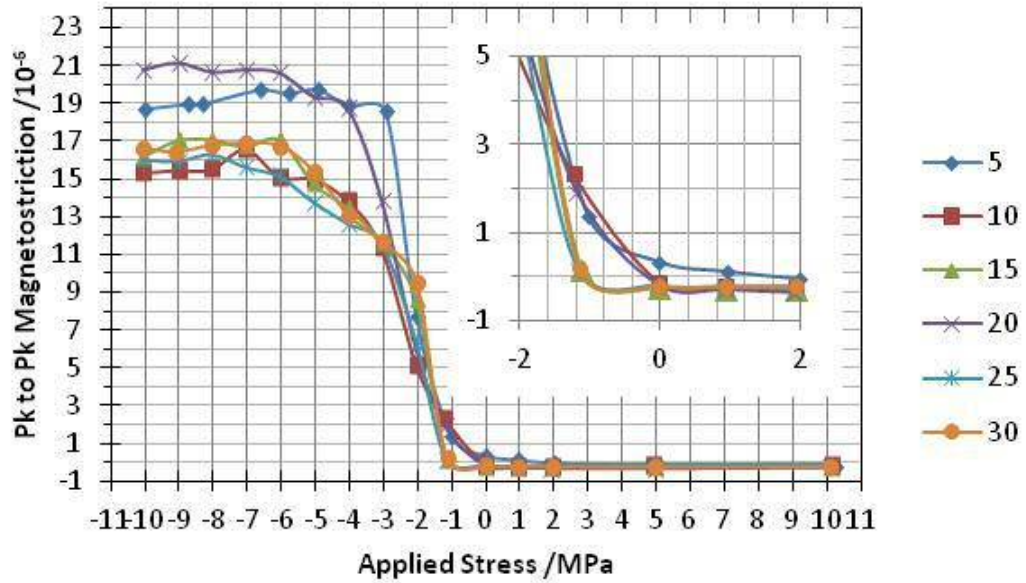


Figure 4.3: *Magnetostriction stress curves for samples coated using $Al(OH)_3$ as a precursor with a P/Al ratio of 3/1 annealed at 850 °C for 5, 10, 15, 20, 25, and 30 seconds*

The figure shows a trend between the improving performance of the coating as annealing time increases. After annealing for 5 seconds, the stress shift for the sample is measured at 1.6 MPa. On increasing the annealing time to 10 seconds, the magnetostrictive effect is measured at a stress of -0.15 MPa a shift of 1.75 MPa. Annealing to 15 seconds shows another large stress shift of 0.95 MPa with the sample measured at a stress of -1.1 MPa. However, on annealing for 20 seconds, the performance of the coatings drops by 1 MPa to -0.1 MPa. After annealing for 25 and 30 seconds, the performance of the samples increases back to the level of the sample annealed for 15 seconds; stresses of -1.1 MPa.

Excluding the sample annealed for 20 seconds, the remaining samples show a trend of increasing performance of the coatings as the annealing time is increased. This would suggest that as the $Al(PO_3)_3$ forms, the coating is able to impart a greater tensile holding onto the substrate than the precursor compounds. However with the outlying sample taken into account it is not possible to conclusively say this. The annealing times chosen for this set of experiments were chosen to track the performance of the coatings up to the

current on-line coating annealing time of 30 seconds. However, in previous studies on the formation of powder $\text{Al}(\text{PO}_3)_3$ the annealing times tracking the metaphosphate formation were much longer (i.e. 2 hours). It is possible that after these relatively short times $\text{Al}(\text{PO}_3)_3$ has not formed and the stress shift observed are due to the drying of the coatings on to the substrate instead. Analysis of the $\text{Al}(\text{NO}_3)_3$ based coatings may help to clarify the situation; if there is a clearly identifiable trend in the performance of the coatings, then it would be possible to assign the results of the sample annealed for 20 seconds as an outlying result.

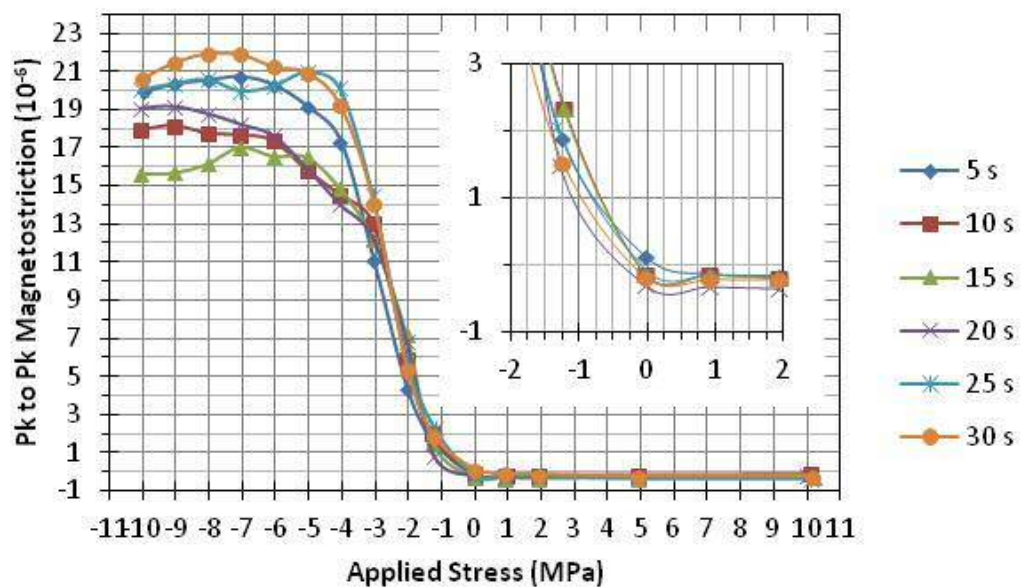


Figure 4.4: *Magnetostriction stress curves for samples coated using $\text{Al}(\text{NO}_3)_3$ as a precursor with a P/Al ratio of 3/1 annealed at 850 °C for 5, 10, 15, 20, 25, and 30 seconds*

Figure 4.4 shows the magnetostriction-stress curves for the aluminium nitrate based coatings. The samples show a much tighter distribution of the samples with a stress shift of 0.25 MPa between the two extreme samples annealed for 30 seconds and 15 seconds with stresses of 0.05 and -0.75 MPa respectively; the stress shifts for all of the samples are shown in table 4.1. With the tight distribution of these samples, it is not possible to determine any existing trend in the samples. This gives solid evidence towards the

annealing time for the samples being too short for $\text{Al}(\text{PO}_3)_3$ to form, and after this time the coatings are simply drying onto the surface of the substrate.

An issue that should be noted with both sets of samples is the de-wetting observed on coating the samples. This results in a lack of full coverage of the coating across the substrate surface. Due to this, the full extent of the performance of the coatings cannot be ascertained and before accurate comparisons of these coatings to the current online orthophosphate coatings can be made, this issue needs to be resolved. One way to do this is to increase the viscosity of the coatings. This can be done by increasing the volume of phosphoric acid in the coating mixture. Chapter 3 shows the results on the effect of increasing the phosphorous/aluminium ratio to 4/1 on the formation of powder aluminium phosphates. The results showed that increasing the ratio still results in $\text{Al}(\text{PO}_3)_3$ formation, making this ratio of reagents suitable for testing as coatings.

	Hydroxide	Nitrate
Annealing Time /s	Measured Stress (Stress Shift from Previous Sample) /MPa	
5	1.6 (N/A)	-0.1 (N/A)
10	-0.15 (1.75)	-0.05 (0.05)
15	-1.1 (0.95)	0.05 (0.1)
20	-0.1 (1.0)	-0.05 (0.1)
25	-1.1 (1.0)	-0.05 (0.0)
30	-1.1 (0.0)	-0.75 (0.8)

Table 4.1: *Tabulated summary for the stress shifts for the coated samples with an Al/P ratio of 3/1*

4.3.2: Coatings with a Phosphorous/Aluminium Ratio of 4/1

Due to the de-wetting issues observed in the previous samples, the P/Al ratio of the samples was increased to 4/1. As in the case of the 3/1 coatings, the powdered versions of the samples were found to form aluminium metaphosphate after annealing to 800 °C through a variety of analysis methods. Increasing the amount of phosphoric acid in the system increases the viscosity of the coatings, which should improve the problem of the samples de-wetting on coating on to the steel substrate. Additionally, the annealing times for the samples across this study are increased to allow for metaphosphate formation; industry ovens are capable of heating the samples to 800 °C in the time given, the laboratory ovens used in this study require additional heating times to bring the sample to 800 °C. This will allow for a full examination on the effects of $\text{Al}(\text{PO}_3)_3$ formation on coating performance.

The magnetostriction-stress curves for the samples coated using $\text{Al}(\text{OH})_3$ as a precursor after annealing to 850 °C for 30 seconds, 5, and 10 minutes are shown in figure 4.5. The samples show that as heating time increases, there is a shift in the stress curves to more negative stresses; indicating that as heating time increases the performance of the coatings improve. After 30 seconds the magnetostrictive effects is observed at -0.25 MPa, shifting to -0.75 MPa after 5 minutes and -1.90 MPa after 10 minutes. This trend is also observed in the nitrate based samples, the stress curves are shown in figure 4.6. After 30 seconds, the magnetostrictive effect is observed at -0.5 MPa, shifting to -0.90 MPa after heating for 5 minutes and after 10 minutes to -1.50 MPa. The data for the nitrate and hydroxide stress curves appear to correlate well, both show curves at similar stresses at the relative annealing times and both show negative shifts as annealing time increases.

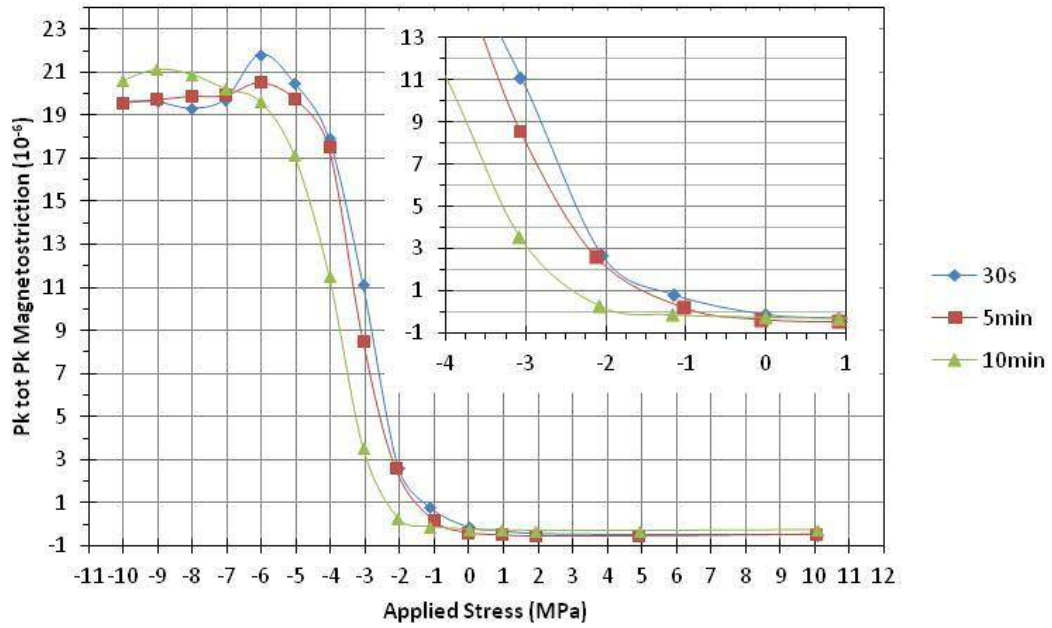


Figure 4.5: *Magnetostriction stress curves for samples coated using $Al(OH)_3$ as a precursor with a P/Al ratio of 4/1 annealed at 850 °C for 0.5, 5, and 10 minutes*

The magnetostriction-stress curves for the chloride based samples are shown in figure 4.7. After 30 seconds of annealing at 850 °C, the magnetostrictive effect is observed at a stress of -0.25 MPa. However, after heating for 5 and 10 minutes, there is no shifts observed in the curves. The improvements in the tensile stress coatings observed from the hydroxide and nitrate curves can be attributed to the formation of an aluminium metaphosphate network across the surface of the steel substrate providing tensile holding. Whilst the powder analysis of the chloride based samples were shown to form aluminium metaphosphate, there was no observed improvement in the performance of the coatings as annealing time is increased. The analysis of the powders across all three of the samples shows that whilst all formed aluminium metaphosphate, there were mechanistic and physical differences between the samples. These differences could explain why there are considerable variations in the loss curves of the chloride based coating and hydroxide and nitrate based coatings.

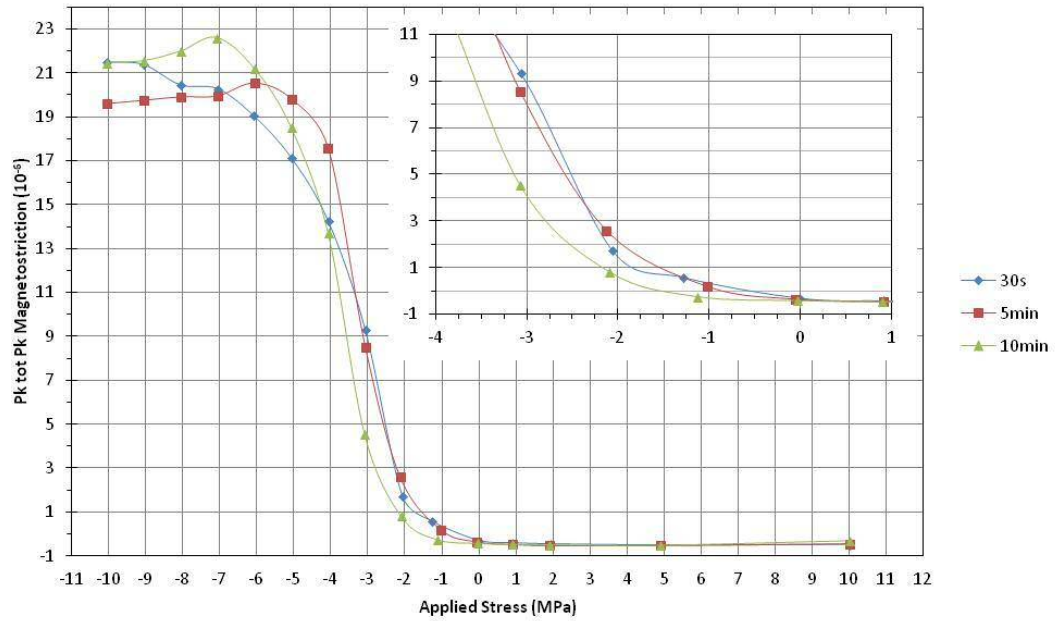


Figure 4.6: *Magnetostriction stress curves for samples coated using $\text{Al}(\text{NO}_3)_3$ as a precursor with a P/Al ratio of 4/1 annealed at 850 °C for 0.5, 5, and 10 minutes*

To analyse the industrial suitability of the coatings, they need to be compared to current aluminium orthophosphate based coatings; the magnetostriction-loss curves are shown in figure 4.8. The sample after annealing for 30 seconds begins to exhibit the magnetostrictive effect at an applied stress of -0.75 MPa. On heating for 5 minutes, the curve shifts by 1 MPa to -1.75 MPa; however, after heating for 10 minutes the curves shift back to -0.75 MPa. From this, it can be stated that there is an improvement in the orthophosphate coating after heating from 30 seconds to 5 minutes but further annealing for 10 minutes results in a worsening in the performance of the samples.

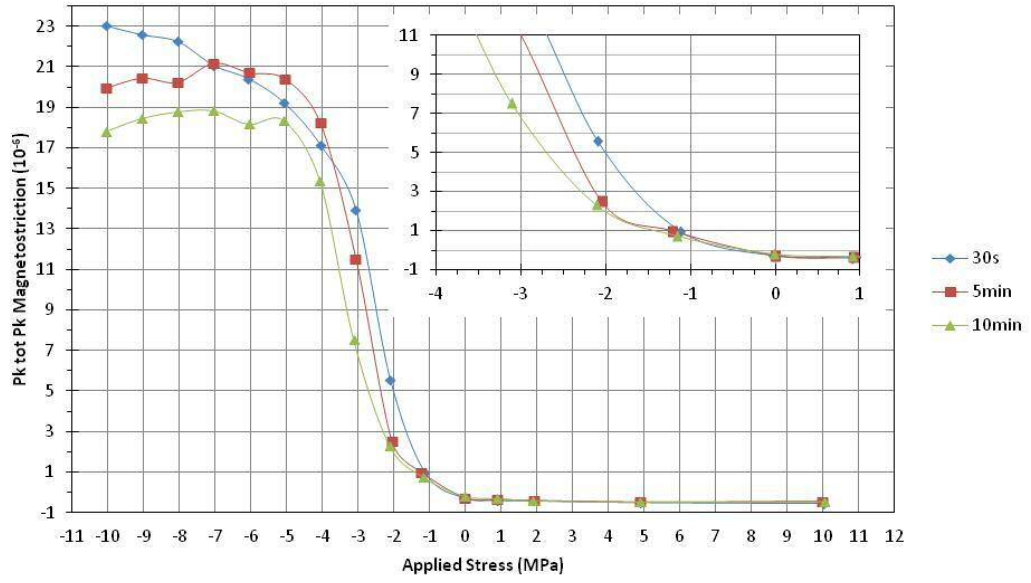


Figure 4.7: Magnetostriction stress curves for samples coated using AlCl_3 as a precursor with a P/Al ratio of 4/1 annealed at 850°C for 0.5, 5, and 10 minutes

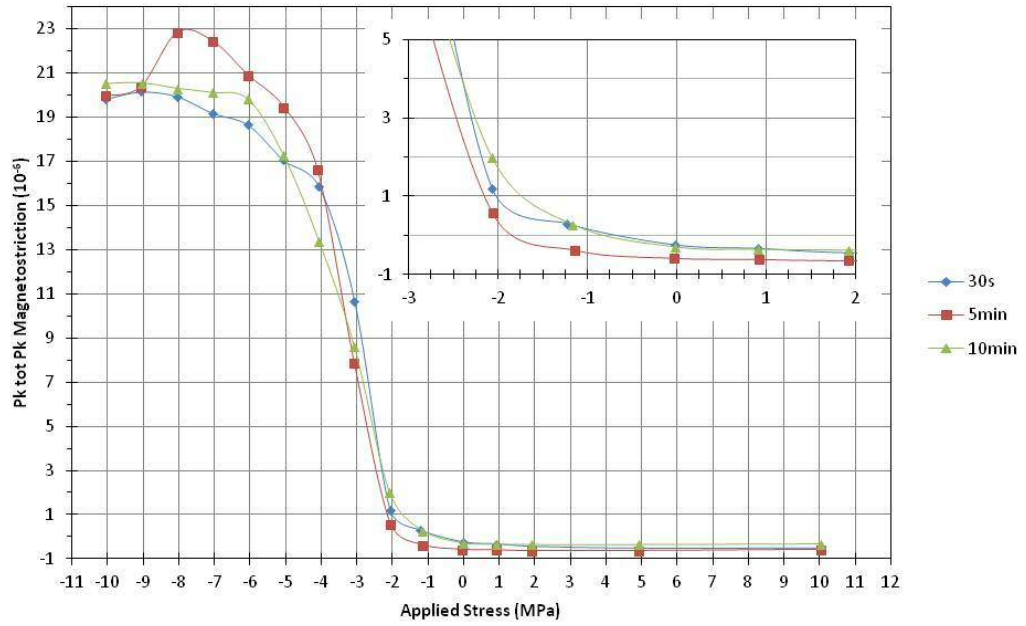


Figure 4.8: Magnetostriction stress curves for samples coated using AlPO_4 annealed at 850°C for 0.5, 5, and 10 minutes

	Hydroxide	Nitrate	Chloride	Orthophosphate
Annealing Time /min	Measured Stress (Stress Shift from Previous Sample) /MPa			
0.5	-0.25 (N/A)	-0.50 (N/A)	-0.25 (N/A)	-0.75 (N/A)
5	-0.75 (0.50)	-0.90 (0.40)	-0.25 (0.0)	-1.75 (1.0)
10	-1.90 (1.15)	-1.50 (0.60)	-0.25 (0.0)	-0.75 (1.0)

Table 4.2: Tabulated summary for the stress shifts for the coated samples with an Al/P ratio of 4/1

To fully understand the effects of the orthophosphate and metaphosphate coatings, and the trends in the magnetostriction-stress curves coatings for the hydroxide based coating and the orthophosphate coating were prepared and heated for extended time periods to examine if further trends develop. Figure 4.9, shows the magnetostriction-stress curves for the coated samples formulated from the hydroxide reaction mixture annealed for the additional times of 20, 30, and 60 minutes. After annealing from 30 seconds to 10 minutes, the previous samples showed an increase in the performance of the coatings seen from the curves shifting to lower stresses. After annealing the samples to 20 minutes, it is observed that there is a clear worsening in the performance of the sample. There is a shift towards higher stresses observed after annealing from 10 to 20 minutes; the sample at 10 minutes has a shift of -2.90 MPa but of only -1.25 MPa after annealing for 20 minutes. Whilst the stress shift of the sample annealed for 20 minutes appears anomalous to the previous trend, continued annealing shows improvements in the performance of the coatings. After annealing for 30 minutes the performance of the coating improves becoming comparable to the coating annealed for 10 minutes. Further annealing for 60 minutes results in further increases in the performance of the coatings, the magnetostrictive effect of these coatings is measured at -2.25 MPa.

Excluding the results of the sample annealed for 20 minutes, shows a clear improvement of the coatings as annealing time increases. This can be attributed to the formation of

aluminium metaphosphate, which can be tested by comparing the effects of extending annealing times on the orthophosphate coatings and chemical testing analysis. Whilst the overall decrease in magnetostriction at the lowest stresses indicates improvements in the coating performance with annealing time, measurement errors are higher in that region making definitive conclusions difficult.

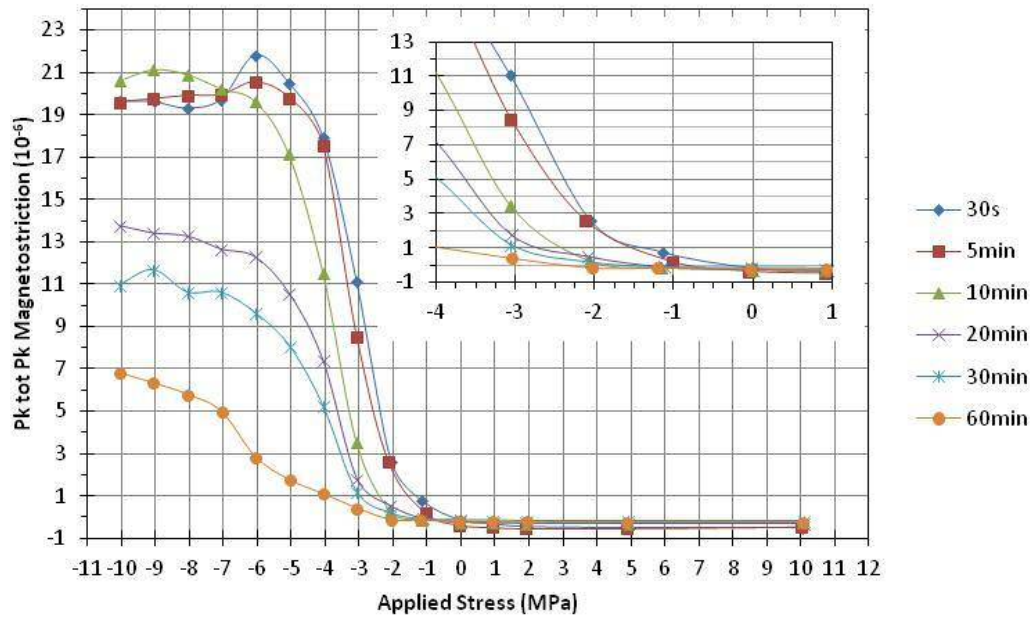


Figure 4.9: Magnetostriction stress curves for samples coated using Al(OH)_3 as a precursor with a P/Al ratio of 4/1 annealed at 850 °C for 0.5, 5, 10, 20, 30, and 60 minutes

The aluminium orthophosphate coatings shown previously (cf fig 4.8) show an improvement in performance after heating from 30 seconds to 5 minutes, but after annealing for 10 minutes the performance dropped. Figure 4.10, shows the magnetostriction-stress curves for additional samples annealed for further times of 20, 30, and 60 minutes. The curves show that after annealing for 20 and further to 30 minutes, there is no change in the performance of the coating from the 10 minute sample with a stress of -0.75 MPa. After annealing for 60 minutes, there is a large drop in the performance of the coatings seen with a shift of 3.75 MPa to 3.00 MPa.

To determine the reasoning behind the decreasing performance of the aluminium orthophosphate coating and the increases in the performance of aluminium metaphosphate coatings, chemical analysis including ATR-IR spectroscopy, XPS, and SEM have been conducted.

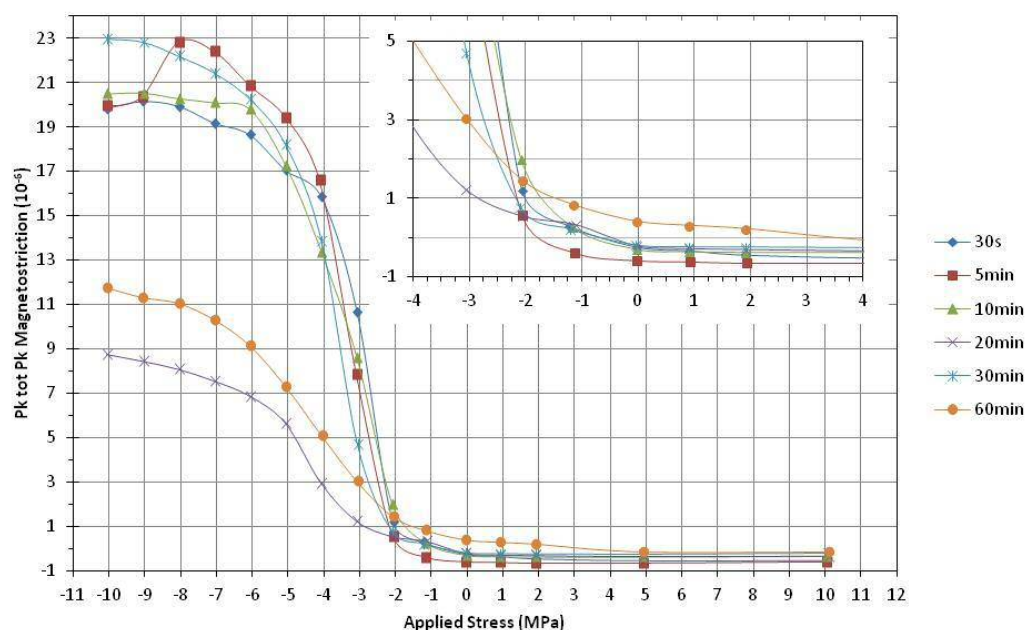


Figure 4.10: Magnetostriction stress curves for samples coated using AlPO_4 annealed at $850\text{ }^\circ\text{C}$ for 0.5, 5, 10, 20, 30, and 60 minutes

	Hydroxide	Orthophosphate
Annealing Time /m	Measured Stress (Stress Shift from Previous Sample) /MPa	
0.5	-0.25 (N/A)	-0.70 (N/A)
5	-0.75 (0.50)	-1.75 (1.05)
10	-1.90 (1.15)	-0.75 (1.00)
20	-1.25 (0.65)	-0.50 (0.25)
30	-1.75 (0.50)	-0.70 (0.20)
60	-2.50 (0.75)	3.55 (4.25)

Table 4.3: Tabulated summary for the stress shifts for the coated samples with an Al/P ratio of 4/1

4.3.2.1: ATR-FTIR Spectroscopy

ATR-IR spectroscopy has been used on the coated samples formulated from aluminium hydroxide and aluminium orthophosphate. IR spectroscopy has previously been used in Chapter 3 in tracking the thermal evolution of aluminium metaphosphate from the reaction of aluminium precursors and phosphoric acid. The spectra were able to show the evolution of metaphosphates from the observance of peaks corresponding to both phosphate units and the linking of those units into metaphosphate networks. IR spectroscopy has also been shown to be able to determine that aluminium orthophosphate does not transition to metaphosphate after annealing to 800 °C. The use of this technique on the coating samples, should give information on whether the effects observed from the magnetostriction data can be attributed to the formation (or non-formation) of aluminium metaphosphate; potentially furthering the argument that metaphosphate coatings are superior to orthophosphate coatings when employed as tensile strength coatings.

Figure 4.11, shows the ATR-FTIR spectra for the coated samples prepared from aluminium hydroxide annealed for 0.5, 5, 10, 20, 30, and 60 minutes. After annealing for 30 seconds, 4 peaks are observed at 985, 960, 870, and 840 cm^{-1} . Analysis of the IR spectra of samples with no phosphate coating applied show that these peaks can be attributed to the forsterite (Mg_2SiO_4) undercoat applied to the steel substrate during production; this implies that there is a potential lack of uniformity in the coating coverage. Heating for 5 minutes shows a loss of intensity of the peaks and are no longer detectable after heating to 10 minutes; also observed after heating for 10 minutes, is the evolution of broad peaks at 1250, 1100, 950, and 800 cm^{-1} . The broad nature of the peaks is in contrast to the strong sharp peaks observed in the analogous powder samples analysed in Chapter 3; however, the location of the peaks fall within the ranges of the powder samples which is indicative of metaphosphate formation^{5, 6}. The peak at 1250 cm^{-1} can be assigned to the presence of $\text{P}=\text{O}$ π bonds and the peak at 1100 cm^{-1} to the presence of $\text{P}-\text{O}$ σ bonds showing the

presence of phosphate in the coatings. The peaks at 950, and 800 cm^{-1} and again the peak at 1100 cm^{-1} , overlap with the bands assigned to the presence of P-O-P bands suggesting that after 10 minutes annealing, metaphosphate is being formed.

Heating further for 20 and then 30 minutes, the FTIR spectra show peaks corresponding to the forsterite undercoating. Their observation in these samples (and their absence in the sample annealed for 10 minutes) indicates a lack of uniformity in the coating thicknesses between the samples. Similar issues were seen in the samples formulated with a P/Al ratio of 3/1 where de-wetting of the samples was observed. The peaks related to phosphate presence are also observed showing that the issue is a lack of uniformity in thickness rather than a void of coating on the substrate. On heating for 60 minutes the only peaks present are those corresponding to the formation of metaphosphate.

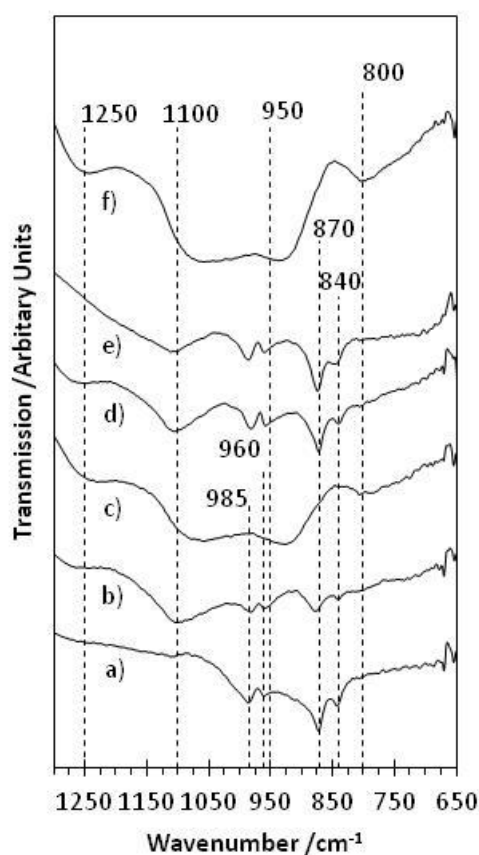


Figure 4.11: ATR-FTIR spectra for the $\text{Al}(\text{OH})_3$ coated samples annealed to 850 °C for a) 0.5 b) 5 c) 10 d) 20 e) 30 and f) 60 minutes

In figure 4.12 the IR spectra for the aluminium orthophosphate coatings are shown. After annealing for 30 seconds and 5 minutes, a broad weak peak is observed at 1060 cm^{-1} which is assigned to the PO_4 stretches in aluminium orthophosphate. Heating for 10 minutes reveals another peak at 690 cm^{-1} assignable to Al-O-P stretches; these peaks confirm the presence of aluminium orthophosphate in the sample⁷ and there is no observable chemical change in the sample after heating for 10 minutes.

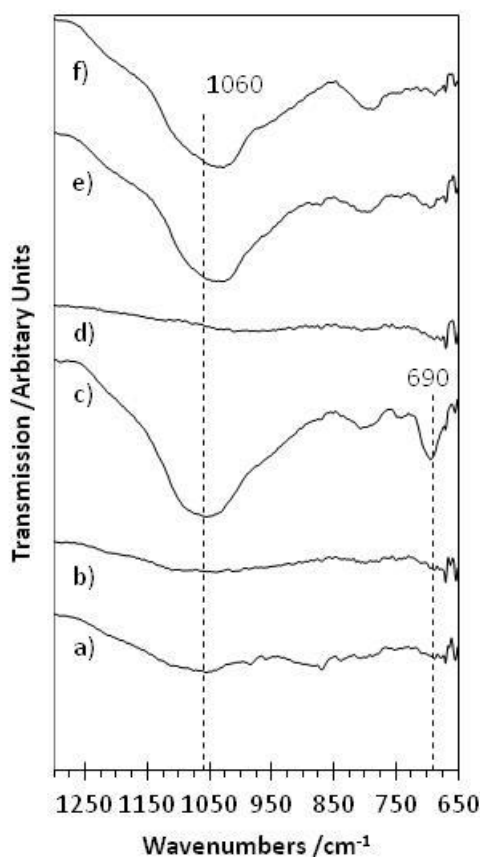


Figure 4.12: ATR-FTIR spectra for the AlPO_4 coated samples annealed to 850 °C for a) 0.5 b) 5 c) 10 d) 20 e) 30 and f) 60 minutes

On heating for 30 and then 60 minutes, there is a noticeable increase in the intensity of the observed peaks. The increased intensity of the peaks could be attributed to the aggregation

of the orthophosphate units. The current argument for the increased performance of metaphosphate coatings over orthophosphate coatings is the formation of a metaphosphate network across the surface providing tensile strength to the substrate. If there is an aggregation of the orthophosphate particles as annealing time increases then this could explain the decrease in coating performance against curing time. To fully understand if these processes are occurring, SEM images have been taken for the samples.

4.3.2.2: Scanning Electron Microscopy

The aggregation of orthophosphates and the formation of metaphosphate networks can be explored with SEM imaging. SEM images should be able to confirm whether or not these factors are occurring and explain the opposing trends observed in the magnetostriction testing data for the meta- and orthophosphate coatings.

Figure 4.13 shows an SEM image for a sample of pickled steel prepared prior to the application of any stress coatings. The image shows the surface is relatively clean, with some residual coating present on the surface.

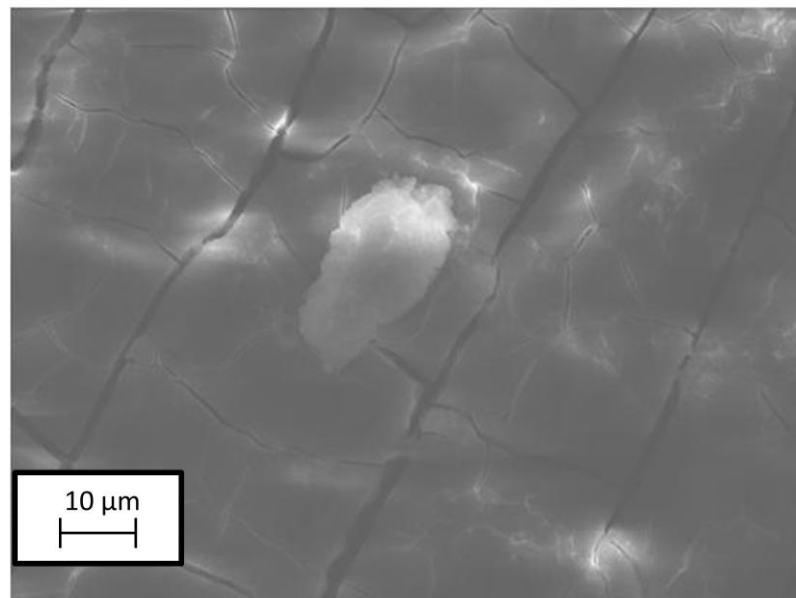


Figure 4.13: SEM Image of pickled steel showing the forsterite undercoating and residual stress coating remain in the surface.

Figure 4.14a-c shows a selection of SEM images for the aluminium metaphosphate coatings prepared from aluminium hydroxide annealed from 30 seconds to 60 minutes. The image for the sample annealed for 5 minutes shows a good coverage of the coating across the sample. The image after annealing for 10 minutes has an interesting appearance with the coating taking on a “Swiss cheese” character. IR spectroscopy showed that after 10 minutes of annealing, aluminium metaphosphate was beginning to form. The metaphosphate forms through the condensation reaction of the aluminium hydroxide and phosphoric acid causing the phosphate units polymerise into metaphosphate. Whilst the SEM image appears to show that water is being driven out of the sample as a result of this condensation, this cannot be definitively concluded from this image alone. On heating to 20 minutes, the sample appears to have dehydrated and the coating appears to have excellent coverage across the substrate. The combination of the SEM images with the IR and magnetostriction testing data is in good agreement the current hypothesis on metaphosphate coatings. The magnetostriction data shows that as the annealing time increases, there is an increase in the performance of the coatings and this agrees with the IR and SEM data which show the formation of an aluminium metaphosphate network across the surface which provide a tensile holding to the substrate.

Figure 4.14d-f shows the SEM images for the coatings prepared from aluminium orthophosphate. For the sample annealed for 5 minutes the image shows that there is very poor coating coverage across the sample. The image is dominated by the substrate with only a small amount of coated detected. The sample annealed to 10 minutes, shows the aggregation of the orthophosphate species. The images shows small particles beginning to aggregate together leaving voids on the coated surface. For the sample annealed for 30 minutes, there appears to be a good coverage of coating across the sample with none of the character of the uncoated sample visible. However, as in the case of the images of the sample annealed for 10 minutes, particle aggregation is observed. The images show the

progression of the particle aggregation, at 10 minutes the aggregation is beginning with the small particles grouping together. At 30 minutes, the aggregation has progressed with larger particles now evident.

The SEM images show a stark contrast between the two coatings. The aggregation of the phosphate particles in the phosphate based coating show that there is a reduced coverage of the surface of the steel substrate compared to the metaphosphate based coatings. The metaphosphate based coatings show a much better coverage from the dehydration reaction of the phosphate units in the formation of aluminium metaphosphate. This improved coverage results in the better imparting of tensile stress onto the substrate which explains the improved performance of the metaphosphate based coatings versus orthophosphate coatings during magnetostriction tests.

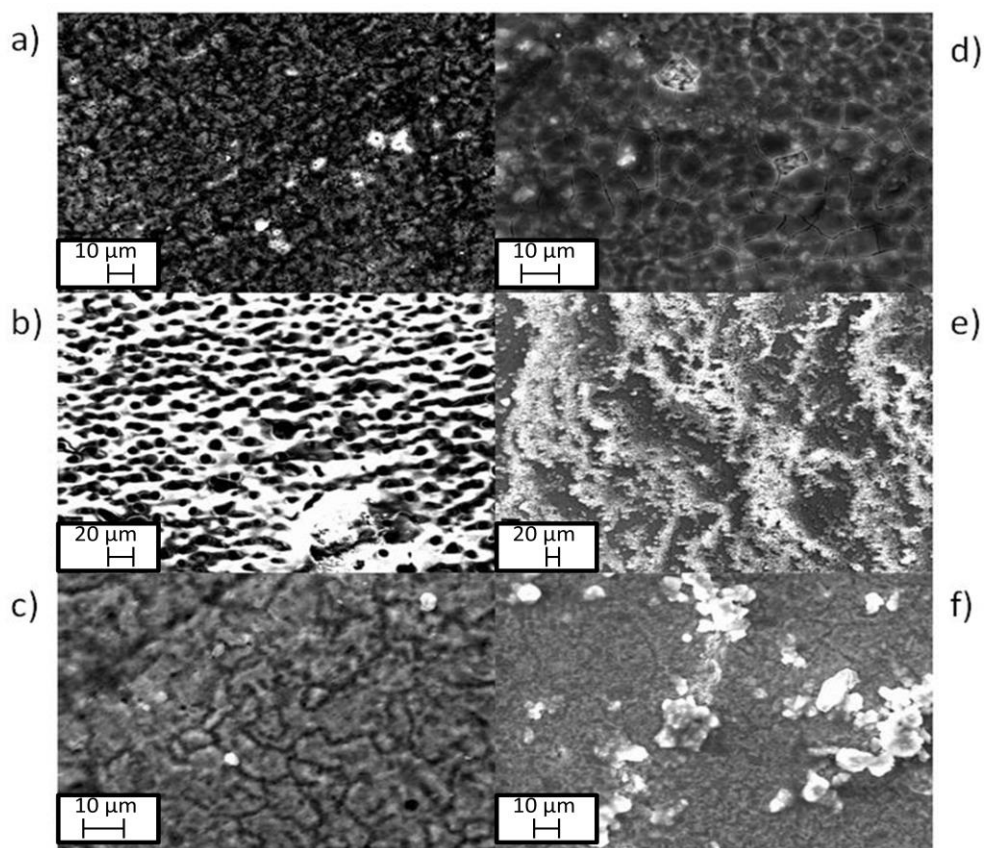


Figure 4.14: SEM images of: $Al(PO_3)_3$ annealed for a) 5 min b) 10 min c) 20 min and $AlPO_4$ d) 5 e) 10 f)

30 min

4.3.2.3: X-Ray Photoelectron Spectroscopy

In Chapter 3, it was shown that the use of x-ray photoelectron spectroscopy (XPS) was extremely powerful in identifying the formation of $\text{Al}(\text{PO}_3)_3$ on the surface of the various powder phosphate samples. XPS can be used to analyse the formation of $\text{Al}(\text{PO}_3)_3$ in the coated samples and in conjunction with the data provide from the IR and SEM analysis, assist in the chemical differentiation of the various coatings presented across this study.

The XP spectra for the O(1s), Al(2p), and P(2p) regions for a sample of pickled steel are shown in figure 4.15, along with a wide survey scan. Across the Al(2p) and P(2p) region there are very weak intensity signal detected at 74.8 and 134.5 eV respectively. The sample was pickled in NaOH to remove the stress coating from the substrate but as seen in the SEM images of the samples, Fig 4.13, some of the pre-existing coating still remains. In the O(1s) region of the spectrum, peaks are observed at 532.6 and 537.4 eV. The former can be assigned to the oxygen species present in the protective undercoating applied to the sample formulated using the magnesium silicate; forsterite (Mg_2SiO_4)⁸. The peak at 537.4 eV is assigned to a Na_{KLL} Auger line from residual sodium present on the surface after the pickling process⁹. This can be corroborated by the presence of the Na(1s) line observed in the wide scan at a bonding energy of 1071.1 eV¹⁰. Additionally, peaks at 154.2 and 103.2 eV are observed in the wide scan of the pickled samples, which are assigned to the Si(2s) and Si(2p) photoelectrons respectively. These signals arise from the forsterite protective undercoating, with the O(1s) element already shown above. The wide scan also shows peaks at 497 and 306 eV; a database search shows the best fit for the peaks would be Na and Mg Auger signals respectively. The Na signal arising from the residual sodium after the pickling process and the Mg signal arising from the magnesium present in the forsterite coating¹¹.

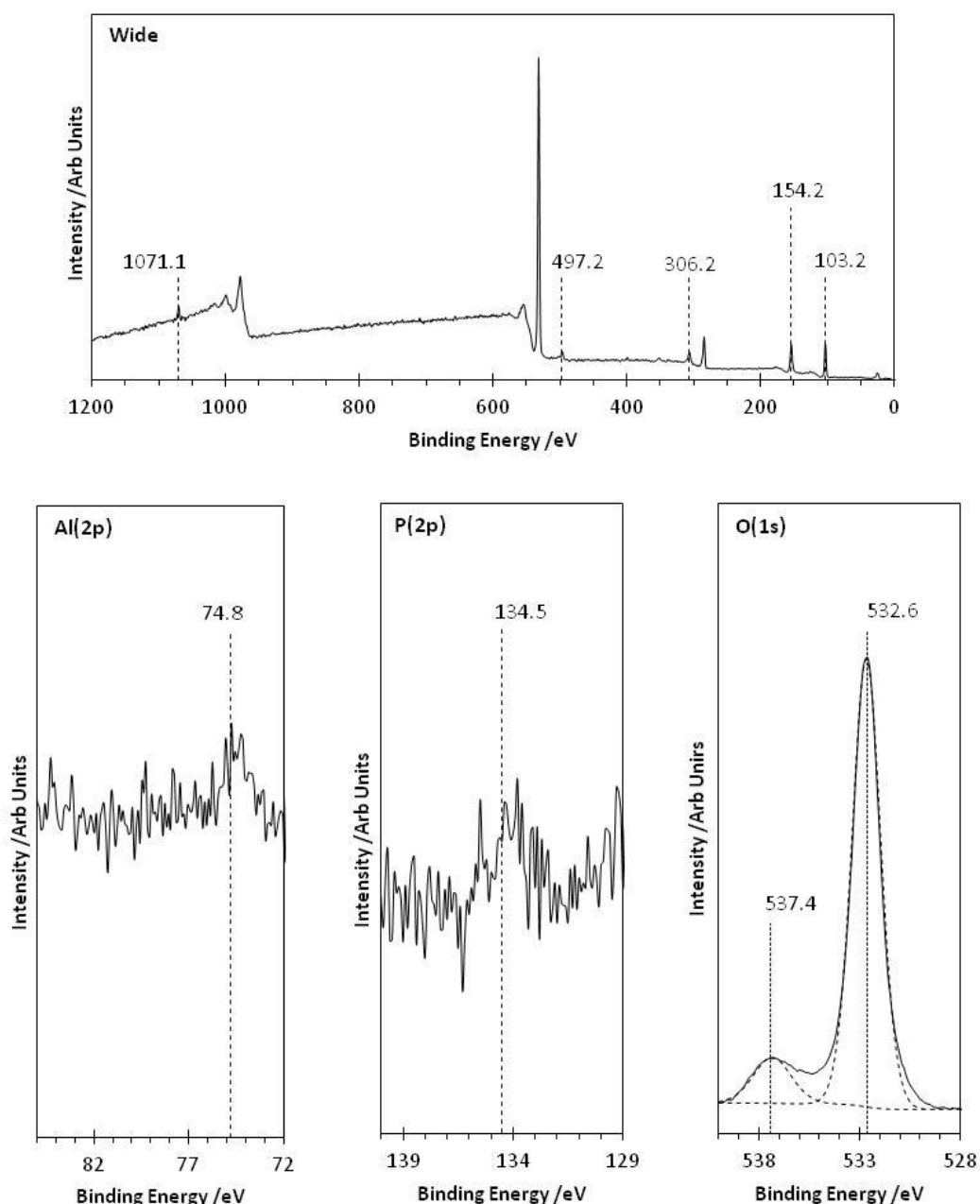


Figure 4.15: XPS spectra for the Al(2p), P(2p), and O(1s) regions and a wide scan for samples of pickled steel substrate.

Figure 4.16 show the Al(2p) region of the XPS spectra for the samples coated using the Al(OH)₃ and AlPO₄ based coatings annealed at 850 °C from 30 seconds to 60 minutes. Aluminium signals were present across all of the samples across the expected range of 74.6 – 75.1 eV, showing that aluminium (Al³⁺) species are present on the surface of the samples. In the spectra of the P(2p) region (figure 4.17), signals are observed at 134 eV. Across both

sets of samples, the intensity of the peaks fluctuates with increasing annealing time with no observable trend. If a trend were present, then it could be argued that as annealing time increases the phosphate species are drawn to the surface or vice versa. This was observed in a number of the powder samples analysed in chapter 3. In the present case however, the differences in intensity probably reflect differences in the surface areas of the points sampled by the XPS.

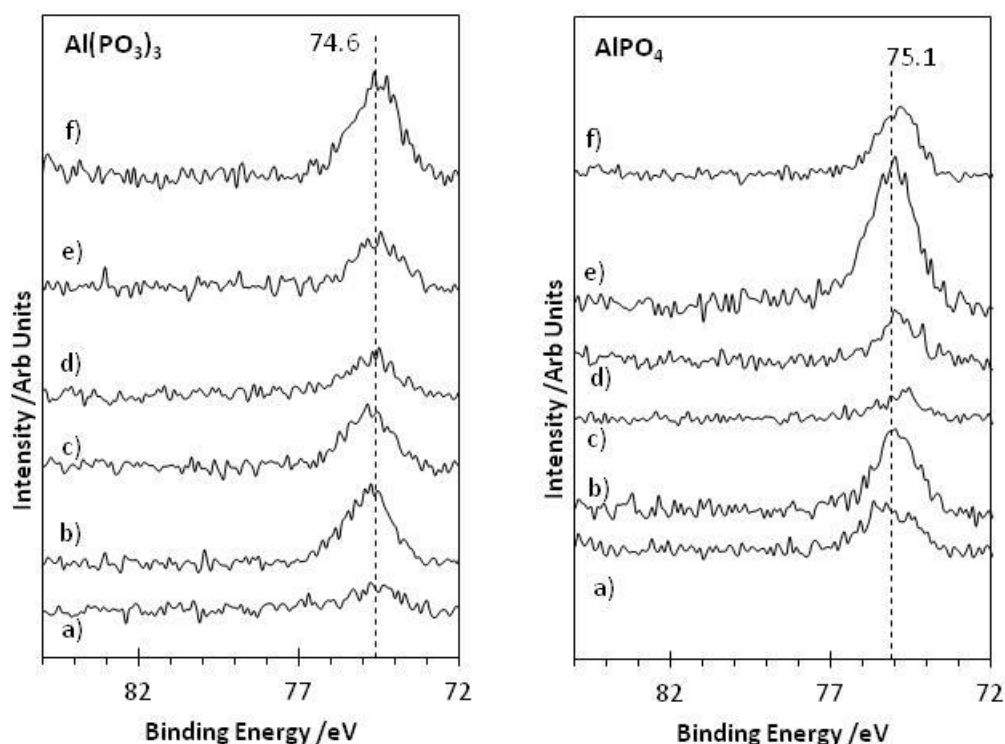


Figure 4.16: XPS spectra of the Al(2p) region of the $\text{Al}(\text{PO}_3)_3$ and AlPO_4 coated samples annealed at 850 °C for a) 0.5, b) 5, c) 10, d) 20, e) 30, and f) 60 minutes.

In the case of the powders, at lower annealing temperatures, no Al(2p) signal was observed with a peak forming at higher annealing temperatures. It was concluded that, at the lower temperatures, the surface was dominated by hydrated phosphate species and that after annealing to higher temperatures fully dehydrated $\text{Al}(\text{PO}_3)_3$ formed on the surface. However, with no observable trend in these coated surfaces the fluctuation in the peak

intensities would suggest that there is no uniformity in the coating between the mixture of the phosphate species and the colloidal silica.

Figure 4.18 shows the XP spectra for the O(1s) region of the coated samples. In the analysis of the powder phosphate samples, two peaks were observed in the formation of $\text{Al}(\text{PO}_3)_3$ at 532.3 and 533.7 eV corresponding to bridging and non-bridging oxygen respectively. As the metaphosphate formed with respect to annealing temperature the ratio of the peak areas shifted towards the bridging oxygen and similar analysis of these coated samples should be able to examine the formation of metaphosphate on the substrate surface. Examining the spectra of the samples with the hydroxide based coating shows only one visible peak after annealing for 30 seconds at 532.8 eV. Whilst this falls into the range seen for phosphate oxygen species, it also matches the binding energy for the oxygen species in the forsterite coating seen from the XPS of the pickled sample. Also, from the low intensity of the Al(2p) and P(2p) peaks of the sample it is fully possible that this peak corresponds to the colloidal silica present in the sample⁸ or the forsterite undercoating. This can be corroborated by the observed presence of peaks in the wide scans of the samples (figure 4.19) at 154.0 and 103.0 eV which are assigned to Si(2s) and Si(2p) species respectively and the Mg Auger signal seen at 306 eV. Due to the overlapping nature of the regions of the oxygen species in the sample, from SiO_2 and $\text{Al}(\text{PO}_3)_3$, conclusive analysis of the samples is difficult. On increasing the annealing time to five minutes, there is no change in the spectrum with the single peak still present at 532.8 eV. For the sample annealed for 10 minutes, an additional peak is observed at 538.4 eV. This peak was also present in the spectrum for the bare sample and attributed to the Na_{KLL} auger line from the presence of sodium on the surface of the sample from the pickling process used to strip the steel of the stress coating prior to the application of the tension coating being analysed⁹. After the sample has been annealed for 60 minutes, two peaks are detected at 531.9 and 533.6 eV. These peaks correspond to the bridging and non-bridging oxygen species present in $\text{Al}(\text{PO}_3)_3$ giving evidence that

metaphosphate is present on the surface of the samples. The ability to distinguish to peaks in the O(1s) signal after this annealing time also coincides with a noted drop in intensity in the Si(2s) and Si(2p) signals, this shows that after annealing for 60 minutes the phosphate component of the coatings is more dominant on the surface. This explains why two peaks are now seen in the O(1s) region after 60 minutes but before only one is observed; at the lower temperatures the surface nature of the coatings is dominated by colloidal silica and the oxygen signal observed corresponds to SiO₂ but after 60 minutes when the metaphosphate is present on the surface two signals are seen for the bridging and non-bridging oxygen. In chapter 3, examination of the ratios of the peak areas was used to track the extent of surface metaphosphate formation; with a shift in relative intensity towards the bridging oxygen peak showing increased metaphosphate production. But with the presence of other oxygen species lying under the curve, doing so in this case would not provide accurate results.

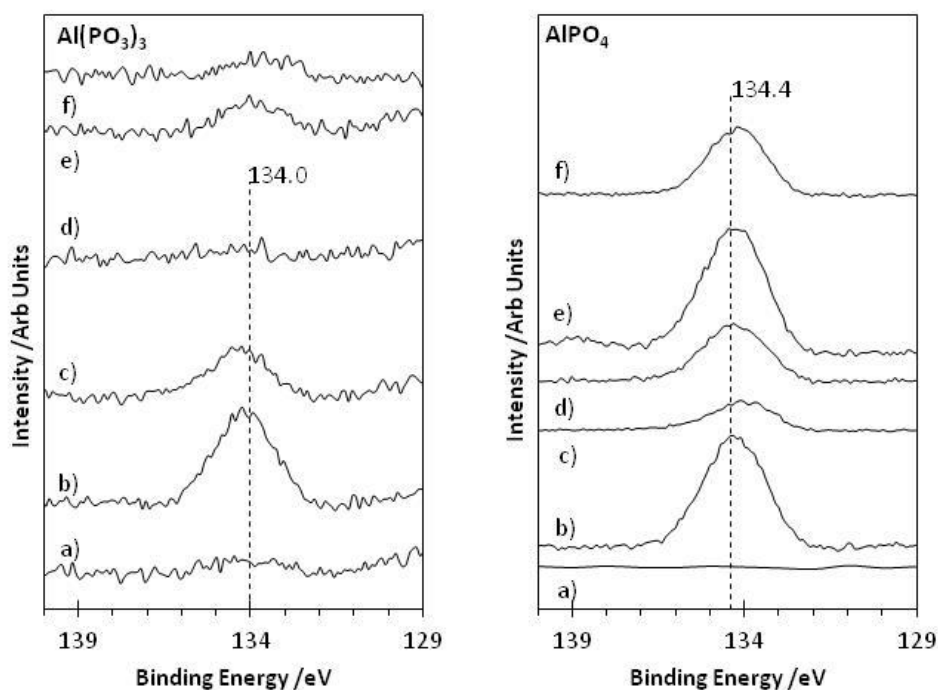


Figure 4.17: XP spectra of the P(2p) region of the Al(PO₃)₃ and AlPO₄ coated samples annealed at 850 °C for a) 0.5, b) 5, c) 10, d) 20, e) 30, and f) 60 minutes.

The O(1s) XP spectra for the samples coated with AlPO_4 are shown in figure 4.18. As with the previous samples, the spectra are dominated by a peak at 532.5 eV which, like the metaphosphate coatings can be attributed to the oxygen species of the forsterite undercoating or the colloidal SiO_2 present in the coating; suggesting a non-uniform coating which was observed in the SEM images illustrating the particle aggregation. The spectra for the samples annealed for 30 seconds and 5 minutes also each contain an additional peak at 535.1 and 536.2 eV respectively. The peak at 535.1 eV can be assigned to residual Na remaining on the surface after the NaOH pickling process which was also observed in a number of previous samples. It should also be noted that unlike the $\text{Al}(\text{PO}_3)_3$ coatings there is no indication of any metaphosphate formation, which confirms the discussion above⁷.

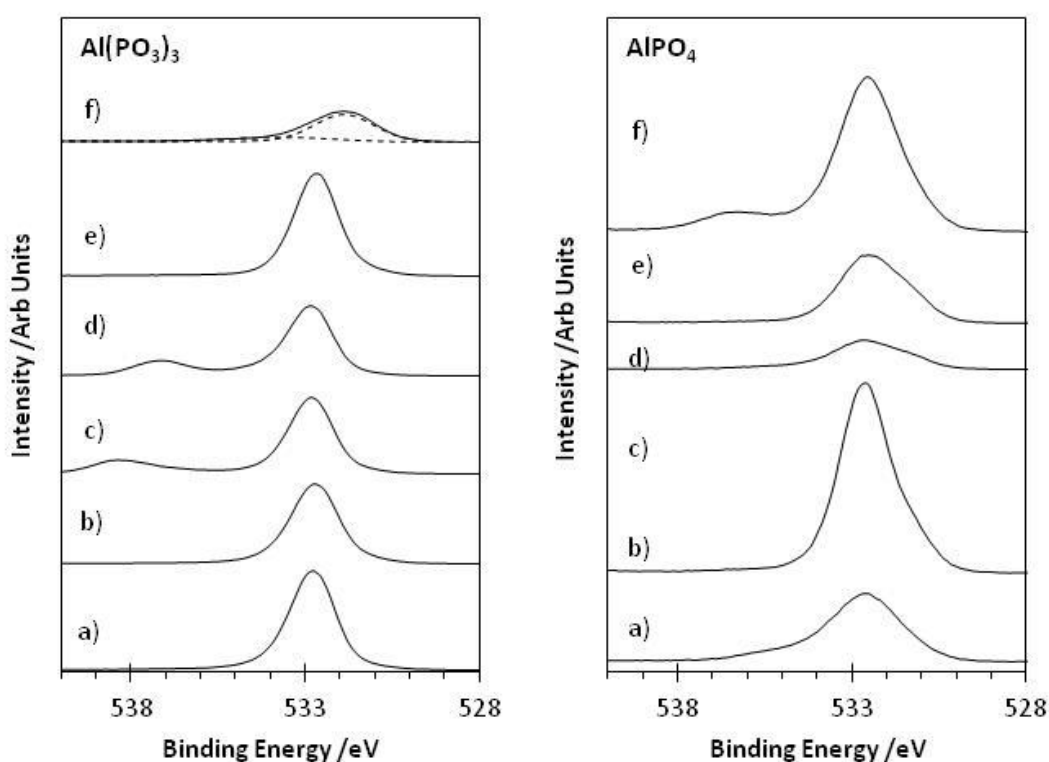


Figure 4.18: XP spectra of the O(1s) region of the $\text{Al}(\text{PO}_3)_3$ and AlPO_4 coated samples annealed at 850 °C for a) 0.5, b) 5, c) 10, d) 20, e) 30, and f) 60 minutes.

Whilst XPS analysis proved to be a powerful and decisive tool in the analysis of surface species on the surface of powder phosphate species, its use in the analysis of the coatings has proven to be more difficult. The presence of additional oxygen species in both the undercoating and in the stress coatings themselves have led to a masking of the peak regions where the oxygen species in the phosphates reside. However, the data has shown that there is evidence for metaphosphate formation in the $\text{Al}(\text{OH})_3$ based coating and no formation of metaphosphate in AlPO_4 based coating; as expected. This data then, coupled with the IR and SEM analysis demonstrates a clear difference in both the chemical and physical make-up of the coatings and that the formation of $\text{Al}(\text{PO}_3)_3$ increases the performance of stress coatings against AlPO_4 based coatings.

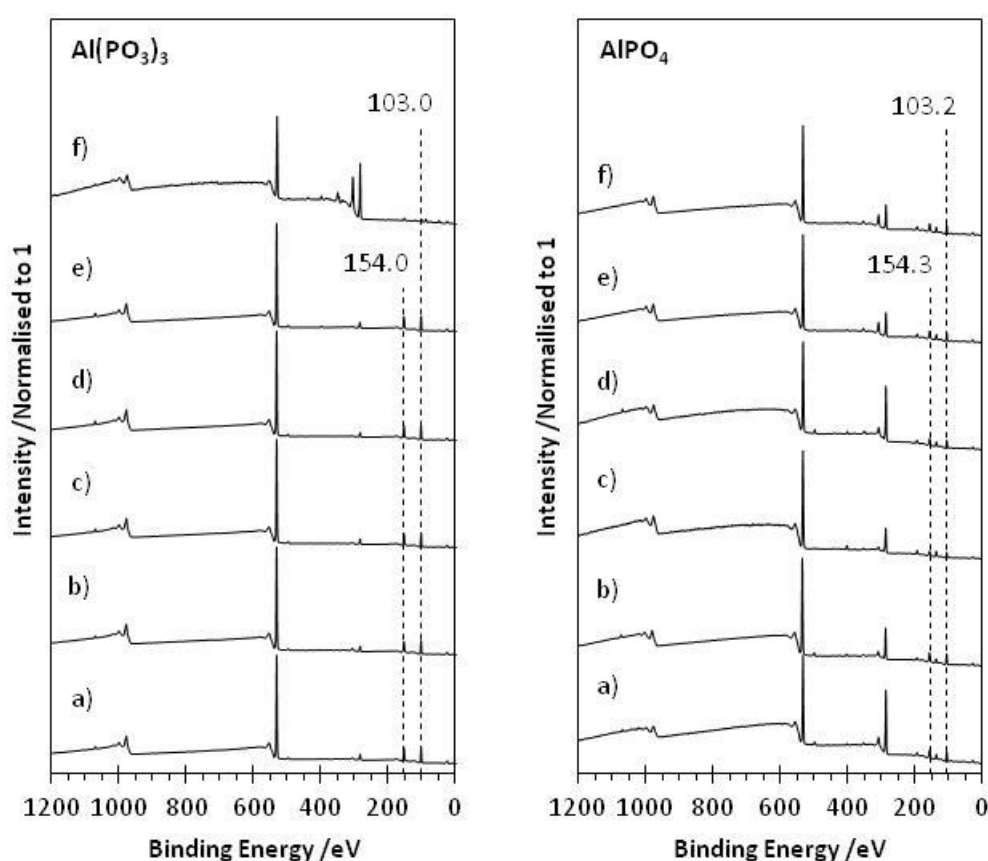


Figure 4.19: Wide-Scan XPS spectra of the $\text{Al}(\text{PO}_3)_3$ and AlPO_4 coated samples annealed at 850 °C for

a) 0.5, b) 5, c) 10, d) 20, e) 30, and f) 60 minutes.

4.4: Stress Relief Annealing Treatment

The process of stress relief annealing (SRA) is used in the preparation of small sizes of samples of coated magnetic steel, such as the Epstein strips used throughout this study. The process of cutting the Epstein strips can result in added stresses in the strip. This additional tension can distort the results of the magnetostrictive testing as it becomes unclear whether the stress comes from the applied coating or the cutting process; this was illustrated in a study by Klimczyk et al that measured the magnetostrictive effect on samples prepared by various cutting techniques¹². In order to reduce the tension applied through the cutting process, the samples are put through an additional annealing process which allows the samples to expand and contract reducing the stress along the sample edges.

To test the effectiveness of the SRA effect on the magnetostrictive properties of coated samples, aluminium metaphosphate and orthophosphate coatings were prepared by coating and annealing for 30 seconds, 10 minutes and 30 minutes. A set of samples were then selected for SRA by heating in a vacuum at 850 °C for 3 hours. The samples were then tested for their magnetostrictive properties to assess the effects of the SRA process on the coatings.

Figure 4.20, shows the magnetostriction stress curves for the coated samples prepared from aluminium hydroxide annealed for 30s. The figure shows that there is a difference of 1 MPa between the samples from the range of -1.5 and -0.5 MPa. After SRA treatment (fig 4.21), the samples are shifted towards negative stresses in the range of -2.9 and -1.9 MPa showing an improvement in the performance of the coatings after the SRA process. It is clear from this data that the SRA process is having an effect on the performance of the coatings. However, what is not clear is whether the improvements in the coating

performance come from the stress relief or the additional annealing time given to the coatings increasing metaphosphate formation.

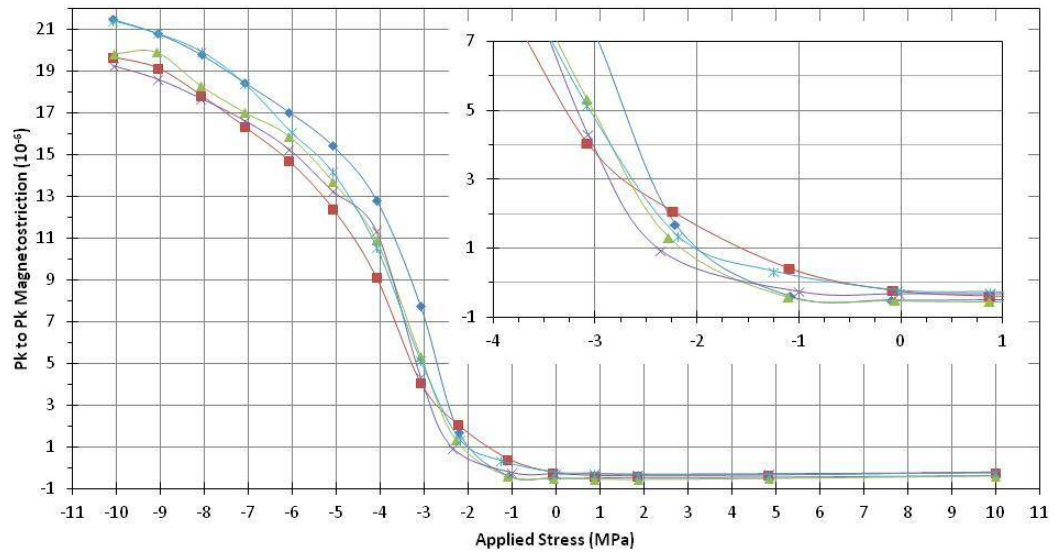


Figure 4.20: *Magnetostriction-stress curves for samples coated with $\text{Al}(\text{PO}_3)_3$ annealed at 850 °C for 30 seconds*

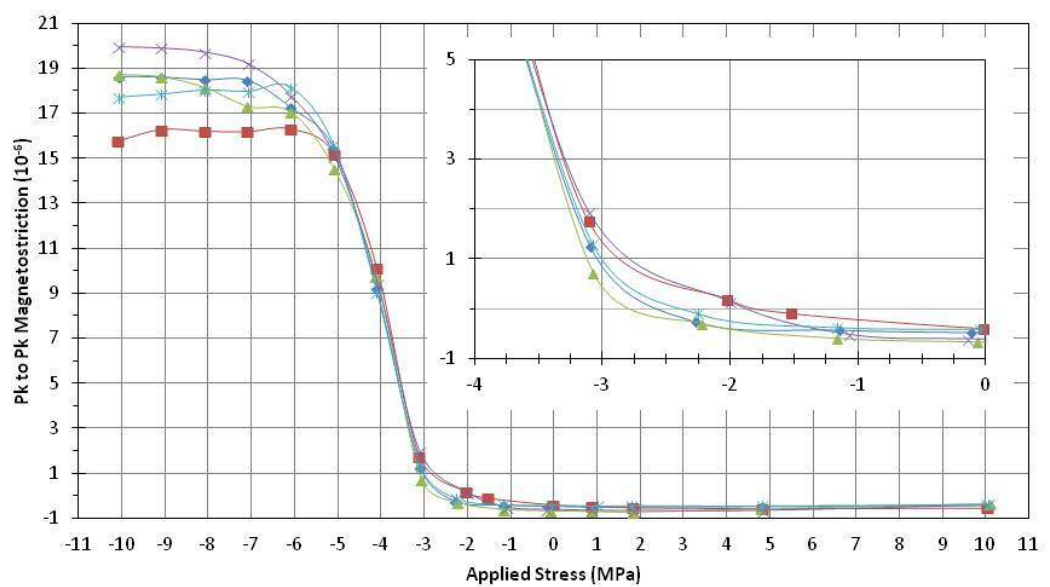


Figure 4.21: *Magnetostriction-stress curves for samples coated with $\text{Al}(\text{PO}_3)_3$ annealed at 850 °C for 30 seconds with subsequent SRA treatment.*

The effects of stress relief annealing were also tested against the longer annealing times of 10 and 30 minutes. Figure 4.22 shows the magnetostriction-stress curves for the coatings annealed for 10 minutes; the curves for the samples range from stresses -1.7 to -1.5 MPa. The stress shifts of the curves fall between those of the samples annealed for 30 seconds and the SRA samples. These samples show an improvement on the samples annealed for 30 seconds, due to the increased annealing time (as shown in section 4.3) but do not perform as well compared to the SRA samples. On annealing further for 30 minutes, the stress curves show a much wider distribution between the samples (fig 4.23). The stress curves for the samples, show a stress distribution ranging from -0.7 to -2.6 MPa. The range of the curves lies along the distribution of all three previous samples making a determination of the relative performance of the coating extremely difficult. The interest of these samples is in the large distribution range of the samples compared to the other samples. The samples annealed for 10 minutes, have a tight distribution of 0.2 MPa and the samples annealed for 30 seconds have a wider distribution of 1 MPa whereas the samples annealed for 30 minutes have a much wider distribution range of 1.9 Pa. An explanation for the differences of the range in stress curves for the different samples may be given from the chemical nature of the coatings at the various annealing times. After 30 seconds of annealing, the coatings still predominantly consist of the precursor $\text{Al}(\text{OH})_3$ and H_3PO_4 and so do not provide the good tensile coverage observed in the samples annealed to higher temperatures. This suggestion holds true for the samples annealed for 10 minutes; the coating at this point is beginning to form $\text{Al}(\text{PO}_3)_3$ and so the coverage of metaphosphate across the samples is beginning, improving the performance and distribution of the stress curves for the coatings. However, the samples annealed for 30 minutes do not continue this improved performance. It has been shown that after annealing for this time metaphosphate has formed and there is a good distribution of the coating across the substrate surface. This leads to the conclusion that there is a lack of uniformity in either the

coating or the substrate. To examine these effects, the stress curves of the analogous samples prepared from the orthophosphate based coating need to be examined. The increasing particle aggregation of the coating as annealing time increases and the effect of this aggregation on the distribution range of the resulting stress curves may help to explain the curves previously examined. A study on selection of substrates is discussed later in this chapter (section 4.5).

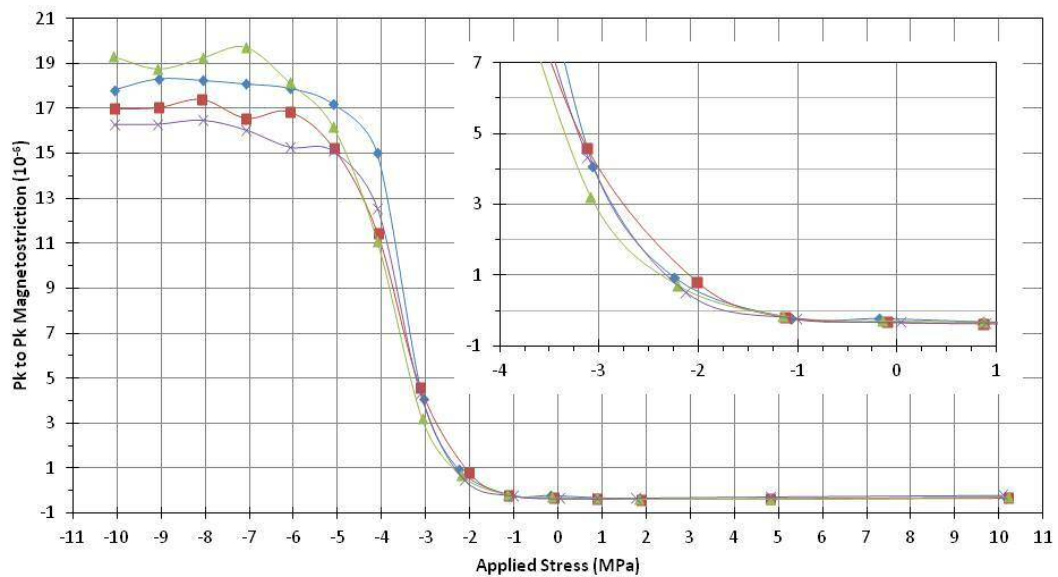


Figure 4.22: *Magnetostriction-stress curves for samples coated with $Al(PO_3)_3$ annealed at 850 °C for 10 minutes.*

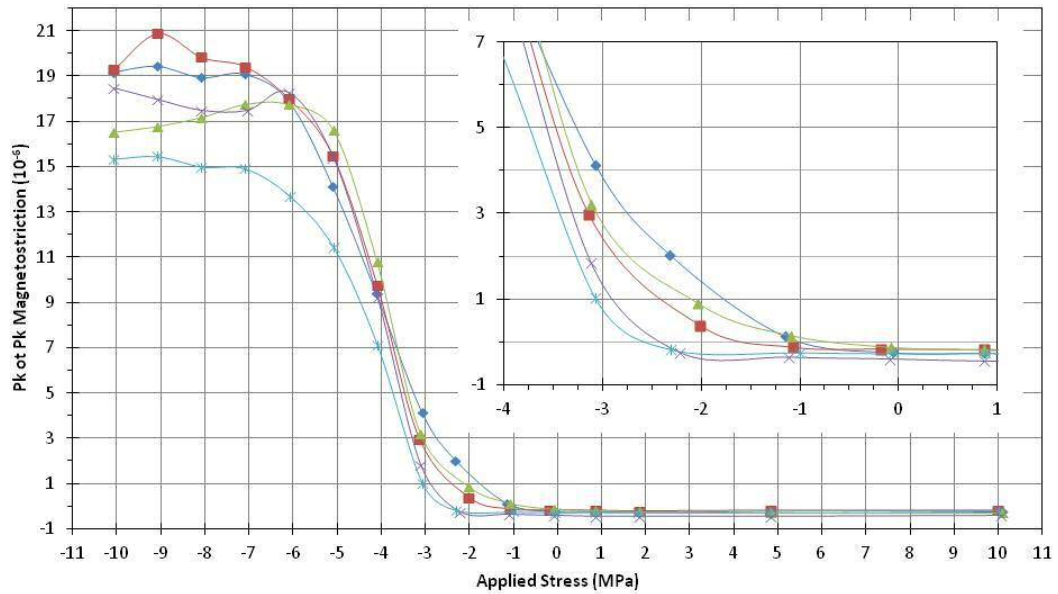


Figure 4.23: Magnetostriction-stress curves for samples coated with $Al(PO_3)_3$ annealed at 850 °C for 30 minutes.

30 sec	30 sec + SRA	10 mins	30 mins
Measured Stresses (MPa)			
-0.50	-1.90	-1.50	-0.75
-0.50	-1.90	-1.50	-1.05
-1.50	-1.40	-1.50	-1.70
-1.50	-2.60	-1.75	-2.4
-1.50	-2.90		-2.6

Table 4.4: Table summarising the stress shifts for the samples coated with $Al(PO_3)_3$.

The stress-curves for the samples prepared from coated samples prepared from $AlPO_4$ and annealed for 30 seconds are shown in figure 4.24 and the samples after SRA treatment in figure 4.25. The curves show that there is a difference of 1.2 MPa between the range of -3.3 and -4.5 MPa. After SRA the samples shift to between -2.5 and -2.7 MPa, showing a

drop in performance after the additional annealing but a much tighter distribution of the curves showing that the SRA process is having a clear effect on the magnetostrictive properties of the coating. The analogous samples using $\text{Al}(\text{OH})_3$ as a precursor showed an increase in performance after the SRA treatment whereas these samples show a drop in performance. This fits the data in section 4.3.2, where coatings prepared from the hydroxide precursor formed $\text{Al}(\text{PO}_3)_3$ after prolonged annealing which resulted in an increase in performance of the coatings under magnetostriction-stress testing. In the orthophosphate coatings the same prolonged annealing resulted in a drop in performance possibly due to the aggregation of the particles resulting in a less effective coverage. However, with both of these processes occurring it is still unclear as to the effect that the SRA treatment is having on the added cutting stresses applied to the steel substrate.

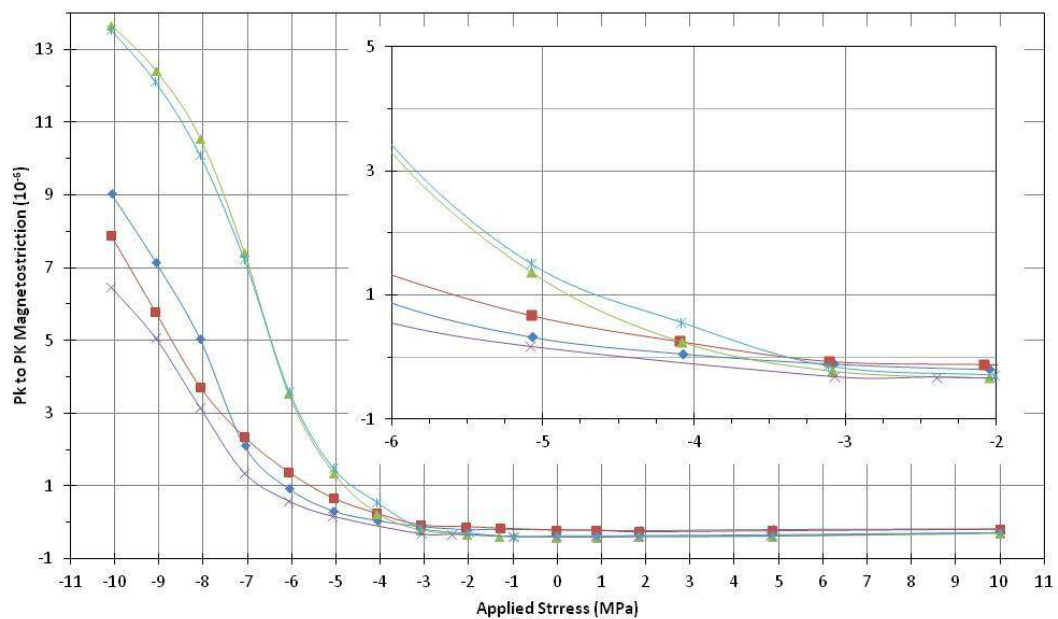


Figure 4.24: *Magnetostriction-stress curves for samples coated with AlPO_4 annealed at 850 °C for 30 seconds.*

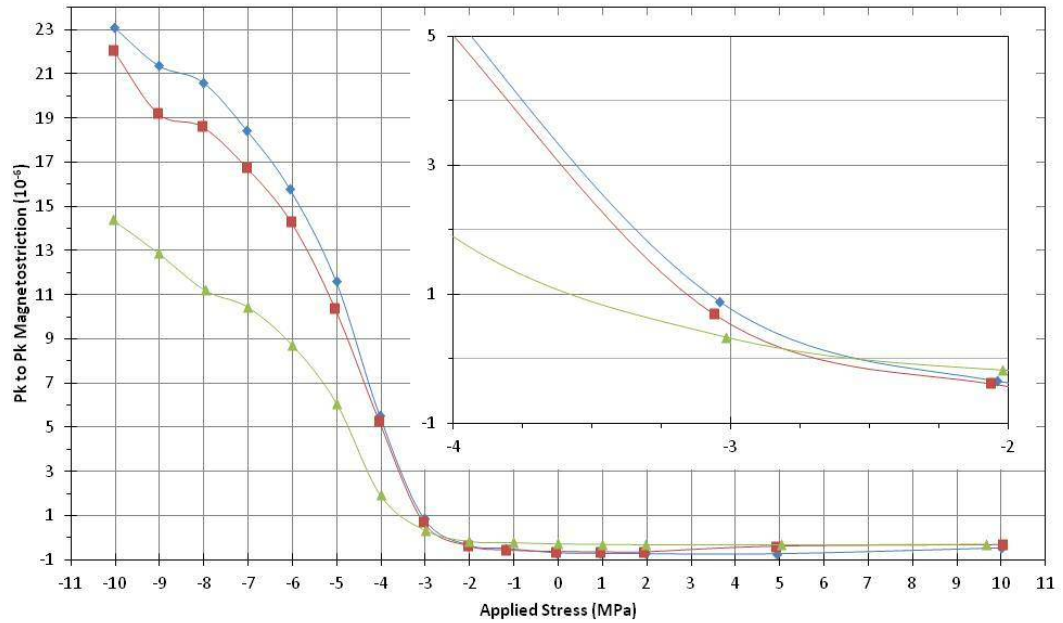


Figure 4.25: *Magnetostriction-stress curves of samples coated with AlPO_4 annealed at 850 °C for 30 seconds with additional SRA treatment.*

Figure 4.26 shows the stress curves for the orthophosphate coatings annealed for 10 minutes. The data show a wide distribution of curves ranging from -2.6 to -3.8 MPa with an outlying sample at +3.1 MPa. This range falls between the samples annealed for 30 seconds and those having undergone SRA treatment. This trend fits the hypothesis that the annealing time for these samples are in-between those for the other samples and so they should be an intermediate in particle aggregation and thus performance. The samples annealed for 30 minutes (figure 4.27) show a tightening of the distribution of curves compared to the 10 minute samples ranging from -1.7 to -2.5 MPa. The range of stress shifts in these curves compared to those of the samples annealed for 10 minutes show an increase in performance which is not expected from the trends previously observed.

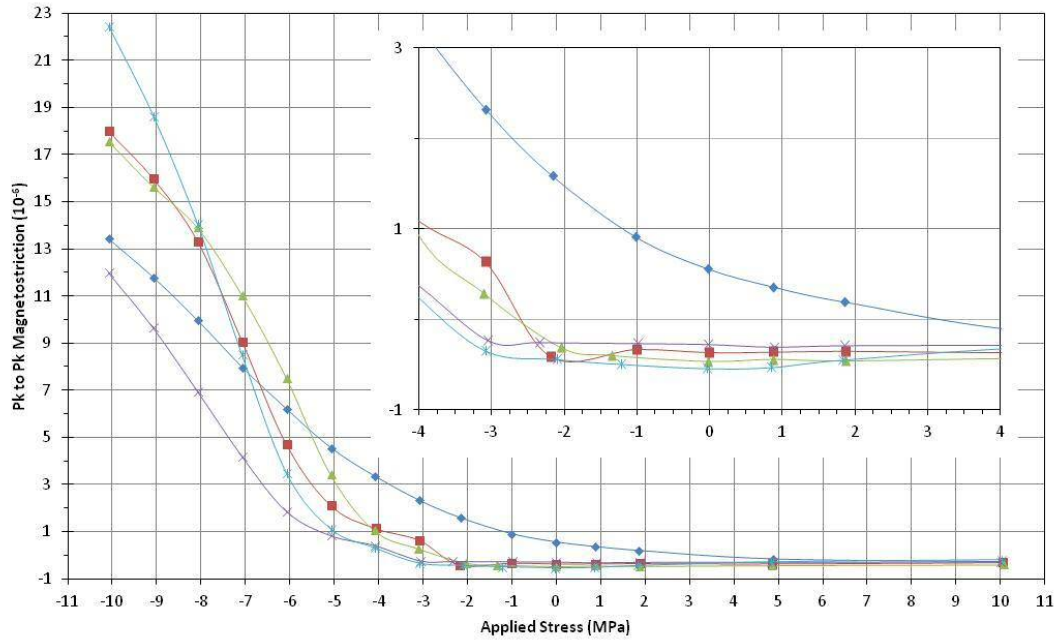


Figure 4.26: Magnetostriction-stress curves for samples coated with AlPO_4 annealed at 850°C for 10 minutes.

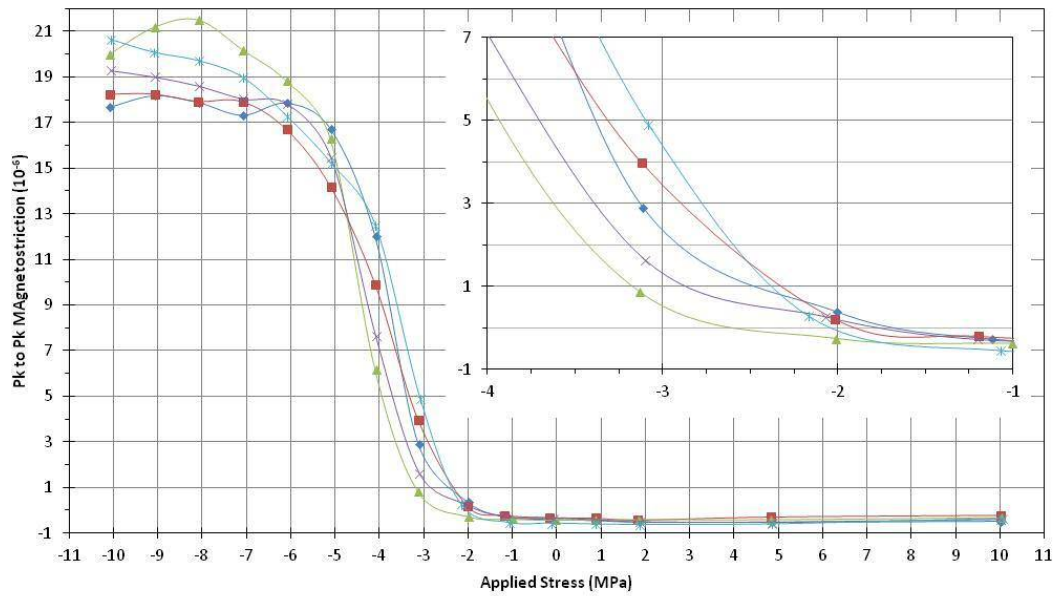


Figure 4.27: Magnetostriction-stress curves for samples coated with AlPO_4 annealed at 850°C for 30 minutes.

Measured Stresses (MPa)			
30 sec	30 sec + SRA	10 min	30 min
-3.35	-2.50	3.00	-1.70
-3.35	-2.50	-2.50	-1.75
-3.70	-2.70	-2.60	-1.85
-3.70		-3.40	-2.05
-4.50		-3.60	-2.60

Table 4.5: Table summarising the stress shifts for the samples coated with AlPO_4 .

From this data, it can be seen that the SRA treatment process is of great importance in determining the performance of coatings in reducing the magnetostrictive effect on magnetic steel substrates. However, distinguishing the effects of the SRA process from the chemical effects of the coatings due to annealing can be very difficult. From this, it can be suggested that Epstein strips should not be used as the substrate in any further studies which examine the effects of annealing time on the performance and composition of coatings. Whilst they are convenient because of their small size, the use of larger sized samples would reduce the stress added from cutting and so would remove the need for SRA treatment. This would give greater clarity to experiments in determining the effects of coating compositions.

4.5: Ensuring Substrate Uniformity

As suggested in section 4.4 information on the uniformity of the substrate is important when examining the effects of the SRA treatment process, to ensure that this is not having an effect on the magnetostriction tests leading to skewed data sets. Previous to this, the

steel substrate was being used as provided (from Cogent Power Ltd.). In this study the substrates will be examined more closely and uniform samples selected from a large batch.

50 steel samples were provided along with mass, power loss (the energy lost through the magnetostrictive effect (W/Kg)) and magnetic flux (the magnetic field density over a given area (A/m)) data for each specimen. Samples were chosen within ± 1 standard deviation in loss and flux and the selection further refined after magnetostriction-stress tests. By selecting samples based on these criteria and testing the magnetostrictive properties of the bare samples, any effects of the substrate can be excluded from the analysis of the magnetostriction stress curves of the coated samples and provide a more conclusive comparison between the performance of the $\text{Al}(\text{PO}_3)_3$ and AlPO_4 based coatings.

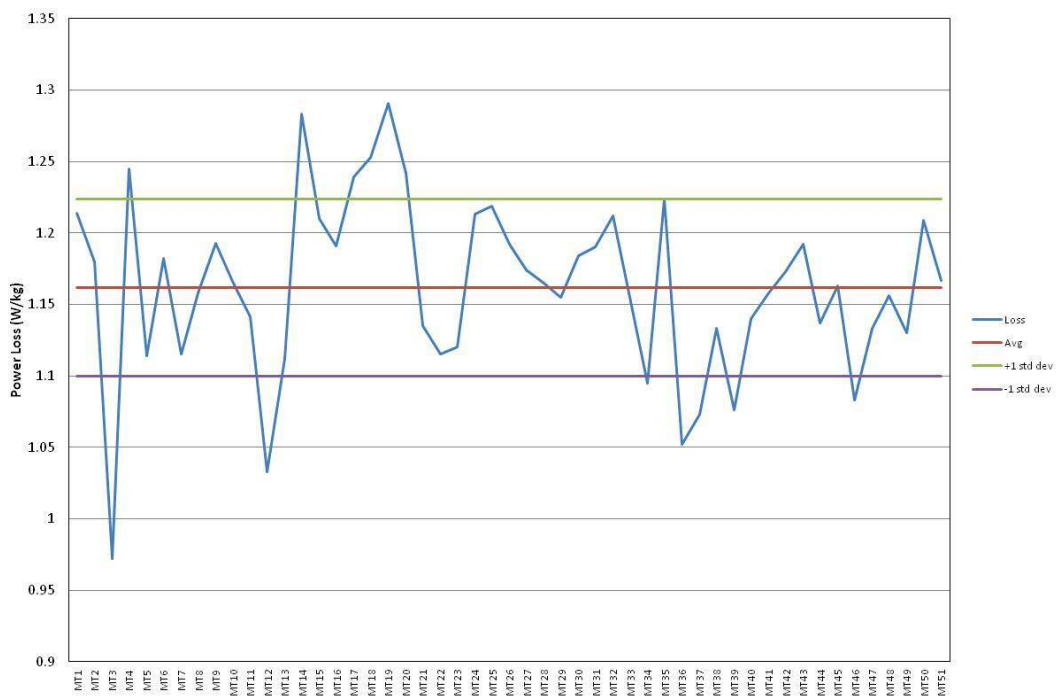


Figure 4.28: Power loss data for the samples selected for testing



Figure 4.29: Flux data for samples MT1 – MT34

Sample ID	Mass (g)	Thickness by mass	Loss	Avg loss	+1std loss	-1std loss	B800	Avg B800	+1std B800	-1std B800
MT1	19.66	0.2809	1.214	1.1619	1.22374	1.10006	1.939	1.90231	1.984094	1.820526
MT6	19.89	0.2842	1.182	1.1619	1.22374	1.10006	1.868	1.90231	1.984094	1.820526
MT7	19.53	0.2790	1.115	1.1619	1.22374	1.10006	1.99	1.90231	1.984094	1.820526
MT8	19.52	0.2789	1.158	1.1619	1.22374	1.10006	1.922	1.90231	1.984094	1.820526
MT9	19.56	0.2794	1.193	1.1619	1.22374	1.10006	1.922	1.90231	1.984094	1.820526
MT10	19.75	0.2822	1.166	1.1619	1.22374	1.10006	1.857	1.90231	1.984094	1.820526
MT13	19.66	0.2809	1.112	1.1619	1.22374	1.10006	1.934	1.90231	1.984094	1.820526
MT16	19.63	0.2804	1.191	1.1619	1.22374	1.10006	1.989	1.90231	1.984094	1.820526
MT21	19.46	0.2780	1.135	1.1619	1.22374	1.10006	2.057	1.90231	1.984094	1.820526
MT22	19.34	0.2763	1.115	1.1619	1.22374	1.10006	2.034	1.90231	1.984094	1.820526
MT25	19.57	0.2796	1.219	1.1619	1.22374	1.10006	1.956	1.90231	1.984094	1.820526
MT26	19.46	0.2780	1.192	1.1619	1.22374	1.10006	1.867	1.90231	1.984094	1.820526
MT27	19.45	0.2779	1.174	1.1619	1.22374	1.10006	1.952	1.90231	1.984094	1.820526
MT28	19.55	0.2793	1.165	1.1619	1.22374	1.10006	2.022	1.90231	1.984094	1.820526
MT29	19.66	0.2809	1.155	1.1619	1.22374	1.10006	1.868	1.90231	1.984094	1.820526
MT30	19.64	0.2806	1.184	1.1619	1.22374	1.10006	1.986	1.90231	1.984094	1.820526
MT31	19.62	0.2803	1.19	1.1619	1.22374	1.10006	1.959	1.90231	1.984094	1.820526
MT32	19.69	0.2813	1.212	1.1619	1.22374	1.10006	1.966	1.90231	1.984094	1.820526
MT33	19.46	0.2780	1.155	1.1619	1.22374	1.10006	1.895	1.90231	1.984094	1.820526
MT34	19.62	0.2803	1.095	1.1619	1.22374	1.10006	1.935	1.90231	1.984094	1.820526

Table 4.6: Table showing the loss and flux (B800) data for the samples selected for coating.

The selected samples prepared from aluminium hydroxide and orthophosphate coatings and annealed for 30 seconds both with and without SRA treatment and tested for their magnetostrictive properties. Figure 4.30 shows the magnetostriction-stress curves for the samples prepared for the $\text{Al}(\text{OH})_3$ based coatings annealed for 30 seconds. There is still a range in the distribution of the stress curves, as observed in previous samples, of 1.1 MPa between the stresses of -0.6 to -1.7 MPa. After SRA treatment (figure 4.31), the performance of the coatings improves with a shift in the curves towards negative stresses between -2.3 and -2.9 MPa; a range of 0.6 MPa. The effects of the increased annealing time do result in an improvement in the performance of the coatings, attributed to the formation of $\text{Al}(\text{PO}_3)_3$. The range of the curves in the samples annealed for 30 seconds is comparable to that of the analogous samples in the previous study, suggesting that the discrepancies are an effect of the chemical nature of the samples. At these annealing times, metaphosphate has not had time to form and so the stress coatings are not giving the uniform tensile hold desired to the substrate. After SRA treatment the range of the curves is tighter than previously observed (0.6 MPa compared to 1 MPa). With a more uniform substrate, it is now possible to conclude that the formation of metaphosphate networks across the surface of the sample gives rise to a coating that is increasing in uniformity across samples.

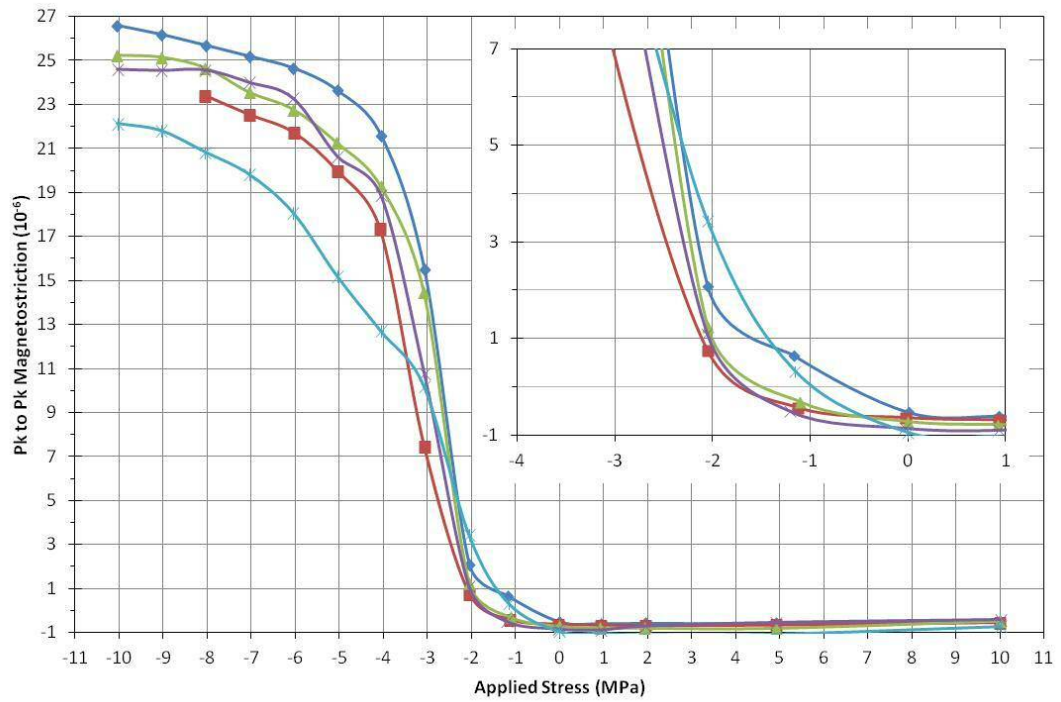


Figure 4.30: Magnetostriction-stress curves for samples coated with $\text{Al}(\text{PO}_3)_3$ annealed at 850°C for 30 seconds.

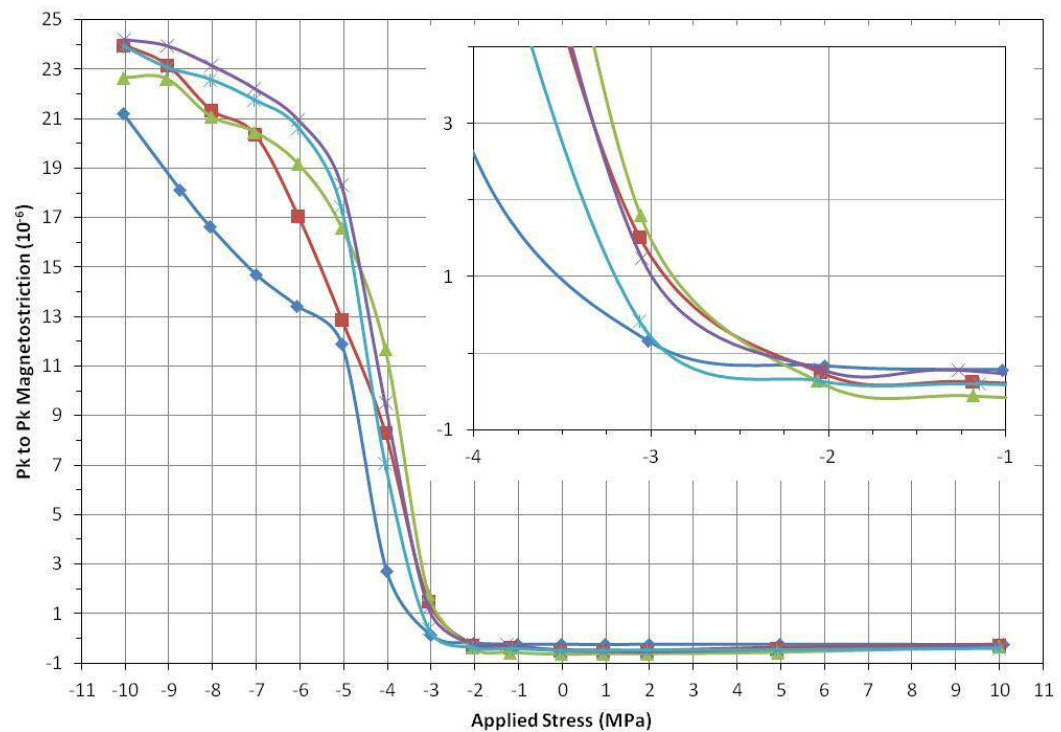


Figure 4.31: Magnetostriction-stress curves for samples coated with $\text{Al}(\text{PO}_3)_3$ annealed at 850°C for 30 seconds with subsequent SRA treatment.

The performance of the OH precursor based coatings can now be compared to those of the orthophosphate coating prepared under the same annealing conditions. Figure 4.32 show the orthophosphate coated samples after annealing for 30 seconds and figure 4.33 the samples after SRA treatment. The samples annealed for 30 seconds, show a stress distribution of 1.4 MPa, ranging from -0.4 to -1.8 MPa. After the SRA process, the distribution of the stress curves tightens to 0.5 MPa and the resistance to the magnetostrictive improves with the curves ranging between the stresses of -2.3 to -2.8 MPa. The performance of the samples annealed for 30 seconds appear comparable to the analogous samples coated with $\text{Al}(\text{OH})_3$ based coatings. This is expected under the current hypothesis as those samples, after this annealing time, have yet to undergo the condensation reaction resulting in the formation of metaphosphate. However, what is unexpected is that after SRA treatment, the performance of the orthophosphate coatings remains comparable to the metaphosphate coatings. The current hypothesis that $\text{Al}(\text{PO}_3)_3$ coatings are superior to AlPO_4 based coatings at reducing the effects of magnetostriction on steel substrates by imparting a greater tensile holding on the steel has been observed in previous results. These results show that the performances of the coatings at reducing the magnetostrictive effect are on par. Across this experiment, uniformity in the substrate was ensured prior to coating and so any difference in the substrate can be discounted from being an explanation for these results. This can then potentially lead to the conclusion that in previous experiments, unaccounted differences in the substrate were skewing the results of the magnetostrictive tests. Alternatively, in the previous study examining the effects of the SRA process, there were difficulties in distinguishing between the effects of the SRA treatment and the chemical processes occurring in the samples with respect to annealing time. As concluded in that study (see section 4.6), the use of a substrate with a larger area, would circumvent the need for the SRA treatment process and so provide greater clarity in the analysis of the results; due to a relatively smaller effect from the

stresses added from cutting across the perimeter against the whole area of sample . That conclusion is echoed in these results, further studies should use larger samples to properly allow for a comparison of the effectiveness of ortho- against metaphosphate coatings.

Measured Stress (MPa)			
$\text{Al}(\text{PO}_3)_3$: 30s	$\text{Al}(\text{PO}_3)_3$: 30s + SRA	AlPO_4 : 30s	AlPO_4 : 30s + SRA
-0.60	-2.30	-0.35	-2.30
-1.00	-2.35	-0.35	-2.60
-1.50	-2.40	-1.50	-2.70
-1.65	-2.80	-1.65	-2.70
-1.70	-2.85	-1.75	-2.75

Table 4.7: Table summarising the stress shifts for the samples coated with $\text{Al}(\text{PO}_3)_3$ and AlPO_4 .

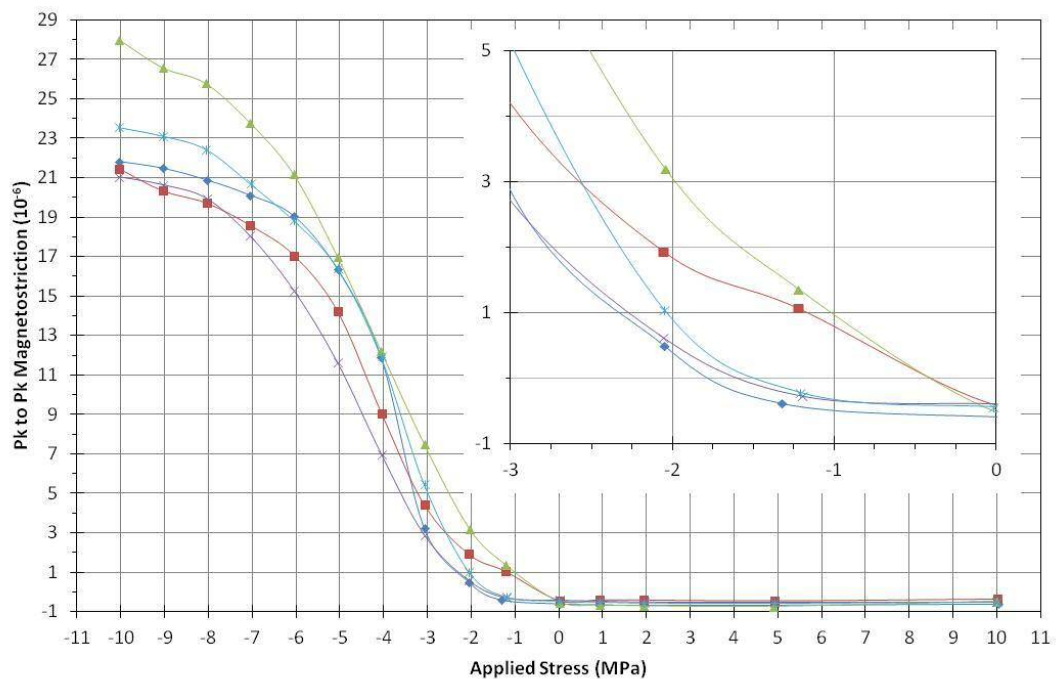


Figure 4.32: Magnetostriction-stress curves for samples coated with AlPO_4 annealed at 850 °C for 30 seconds.

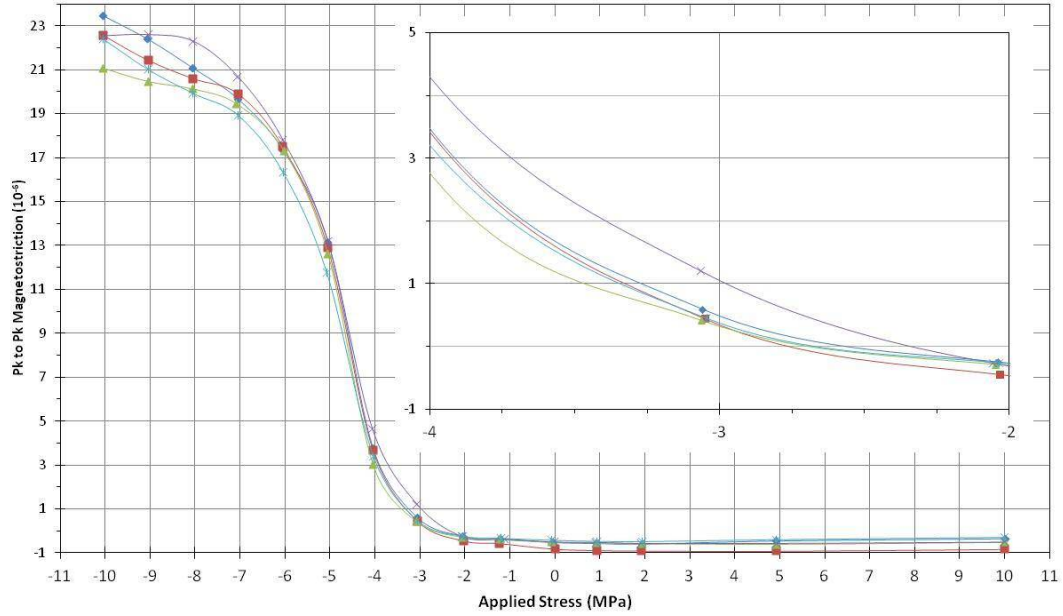


Figure 4.33: *Magnetostriction-stress curves for samples coated with AlPO_4 annealed at 850 °C for 30 seconds with subsequent SRA treatment.*

4.6: Summary

In this chapter, the formation of $\text{Al}(\text{PO}_3)_3$ tensile stress coatings and their relative effectiveness versus AlPO_4 coatings at reducing the magnetostrictive effect have been examined. The reaction of the precursors $\text{Al}(\text{OH})_3$, $\text{Al}(\text{NO}_3)_3$, and AlCl_3 with H_3PO_4 was shown to form powder $\text{Al}(\text{PO}_3)_3$ in Chapter 3 and in this chapter this reaction is implemented as a film coating.

The initial testing data showed that there was an issue of de-wetting on the coatings that was attributed to low viscosity of the coating. This issue was solved with the addition of more H_3PO_4 to the coating mixture raising the P/Al ratio to 4/1.

Whilst the analysis of the powdered samples in Chapter 3 was able to provide a conclusive answer to the question of $\text{Al}(\text{PO}_3)_3$ formation, the chemical analysis of the film coatings has proven to be less definitive. The presence of additional oxygen species, from the colloidal silica and forsterite under-coating, made resolving metaphosphate species in the O(1s)

region of XP spectra difficult. In the IR analysis, peaks were broader and with a lower intensity compared to powdered samples making a comparative peak analysis less convincing.

In testing, the magnetostrictive properties of the samples formulated from Al(OH)_3 and H_3PO_4 showed a general trend of performance improvement with respect to annealing time. Whilst, as the discussed above, the presence of the metaphosphate is not conclusively proven in the deposited films, the evidence from the behaviour of the powder samples in Chapter 3 does suggest this improvement can be attributed to the formation of $\text{Al(PO}_3)_3$ in the coatings. This trend of improvement was not observed in the AlPO_4 coated samples. SEM images showed that the orthophosphate samples were prone to particle aggregation with increasing annealing time whilst the metaphosphate coatings showed a more uniform coverage of the substrate; which was hypothesised to be an adventitious property of metaphosphate coatings, providing a greater tensile hold to the substrate.

Stress relief annealing (SRA) which removes the additional stresses added to the substrate during cutting was studied with the aim of reducing the experimental variability of the magnetostrictive measurements. Difficulties came from distinguishing the effects of the SRA treatment and the coatings on the magnetostrictive properties of the samples.

Whilst the data shown in this chapter would suggest that the $\text{AlX}_3 + \text{H}_3\text{PO}_4$ based coatings can outperform AlPO_4 coatings at reducing the magnetostrictive effect on magnetic steels, additional work should be carried out to corroborate this including a comparison of the coatings on larger sizes of substrate to remove the need for SRA treatment.

4.7: References

1. B. Cullity and C. Graham, *Introduction to Magnetic Material*, John Wiley & Sons., 2009.
2. P. Klimczyk, PhD Thesis in *Novel Techniques for Characterisation and Control of Magnetostriction in G.O.S.S.*, Cardiff University, 2012.
3. O. Tanaka, H. Kobayashi and E. Minematsu, *Journal of Materials Engineering*, 1991, **13**, 161-168.
4. D. Poultney and D. Snell, *Journal of Magnetism and Magnetic Materials*, 2008, **320**, e649-e652.
5. R. L. Frost, *Spectrochimica Acta Part a-Molecular and Biomolecular Spectroscopy*, 2004, **60**, 1439-1445.
6. A. John, D. Philip, K. R. Morgan and S. Devanarayanan, *Spectrochimica Acta Part a-Molecular and Biomolecular Spectroscopy*, 2000, **56**, 2715-2723.
7. V. L. Bemmer, PhD Thesis in *The Properties of Electrical Steels and Their Coatings*, Cardiff University, 2013.
8. H. Seyama, M. Soma and A. Tanaka, *Chemical Geology*, 1996, **129**, 209-216.
9. J. F. Moulder, W. F. Stickle, P. E. Sobol and B. K.D., *Handbook of X-Ray Photoelectron Spectroscopy*, Perkin Elmer Corporation, 1992.
10. N. X.-R. P. S. Database, srdata.nist.gov/xps, Accessed Aug 13 2015.
11. N. X. Database, srdata.nist.gov/xps, Accessed Apr 2017.
12. P. K. Klimczyk, P. Anderson, A. Moses and M. Davies, *Ieee Transactions on Magnetics*, 2012, **48**, 1417-1420.

Chapter 5: Mullite Powders as Tensile

Stress Coatings

Contents

5.1 Introduction	139
5.1.1 Mullite	139
5.1.2 The Jahn-Teller Effect.....	142
5.2 The Combination of Mullite and Aluminium Phosphate	143
5.2.1 Vibrational Spectroscopy of Phosphate-Mullite Powders	143
5.2.1.1 ATR-FTIR Spectroscopy	143
5.2.1.2 Raman Spectroscopy.....	148
5.2.2 Magnetostrictive Testing of Phosphate-Mullite Coatings	150
5.2.2.1 Magnetostriction of Mullite-Phosphate Coatings	151
5.2.2.2 Magnetostrictive Testing of Pure Mullite Coatings	153
5.3 The Low Temperature Synthesis of Nano-Scale Mullite	156
5.3.1 CuSO ₄ as a Catalyst.....	157
5.3.1.1 Vibrational Spectroscopy	157
5.3.1.2 X-Ray Diffraction	159
5.3.1.3 Scanning Electron Microscopy	161
5.3.2 [Fe(CN) ₆] ₃ K ₃ as a Catalyst	164
5.3.2.1 Vibrational Spectroscopy	164
5.3.2.2 X-Ray Diffraction	165
5.3.2.3 Scanning Electron Microscopy	167
5.3.3 Fe(NO ₃) ₃ ·9H ₂ O as a Catalyst	169
5.3.3.1 Vibrational Spectroscopy	169
5.3.3.2 X-Ray Diffraction	170
5.3.3.3 Scanning Electron Microscopy	172
5.3.4 CrCl ₃ as a Catalyst.....	173
5.3.4.1 Vibrational Spectroscopy	173
5.3.4.2 X-Ray Diffraction	174

5.3.4.3 Scanning Electron Microscopy	176
5.3.5 Mn(OAc) ₃ as a Catalyst.....	177
5.3.5.1 Vibrational Spectroscopy	177
5.3.5.2 X-Ray Diffraction	178
5.3.5.3 Scanning Electron Microscopy	180
5.4 Summary	181
5.5 References	182

5.1 Introduction

In this chapter, the aluminosilicate mullite ($\text{Al}_6\text{Si}_2\text{O}_{13}$), known as porcelainite, is examined both in its low temperature formation and in its uses as an additive in tensile stress coatings. Chemical analysis is given for the addition of mullite to the aluminium phosphate reaction mixtures and magnetostriction testing data for their use as tensile coatings. Subsequently, the low temperature synthesis of mullite is examined to investigate the formation of mullite under the prescribed reaction conditions used by Cogent Power Ltd. This will examine a hypothesis based on the addition of Jahn-Teller active compounds

5.1.1 Mullite

Mullite ($\text{Al}_6\text{Si}_2\text{O}_{13}$), is an important and widely studied mineral compound used in the ceramics industry in porcelain due to the formation of an high aspect ratio needle structure which increases mechanical strength and thermal shock properties and as a refractory material due to its high melting point¹⁻⁶.

Mullite possesses two crystalline phases, an orthorhombic structure ($a = 0.76 \text{ nm}$, $b = 0.77 \text{ nm}$ and $c = 0.29 \text{ nm}$) and a tetragonal structure ($a = b = 0.76 \text{ nm}$, $c = 0.29$)^{7, 8}. Of these the orthorhombic structure is the most preferable for use in practical applications due to it being the more stable phase of the two. There also exists a spinel phase of mullite, observation of this phase occurs during the partial synthesis of mullite or when reaction conditions are inadequate for the formation of either the tetragonal or orthorhombic mullite structures⁷. XRD analysis of the crystal structure of mullite shows that Al-O octahedral chains occupy the corners and centre of the unit cell. The chains are cross-linked by Si-O and Al-O tetrahedra⁹ as shown in figure 5.1.

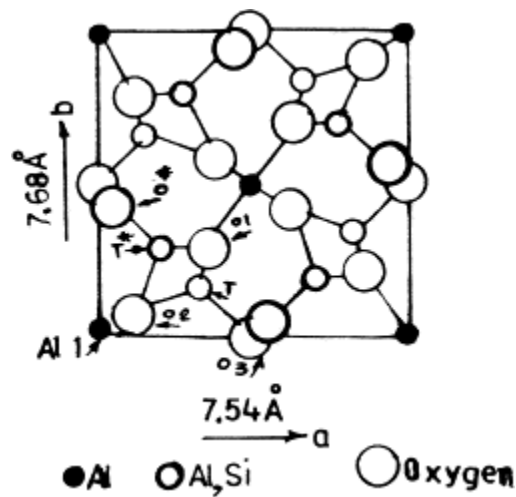


Figure 5.1: Crystal Structure of mullite showing cross linking of alumina and silica chains (Taken from Ref¹⁰)

A very widely used route for the synthesis of mullite is by the sol-gel method, via the reaction of an alumina source and a silica source, due to the formation of products of high purity. There are numerous precursors used in the sol-gel synthesis of mullite but they generally fall into the categories of inorganic metal salts and alkoxides; first used by Roy¹¹. They are now widely used by many and are primarily tetraethylorthosilicate (TEOS) and aluminium nitrate nonahydrate (ANN)^{12,13}.

The largest obstacle to overcome in the sol-gel mullite synthesis is the achievement of homogeneity of the precursors and preventing phase separation; meaning that factors such as solvent, solution pH and water for hydrolysis must be controlled to ensure an adequate synthesis tailored for needs. The temperature of formation for orthorhombic mullite has a very large variance and this had been attributed to the amount of water in the system. Water is a necessary component in mullite synthesis due to a hydrolysis step in the reaction mechanism. However, an excess of water can lead to phase heterogeneity which results in a rise in reaction temperature; this can lead to a variance in temperature between syntheses of around 350°C meaning the formation orthorhombic mullite occurs between 1000°C and 1350°C¹⁴⁻¹⁶. A study by Huling^{17, 18} achieved a low temperature orthorhombic mullite synthesis by evaporating water over a gel of the precursors: ANN and TEOS; this study could prove useful as it uses a potential precursor in the formation of aluminium

metaphosphate (ANN) and so could open the way towards a simultaneous synthesis of mullite and metaphosphate. A 2009 study by Bagchi et al¹⁹ managed the synthesis of mullite at temperatures as low as 600°C, by adding small amounts of copper(II) sulphate to an aqueous reaction mixture of ANN, TEOS and Al(ⁱOPr)₃. The authors suggested that the low temperature of mullite formation was due to the Jahn-Teller effect from the copper ion causing a strain on the alumina-silica complexes allowing for macroscopic phase changes at these relatively low temperatures.

There have been a few studies of the attempted combined usage of mullite and phosphates for various uses. Bao and Nicholson in 2005 attempted to synthesise aluminium orthophosphate nanoparticles and coating them onto mullite fibres²⁰. To coat the phosphate onto the mullite strands they pre-treated the mullite with a cationic electrolyte (PDADMA); this gave the mullite a positive surface charge allowing an interaction with the anionic phosphate. Wang et al in 2008²¹ attempted a simultaneous synthesis of mullite and aluminium phosphate; they used ANN, H₃PO₄ and TEOS in an attempt to form AlPO₄-SiO₂ powders. However, their XRD data showed that at temperatures below 1000°C the sample remained amorphous and so unsuitable for the commercial setup used by Cogent Power Ltd.

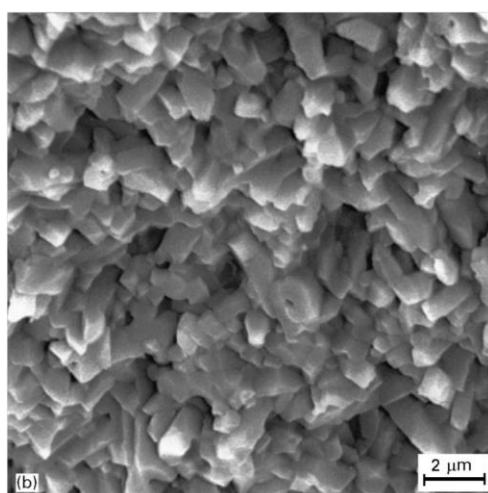


Figure 5.2: SEM image of mullite illustrating the high aspect ratio needles mullite is known to form²²

5.1.2 The Jahn-Teller Effect

The Jahn-Teller effect occurs in non-linear complexes that are orbitally degenerate and asymmetrically filled in the ground state. In order to remove the degeneracy, increase stability and lower the complex's energy, the complex distorts itself. Complexes which exhibit the Jahn-Teller effect are octahedral complexes with the electronic configurations of d^1 , d^2 , d^4 , low spin d^5 , high spin d^6 , d^7 , and d^9 and tetrahedral d^1 , d^3 , d^4 , d^6 , d^8 , and d^9 . The Jahn-Teller distortion occurs most effectively when there is an asymmetric population of orbitals²³.

Jahn-Teller distortions can be described as being either strong or weak, and dictate the type of distortion observed. Strong Jahn-Teller distortions occur when the orbital asymmetry occurs in the e_g orbital set. In order to reduce the orbital degeneracy, the compound distorts so as to lower the energy of the orbitals along the z-axis (d_{z^2} , d_{xz} , d_{yz}). This results in the elongation of the axial bonds as shown in figure 5.3.

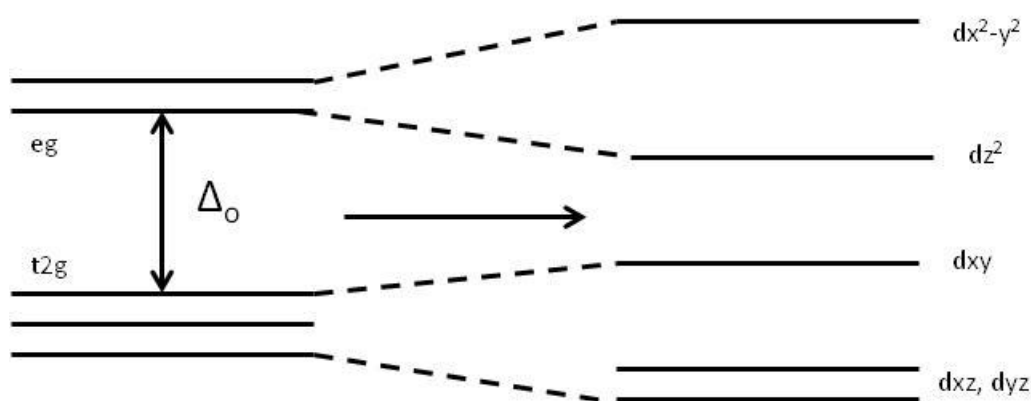


Figure 5.3: The splitting of d-orbitals of a metal complex after exhibiting the strong Jahn-Teller effect

Alternatively, in weak Jahn-Teller distortions the opposite occurs. In these cases, the asymmetry occurs in the t_{2g} orbital set. The orbital degeneracy is reduced by raising the energy of the orbitals on the z-axis, resulting in a compression of the axial bonds (figure

5.4). The nomenclature of the strong/weak Jahn-Teller effects arises due to the degree of bond length distortions being greater in strong Jahn-Teller distortions²⁴.

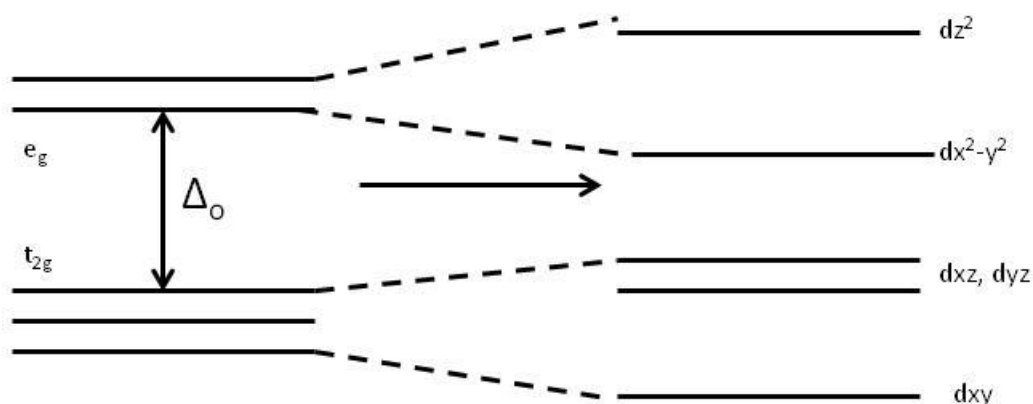


Figure 5.3: The splitting of d-orbitals of a metal complex after exhibiting the weak Jahn-Teller effect

5.2 The Combination of Mullite and Aluminium Phosphate

To examine the effects of mullite on the formation of aluminium metaphosphate, aluminium phosphate powders from various precursors were synthesised as described in chapter 3 with the addition of mullite powders. The following sections analyse the effects of the addition of mullite into the aluminium phosphate mixture using ATR-FTIR and Raman to examine metaphosphate formation and magnetostriction testing data to determine the suitability of the phosphate-mullite mixture as tensile strength coatings.

5.2.1 Vibrational Spectroscopy of Phosphate-Mullite Powders

5.2.1.1 ATR-FTIR Spectroscopy

The samples formulated using aluminium hydroxide ($\text{Al}(\text{OH})_3$), without the addition of mullite were found to form aluminium metaphosphate ($\text{Al}(\text{PO}_3)_3$) on annealing to 800 °C. This was observed in the IR spectra, with the evolution of distinct peaks relating to the formation of Al-O-P bonds indicating the formation of aluminium phosphate and P-O-P bonds showing the linking of phosphate units into metaphosphate. Figure 5.4 shows the IR

spectra for these samples after annealing to 300, 500, and 800 °C. The spectra show an evolution of peaks at 500 and 800 °C with the peaks at 738 and 730 cm^{-1} assigned to Al-O-P bands and the peaks at 1070, 1060, 1025, and 811 cm^{-1} to P-O-P²⁵⁻²⁷.

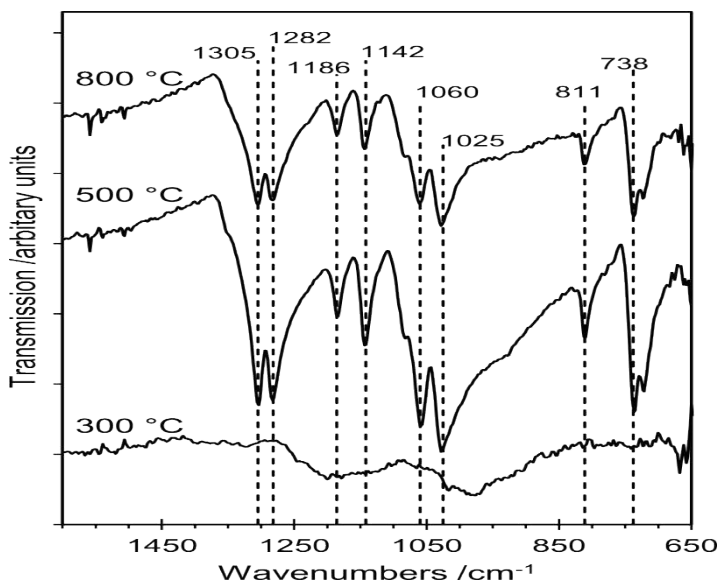


Figure 5.4: ATR-FTIR spectra for phosphate samples prepared from $\text{Al}(\text{OH})_3$ annealed to 300, 500 and 800 °C

The ATR-FTIR spectra for the hydroxide based samples with the addition of mullite (powder produced via the method shown in section 2.2.3) are shown in figure 5.5. The samples annealed at 300 and 500 °C show no evolution of peaks corresponding to the formation of aluminium phosphates. On heating to 800 °C there is an emergence of weak intensity peaks. Peaks evolved at 1305 and 1282 cm^{-1} are assigned to P=O π -bands and the peaks at 1186 and 1142 cm^{-1} assigned to P-O σ -bonds; which show the presence of phosphate. There are peaks present at 738 and 730 cm^{-1} showing that aluminium phosphate being formed and the presence of peaks at 1070, 1060, 1025, 811 cm^{-1} show that the phosphate units are polymerising to form aluminium metaphosphate^{25, 26}.

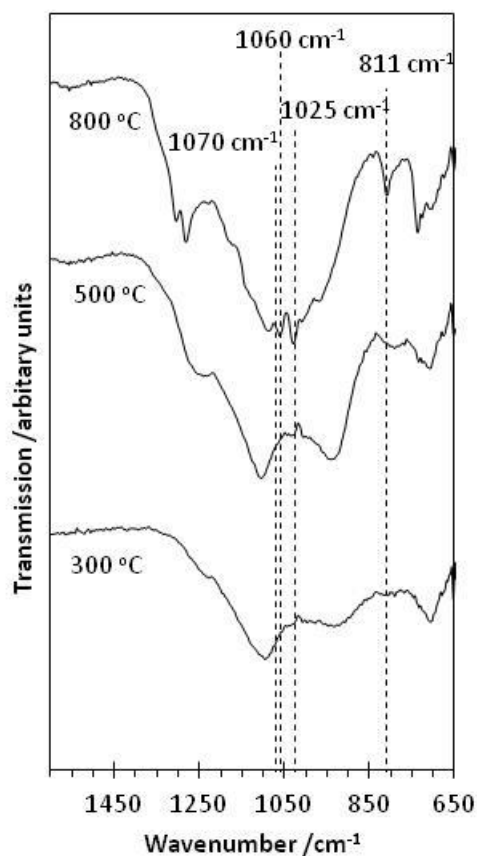


Figure 5.5: ATR-FTIR spectra for phosphate samples prepared from AlOH_3 with the addition of mullite powders annealed to 300, 500 and 800 °C

The presence of these peaks in the data gives evidence that the addition of mullite to the phosphate reaction mixture does not appear to have an effect on the formation of aluminium metaphosphate. This gives a good indication that this mixture may have viability in use as a tensile strength coating for use on magnetic steel substrates.

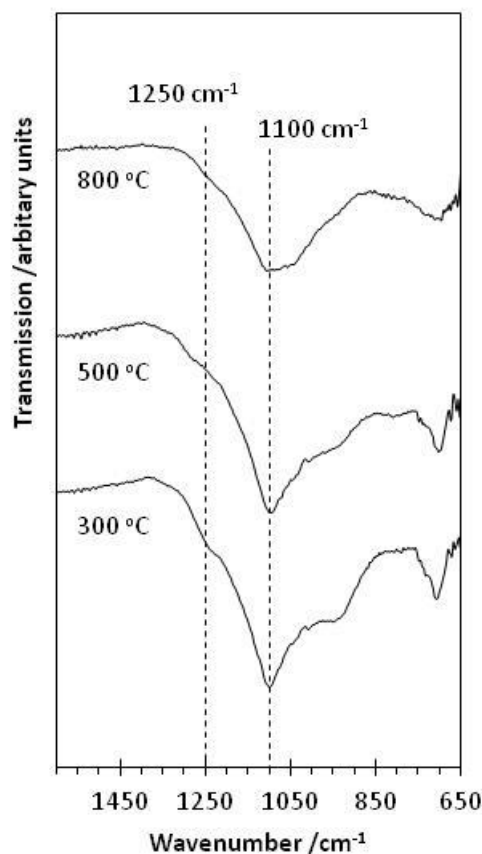


Figure 5.6: ATR-FTIR spectra for phosphate samples prepared from $\text{Al}(\text{NO}_3)_3$ with the addition of mullite powders annealed to 300, 500 and 800 °C

Mullite has also been added to reaction mixture of aluminium nitrate ($\text{Al}(\text{NO}_3)_3$) and phosphoric acid (H_3PO_4). Figure 5.6 shows the IR spectra of those samples annealed to 300, 500, and 800 °C. At 300 °C, the spectrum is dominated by the presence of a series of broad peaks. The peak at approximately 700 cm^{-1} is being assigned to Al-O-P bands suggesting the formation of aluminium phosphate. The broad bands at 1100 and 1250 cm^{-1} are indicative of the asymmetric and symmetric stretches of the PO_4^{3-} unit²⁸. This data shows that at 300 °C, the addition of mullite causes the sample to form aluminium orthophosphate (AlPO_4). On heating to 500 °C and again to 800 °C, there are no changes observed in the spectra, suggesting that after 300 °C the aluminium orthophosphate/mullite mixture is stable and that there is no conversion to metaphosphate. The lack of formation of aluminium

metaphosphate after the formation of orthophosphate is not surprising. The work by Bemmer²⁸ has already documented the thermal stability of aluminium orthophosphate across these temperature ranges and found that there is no conversion of aluminium orthophosphate to metaphosphate by 800 °C. Contrasting with the hydroxide based samples; there is a clear difference in that the use of aluminium nitrate sample caused the formation of aluminium orthophosphate and the use of aluminium hydroxide resulted in the formation of aluminium metaphosphate. From this, it could be hypothesized that the hydroxide samples would outperform the nitrate samples as tensile coatings, but the performance of mullite in tensile coatings has yet to be evaluated.

The aluminium chloride (AlCl_3) and mullite based samples show a similar situation to those of the nitrate based samples. The sets of broad peaks are observed across the temperature range at 700 cm^{-1} attributable to Al-O-P bonds and 1100 cm^{-1} attributed to PO_4^{3-} stretches²⁸. This again shows the formation of aluminium orthophosphate rather the aluminium metaphosphate as seen in the samples formed without the addition of mullite (figure 5.7). Another notable difference between the samples is in their physical appearance. The samples formed without the addition of mullite annealed to 400 and 500 °C were wet and tacky in nature, meaning they were unsuitable for analysis using an ATR crystal. The samples formed with mullite however were found to be much drier powders after annealing to 400 and 500 °C. The wetness of the samples in the absence of the mullite was attributed to the aggregation of hydrated phosphate species on the surface of the samples which dehydrated on the polymerisation of the phosphate units to form aluminium metaphosphate at 800 °C. In the case of the mullite containing samples, there is no condensation reaction occurring in the samples rather the formation of aluminium orthophosphate and this appears to cause the powders to dry much faster. Due to this, the samples annealed to 300 and 500 °C are suitable for analysis by ATR-IR.

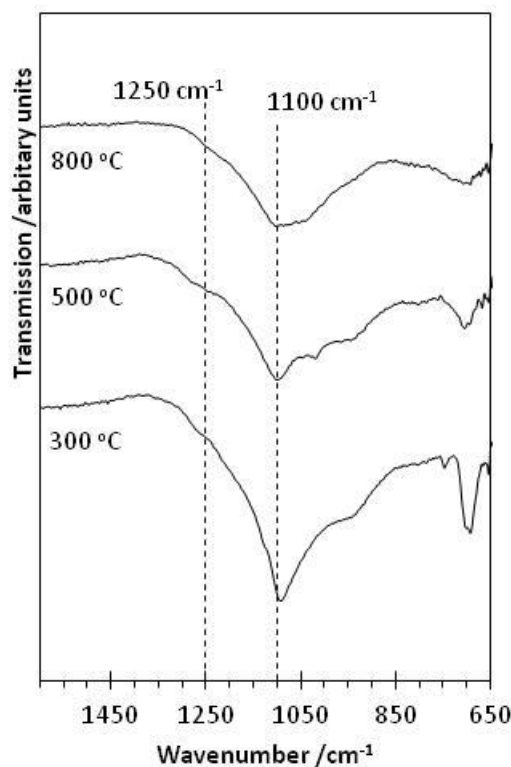


Figure 5.7: ATR-FTIR spectra for phosphate samples prepared from AlCl_3 with the addition of mullite powders annealed to 300, 500 and 800 °C

5.2.1.2 Raman Spectroscopy

The Raman spectra for the samples annealed to 800 °C are shown in figure 5.8. The IR spectra for the hydroxide based sample showed the formation of aluminium metaphosphate and evidence for this is also present in the Raman spectra. The peaks at 640 and 690 cm^{-1} are assigned to P-O-P symmetric stretches^{25, 26}. These peaks are also observed with the nitrate and chloride based samples, but with a lower relative intensity. This fits with the IR data which showed minimal indication of metaphosphate formation, the peaks present (at 1145 and 1150 cm^{-1}) corresponding to the formation of aluminium orthophosphate. All of the spectra also show peaks present at 1145 and 1150 cm^{-1} these

peaks correspond to orthophosphate stretches, which again falls in line with the IR data suggesting formation of aluminium orthophosphate^{25, 26}.

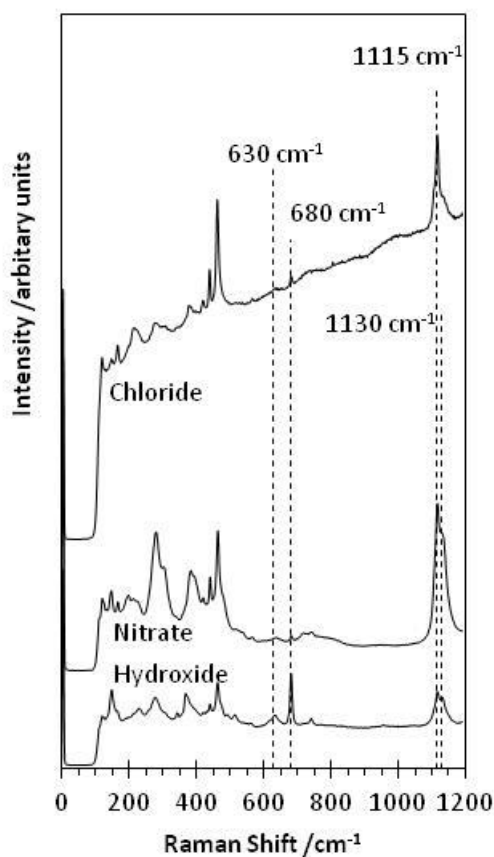


Figure 5.8: Raman spectra for phosphate samples with the addition of mullite powders annealed to 800 °C

Comparing the Raman spectra of these samples to those without the addition of mullite (figure 5.9), allows for a greater analysis of the effects of the addition of mullite to the reaction mixture. In the samples without mullite, the intensities of the orthophosphate region are significantly weaker compared to those with mullite; this agrees with the FTIR results which indicate that all of the samples without mullite formed metaphosphate rather than orthophosphate. The intensities of the peaks corresponding to the P-O-P symmetric stretches are also much greater in the samples without mullite; again, this is clearly explained by those samples forming aluminium metaphosphate.

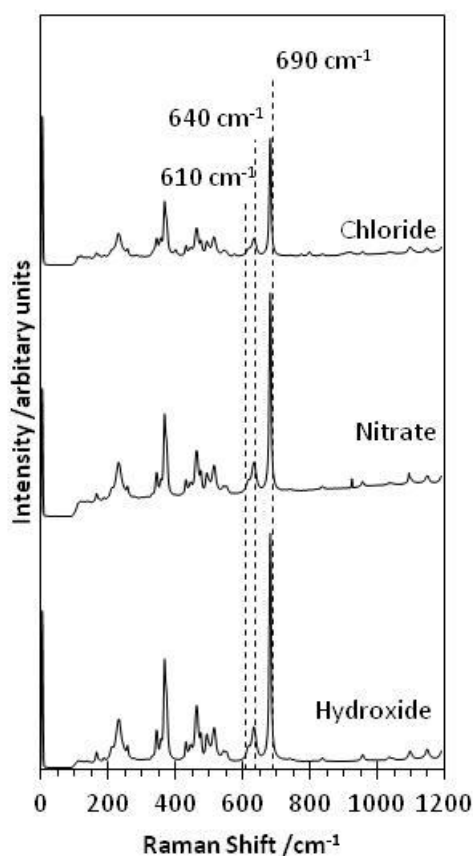


Figure 5.9: Raman spectra for phosphate samples without the addition of mullite powders annealed to 800 °C

5.2.2 Magnetostrictive Testing of Phosphate-Mullite Coatings

To test the effectiveness of the phosphate-mullite mixtures as tensile strength coatings, the three phosphate mixtures with the addition of mullite were prepared as coatings as described in section 2.2.6 and tested for their magnetostrictive properties. The coatings are compared against their analogues without the addition of mullite, an aluminium orthophosphate coating (the current online standard) and the effectiveness of a purely mullite coating. The cases of the analogous samples without the addition of mullite have been discussed in the previous chapter (chapter 4). Here the hydroxide and nitrate based samples show a steady shift towards lower stresses as annealing time increases, which was attributed to the formation of aluminium metaphosphate.

5.2.2.1 Magnetostriction of Mullite-Phosphate Coatings

The mixtures of the three aluminium precursors ($\text{Al}(\text{OH})_3$, $\text{Al}(\text{NO}_3)_3$, and AlCl_3) and phosphoric acid with the addition of mullite powders were prepared and coated onto a single side of a magnetic steel substrate sample. The coatings were then cured at 850 °C for time periods of 30 seconds, 5 and 10 minutes.

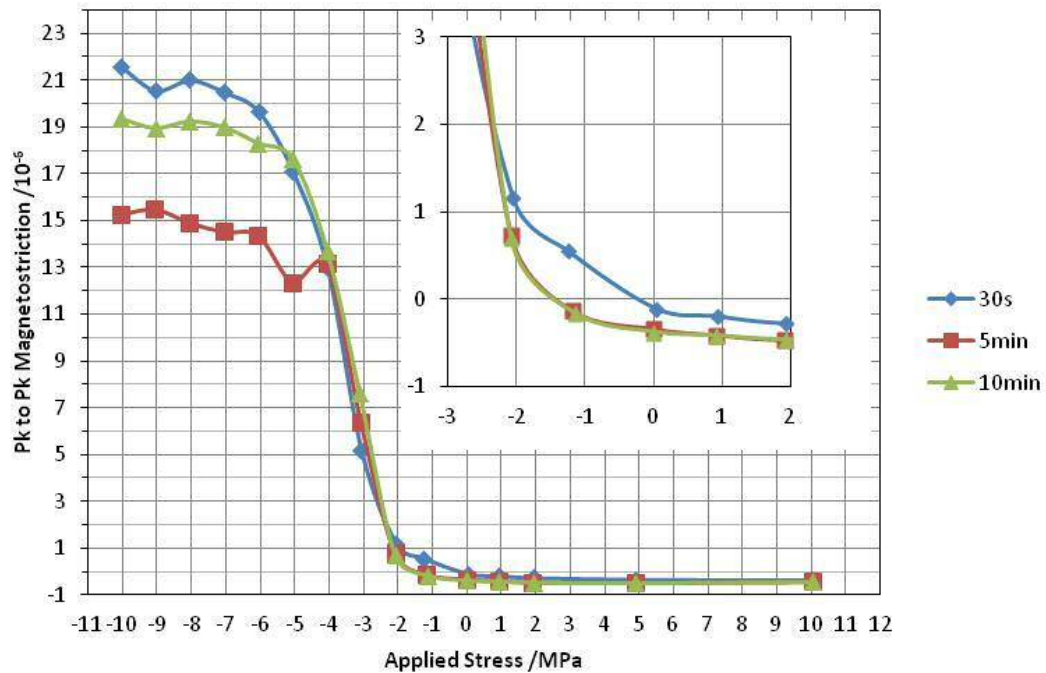


Figure 5.10: Magnetostriction-stress curves for the mullite-phosphate coatings prepared from $\text{Al}(\text{OH})_3$ and annealed at 850 °C for 30 seconds, 5 minutes and 10 minutes

The magnetostriction-stress curves for the samples formed from aluminium hydroxide are shown in figure 5.10. The curve at 30 seconds shows that the sample begins to exhibit the magnetostrictive effect at an applied stress of -0.25 MPa. On heating for 5 minutes, the curve shifts to -1.5 MPa and no further shift is observed on heating to 10 minutes. The samples heated for 5 and 10 minutes show an increase in performance of 1.5 MPa. This improvement in performance of the coatings can be attributed to the longer annealing times allowing for the formation of, albeit little, aluminium metaphosphate.

The mullite-phosphate samples formulated from aluminium nitrate are examined in figure 5.11. There are clear differences in the magnetostriction-stress curves for these samples when compared to those of the hydroxide based samples. The sample annealed for 30 seconds at 850 °C exhibit a magnetostrictive effect at -1.5 MPa with no shifts observed when annealing up to 5 minutes. However, after heating for 10 minutes, the sample shifts towards higher stresses by 0.75 MPa, leading to a worsened performance of this sample. This trend is also observed in the chloride based samples in figure 5.12. The samples annealed for 30 seconds and 5 minutes exhibit magnetostriction at -1.5 MPa with the samples annealed for 10 minutes shifting to -0.75 MPa.

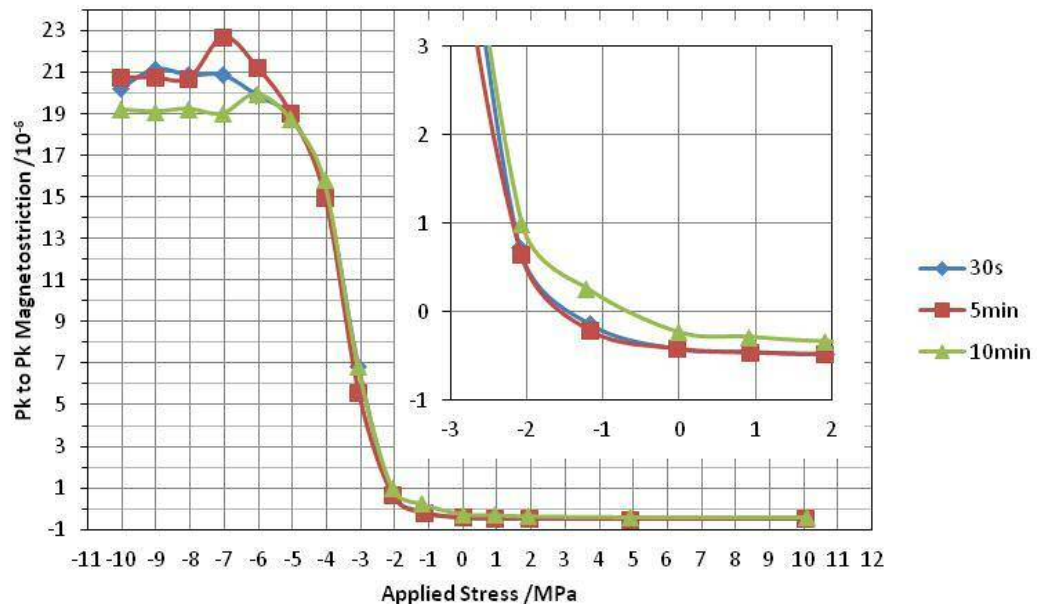


Figure 5.11: Magnetostriction-stress curves for the mullite-phosphate coatings prepared from $Al(NO_3)_3$ and annealed at 850 °C for 30 seconds, 5 minutes and 10 minutes

The comparison between the hydroxide sample and the nitrate and chloride samples can be explained by the hydroxide samples forming some aluminium metaphosphate. Previous analysis of aluminium orthophosphate coatings (Chapter 4) showed that after prolonged annealing times an aggregation of orthophosphate units occurred which was attributed to

the worsening performance of the coating compared to metaphosphate coatings. If the nitrate and chloride based samples also undergo this aggregation after 10 minutes of heating at 850 °C; this would explain the drop off in performance of the coatings.

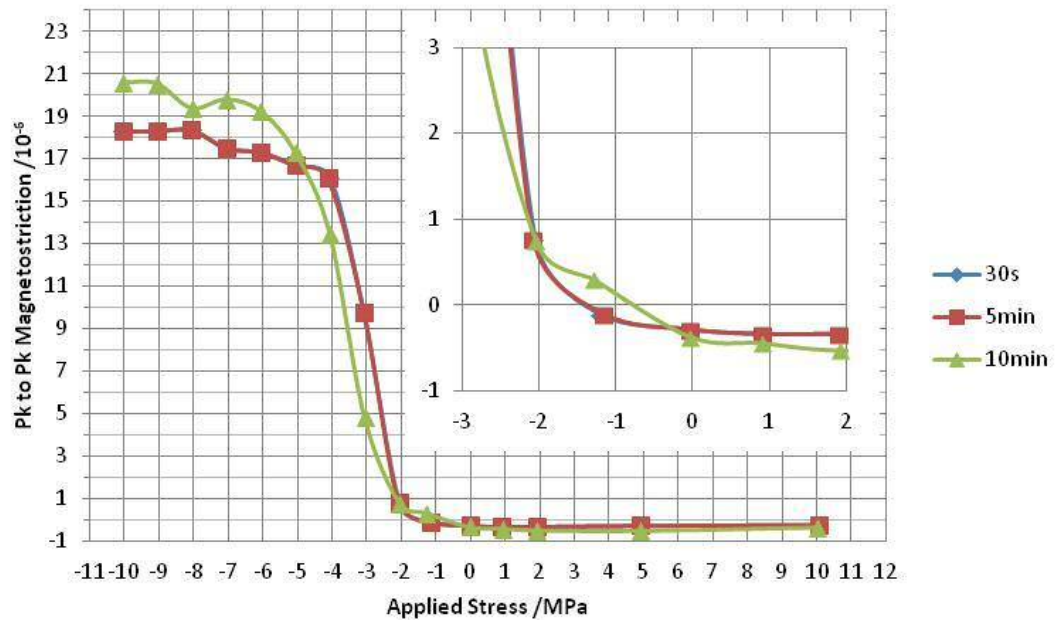


Figure 5.12: Magnetostriction-stress curves for the mullite-phosphate coatings prepared from $AlCl_3$ and annealed at 850 °C for 30 seconds, 5 minutes and 10 minutes

5.2.2.2 Magnetostrictive Testing of Pure Mullite Coatings

The coating samples prepared are the reaction mixture for the preparation of mullite powders and pre-prepared mullite powders and are detailed in section (2.2.3). The magnetostriction curves for the mullite reaction mixture coatings annealed to 850 °C for 30 seconds, 5, and 10 minutes are shown in figure 5.13. The samples show a shift towards lower stresses as annealing time increases; at 30 seconds the magnetostrictive effects are observed at 1 MPa and at -0.75 and -1.75 for 5 and 10 minutes respectively. This data shows that as annealing time increases the performance of the coating improves. This could be attributable to mullite beginning to form from the reaction mixture and imparting

tensile holding to the magnetic steel substrate. The oscillation in the curve at stresses below -3.0 MPa indicates an error in the measurement system or a defect in the substrate; reducing the reliability of the analysis of this data set.

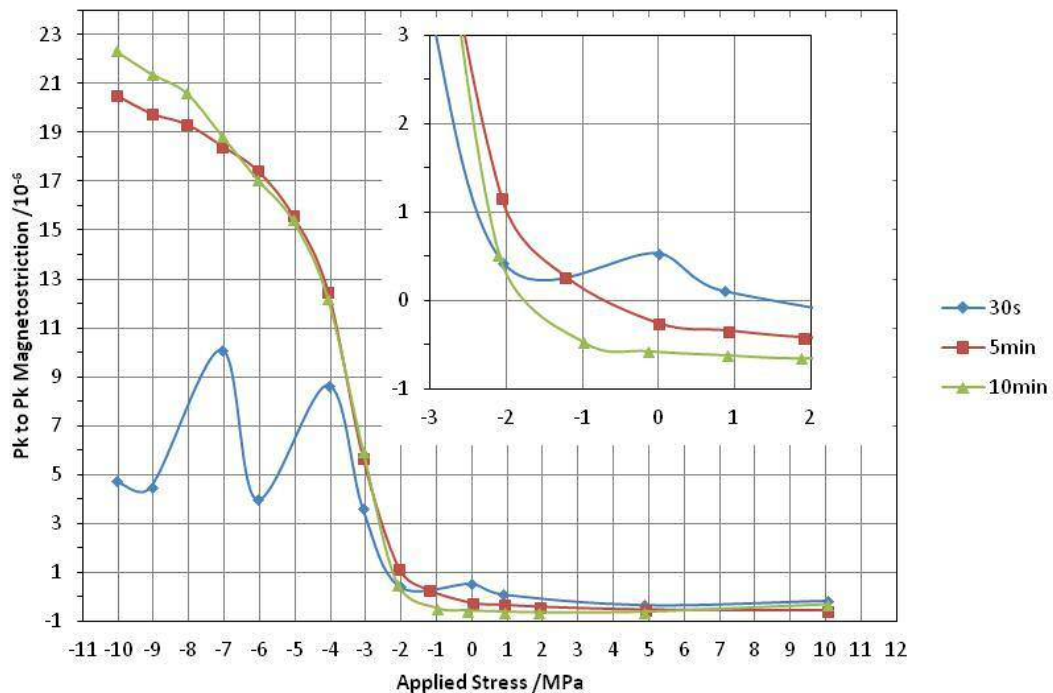


Figure 5.13: *Magnetostriction-stress curves for the mullite prepared from the mullite reaction mixture and annealed at 850 °C for 30 seconds, 5 minutes and 10 minutes*

In figure 5.14, the magnetostriction stress curves for the samples formed from use of mullite powders are presented. These curves show that as the coatings are heated from 30 seconds to 5 minutes, there is a shift in the curves from -1.25 to -1.75 MPa, an improvement of 0.50 MPa. However, on increasing the annealing time to 10 minutes, a shift towards positive stresses is observed, shifting to -0.5 MPa. This drop in performance after increased annealing times, was also observed in the mullite-phosphate samples prepared using aluminium nitrate and chloride. Here the explanation was attributed to formation of aluminium orthophosphate which on extended heating times exhibited particle aggregation resulting in a drop in performance of the coatings. If the mullite

particles are also aggregating, this would explain why there is a decrease in the performance in the coatings after annealing for 10 minutes.

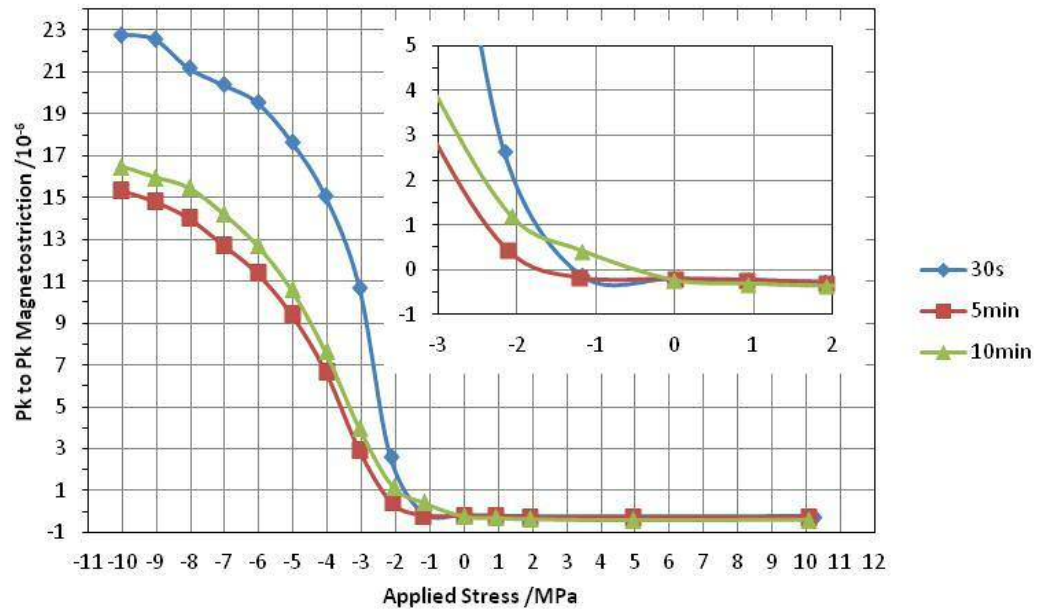


Figure 5.14: *Magnetostriction-stress curves for the mullite prepared from mullite powder and annealed at 850 °C for 30 seconds, 5 minutes and 10 minutes*

A major issue encountered when preparing the samples using the mullite was the large powder size used. The powder was too large for the coating rollers and was noticeable from the sounds of the grinding of the powders against the rolling bar and steel substrate. If the large particle size results in poor distribution of the mullite across the substrate then this may skew the results of the magnetostriction data. Investigations into forming mullite with smaller particle sizes were undertaken and are discussed in section 5.3 below.

5.3 The Low Temperature Synthesis of Nano-Scale Mullite

As stated above, the large crystallites formed in the mullite synthesis are not suitable for the coating methods used by Cogent Power Ltd. In this section, the synthesis of smaller crystals is examined. Also explored is the mechanism proposed by Bagchi for the low temperature synthesis of mullite¹⁹. The discussion proposed that the addition of copper sulphate facilitates the formation of mullite with the Cu^{2+} ion catalysing the effect from the Jahn-Teller effect; here this hypothesis is test through the use of various other additives, with varying degrees of Jahn-Teller activity. Bagchi also observed the formation of nano-scale mullite, which will also be tested for with the use of the various additives.

The various samples were formulated using the method used by Bagchi et al, described in section 2.2.3; additives were substituted for one another whilst keeping the molar concentrations equivalent and are detailed in Table 5.1. Samples were taken after 2 hours annealing at 300, 500, and 800 °C to test the temperature of mullite evolution and at 0.5, 1, and 2 hours at 800 °C to examine whether annealing time has any noticeable effect on mullite formation and particle size. The samples were tested for mullite formation using FTIR spectroscopy and XRD (figure 5.15), scanning electron microscopy is used to examine the particle size of the formed products.

<u>Additive</u>	<u>Oxidation State</u>	<u>Exhibited Jahn-Teller Effect</u>
CuSO_4	$\text{Cu}^{2+} (\text{d}^9)$	Strong
$[\text{Fe}(\text{CN})_6]\text{K}_3$	$\text{Fe}^{3+} (\text{low-spin } \text{d}^5)$	Weak
$\text{Fe}(\text{NO}_3)_3 \cdot 9\text{H}_2\text{O}$	$\text{Fe}^{3+} (\text{high-spin } \text{d}^5)$	None
CrCl_3	$\text{Cr}^{3+} (\text{d}^3)$	None
$\text{Mn}(\text{OAc})_3$	$\text{Mn}^{3+} (\text{d}^3)$	Strong High-Spin/ Weak low-spin

Table 5.1: *Tabulate summary of the various additives used in the synthesis of mullite, showing the Jahn-Teller effect exhibited by the complexes.*

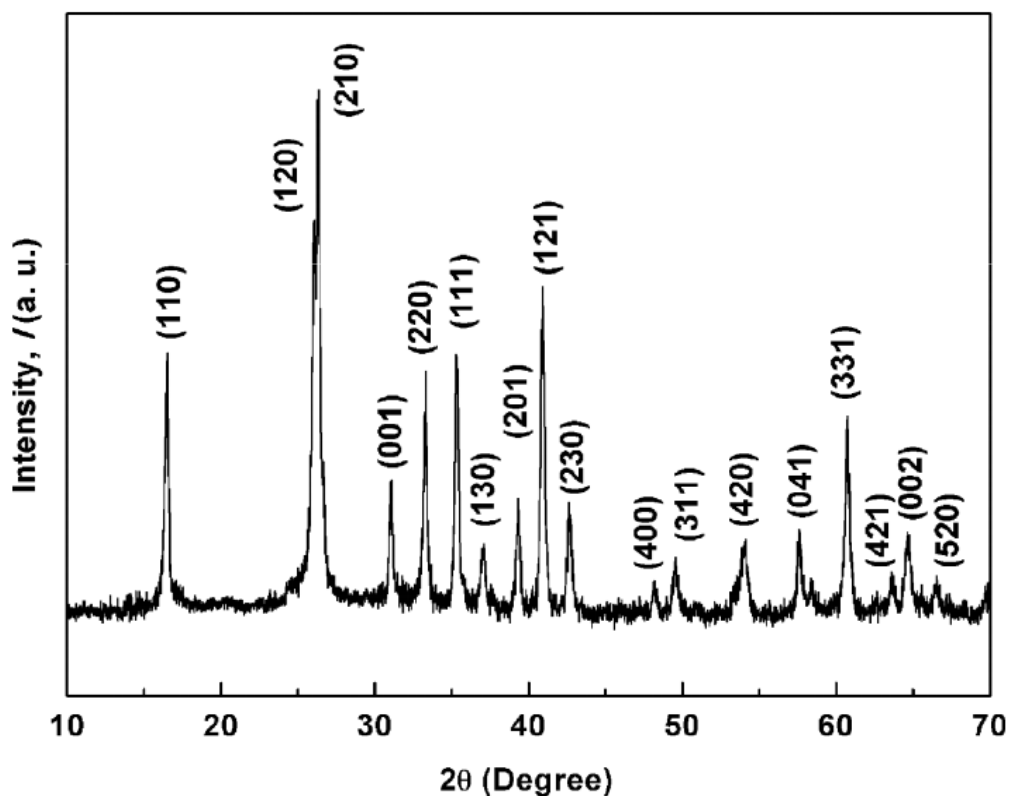


Figure 5.15: XRD of a mullite sample; taken from reference²⁹

5.3.1 CuSO₄ as a Catalyst

The addition of Cu²⁺ ions was the method proposed by Bagchi et al reporting the formation of nano-scale mullite by 800 °C. This has been the synthesis method used throughout section 5.2 to examine the effects of mullite on phosphate coatings

5.3.1.1 Vibrational Spectroscopy

Figure 5.16 show the IR spectra for the mullite samples annealed at 300, 500 and 800 °C for 2 hours and Figure 5.17 the spectra for samples annealed for 0.5, 1, and 2 hours at 800 °C. At 300 °C, there are a number of very weak peaks observed. The peak observed at 740 cm⁻¹ and the broad band at 800-1000 cm⁻¹ are assignable to AlO₄ tetrahedra¹⁹ expected in mullite. However, to fully confirm mullite formation peaks would need to observe additionally at 560 and 1130 cm⁻¹ corresponding to AlO₆ octahedra and SiO₂ tetrahedra¹⁹.

From the low intensity of the two observed peaks, it is possible that the second sets of peaks are present and simply not distinguishable from the baseline.

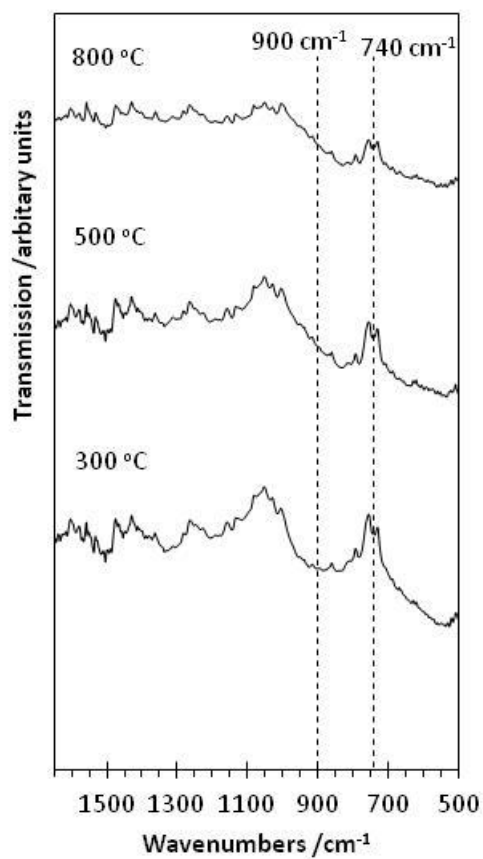


Figure 5.16: ATR-FTIR spectra for mullite samples prepared with the addition of $\text{Cu}(\text{SO}_4)$ annealed to 300, 500 and 800 °C

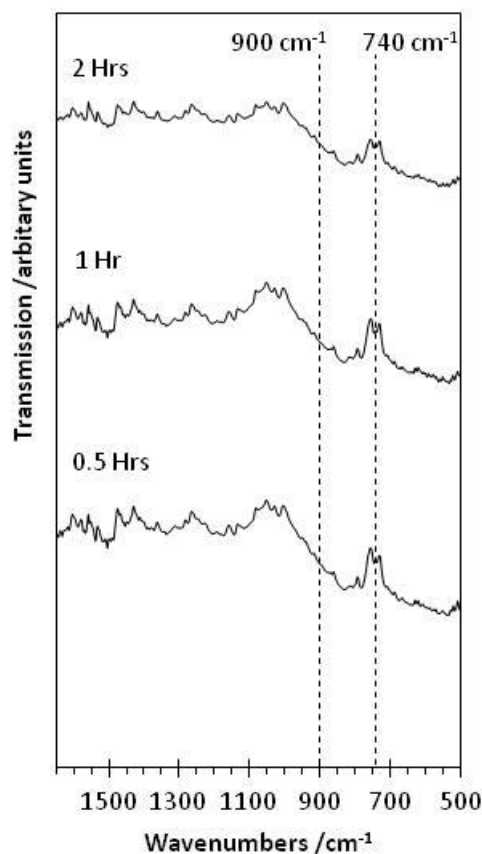


Figure 5.17: ATR-FTIR spectra for mullite samples prepared with the addition of $\text{Cu}(\text{SO}_4)$ annealed to $800\text{ }^\circ\text{C}$ for 0.5, 1 and 2 hours

5.3.1.2 X-Ray Diffraction

XRD patterns for the samples annealed to 300 , 500 and $800\text{ }^\circ\text{C}$ are shown in figure 5.18. The patterns show no evolution of crystalline species at 300 and $500\text{ }^\circ\text{C}$, with the observation of amorphous halos at these temperatures. By $800\text{ }^\circ\text{C}$, there is an evolution of peaks observed that can be attributed to the formation of mullite^{5, 30, 31}. However, the intensity of the peaks are very weak, giving an indication that using copper sulphate only gives limited formation of mullite at these temperatures. This was noted by Bagchi who studied the effects of copper concentration in the reaction mixture, it was seen that increasing concentrations of copper led to a reduction in amount of mullite formed¹⁹. The low intensity of the peaks also corroborates well with the IR data which showed only very

low intensity peaks corresponding to the formation of mullite. When annealing at 800 °C over 0.5, 1 and 2 hours (figure 5.19), after annealing as short as 30 minutes mullite formation is observed, showing that only a short time period is required at 800 °C to facilitate the formation of mullite using CuSO_4 as an additive and annealing beyond 30 minutes does not have a major effect on increasing mullite formation.

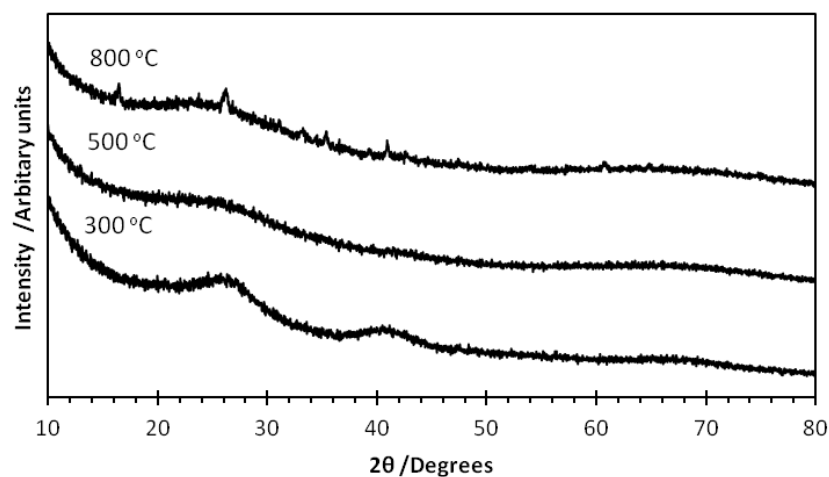


Figure 5.18: XRD data for mullite samples prepared with the addition of $\text{Cu}(\text{SO}_4)$ annealed to 300, 500 and 800 °C

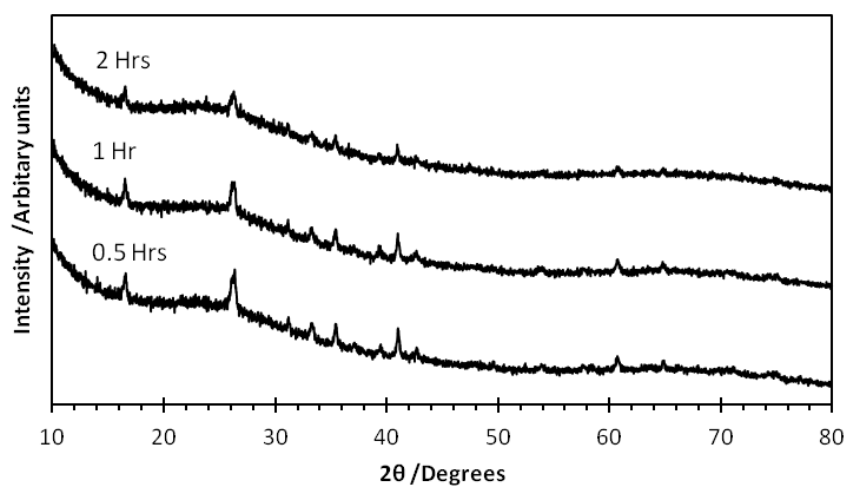


Figure 5.19: XRD data for mullite samples prepared with the addition of $\text{Cu}(\text{SO}_4)$ annealed 800 °C for 0.5, 1, and 2 hours

5.3.1.3 Scanning Electron Microscopy

Scanning electron microscopy (SEM) was used to examine the particle sizes formed over the course of the reaction. Figures 5.20 show the images taken for the samples taken at 300, 500, and 800 °C after 2 hours annealing. At 300 °C, wide scan show particles of varying size and shape the largest observed having a diameter of approximately 200 μm . On closer magnification onto the particles, smaller flake like particles are seen covering the surface of the larger particles with a size of approximately 10 – 20 μm . On heating to 500 °C, a similar situation in particle size is observed with a variety of sizes seen across wide scans. Tighter scans again show the presence of small flake like particles with sizes of around 10 – 20 μm . The similarities in the comparison of these SEM images do correspond to the XRD data which show no mullite formation when transitioning from 300 to 500 °C, the SEM show no change in the morphology of the particles or the formation of the high aspect ratio needle structures that mullite can form. After annealing to 800 °C, it is evident from the wide scans that particle aggregation may have occurred, with the largest particle size now measured at approximately 300 μm ; under higher magnification however, the smaller flake like particles are still visible again with a size of approximately 10 -20 μm . The SEM images for the samples annealed at 800 °C over various time periods, allow for analysis of the effects of annealing time on particle size and shape. After annealing for 0.5 and 1 hours, the images appear similar to those of the samples annealed for 2 hours, the presence of large aggregated particles are observed with smaller flake like particles covering their surface.

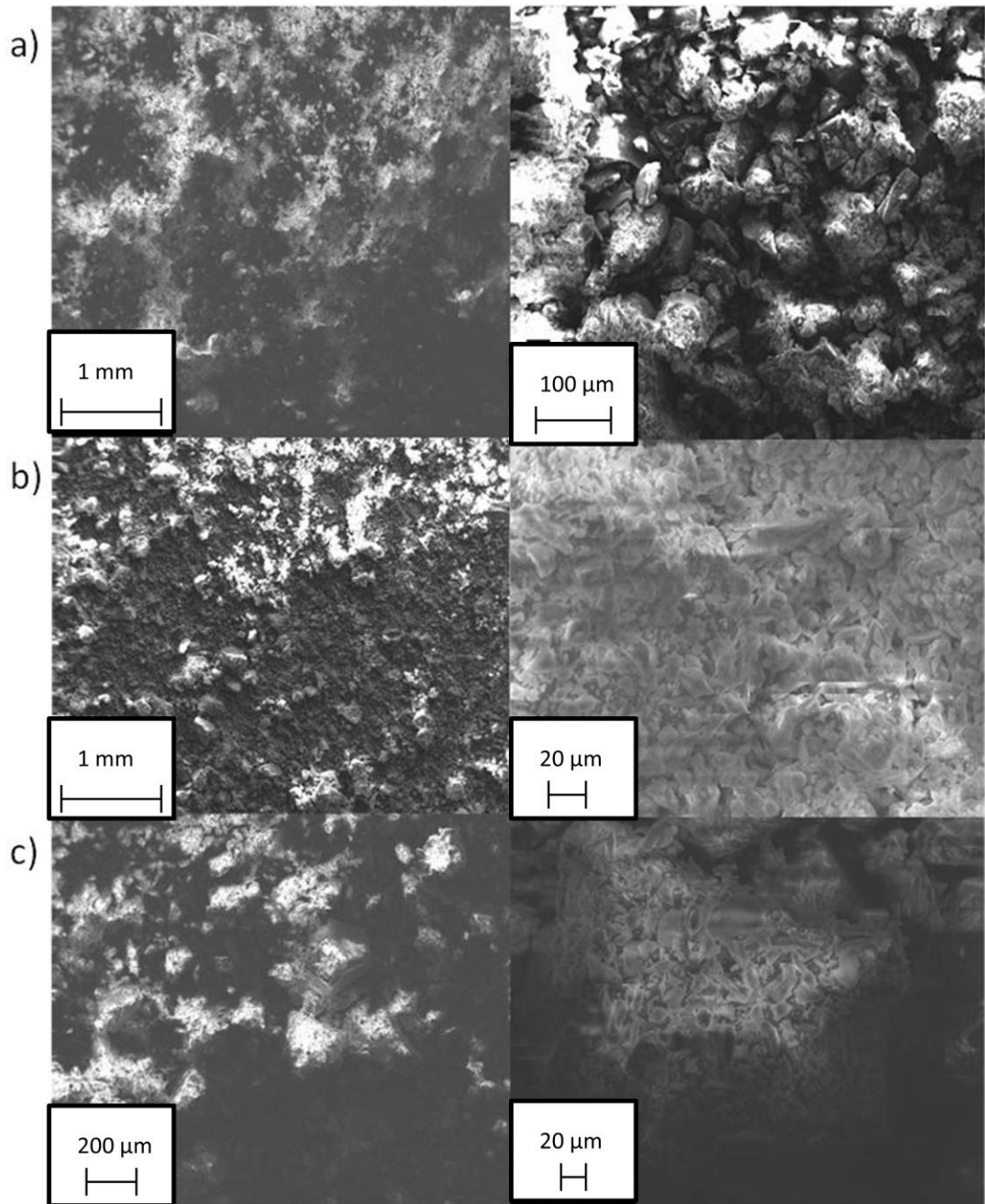


Figure 5.20: SEM Images of mullite samples prepared with the addition of $\text{Cu}(\text{SO}_4)$ annealed to a) 300, b) 500 and c) 800 °C

Despite the XRD samples showing that mullite had been formed by 800 °C, the SEM images do not indicate the formation of the high aspect ratio needle structures that mullite is known to form. This is consistent with the XRD showing low signal intensity for the peaks suggesting that only a minimal amount of mullite has been formed using this synthesis method. Additionally, Bagchi et al reported, using this method, the formation of nano-scale mullite with average particle sizes of approximately 20 nm where as in this study, the particles were measured in the micron range. A possible answer to this is due to the method used by Bagchi to analyse the particle size; the Scherrer equation (Equation 5.1.). This method uses line widths in XRD data to calculate the average crystallite size in the samples corresponding to analysed diffraction line. However, this equation is accurate only for analysis of grain sizes below 0.1 – 0.2 µm. From this, it can be shown that whilst there may be the formation of nano-scale grains the annealing process causes the formation of large particle aggregates.

$$\tau = (K\lambda)/(\beta\sin\theta)$$

Equation 5.1: *The Scherrer equation for the calculation of mean crystallite size from XRD line widths,*

where: K = shape factor, λ = x-ray wavelength, β = FWHM, ϑ = Bragg angle.

5.3.2 $[\text{Fe}(\text{CN})_6]\text{K}_3$ as a Catalyst

Potassium hexacyanoferrate, with the Fe^{3+} ion, is a d^5 low-spin weakly Jahn-Teller active complex.

5.3.2.1 Vibrational Spectroscopy

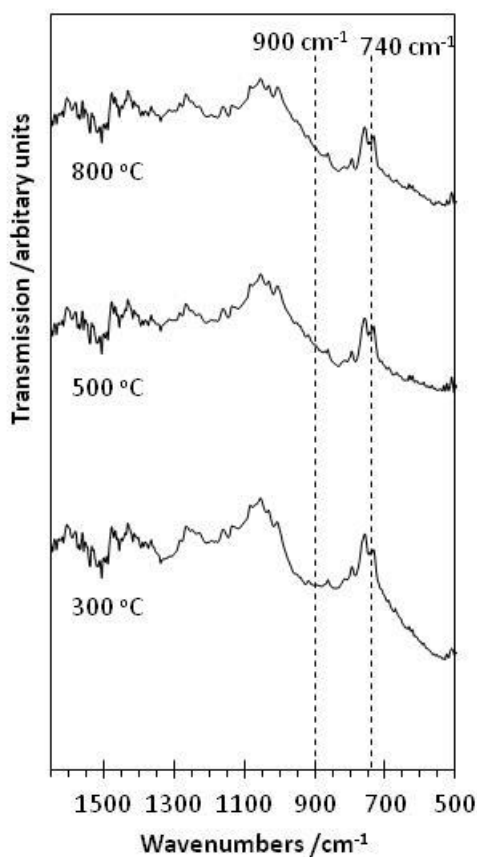


Figure 5.21: ATR-FTIR spectra for mullite samples prepared with the addition of $[\text{Fe}(\text{CN})_6]^{3-}$ annealed to 300, 500 and 800 °C

The IR spectra for the samples are shown in figures 5.21 and 5.22 and have a similar profile to those of the Cu^{2+} dosed samples. The samples show the presence of the peaks corresponding to AlO_4 tetrahedra at 740 and 800-1000 cm^{-1} . These spectra also show an absence of the peaks at 560 and 1130 cm^{-1} . Again, due to weak intensity of the peaks present it is unclear the unseen peaks are truly absent or simply indistinguishable from the baseline; as such mullite formation cannot be determined from the IR spectra alone.

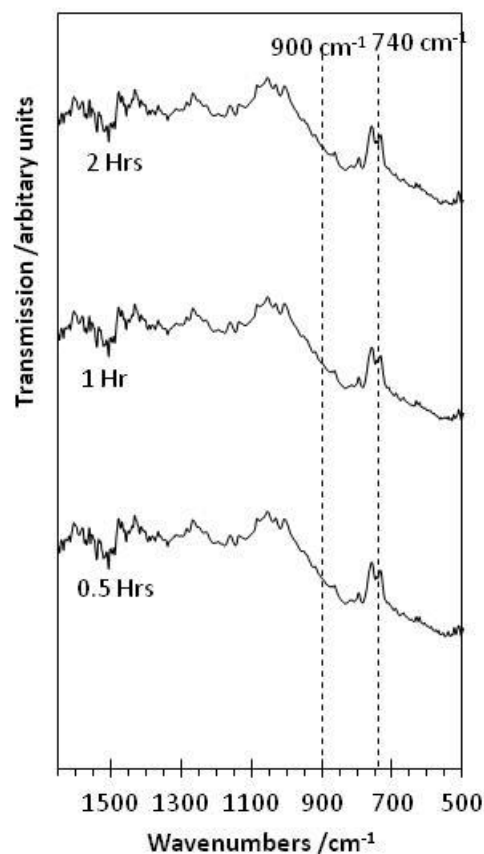


Figure 5.22: ATR-FTIR spectra for mullite samples prepared with the addition of $\text{Fe}(\text{CN})_6^{3-}$ annealed to 800 °C for 0.5, 1 and 2 hours

5.3.2.2 X-Ray Diffraction

Figure 5.23 shows the XRD data for the samples annealed at 300, 500, and 800 °C for two hours. As with the copper sulphate samples, no peaks are observed at 300 and 500 °C showing that these samples are amorphous. On heating to 800 °C, peaks emerge which correspond to the formation of mullite. Across the samples annealed for various times at 800 °C, shown in figure 5.24, mullite peaks are present from annealing from 30 minutes to 2 hours. There is an increase in the intensity of the peaks as the annealing time increases, showing that mullite formation is not complete by 0.5 hours and continues to be formed as annealing continues at 800 °C.

The peak intensities observed for the iron doped samples are much higher than those of the copper doped samples, suggesting that changing the metal used as an additive has an effect on mullite formation; potentially due to the nature of the Jahn-Teller effect. CuSO_4 and $\text{Fe}(\text{NO}_3)_3$ exhibit the Jahn-Teller effect in different ways; CuSO_4 has the strong Jahn-Teller effect and $\text{Fe}(\text{NO}_3)_3$ the weak effect. In the strong effect of an octahedral complex, the 2 axial bonds are elongated and so are longer than the 4 equatorial bonds. In the weak effect, the opposite is true; the 2 axial bonds are compressed and are shorter than the equatorial bonds. Since the addition of the Jahn-Teller active compounds causes a destabilisation of the alumina-silicate matrix causing the formation of mullite at lower temperatures, it may be that the compression of the axial bonds in the Jahn-Teller effect favour the formation of mullite.

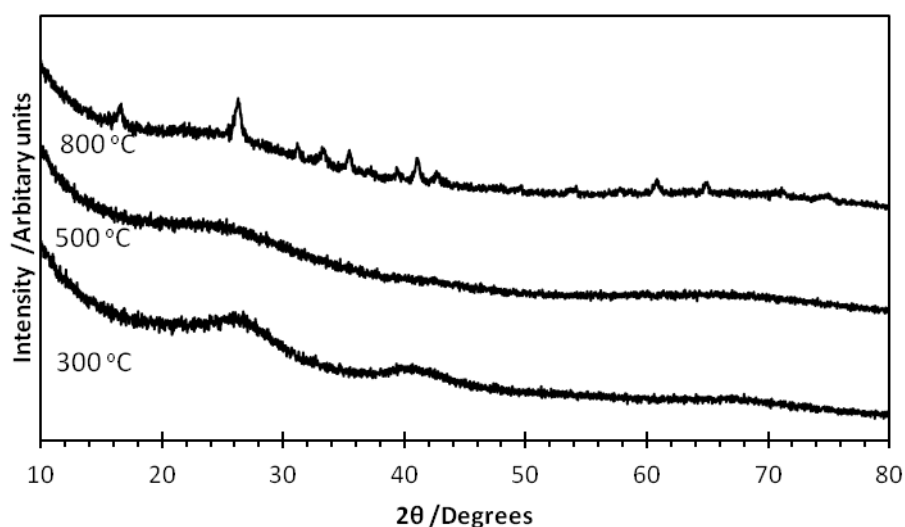


Figure 5.23: XRD data for mullite samples prepared with the addition of $\text{Fe}(\text{CN})_6^{3-}$ annealed to 300, 500 and 800 °C

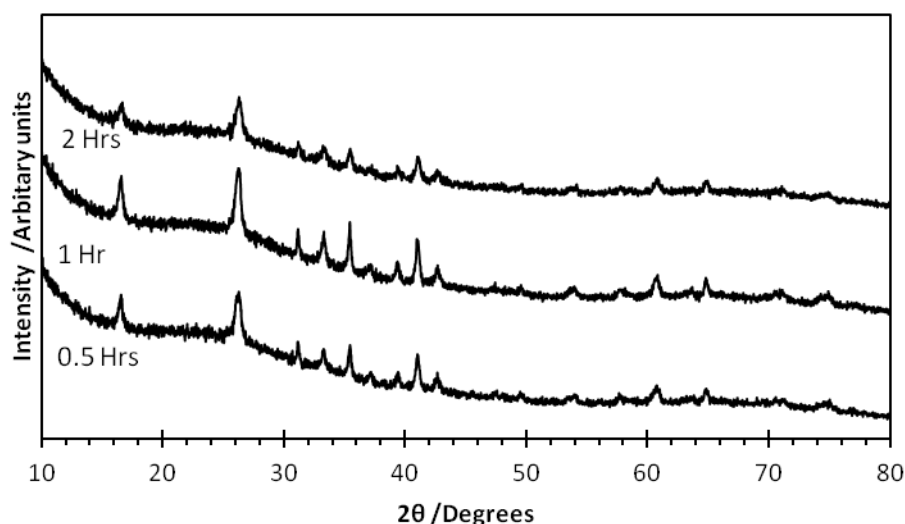


Figure 5.24: XRD data for mullite samples prepared with the addition of Fe(CN)_6^{3-} annealed 800 °C for 0.5, 1, and 2 hours

5.3.2.3 Scanning Electron Microscopy

The SEM images from the Fe doped samples at 300 °C (figure 5.25) are comparable to the Cu doped samples. The low magnification images show the presence of relatively large particles with an approximate size of 100 μm . Increasing the magnification reveals the presence of smaller flake like particles present on the surface of the larger particles sized around 10 μm . Heating to 500 °C, shows that aggregation of the particles has occurred with particles of 200 μm being observed. As well as the flake like particles being observed, there are also some needle shaped particles seen upon higher magnification. This high aspect ratio is known to form on mullite synthesis which gives indication of the formation of mullite. At 800 °C, the large particles and small flake particles are still observed but no high aspect ratio particles are observed. This suggests that using this method does not cause mullite to form its needle like structure when annealed up to 800 °C. This coupled with the XRD data and the XRD and SEM data for the Cu doped samples suggests that whilst doping the reaction mixture with Jahn-Teller active compounds does reduce the temperature

required to begin to form mullite, higher temperatures are required to for full conversion to mullite and formation of the high aspect ratio needles.

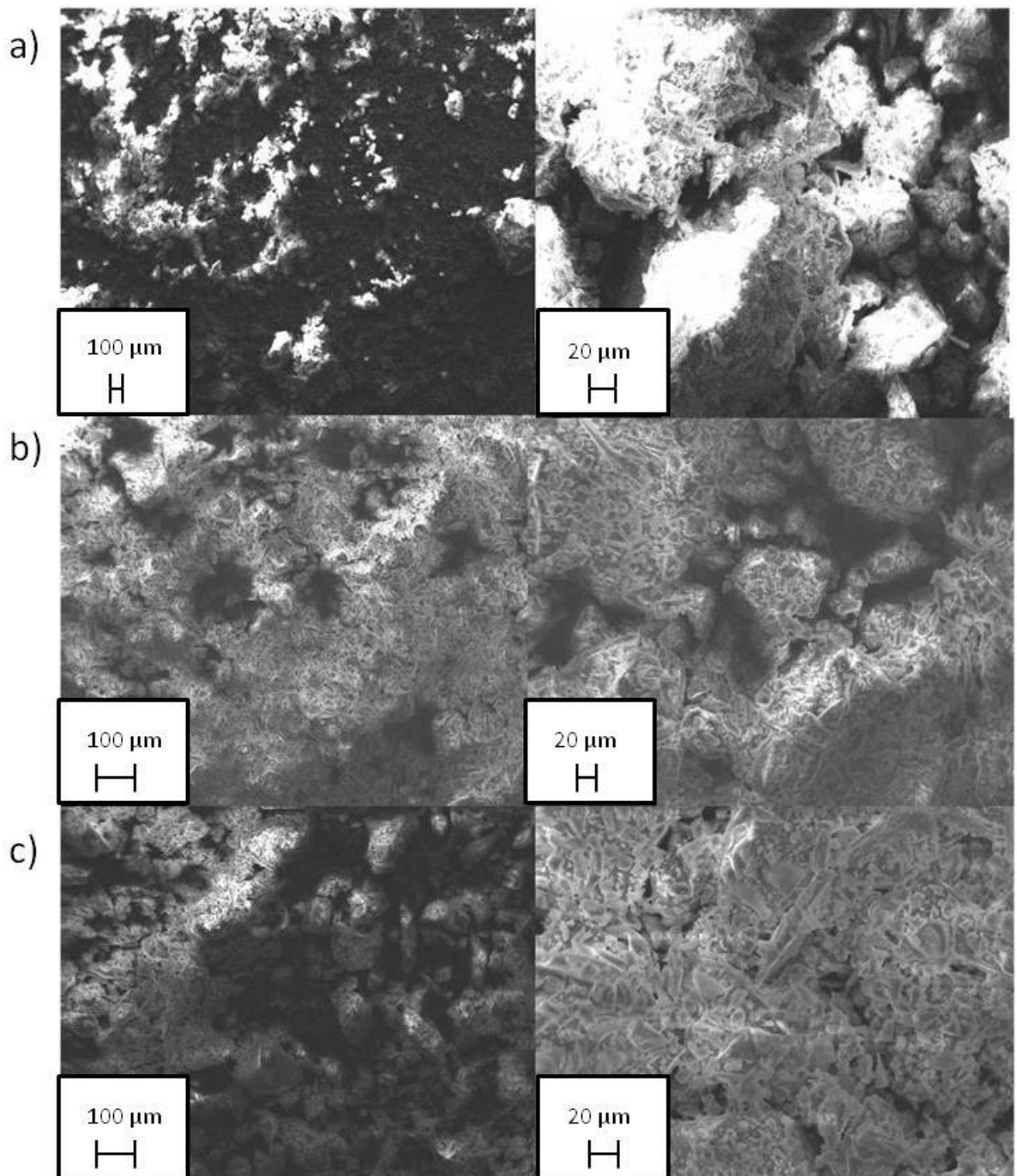


Figure 5.25: SEM Images of mullite samples prepared with the addition of $\text{Fe}(\text{CN})_6^{3-}$ annealed to a)

300, b) 500 and c) 800 °C

5.3.3 $\text{Fe}(\text{NO}_3)_3 \cdot 9\text{H}_2\text{O}$ as a Catalyst

Iron nitrate $\text{Fe}(\text{NO}_3)_3 \cdot 9\text{H}_2\text{O}$ is a high-spin $d^5 \text{Fe}^{3+}$ complex which is not Jahn-Teller active.

5.3.3.1 Vibrational Spectroscopy

Figures 5.26 and 5.27 show the IR spectra for the samples prepared from $\text{Fe}(\text{NO}_3)_3 \cdot 9\text{H}_2\text{O}$ after annealing for 300 and 500 °C for 2 hours and for 800 °C for 0.5, 1 and 2 hours. The spectra show the same profiles observed in the copper sulphate and hexacyanoferrate samples. Analysis of the previous IR samples gave an indication, but not definitive proof, that mullite is being formed. Here, this is also the case with the observance of the peaks corresponding to AlO_4 tetrahedra; however based on the current hypothesis, this is not expected.

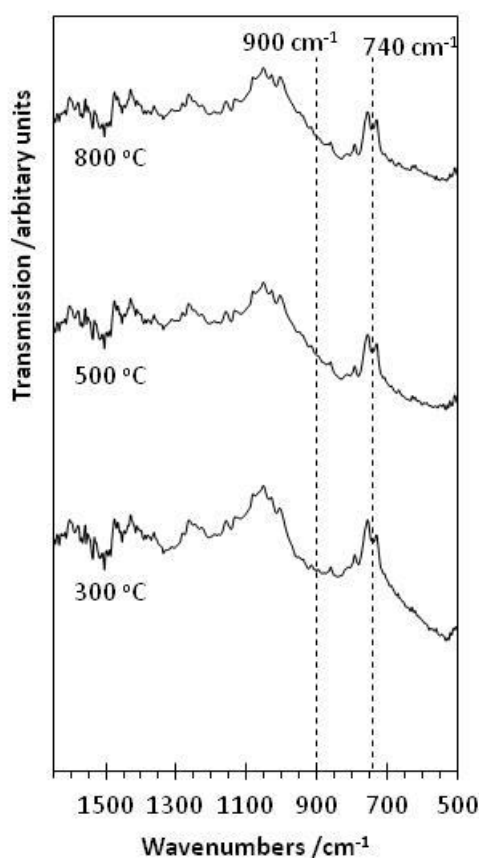


Figure 5.26: ATR-FTIR spectra for mullite samples prepared with the addition of $\text{Fe}(\text{NO}_3)_3$ annealed to 300, 500 and 800 °C

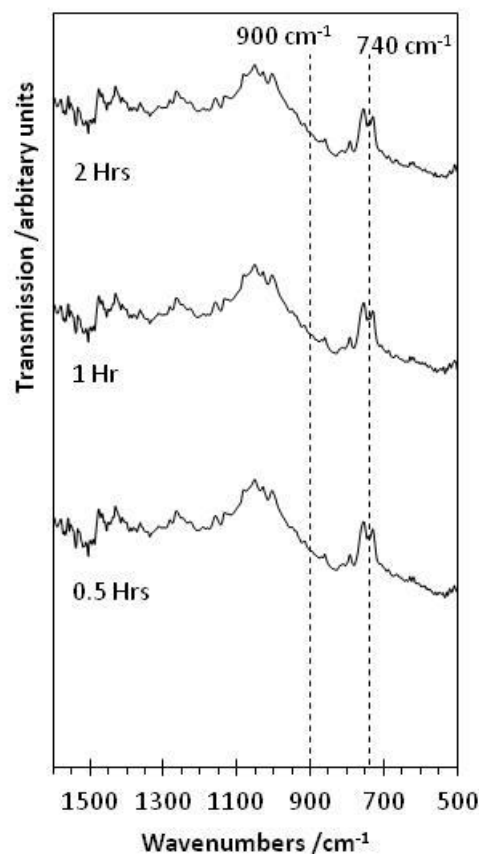


Figure 5.27: ATR-FTIR spectra for mullite samples prepared with the addition of $\text{Fe}(\text{NO}_3)_3$ annealed to $800\text{ }^\circ\text{C}$ for 0.5, 1 and 2 hours

5.3.3.2 X-Ray Diffraction

The XRD data for the samples annealed up to $800\text{ }^\circ\text{C}$ are shown in figure 5.28. The samples at 300 and $500\text{ }^\circ\text{C}$, show that there is no mullite formation and that the samples are non-crystalline. This is in line with the copper sulphate and iron nitrate based samples which also did not show any evolution of mullite or any crystalline species. On annealing further to $800\text{ }^\circ\text{C}$, there is an evolution of peaks corresponding to the formation of mullite. Analysis of the samples annealed for 0.5 and 1 hours (figure 5.29), also show the formation of mullite.

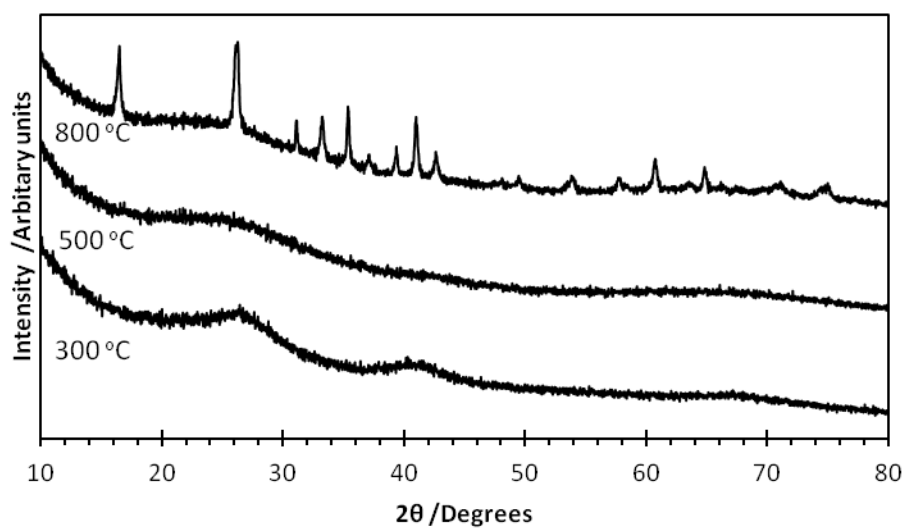


Figure 5.28: XRD data for mullite samples prepared with the addition of $\text{Fe}(\text{NO}_3)_3$ annealed to 300, 500 and 800 °C

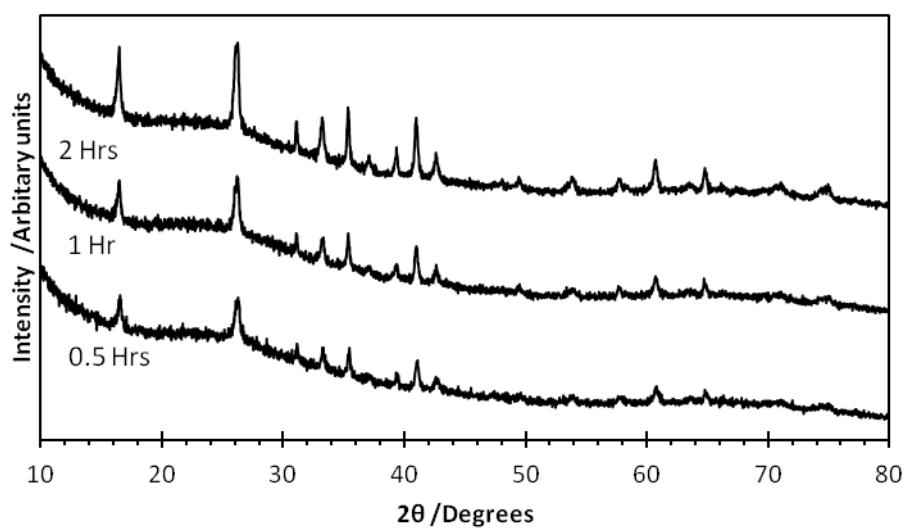


Figure 5.29: XRD data for mullite samples prepared with the addition of $\text{Fe}(\text{NO}_3)_3$ annealed 800 °C for 0.5, 1, and 2 hours

5.3.3.3 Scanning Electron Microscopy

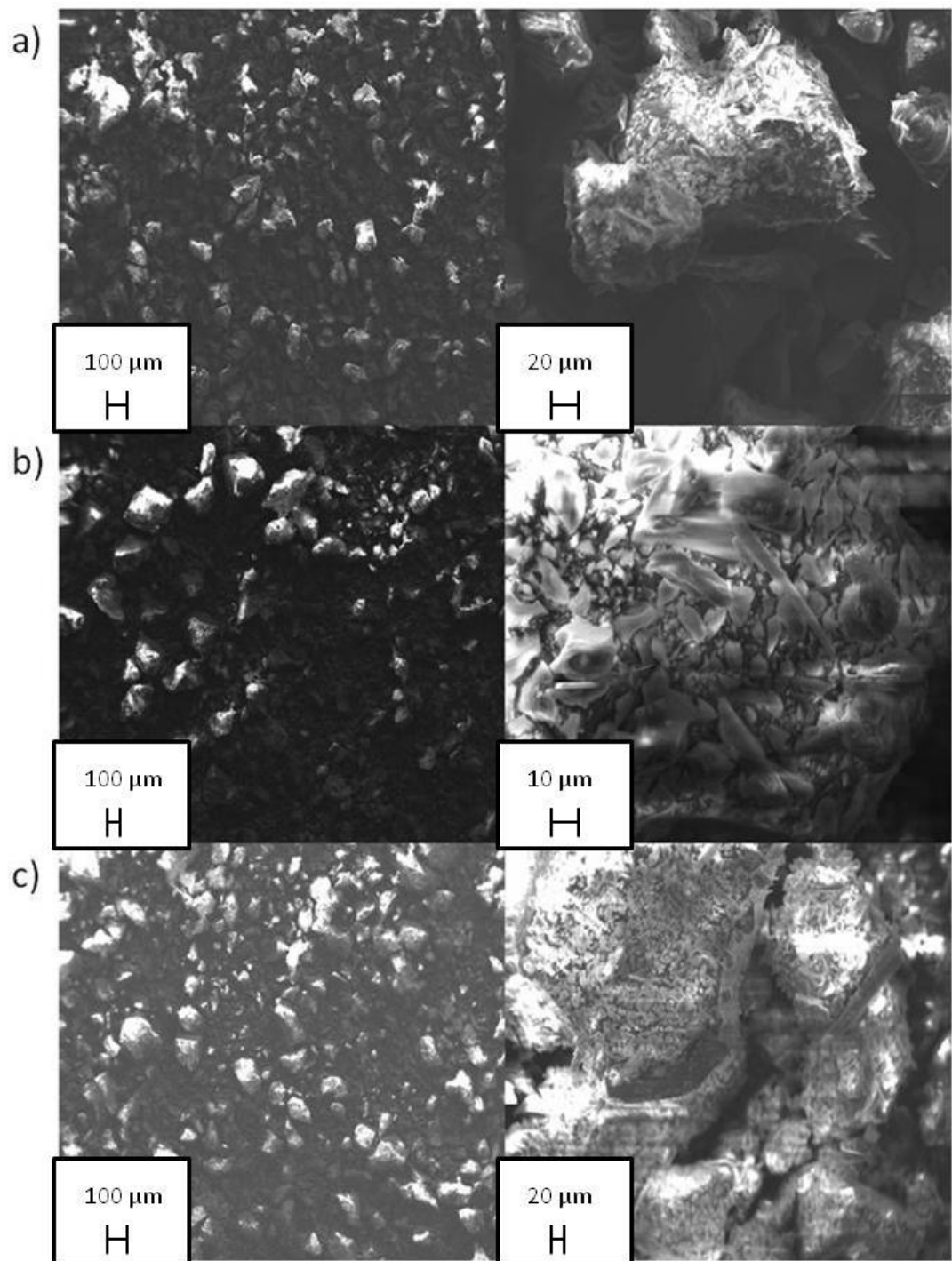


Figure 5.30: SEM Images of mullite samples prepared with the addition of $\text{Fe}(\text{NO}_3)_3$ annealed to a) 300, b) 500 and c) 800 °C

The SEM images for the samples are given in figure 5.30. The samples at 300 °C, show similar particle sizes to the previous samples. The sample consists of larger particles with sizes of 100 – 200 µm, viewable on wide magnification scans. On increasing magnification, the smaller flake like particles with sizes of approximately 10 µm are observed. On increasing the annealing temperatures to 500 and 800 °C, the images show little change from the lower temperature samples. The images are dominated by the larger particles low magnification scans with the smaller 10 µm particles visible at higher magnification scans. The scans at 500 °C, also show evidence of the formation of high aspect ratio needle particles. This again with the previous Fe doped sample gives increasing evidence towards mullite formation.

5.3.4 CrCl₃ as a Catalyst

The Cr³⁺ ion is a d³ which does not exhibit any Jahn-Teller effects and does not have any high/low spin metal-ligand effects to consider. Using this complex as an additive in the mullite reaction mixture could give more definitive evidence for the Jahn-Teller assisted low temperature formation of mullite.

5.3.4.1 Vibrational Spectroscopy

The IR spectra for the Cr doped samples annealed to 300, 500, and 800 °C are given in figure 5.31 and 5.32. The sample from 300 °C, shows the presence of peaks at 1325, 1400 and 925 cm⁻¹. The bands at 1325 and 1400 cm⁻¹ have been assigned to the presence of nitrate and organic groups whilst the assignment of the band at 925 cm⁻¹ is given to Si-OH vibrations. On heating to 500 and 800 °C, these bands disappear which indicates that these volatile components have been removed from the samples. These samples show a clear difference from the Fe and Cu doped samples which showed peaks relating to the formation of mullite. The absence these peaks indicate that there is no mullite formation using chromium chloride as an additive.

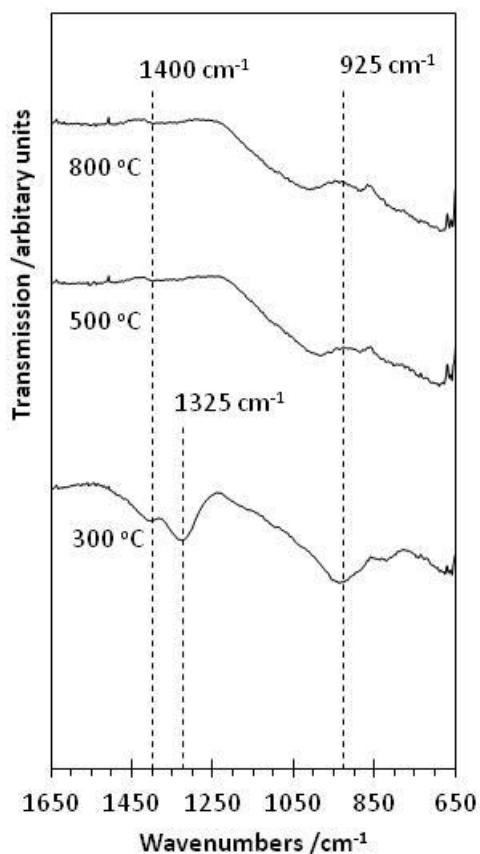


Figure 5.31: ATR-FTIR spectra for mullite samples prepared with the addition of CrCl_3 annealed to 300, 500 and 800 °C

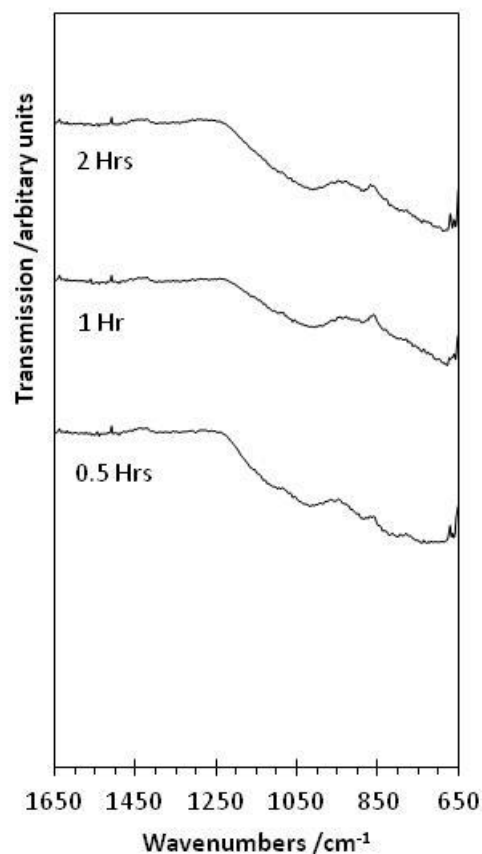


Figure 5.32: ATR-FTIR spectra for mullite samples prepared with the addition of CrCl_3 annealed to 800 °C for 0.5, 1 and 2 hours

5.3.4.2 X-Ray Diffraction

The x-ray diffraction data for the Cr doped samples annealed at 300, 500, and 800 °C agree shown in figure 5.33, and for the samples annealed for 0.5, 1, and 2 hours at 800 °C in figure 5.34. There is no indication of any mullite formation, across the samples, as curing temperature increases. This corroborates the IR data which also did not show any of the peaks indicative of mullite formation.

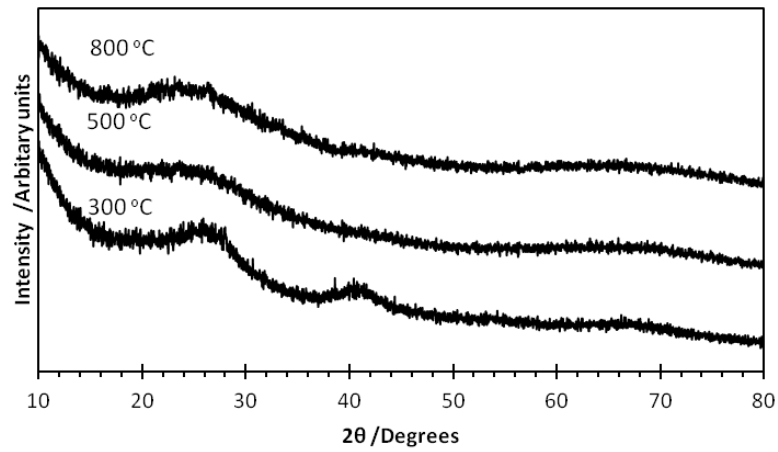


Figure 5.33: XRD data for mullite samples prepared with the addition of CrCl_3 annealed to 300, 500 and 800 °C

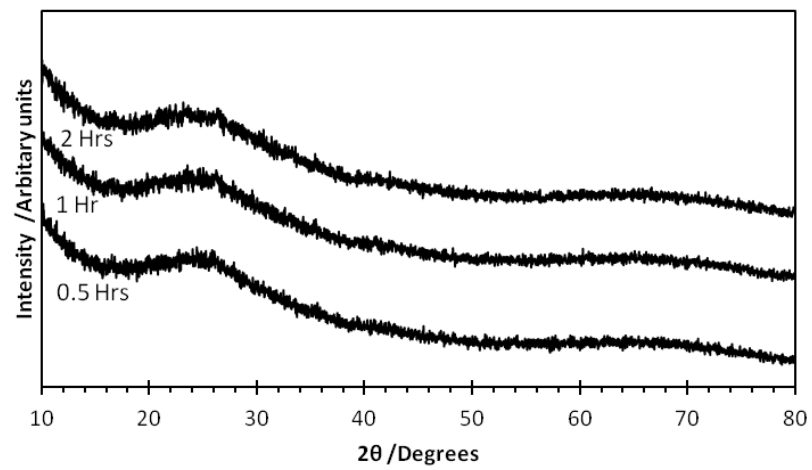


Figure 5.34: XRD data for mullite samples prepared with the addition of CrCl_3 annealed 800 °C for 0.5, 1, and 2 hours

5.3.4.3 Scanning Electron Microscopy

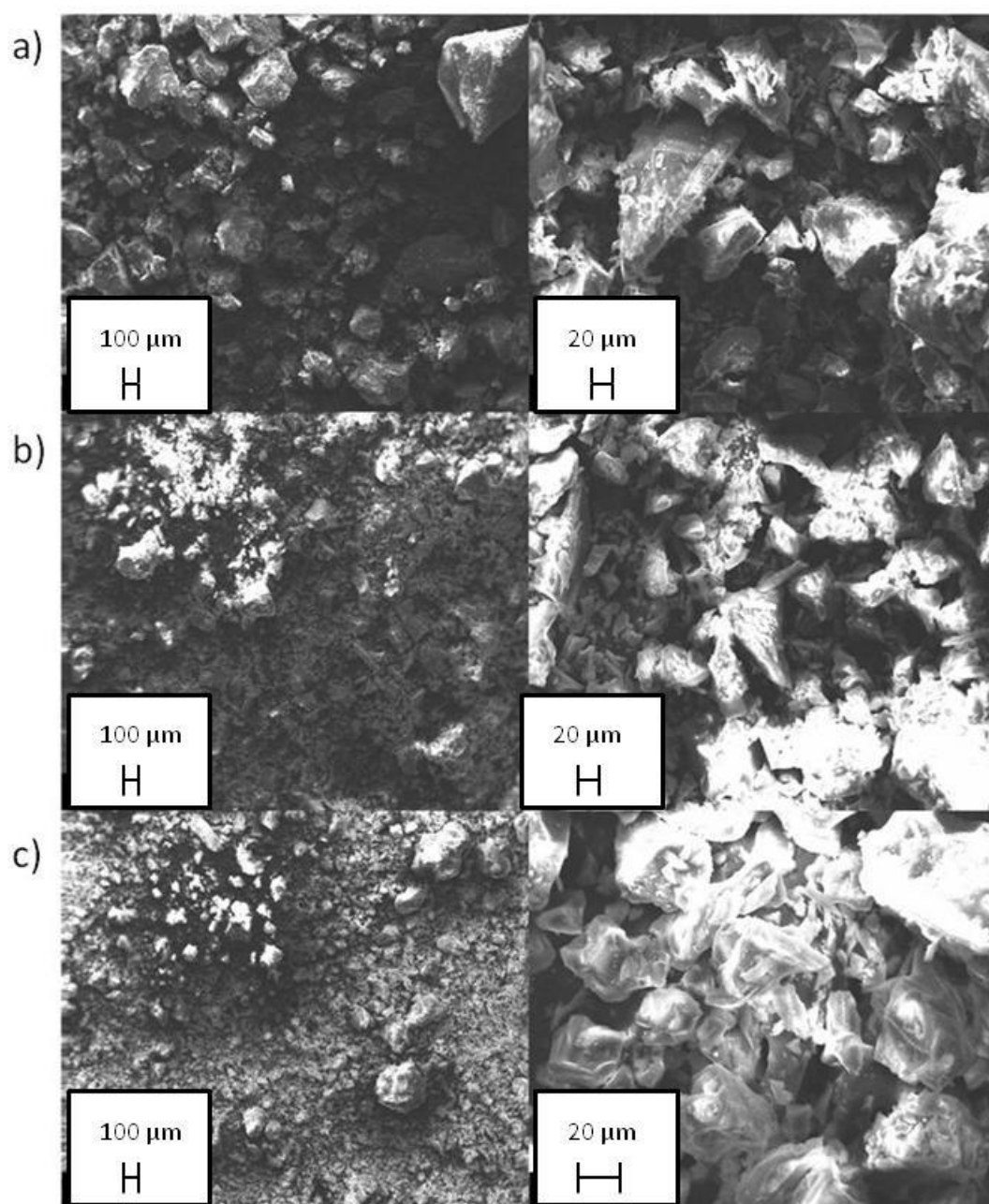


Figure 5.35: SEM Images of mullite samples prepared with the addition of CrCl₃ annealed to a) 300, b) 500 and c) 800 °C

Since the IR and XRD data for the Cr doped samples did not show any mullite formation, it would be interesting to see whether the shape and size formed particles differs in these particles compared to those of the Cu and Fe doped samples. SEM images for the Cr doped samples are shown in figure 5.35. Whilst the overall profiles of these samples are similar to the Cu and Fe doped samples, there is the presence of the large particles and smaller flake like particles, there are noticeable differences. The sizes of the larger particles are noticeably larger in the Cr doped samples; the Cu and Fe doped sample measured between 100 – 200 μm where as there are some particles measured at 300 μm for the Cr samples annealed to 300 $^{\circ}\text{C}$. In the 300 $^{\circ}\text{C}$ there was a significantly less number of the smaller flake particles observed. This would suggest that a greater degree of particle aggregation is occurring in the Cr doped samples without the formation of mullite. In the samples annealed to 500 and 800 $^{\circ}\text{C}$, also show a lower number of the smaller flake like particles again showing that there is increased aggregation of these samples compared to those that formed mullite.

5.3.5 $\text{Mn}(\text{OAc})_3$ as a Catalyst

Manganese acetate ($\text{Mn}(\text{OAc})_3$) with the Mn^{3+} cation is a d^3 metal which exhibits a strong Jahn-Teller effect in the high spin state and a weak Jahn-Teller effect in the low spin state.

5.3.5.1 Vibrational Spectroscopy

The IR spectra for the samples synthesised with the addition Mn^{3+} of are shown in figures 5.36 and 5.37. The profiles of the spectra are similar to those of the Cr doped samples. The bands present at 1325 and 925 cm^{-1} are again assigned to organic/nitrate species and Si-OH vibrations respectively. Again after heating to 500 and 800 $^{\circ}\text{C}$, these peaks disappear showing the removal of these species from the samples. Across all of the samples, there is no indication of the formation of mullite.

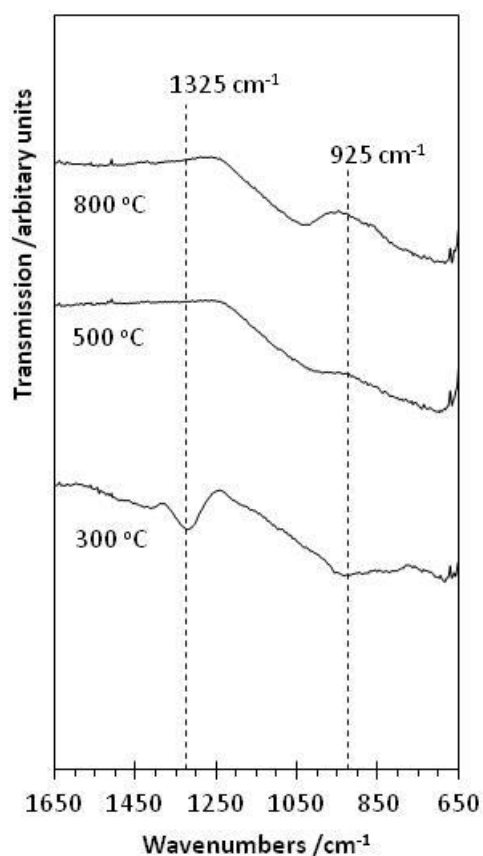


Figure 5.36: ATR-FTIR spectra for mullite samples prepared with the addition of $\text{Mn}(\text{OAc})_3$ annealed to 300, 500 and 800 °C

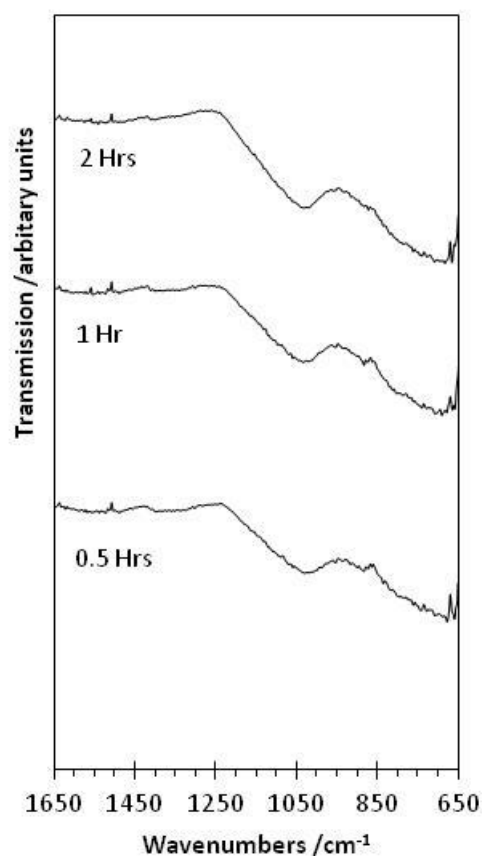


Figure 5.37: ATR-FTIR spectra for mullite samples prepared with the addition of $\text{Mn}(\text{OAc})_3$ annealed to 800 °C for 0.5, 1 and 2 hours

5.3.5.2 X-Ray Diffraction

The diffraction data for the Mn doped samples annealed to 300, 500, and 800 °C for 2 hours are shown in figure 5.38 and at 800 °C for 0.5, 1, and 2 hours are shown in figure 5.39. The profiles of the spectra show the same pattern as those of the Cr doped samples. There is no observable evolution of mullite across any of the samples annealed from 300 to 800 °C; which is also seen in IR data.

Since Mn^{3+} is Jahn-Teller active in both the high and low spin electronic states, mullite is expected to form using the current hypothesis that Jahn-Teller active compounds aid the low temperature formation of mullite; a theory that has been positively tested with the previous samples. A plausible reason for the lack of mullite formation may come from the

stability of the Mn^{3+} ion. The 3+ oxidation state of manganese is not the preferred state for the manganese cation. Both the 2+ and 4+ oxidation states are the more energetically preferred states. It is possible that either an oxidation or reduction of the manganese ion occurs to allow it to achieve the 2+ or 4+ oxidation state.

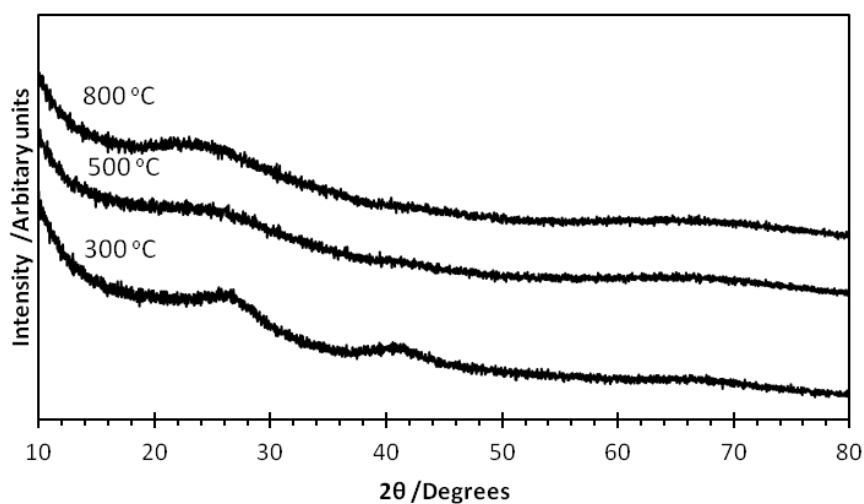


Figure 5.38: XRD data for mullite samples prepared with the addition of $\text{Mn}(\text{OAc})_3$ annealed to 300, 500 and 800 °C

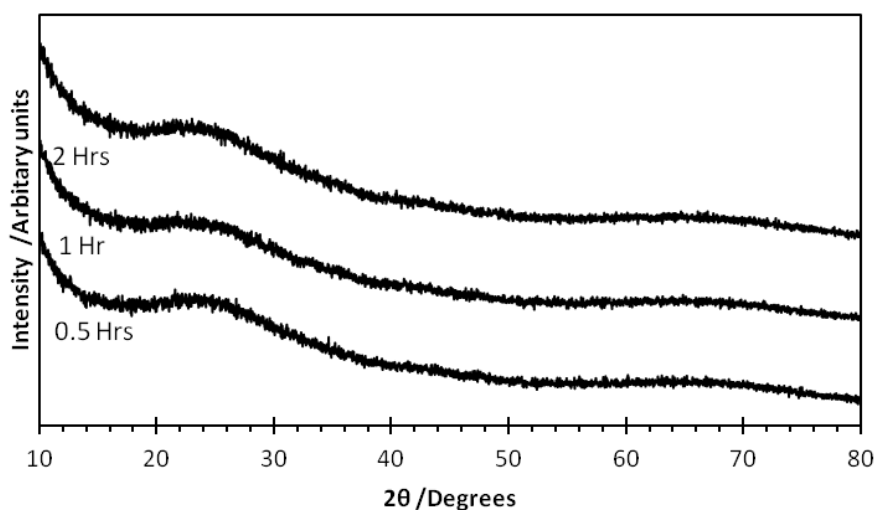


Figure 5.39: XRD data for mullite samples prepared with the addition of $\text{Mn}(\text{OAc})_3$ annealed 800 °C for 0.5, 1, and 2 hours

5.3.5.3 Scanning Electron Microscopy

The SEM images for the Mn doped samples (fig 5.40) also show the same patterns on annealing as the Cr based samples. The Mn samples across all temperature ranges show, again, less of the smaller flake like particles than the Cu and Fe doped samples. This again shows that there is increased particle aggregation within the samples that do not form mullite.

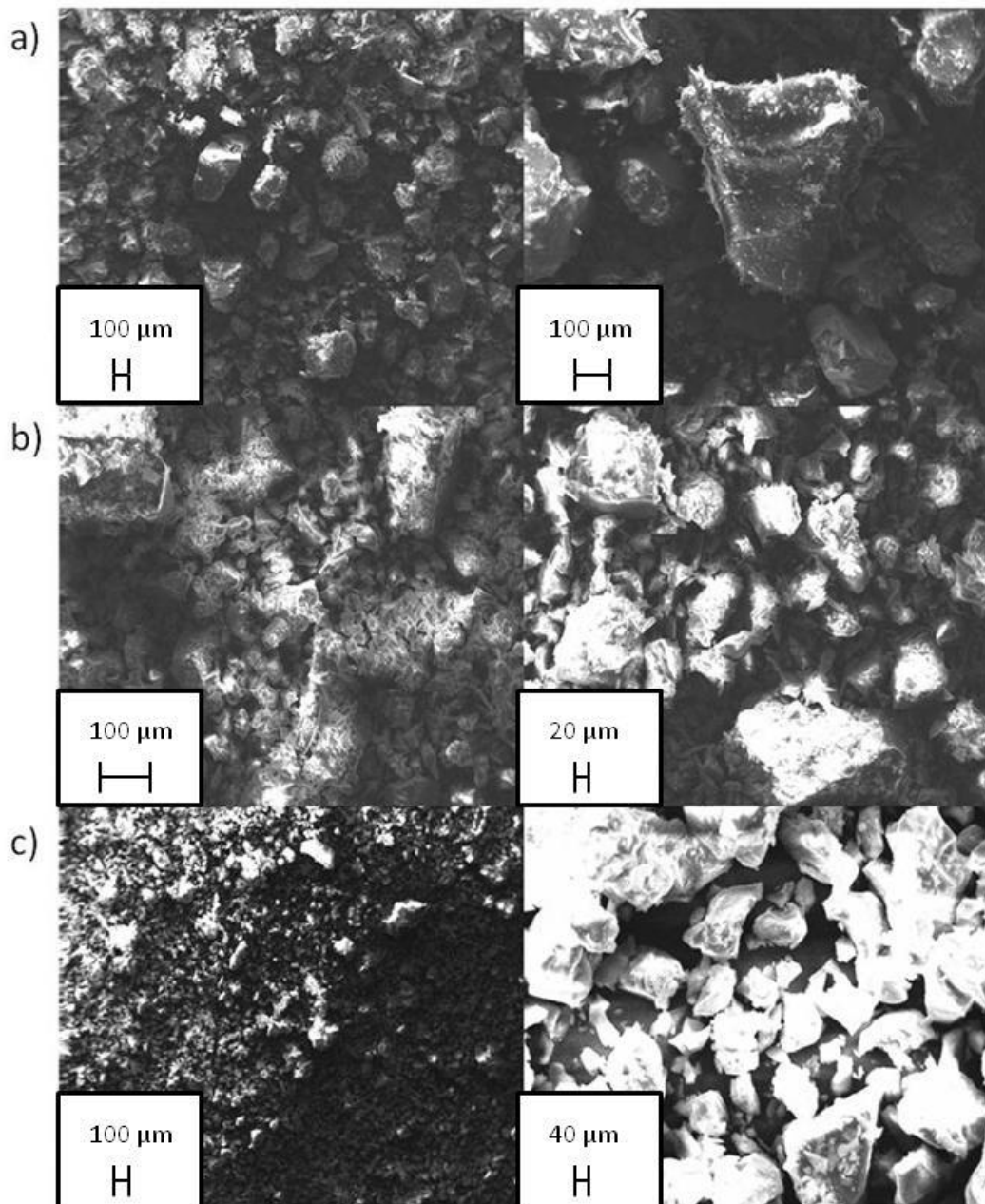


Figure 5.40: SEM Images of mullite samples prepared with the addition of $\text{Mn}(\text{OAc})_3$ annealed to a) 300, b) 500 and c) 800 °C

5.4 Summary

In this Chapter, the synthesis of mullite and its effects on both phosphate powder formation and in tensile strength coatings has been studied. The addition of mullite powders to the reaction mixture of phosphoric acid and aluminium precursors inhibited the formation of aluminium metaphosphate. The samples analysed using aluminium hydroxide as a precursor showed that a minimal amount of metaphosphate formed; however in the aluminium nitrate and chloride based samples; aluminium orthophosphate was the main product. The effects of orthophosphate formation versus metaphosphate formation were seen in the magnetostriction testing data of the coatings. The nitrate and chloride based coatings showed a decrease in performance after extended annealing times which was attributed to the aggregation of the orthophosphate particles; the hydroxide based coatings did not follow this trend due to the formation of metaphosphate. This drop in performance was also observed in the pure mullite coatings, which attributed again to particle aggregation.

Due to the large nature of the mullite particles used, an attempt to form nano-scale low temperature mullite was undertaken. Using a variety of additives, it was shown that the addition of Jahn-Teller active metal complexes resulted in the formation of mullite. The lack of evidence of mullite formation seen from the IR and XRD from the CrCl_3 doped samples corroborates the hypothesis that the addition of a non-Jahn-Teller active compound does not facilitate the low temperature synthesis of mullite. This data fits the theory that the addition of Jahn-Teller active species is required for the low temperature synthesis of mullite; Cr^{3+} is a d^3 metal and so does not exhibit any Jahn-teller effect. Additionally, no mullite was observed in the $\text{Mn}(\text{OAc})_3$ samples despite $\text{Mn}^{3+}(d^3)$ exhibiting a Jahn-Teller effect in both high and low-spin configurations. This was attributed to the relative instability of the Mn^{3+} oxidation state compared to the preferred Mn^{2+} and Mn^{4+} states.

This shows that any J-T active compounds used in the low temperature synthesis of mullite is required to be in a stable oxidation state.

The iron nitrate complex is high spin d^5 system, meaning that it does not exhibit any Jahn-Teller effects. However if the Fe^{3+} ion complexes with the precursor reagents, then the system may become low spin, meaning that a weak Jahn-Teller effect would be observed. This indicates that care must be taken when choosing an additive for low temperature mullite synthesis; as when the additive ion complexes with the reaction precursors, the system may switch between high and low spin. For mullite formation to occur this work suggests that the oxidation state of the dopant ion must be Jahn-Teller active when in its low spin state. Confirmation of this can be tested through the use of a compound that exhibits a Jahn-Teller effect in high-spin configurations, but no effect under low-spin configuration; this can be achieved through the use of a d^6 complex. If no mullite is formed under these reaction conditions then the requirement that additives are required to be Jahn-Teller active in their low-spin configuration can be proven.

5.5 References

1. Y. Okamoto, H. Fukudome, K. Hayashi and T. Nishikawa, *Journal of the European Ceramic Society*, 1990, **6**, 161-168.
2. T. Kumazawa, S. Kanzaki, S. Ohta and H. Tabata, *Nippon Seramikkusu Kyokai Gakujutsu Ronbunshi-Journal of the Ceramic Society of Japan*, 1988, **96**, 85-91.
3. W. Kollenberg and H. Schneider, *Journal of the American Ceramic Society*, 1989, **72**, 1739-1740.
4. H. Schneider and K. MacKenzie, *Journal of the European Ceramic Society*, 2001, **21**, III-III.
5. S. Ilic, S. Zec, M. Miljkovic, D. Poleti, M. Posarac-Markovic, D. Janackovic and B. Matovic, *Journal of Alloys and Compounds*, 2014, **612**, 259-264.
6. P. A. Lessing, R. S. Gordon and K. S. Mazdiyasi, *Journal of the American Ceramic Society*, 1975, **58**, 149-149.
7. L. S. Cividanes, T. M. B. Campos, L. A. Rodrigues, D. D. Brunelli and G. P. Thim, *Journal of Sol-Gel Science and Technology*, 2010, **55**, 111-125.
8. J. Ossaka, *Nature*, 1961, **191**, 1000-8.
9. M. Tokonami, Y. Nakajima and N. Morimoto, *Acta Crystallographica Section A*, 1980, **36**, 270-276.

10. S. Chaudhun, S. Patra and A. Chakraborty, *Journal of the European Ceramic Society*, 1999, **19**, 2941-2950.
11. R. Roy, *Journal of the American Ceramic Society*, 1956, **39**, 145-146.
12. E. Tkalcec, R. Nass, J. Schmauch, H. Schmidt, S. Kurajica, A. Bezjak and H. Ivankovic, *Journal of Non-Crystalline Solids*, 1998, **223**, 57-72.
13. U. Selvaraj, S. Komarneni and R. Roy, *J. Solid State Chem.*, 1993, **106**, 73-82.
14. C. Gerardin, S. Sundaresan, J. Benziger and A. Navrotsky, *Chemistry of Materials*, 1994, **6**, 160-170.
15. D. J. Cassidy, J. L. Woolfrey, J. R. Bartlett and B. Ben-Nissan, *Journal of Sol-Gel Science and Technology*, 1997, **10**, 19-30.
16. X.-H. Jin, L. Gao and J.-K. Guo, *Journal of the European Ceramic Society*, 2002, **22**, 1307-1311.
17. J. C. Huling and G. L. Messing, *Journal of Non-Crystalline Solids*, 1992, **147**, 213-221.
18. J. C. Huling and G. L. Messing, *Journal of the American Ceramic Society*, 1989, **72**, 1725-1729.
19. B. Bagchi, S. Das, A. Bhattacharya, R. Basu and P. Nandy, *Journal of the American Ceramic Society*, 2009, **92**, 748-751.
20. Y. Bao and P. S. Nicholson, *Journal of the American Ceramic Society*, 2006, **89**, 465-470.
21. Y. Wang and J. Liu, *International Journal of Applied Ceramic Technology*, 2009, **6**, 190-194.
22. C. Baudin, *Journal of Materials Science*, 1997, **32**, 2077-2086.
23. S. D.F. and A. P.W., *Inorganic Chemistry, Fourth Edition*, Oxford University Press, 2006.
24. M. Winter, *d-Block Chemistry*, Oxford University Press, 1994.
25. R. L. Frost, *Spectrochimica Acta Part a-Molecular and Biomolecular Spectroscopy*, 2004, **60**, 1439-1445.
26. A. John, D. Philip, K. R. Morgan and S. Devanarayanan, *Spectrochimica Acta Part a-Molecular and Biomolecular Spectroscopy*, 2000, **56**, 2715-2723.
27. H. J. Han and D. P. Kim, *Journal of Sol-Gel Science and Technology*, 2003, **26**, 223-228.
28. V. L. Bemmer, PhD Thesis in The Properties of Electrical Steels and Their Coatings, Cardiff University, 2013.
29. P. Y. Zhang, J. C. Liu, H. Y. Du, S. Li and R. Xu, *Chemical Communications*, 2010, **46**, 3988-3990.
30. B. Chu, G. Tobias, C. Salzmann, B. Ballesteros, N. Grobert, R. Todd and M. Green, *Journal of Materials Chemistry*, 2008, **18**, 5344-5349.
31. D. J. Cassidy, J. L. Woolfrey, J. R. Bartlett and B. BenNissan, *Journal of Sol-Gel Science and Technology*, 1997, **10**, 19-30.

Chapter 6: Conclusions and Future Work

Contents

6.1: Introduction	186
6.2: Conclusions	186
6.2.1: Aluminium Metaphosphate Powders	186
6.2.2: Analysis of Tensile Stress Coatings	188
6.2.3: Mullite Powders and Their Applications as Stress Coatings	189
6.3: Future Work	190
6.4: References	191

6.1: Introduction

The goal of this thesis has been to examine and improve tensile stress coatings for applications on electrical steels. The coatings impart tension onto the substrate which provides a physical holding to counteract the magnetostrictive effect which reduces power losses. The work progresses from previous findings that magnesium phosphates outperform aluminium analogues at reducing the effects of magnetostriction but were prone to hydration¹ which reduced the coatings efficiency. It was concluded that the higher performance of the magnesium phosphate coatings was due to the formation of magnesium metaphosphate on annealing; this transition did not occur in the aluminium orthophosphate based coatings. Chapter 3 examined the formation of aluminium metaphosphate from aluminium precursors through an array of bulk and surface analysis techniques. Chapter 4 investigated the performance of these compounds as tensile stress coatings, comparing them against the current on-line standard aluminium orthophosphate based coatings. Chapter 5 studies the use of mullite as an alternative to phosphate based coatings; examining both their application as a coating and their low temperature synthesis. The conclusions of the work across the various chapters are detailed in the following section and a summary of potential future work is given to guide further research in the field.

6.2: Conclusions

6.2.1: Aluminium Metaphosphate Powders

The theme of chapter 3 was the examination of the formation of aluminium metaphosphate ($\text{Al}(\text{PO}_3)_3$) powders using readily available precursors, studying the chemistry of their formation and susceptibility towards thermal hydration. Unlike its magnesium analogues, aluminium orthophosphate does not transform to metaphosphate

on annealing to 800 °C. As an alternative to the orthophosphate, the formation of metaphosphate has been attempted through the use of precursors.

From the reaction of aluminium precursors (hydroxide ($\text{Al}(\text{OH})_3$), nitrate ($\text{Al}(\text{NO}_3)_3$) and chloride (AlCl_3)) with phosphoric acid (H_3PO_4), $\text{Al}(\text{PO}_3)_3$ was found to form by 800 °C in all cases. Bulk analysis of the samples at transitional temperatures showed a variation in the mechanisms of formation when using different precursors. This was most notable in the ^{31}P NMR which showed the presence of various intermediate compounds; this included the cubic and monoclinic $\text{Al}(\text{PO}_3)_3$ phases, both of which were present in the nitrate based samples at 800 °C where as the hydroxide or chloride samples were fully cubic metaphosphate.

Vibrational spectroscopy showed the $\text{Al}(\text{PO}_3)_3$ samples were stable towards thermal hydration after periodic testing of samples within a humidity chamber. This showed a positive difference between aluminium and magnesium metaphosphates and gave solid evidence that the samples were suitable for use as tensile stress coatings.

Analysis of the surfaces of the samples yielded very interesting results. As with the bulk analysis, there was a marked difference between the samples examined at intermediate temperatures. The nitrate and chloride samples at lower temperature showed a lack of aluminium species on the surfaces of the compounds, this led to the conclusion that there was an aggregation of hydrated phosphate species present on the surfaces at lower annealing temperatures.

The combination of the O(1s) XP spectra with the bulk analysis allowed for a re-analysis of the currently accepted assignments of the O(1s) region. The work by Gresch et al. on sodium phosphates, assigned the higher binding energy peak to bridging oxygen and the lower binding energy peak to non-bridging oxygen² whilst observing the same trend of

increased intensity of the peak as metaphosphate formed. Through analysing the shifts of the peak ratios and combining this with the bulk analysis which shows full conversion to metaphosphate by 800 °C, we propose the assignments given by Gresch should be used limitedly and with caution outside of analysis of sodium phosphates.

6.2.2: Analysis of Tensile Stress Coatings

An analysis of the performance of tensile stress coatings was presented and discussed in chapter 4. Following on from the results discussed in chapter 3, the preparation of aluminium metaphosphate coating mixtures was attempted using the reaction of aluminium precursors and phosphoric acid. Positive confirmation, through the use of vibrational and XP spectroscopy, of the formation of aluminium metaphosphate in the coatings proved more difficult than with the powder samples in chapter 3. This was attributed to the addition of colloidal silica in the coating mixture, which was absent in the powder samples, obscuring the O(1s) region of the XP spectra. Additionally the peak profiles in IR spectra of the samples, showed a broader character than those of the sharper better defined peaks of powder samples; with a lack of coating uniformity observed across samples through the assignment of peaks to the forsterite undercoating.

Initial testing data of the coatings ability to inhibit the effect of magnetostriction was difficult to ascertain due to a de-wetting issue observed on the coated substrate. This issue was addressed by increasing the P:Al ratio from 3/1 to 4/1, allowing for a more accurate data set to be collected. To test the performance of the coatings they were measured against the current standard coatings based on aluminium orthophosphate (AlPO_4). The testing data showed a general trend towards improvements in performance with respect to annealing time for the $\text{Al}(\text{PO}_3)_3$; this trend was absent in the case of the AlPO_4 coatings. The improvements were attributing to the increasing formation of metaphosphate within the coatings and are highlighted in SEM images which showed the formation of a good coating

coverage across the surface of the substrate. Comparatively, AlPO_4 coatings were subject to particle aggregation leading to a poor coating coverage.

To ensure an accurate analysis of the performance of the stress coatings, additional testing was undertaken on the coated samples. Firstly, the effect of the stress relief annealing (SRA) process was examined; this process removes the stress in the substrate which is added during the cutting process. Whilst the SRA treatment process was shown to be an important factor in stress shifts of the samples, it proved difficult to distinguish between the effects of SRA and the chemical effects of the coatings. The second consideration was to ensure a good uniformity between the substrates used for testing. This procedure set up parameters to minimise deviations in the magnetic properties of the steel substrate samples. This process provided some clarity to the results but ambiguity due to the effects of SRA is still present. This lead to the conclusion that rather than using Epstein strips (approx. 5 x 30 cm) the performance of meta- vs. ortho-phosphate coatings needs to be tested on substrate sizes large enough that the SRA process is not required.

6.2.3: Mullite Powders and Their Applications as Stress Coatings

Chapter 5 examined the use of mullite as an alternative to phosphate based tensile strength coatings. The first part of the work examined the application of mullite powders in stress coatings. Mullite powders were added to phosphate reaction mixtures covered in chapter 3. Vibrational spectroscopy showed that the addition of mullite powders to the reaction mixture inhibited the formation of aluminium metaphosphate. The data showed that the main product of the reaction was AlPO_4 with only a small amount of $\text{Al}(\text{PO}_3)_3$ formed from the reaction of aluminium hydroxide and phosphoric acid. This is in contrast to the work presented in chapter 3 which showed full metaphosphate formation by 800 °C.

This lack of metaphosphate formation was echoed in the magnetostriction testing data. In all the nitrate and chloride samples a decrease in performance in inhibiting the

magnetostrictive effect with respect to increasing annealing times was shown; this was attributed to the aggregation of orthophosphate particles. However, the hydroxide samples did not show this trend with the partial formation of metaphosphate.

Analysis was also undertaken on the formation of nano-scale mullite at low temperatures. This work follows the synthesis methods prescribed by Bagchi et al.³, using the addition of CuSO_4 to promote the formation of mullite by 800 °C. In this work the addition of various additives were used to test the hypothesis that Jahn-Teller active compounds promote the low temperature formation of mullite. The results show that these compounds do promote mullite formation with evidence pointing towards that the complexes are Jahn-Teller active in their low-spin electron state and are a stable oxidation state. However, analysis of the particle sizes of the compounds showed that the synthesis of nano-scale mullite was not achieved with the size of the aggregates being measured between approximately 100 and 200 μm .

6.3: Future Work

The initial scope of this project was the broad topic of improving the performance of magnetic steel coatings. The body of the work focuses on a number of subjects to that end: the formation of aluminium metaphosphates stable to thermal hydration, their suitability as tensile stress coatings compared to aluminium orthophosphate, and the design of mullite powders and coatings as an alternative to traditional phosphate coatings. Whilst the studies have produced findings which advance the subject, there are a number of experiments which can be planned to further the work.

The testing of the applications of aluminium metaphosphate as a tensile strength coating yielded interesting results. However, there was a degree of ambiguity in the analysis of the results due to the additional stresses added when cutting the substrate samples. This

ambiguity can be removed by using larger samples than the Epstein strips currently used. The larger samples would lead to a reduction of the stress added when cutting and would mean that the SRA treatment process is not required. This would lead to a full analysis of the effects of the stress added to the steel by the coatings being assessable.

The work on mullite could lead to new avenues for investigations into tensile stress coatings. If work continues into forming nano-scale mullite its applications as a stress coating can be assessed. With the work indicating that metaphosphates outperform orthophosphates by forming a film across the surface, investigations should begin on assessing the performance of other materials which mimic the coating qualities of metaphosphates. Additionally, the attempted formation of mullite using a d^6 complex could be attempted to solidify the findings in chapter 5; that for mullite to form the dopant ion must be in a low spin state. Due to d^6 only exhibiting mullite formation in the high-spin state.

6.4: References

1. V. L. Bemmer, Ph D Thesis in The Properties of Electrical Steels and Their Coatings, Cardiff University, 2013.
2. R. Gresch, W. Mullerwarmuth and H. Dutz, *Journal of Non-Crystalline Solids*, 1979, **34**, 127-136.
3. B. Bagchi, S. Das, A. Bhattacharya, R. Basu and P. Nandy, *Journal of the American Ceramic Society*, 2009, **92**, 748-751.